



HAL
open science

Modeling of random heterogeneous materials from microscale to macroscale

Vinh Phuc Tran

► **To cite this version:**

Vinh Phuc Tran. Modeling of random heterogeneous materials from microscale to macroscale. Engineering Sciences [physics]. Université Paris Est, École des Ponts Paris Tech, 6-8 avenue Blaise Pascal, 77455 Marne La Vallée, 2016. English. NNT : . tel-01518585v1

HAL Id: tel-01518585

<https://theses.hal.science/tel-01518585v1>

Submitted on 4 May 2017 (v1), last revised 22 Mar 2018 (v2)

HAL is a multi-disciplinary open access archive for the deposit and dissemination of scientific research documents, whether they are published or not. The documents may come from teaching and research institutions in France or abroad, or from public or private research centers.

L'archive ouverte pluridisciplinaire **HAL**, est destinée au dépôt et à la diffusion de documents scientifiques de niveau recherche, publiés ou non, émanant des établissements d'enseignement et de recherche français ou étrangers, des laboratoires publics ou privés.



Distributed under a Creative Commons Attribution - NonCommercial - NoDerivatives 4.0
International License

UNIVERSITÉ — — PARIS-EST

ÉCOLE DOCTORALE SCIENCE INGÉNIERIE ET ENVIRONNEMENT

THÈSE DE DOCTORAT
Spécialité Mécanique

Modélisation à plusieurs échelles d'un milieu continu
hétérogène aléatoire

Vinh Phuc TRAN

Thèse dirigée par Monsieur

Karam SAB

et co-encadrée par Messieurs

Sébastien BRISARD

Johann GUILLEMINOT

et soutenue le 05 octobre 2016 devant le jury composé de

M. Samuel FOREST	<i>Président du jury</i>
M. Martin OSTOJA-STARZEWSKI	<i>Rapporteur</i>
M. Bernhard PICHLER	<i>Rapporteur</i>
M. Sébastien BRISARD	<i>Examineur</i>
M. Johann GUILLEMINOT	<i>Examineur</i>
M. Karam SAB	<i>Directeur de thèse</i>

Résumé

Modélisation à plusieurs échelles d'un milieu continu hétérogène aléatoire

Lorsque les longueurs caractéristiques sont bien séparées, la théorie de l'homogénéisation propose un cadre théorique rigoureux pour les matériaux hétérogènes. Dans ce contexte, les propriétés macroscopiques peuvent être calculées à partir de la résolution d'un problème auxiliaire formulé sur un volume élémentaire représentatif (avec des conditions limites adéquates). Dans le présent travail, nous nous intéressons à l'homogénéisation de matériaux hétérogènes décrits à l'échelle la plus fine par deux modèles différents (tous deux dépendant d'une longueur caractéristique spécifique) alors que le milieu homogène équivalent se comporte, dans les deux cas, comme un milieu de Cauchy classique.

Dans la première partie, une microstructure aléatoire de type Cauchy est considérée. La résolution numérique du problème auxiliaire, réalisée sur plusieurs réalisations, implique un coût de calcul important lorsque les longueurs caractéristiques des constituants ne sont pas bien séparées et/ou lorsque le contraste mécanique est élevé. Pour surmonter ces limitations, nous basons notre étude sur une description mésoscopique du matériau combinée à la théorie de l'information. Dans cette mésostructure, obtenue par filtrage, les détails les plus fins sont lissés.

Dans la seconde partie, nous nous intéressons aux matériaux à gradient dans lesquels il existe au moins une longueur interne, qui induit des effets de taille à l'échelle macroscopique. La microstructure aléatoire est décrite par un modèle à gradient de contrainte récemment proposé. Malgré leur similarité conceptuelle, nous montrerons que le modèle à gradient de contrainte et de déformation définissent deux classes de matériaux distinctes. Nous proposons ensuite des approches simples (méthodes de champs moyens) pour mieux comprendre les hypothèses de modélisation. Les résultats semi-analytiques obtenus nous permettent d'explorer l'influence des paramètres du modèle sur les propriétés macroscopiques et constituent la première étape vers la simulation en champs complets.

Mots-clés: Homogénéisation, Modélisation probabiliste, Micromécanique, Matériaux à gradient.

Abstract

Modeling of random heterogeneous materials: from microscale to macroscale

If the length-scales are well separated, homogenization theory can provide a robust theoretical framework for heterogeneous materials. In this context, the macroscopic properties can be retrieved from the solution to an auxiliary problem, formulated over the representative volume element (with appropriate boundary conditions). In the present work, we focus on the homogenization of heterogeneous materials which are described at the finest scale by two different materials models (both depending on a specific characteristic length) while the homogeneous medium behaves as a classical Cauchy medium in both cases.

In the first part, the random microstructure of a Cauchy medium is considered. Solving the auxiliary problem on multiple realizations can be very costly due to constitutive phases exhibiting not well-separated characteristic length scales and/or high mechanical contrasts. In order to circumvent these limitations, our study is based on a mesoscopic description of the material, combined with information theory. In the mesostructure, defined by a filtering framework, the fine-scale features are smoothed out.

The second part is dedicated to gradient materials which induce microscopic size-effect due to the existence of microscopic material internal length(s). The random microstructure is described by a newly introduced stress-gradient model. Despite being conceptually similar, we show that the stress-gradient and strain-gradient models define two different classes of materials. Next, simple approaches such as mean-field homogenization techniques are proposed to better understand the assumptions underlying the stress-gradient model. The obtained semi-analytical results allow us to explore the influence on the homogenized properties of the model parameters and constitute a first step toward full-field simulations.

Keywords: Homogenization, Probabilistic modeling, Micromechanics, Gradient materials.

Remerciements

Ce travail n'aurait pu voir le jour sans une aide de financement de l'État gérée par l'Agence Nationale de la Recherche au titre du programme Investissements d'Avenir (ANR-11-LABX-022-01). Cette thèse a été réalisée au sein du laboratoire Navier en partenariat avec le laboratoire MSME. Je remercie en premier lieu M. Michel Bornert et M. Julien Yvonnet pour m'avoir permis d'effectuer cette thèse au sein de leurs équipes.

Je tiens à remercier le directeur de cette thèse, Karam Sab, pour sa direction, ses multiples conseils, ses disponibilités, pour m'avoir soutenu, toujours montré intérêt et bienveillance envers mon travail malgré ses nombreuses responsabilités.

Je souhaite exprimer toute ma gratitude à Johann Guilleminot pour son encadrement, son écoute, ses remarques et sa patience. Je le remercie également pour le temps qu'il m'a accordé et sa gentillesse. J'ai été extrêmement sensible à ses qualités humaines d'écoute et de compréhension tout au long de ce travail doctoral. Pour tout cela, sa confiance et son encouragement, je le remercie vivement.

Je souhaite exprimer toute ma reconnaissance profonde à Sébastien Brisard, qui m'a encadré au quotidien dès mon premier jour à Navier. Au moment où s'achève cette thèse, je mesure donc toute ma chance de m'être formé auprès d'un grand personnalité. Il m'a fait partager sa façon de comprendre et sa passion pour la mécanique et l'informatique scientifique. Je regretterai des nombreuses matinées passées dans son bureau pour nos discussions longues et stimulantes. Il a pour moi été un interlocuteur privilégié. Petit à petit, Sébastien m'a appris à reconnaître la valeur scientifique d'un résultat. Je lui suis reconnaissant de m'avoir fait bénéficier tout au long de ce travail de sa grande compétence, de sa rigueur intellectuelle, de son ouverture d'esprit que je n'oublierai jamais. Je le remercie de m'avoir enseigné, soutenu, motivé, encouragé et toujours m'a fait avancer. Un grand merci à toi!

Je souhaite vivement remercier M. Samuel Forest de m'avoir fait l'honneur de présider ce jury. Merci pour son critique et ses suggestions constructives. Je tiens à remercier M. Bernhard Pichler et M. Martin Ostojca-Starzewski pour avoir consacré leur temps précieux à examiner de ce mémoire de thèse. Qu'ils trouvent en ces quelques mots le témoignage de ma reconnaissance.

Je remercie M. Annael Lemaître de m'avoir autorisé à utiliser le cluster de calcul à l'IFSTTAR. Merci pour son aide et sa compréhension lors des *segmentation fault*.

Je remercie à tous les chercheurs, ingénieurs, techniciens, thésards, post-docs et stagiaires que j'ai côtoyés, qui m'ont accompagné et avec qui j'ai passé d'excellents moments au laboratoire Navier. Je salue aussi ceux avec qui j'ai partagé le bureau au cours de ces trois ans : Aissam, Elias, Francis, Rawad, Romain B. et Vianney. Je remercie mes compatriotes : Dong, Nam Nghia, Tien Hoang, Thanh Tung, Van Linh, Van Tri, Vinh Du. Je remercie enfin Rachida Atmani, Géraldine Vue, Marie-Françoise Kaspi, Sandrine Coqueret et Cécile Blanchement qui se sont

occupées des aspects administratifs et pratiques de la thèse.

Je remercie mes amis de toujours. Votre présence à ma soutenance m'a beaucoup touché.

Merci à mes amis Dinh Cuong et Danh Huong. Merci à mon père, ma mère et mon frère pour leur soutien et leurs encouragements sans faille.

Merci à tous,
Vinh Phuc Tran

Contents

I	General introduction	11
II	Stochastic modeling of mesoscopic elasticity random field	15
1	Introduction	17
1.1	Homogenization of linear elastic heterogeneous materials	17
1.1.1	Preliminaries and definition of scales	17
1.1.2	Definition of the apparent properties	19
1.2	Numerical simulation of mesoscopic elasticity tensors	20
1.2.1	Local upscaling	21
1.2.2	Filtering framework	22
1.3	Outline of the first part	23
2	Monte Carlo simulations of the mesoscopic stiffness tensor	25
2.1	Generation of the elasticity fields	25
2.1.1	Generation of microstructures	26
2.1.2	Computation of the apparent stiffness tensor of the microstructure	26
2.1.3	Computation of the mesoscopic stiffness tensor random field	27
2.2	Characterization of the mesoscopic random fields	29
2.2.1	Degree of asymmetry	29
2.2.2	Material symmetry	30
2.2.3	Second-order characterization	32
3	Stochastic framework	37
3.1	Methodology	37
3.2	Construction of an information-theoretic model for the probability density functions	38
3.3	Definition of the mesoscale moduli random fields	39
3.4	On the generation of Gaussian random fields	41
3.4.1	Krylov subspace method	42
3.4.2	Algorithmic issues	43
3.4.3	Numerical scaling test for the generation of Gaussian random field	44
3.5	Calibration of the probabilistic model	44
3.5.1	Identification through statistical estimators	45
3.5.2	Identification through the maximum likelihood method	46
3.6	Validation of the information-theoretic probabilistic model	49

3.6.1	Validation on mesoscale quantities of interest	49
3.6.2	Validation based on apparent properties	50
4	Conclusions and perspectives	53
III	Stress-gradient elasticity model	55
5	Introduction	57
5.1	Higher order models	58
5.1.1	Cosserat (micropolar) model	58
5.1.2	Couple stress model	59
5.1.3	Micromorphic model	60
5.2	Higher grade models	61
5.2.1	First strain gradient elasticity	61
5.2.2	Second strain gradient elasticity	63
5.3	Homogenization of generalized continua	64
5.3.1	Some remarks on the homogenization of generalized continua	64
5.3.2	Mean field homogenization methods	65
5.3.3	Variational principles and bounds	67
5.4	Methodology	67
6	The stress-gradient model	69
6.1	Preliminary linear algebra	69
6.1.1	Linear algebra of the trace and the trace-free part of third rank tensors	70
6.1.2	The \boxtimes -product of a fourth-rank tensor and a second-rank tensor	71
6.2	Derivation of the stress-gradient model by minimizing the complementary energy	71
6.2.1	Complementary strain energy of stress-gradient bodies	71
6.2.2	Equilibrium of a clamped, stress-gradient body	72
6.2.3	Extension to stress-free and mixed boundary conditions	73
6.3	Contribution of the trace of the stress gradient	74
6.4	Energy principles	74
6.4.1	Minimum complementary energy principle	75
6.4.2	Minimum potential energy principle	75
6.5	Linear stress-gradient elasticity	76
6.5.1	General form of isotropic compliance tensor	76
6.5.2	Simplified stress-gradient model	77
6.6	Saint-Venant problem: existence of boundary layers	78
6.6.1	Saint-Venant pure bending problem	78
6.6.2	Discussion	80
7	Homogenization of stress-gradient materials	83
7.1	General framework	83
7.1.1	Effective compliance of a representative volume element	83
7.1.2	Apparent compliance of a statistical volume element	84

7.1.3	Hill–Mandel lemma for stress-gradient materials	85
7.1.3.1	Kinematic uniform boundary conditions (KUBC)	86
7.1.3.2	Static uniform boundary conditions (SUBC)	86
7.1.3.3	Periodic boundary conditions (PBC)	87
7.1.3.4	Mixed boundary conditions (MBC)	87
7.1.4	Discussion of the boundary conditions KUBC, SUBC, PBC and MBC .	88
7.1.5	Softening size-effect in stress-gradient materials	89
7.2	Eshelby’s spherical inhomogeneity problem	90
7.2.1	General description	90
7.2.2	Isotropic loading at infinity	91
7.2.3	Uniaxial loading at infinity	94
7.2.4	The dilute stress concentration tensor of spherical inhomogeneities . . .	96
7.3	Mori-Tanaka estimates of the effective properties	97
8	Hashin-Shtrikman variational principle and bounds	101
8.1	Hashin-Shtrikman variational principle	101
8.2	Green operators of an infinite body	103
8.2.1	On the relationship between the four Green operators	103
8.2.2	Evaluation of $\hat{\mathbf{\Gamma}}_{e\tau}^{\infty}$	105
8.3	Hashin-Shtrikman bounds	107
8.3.1	Evaluation of the functional of Hashin and Shtrikman for phase-wise constant polarization fields	107
8.3.2	Optimization of the functional of Hashin and Shtrikman	109
8.3.3	On the choice of the two-point probability function	110
8.3.3.1	Debye’s correlation function	110
8.3.3.2	The model of Verlet and Weis	111
8.3.3.3	Discussions	114
9	Conclusions & Perspectives	119
IV	Closing remark	123
V	Appendix	127
A	Numerical resolution of the auxiliary problem	129
B	Toeplitz and Circulant matrix	133
B.1	Circulant matrix	133
B.2	Multilevel circulant matrix	134
B.3	Toeplitz matrix	134
B.4	Multilevel Toeplitz matrix	135

C On Eshelby's spherical inhomogeneity problem	137
C.1 Strain compatibility conditions	137
C.2 General solution	138
D Green operators: Matrix formulation	141
E Green operators: Simplification	145
F Walpole's tensor basis	147
G Stress-gradient Hill's tensor	149

Part I

General introduction

Heterogeneous materials play a predominant role in the engineering industry due to their enhanced physical (e.g. mechanical, electrical, etc.) properties. When achieved in a proper manner, the mixture of different constituents enables the tailored design of a material taking advantage of the properties of each constituent. Composites, geomaterials and concrete are popular examples of heterogeneous materials which abound in everyday life and applications. In this context, the construction of both (semi-)analytical and numerical multiscale methods providing predictive results on some properties of interest at the macroscale is of paramount importance. In practice, performing such a scale transition can be computationally intensive, especially when many length scales are involved. If the latter are well separated, in the sense that they differ by one or several orders of magnitude, the homogenization theory provides a robust framework to model such heterogeneous materials at the macroscale. In addition to the upscaling procedure, it should be noticed that the representation of information at relevant scales is also a critical ingredient in order to ensure predictiveness in the computation of the macroscopic properties. In the present work, we investigate the homogenization task starting from descriptions of the heterogeneous material at two different scales (each of which being defined by a specific length scale). While the homogeneous medium (at the macroscale) is described, in both cases, by a classical Cauchy model, the description of the random material at the finest scale differs.

In the first part of this thesis, the heterogeneous material is described, at the microscale, by a Cauchy medium involving constitutive phases exhibiting non-separated characteristic length scales and potentially, high mechanical contrasts. As mentioned previously, the computational homogenization of such random microstructures requires a large computation time, as well as large memory and storage capacities. In order to circumvent these limitations, we investigate the definition of a multiscale framework relying on the description of the material at a mesoscale, where fine-scale features are smoothed out, and building upon the combination of a filtering framework (proposed elsewhere) and information theory.

In the second part of this work, the random microstructure is described using a stress-gradient model that was recently proposed in the literature. Like its strain-gradient counterpart, the stress-gradient model introduces at least one material internal length which in turn induces macroscopic size-effects (such as those typically encountered with nanomaterials). However, stress-gradient models are shown in this work to induce so-called softening size-effects, while strain-gradient models are known to induce stiffening size-effects. As such, both models are to be used with different classes of materials. While strain-gradient models have been known for several decades, stress-gradient models are still relatively new, and simple approaches are still needed to fully understand the implications of the underlying modeling assumptions. With this goal in mind, we address the homogenization of stress-gradient materials with mean-field (Eshelby-based) approaches. Our semi-analytical derivations, which can be considered as a first step towards numerical homogenization, allow us to explore the influence of parameters such as the material internal length or the correlation length.

The two parts of this work provide two complementary approaches to the problem of scale transition in situations where the correlation length plays a significant role. Of course, these two approaches are not mutually exclusive, and might be combined to produce for example a mesoscopic description of a heterogeneous, stress-gradient material.

Part II

Stochastic modeling of mesoscopic elasticity random field

Chapter 1

Introduction

The numerical simulation of heterogeneous materials is a challenging computational task. If the length scales are well separated (in a sense to be defined), homogenization theory can provide a robust framework to model such materials at different scales. In this setting, the simulation of heterogeneous materials is usually considered at two length scales, namely (i) the *microscopic* scale, where the material under consideration is described as a statistically homogeneous and ergodic microstructure, and (ii) the *macroscopic* scale, where the heterogeneous material is substituted with an equivalent, yet homogeneous material. In practice, the homogenization procedure requires the resolution of an auxiliary boundary value problem (see section 1.1.2) that can be computationally expensive in some cases of practical interest. This is notably the case of random microstructures for which the analysis must be carried out over a large number of realizations, or that of three-dimensional microstructures exhibiting multiple not well-separated characteristic length scales and/or potentially involving constitutive phases with high contrasts of mechanical properties (Kanit et al., 2003; Bignonnet et al., 2014).

In order to overcome this shortcoming, one possibility is to perform the homogenization task at an intermediate *mesoscopic* scale where the fine-scale features of the microstructure are smoothed. One advantage of introducing such a mesoscale (between the microscopic and the macroscopic ones) is that the aforementioned auxiliary problem (to be defined in section 1.1) can subsequently be solved on a coarser discretization mesh, hence reducing the computational effort associated with numerical homogenization methods.

In this introductory chapter, we first recall in section 1.1 some preliminaries associated with the homogenization of linear heterogeneous materials in elastostatics. Section 1.2 is then concerned with a literature survey on the numerical simulation of mesoscale elasticity tensors. The outline of the first part is finally given in section 1.3.

1.1 Homogenization of linear elastic heterogeneous materials

1.1.1 Preliminaries and definition of scales

The homogenization of heterogeneous materials is usually considered between the microscopic and macroscopic scales, and requires the so-called assumption of *scale separation* (see Bornert

et al. (2001) and Ostoja-Starzewski (2006), among others) to be satisfied

$$d \ll L_{\text{RVE}} \ll L_{\text{macro}}. \quad (1)$$

In the equation above, d is the characteristic size of the heterogeneities, L_{RVE} is the size of the Representative Volume Element (RVE) associated with the random microstructure and L_{macro} is either the characteristic size of the structure or the characteristic length of the loading that the structure undergoes. The macroscopic behavior of heterogeneous materials is then characterized by an *effective* stiffness tensor, denoted by \mathbf{C}_{eff} , which relates the macroscopic strain $\langle \boldsymbol{\varepsilon} \rangle$ to the macroscopic stress $\langle \boldsymbol{\sigma} \rangle$ through

$$\langle \boldsymbol{\sigma} \rangle = \mathbf{C}_{\text{eff}} : \langle \boldsymbol{\varepsilon} \rangle, \quad (2)$$

where $\langle \cdot \rangle$ denotes volume averages over the RVE, that is

$$\langle \boldsymbol{\sigma} \rangle = \frac{1}{V} \int_{\Omega} \boldsymbol{\sigma} \, dV, \quad \langle \boldsymbol{\varepsilon} \rangle = \frac{1}{V} \int_{\Omega} \boldsymbol{\varepsilon} \, dV. \quad (3)$$

Except for periodic media (defined by a unit cell), the size of the RVE is mathematically infinite. In practice, the effective stiffness tensor \mathbf{C}_{eff} is then computed as the limit of a sequence $\{\mathbf{C}_{\text{app}}\}$ of homogenized, *apparent* stiffness tensors indexed by the finite size L of the mesoscopic domain $\Omega \subset \mathbb{R}^d$ over which the homogenization is performed – here, the limit holds in the sense that $L \rightarrow +\infty$ (Huet, 1990; Sab, 1992; Ostoja-Starzewski, 2006). Such mesoscopic domains are referred to as Statistical Volume Elements (SVE in short), and the characteristic length L_{meso} is such that

$$d < L_{\text{meso}} \text{ and } L_{\text{meso}} < L_{\text{RVE}}. \quad (4)$$

A schematic representation of scales is shown in figure 1.1, where the smoothing of microscopic features at mesoscale can notably be seen.

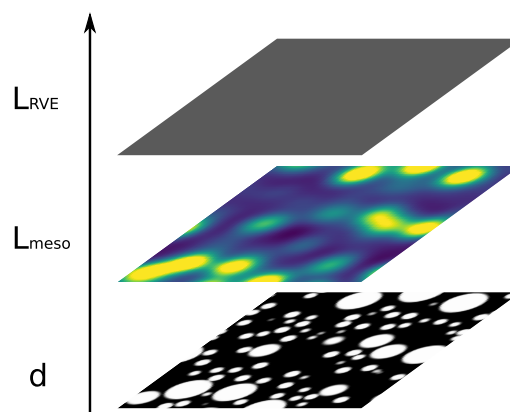


Figure 1.1. Schematic representations of the microscale, mesoscale and macroscale.

As opposed to the RVE, a SVE is characterized by apparent elastic properties that depend on the prescribed boundary conditions (as well as on L , by definition) and exhibit a non-zero level of statistical fluctuations for finite values of L . A natural quantity of interest is then the statistical (or ensemble) average of the apparent properties, which necessitates in turn the

numerical homogenization task to be performed over a large number of realizations in order to ensure the convergence of the statistical estimator. When a mesoscale description defined by a characteristic length L_{meso} is considered in order to speed up computations (by introducing, as briefly stated in the introduction, smoother coefficients in the system of stochastic partial differential equations to be solved), a desired requirement is that the homogenization of the material at microscale and mesoscale leads to the same effective behavior. In this work, we will refer to this property as the *macroscopic consistency condition*, and we note that this property does not hold for all the mesoscopic simulation techniques proposed elsewhere. The choice of L_{meso} is key to ensuring the “smoothness” of the elasticity tensor random field at mesoscale. In practice, an appropriate value of L_{meso} must be selected as a compromise between sample-path regularity, which facilitates the mathematical modeling and can be enforced by retaining a large value of L_{meso} , and computational cost (since large values of L_{meso} require solving boundary value problems over larger domains when the mesoscopic field is obtained by local upscaling; see below).

1.1.2 Definition of the apparent properties

We now consider a statistical volume element $\Omega \subset \mathbb{R}^d$ of finite size L . The microscopic stiffness tensor at point $\mathbf{x} \in \Omega$ is denoted by $\mathbf{C}(\mathbf{x})$ and depends on the observation point, due to material heterogeneity. The apparent stiffness tensor associated with the microstructure and domain Ω can be retrieved from the solution to the following auxiliary problem

$$\nabla \cdot \boldsymbol{\sigma} = \mathbf{0}, \quad (5a)$$

$$\boldsymbol{\sigma}(\mathbf{x}) = \mathbf{C}(\mathbf{x}) : \boldsymbol{\varepsilon}(\mathbf{x}), \quad (5b)$$

$$\boldsymbol{\varepsilon}(\mathbf{x}) = \nabla^s \mathbf{u}, \quad (5c)$$

where $\boldsymbol{\varepsilon}(\mathbf{x})$ is the local strain derived from displacement $\mathbf{u}(\mathbf{x})$, $\boldsymbol{\sigma}(\mathbf{x})$ denotes the local stress, $\nabla \cdot \boldsymbol{\sigma}$ denotes the divergence of stress field and $\nabla^s \mathbf{u}$ is the symmetric part of the displacement gradient. This problem has to be complemented with suitable boundary conditions so as to ensure the well-posedness of the formulation. To this aim, static uniform boundary conditions (SUBC), kinematic uniform boundary conditions (KUBC) and periodic boundary conditions (PBC) satisfying the Hill–Mandel lemma (Hill, 1963)

$$\langle \boldsymbol{\sigma} : \boldsymbol{\varepsilon} \rangle = \langle \boldsymbol{\sigma} \rangle : \langle \boldsymbol{\varepsilon} \rangle \quad (6)$$

are usually adopted (see Huet (1990) for theoretical derivations, as well as Kanit et al. (2003) for numerical investigations). As mentioned above, and under the assumption of statistical homogeneity and ergodicity, it was shown that the apparent stiffness computed with any of the above boundary conditions converges to the effective stiffness \mathbf{C}_{eff} (Sab, 1992) as $L \rightarrow +\infty$. Furthermore, the numerical results obtained in Kanit et al. (2003) suggest that PBC lead to faster convergence towards the effective properties than KUBC and SUBC.

In the present work, we adopt the PBC to compute the apparent stiffness tensor. In this case, the loading parameter is the macroscopic strain $\bar{\boldsymbol{\varepsilon}}$. The body Ω is subjected to the following displacement field on the boundary $\partial\Omega$

$$\mathbf{u}(\mathbf{x}) = \bar{\boldsymbol{\varepsilon}} \cdot \mathbf{x} + \mathbf{u}^{\text{per}}(\mathbf{x}), \quad (7)$$

where the periodic fluctuation part of the displacement field about its macroscopic counterpart $\bar{\boldsymbol{\varepsilon}} \cdot \mathbf{x}$ is denoted by $\mathbf{u}^{\text{per}}(\mathbf{x})$. At the interface between two materials, the displacement and traction vector are both required to be continuous. It follows that $\boldsymbol{\sigma}(\mathbf{x}) \cdot \mathbf{n}$ is skew periodic, where \mathbf{n} is the outer normal to the boundary of Ω . Owing to the linearity of problem (5), the macroscopic stress depends linearly on the macroscopic strain

$$\langle \boldsymbol{\sigma} \rangle = \mathbf{C}_{\text{PBC}} : \bar{\boldsymbol{\varepsilon}} = \mathbf{C}_{\text{PBC}} : \langle \boldsymbol{\varepsilon} \rangle, \quad (8)$$

where \mathbf{C}_{PBC} is the apparent stiffness associated with the periodic boundary conditions under consideration. The apparent compliance is then obtained by inversion, that is:

$$\mathbf{S}_{\text{PBC}} = (\mathbf{C}_{\text{PBC}})^{-1}. \quad (9)$$

The PBC problem is defined by equation (5) complemented with the periodic boundary conditions defined by equation (7). In practice, the auxiliary problem defined in equations (5), (7) can numerically be solved by the finite element method (Gusev, 1997; Kanit et al., 2003) or fast Fourier transform (FFT) based methods (Moulinec and Suquet, 1994, 1998) for instance. Methods to define mesoscopic elasticity tensor random fields are reviewed in the next section.

1.2 Numerical simulation of mesoscopic elasticity tensors

Mesoscopic elasticity tensor random fields are usually defined and considered within a two-step homogenization method.

In the first step, the SVE Ω of finite size L is partitioned into a finite set of subdomains (or windows), the size of which defines the characteristic length L_{meso} , and local boundary value problems are solved over all subdomains. The latter are subsequently assigned local homogenized behavior, hence defining a mesostructure characterized by the random field of apparent properties.

In the second step, the boundary value problem defined by the mesostructure over the SVE Ω is solved using a coarser discretization mesh. The obtained results are then plugged into a numerical homogenization method in order to estimate the effective properties. In a non-exhaustive manner, the mesoscopic elasticity tensors can be defined through the convolution with a weight function (Bignonnet et al., 2014; Yue and E, 2007), the multiscale finite element method (Hou and Wu, 1997) (where microscale information is captured by the localized basis functions constructed in coarser elements), the moving-window technique (Baxter and Graham, 2000) and local-global upscaling (Farmer, 2002) (see also Baxter et al. (2001); Graham and Baxter (2001); Ostoja-Starzewski (1998); Sena et al. (2013)).

As the mesoscopic fields depend on the choice of both the boundary conditions (that are prescribed on each subdomain) and the dimensionless parameter $\delta = L_{\text{meso}}/d$ (see equation (4)), it follows that mesoscopic tensors are not uniquely defined. For SUBC and KUBC, mesoscopic elasticity fields can be generated from realizations of a microstructure by the local upscaling method (Ostojca-Starzewski, 1994, 1998, 2006, 2007), where two random fields corresponding to each boundary condition (KUBC, SUBC) are considered. The material response at mesoscale domain is then bounded from above and below (Huet, 1990). For PBC, the mesoscopic elasticity

tensor can be defined by the moving-window technique (Baxter and Graham, 2000) or a filtering framework (Bignonnet et al., 2014), for instance.

We now focus on the local upscaling technique Ostoja-Starzewski (2007) and the filtering framework introduced in Bignonnet et al. (2014) as ways to simulate mesoscopic elasticity tensor random fields.

1.2.1 Local upscaling

The local upscaling method has been proposed and investigated in Ostoja-Starzewski (1994, 1998, 2006, 2007) (see also Sena et al. (2013)). In the spirit of the seminal work by Huet Huet (1990), the local upscaling method aims at bounding the material response at mesoscale by two random fields corresponding to KUBC and SUBC problems respectively. The general methodology can be summarized as follows.

- First, N realizations of the random microstructure are generated by means of a standard Monte Carlo approach, for instance.
- Second, and for each realization θ of the microstructure, mesoscale subdomains of size L_{meso} are virtually created and characterized by the dimensionless parameter $\delta = L_{\text{meso}}/d$, with d the characteristic size of the heterogeneities.
- For each subdomain, auxiliary boundary value problems are then solved under KUBC and SUBC, which allows the apparent stiffness and compliance tensors $\mathbf{C}_{\text{KUBC}}^\delta(\theta)$ and $\mathbf{S}_{\text{SUBC}}^\delta(\theta)$ associated with the realization θ of the microstructure to be computed. Note that the following inequality holds Huet (1990)

$$\left(\mathbf{S}_{\text{SUBC}}^\delta(\theta)\right)^{-1} \leq \mathbf{C}_{\text{KUBC}}^\delta(\theta). \quad (10)$$

In the present work, $\mathbf{A} \leq \mathbf{B}$ is to be understood in the sense of associated quadratic forms. It was shown in Huet (1990) that the effective properties are bounded from above and below by the apparent properties corresponding to SUBC and KUBC problems

$$\mathbb{E}\left\{\left(\mathbf{S}_{\text{SUBC}}^\delta\right)^{-1}\right\} \leq \mathbf{C}_{\text{eff}} \leq \mathbb{E}\left\{\mathbf{C}_{\text{KUBC}}^\delta\right\}. \quad (11)$$

When δ tends to infinity (that is, for $L_{\text{meso}} \rightarrow +\infty$), the SVE approaches the RVE limit, in which case the mesoscopic stiffness and compliance tensors (defined for KUBC and SUBC respectively) become deterministic and converge to the associated effective tensors. It should be noted that the material symmetry exhibited at mesoscale usually differs from the ones exhibited at microscale and macroscale, and that realizations of mesoscopic random fields are generally found to be anisotropic. Moreover, the gap between the lower and upper bounds becomes more significant at large mechanical contrasts (Ostoja-Starzewski, 1998, 2006).

As an illustration, the local upscaling approach was recently employed to quantitatively characterize the correlation structure of the mesoscopic stiffness and compliance random fields for a two-dimensional random checkerboard microstructure Sena et al. (2013). The analysis was completed on the eight-rank normalized covariance tensor $\mathcal{R}(\mathbf{x}, \mathbf{y})$ of the stiffness random field defined as

$$\mathcal{R}_{ijklpqrs}(\mathbf{x}, \mathbf{y}) = \frac{\mathbb{E}\{[C_{ijkl}(\mathbf{x}) - \mathbb{E}\{C_{ijkl}(\mathbf{x})\}][C_{pqrs}(\mathbf{y}) - \mathbb{E}\{C_{pqrs}(\mathbf{y})\}]\}}{[(\mathbb{E}\{C_{ijkl}(\mathbf{x})^2\} - \mathbb{E}\{C_{ijkl}(\mathbf{x})\}^2)(\mathbb{E}\{C_{pqrs}(\mathbf{y})^2\} - \mathbb{E}\{C_{pqrs}(\mathbf{y})\}^2)]^{1/2}}. \quad (12)$$

A similar normalized covariance tensor was defined for the compliance random field. Note that owing to statistical homogeneity and isotropy, $\mathcal{R}_{ijklpqrs}(\mathbf{x}, \mathbf{y})$ only depends on the norm of the lag vector $\boldsymbol{\tau} = \mathbf{x} - \mathbf{y}$, that is $\mathcal{R}(\mathbf{x}, \mathbf{y}) = \mathcal{R}(\|\mathbf{x} - \mathbf{y}\|)$ (with a slight abuse of notation). The study was conducted for various values of volume fraction and mechanical contrast, hence providing an extensive database for the construction of analytical correlation functions for mesoscopic stiffness (or compliance) random fields.

1.2.2 Filtering framework

In this section, we briefly recall the theoretical filtering framework for periodic homogenization introduced by [Bignonnet et al. \(2014\)](#). As mentioned in section 1.1, the apparent stiffness \mathbf{C}_{PBC} relates the macroscopic strain $\langle \boldsymbol{\varepsilon} \rangle = \bar{\boldsymbol{\varepsilon}}$ (see equation (7)) to the macroscopic stress $\langle \boldsymbol{\sigma} \rangle$

$$\langle \boldsymbol{\sigma} \rangle = \mathbf{C}_{\text{PBC}} : \langle \boldsymbol{\varepsilon} \rangle. \quad (13)$$

Because of the linearity of the problem defined by equation (5), the local strain $\boldsymbol{\varepsilon}(\mathbf{x})$ depends linearly on the macroscopic strain $\langle \boldsymbol{\varepsilon} \rangle$. This linear relationship is expressed through the strain localization tensor $\mathbf{A}(\mathbf{x})$

$$\boldsymbol{\varepsilon}(\mathbf{x}) = \mathbf{A}(\mathbf{x}) : \langle \boldsymbol{\varepsilon} \rangle. \quad (14)$$

Suppose now that equation (5) is resolved, so that the local strain $\boldsymbol{\varepsilon}(\mathbf{x})$ and the local stress $\boldsymbol{\sigma}(\mathbf{x})$ are known. The so-called *mesoscopic strain* and *mesoscopic stress* fields are then obtained through a convolution with a compact support kernel ρ , that is

$$\tilde{\boldsymbol{\sigma}}(\mathbf{x}) = \int_{\mathbb{R}^d} \rho(\mathbf{x} - \mathbf{y}) \boldsymbol{\sigma}(\mathbf{y}) dV_{\mathbf{y}} = (\rho * \boldsymbol{\sigma})(\mathbf{x}), \quad (15a)$$

$$\tilde{\boldsymbol{\varepsilon}}(\mathbf{x}) = \int_{\mathbb{R}^d} \rho(\mathbf{x} - \mathbf{y}) \boldsymbol{\varepsilon}(\mathbf{y}) dV_{\mathbf{y}} = (\rho * \boldsymbol{\varepsilon})(\mathbf{x}), \quad (15b)$$

where the kernel ρ satisfies the following normalization property

$$\int_{\mathbb{R}^d} \rho(\mathbf{x}) dV_{\mathbf{x}} = 1. \quad (16)$$

It can be verified that the mesoscopic stress $\tilde{\boldsymbol{\sigma}}$ (resp. the mesoscopic strain $\tilde{\boldsymbol{\varepsilon}}$) are statically (resp. kinematically) admissible. Introducing the fourth-order tensor $\tilde{\mathbf{C}}$ defined as follows

$$\tilde{\mathbf{C}}(\mathbf{x}) = (\rho * (\mathbf{C} : \mathbf{A})(\mathbf{x})) : (\rho * \mathbf{A})^{-1}(\mathbf{x}), \quad (17)$$

it can readily be shown ([Bignonnet et al., 2014](#)) that $\tilde{\boldsymbol{\sigma}}(\mathbf{x}) = \tilde{\mathbf{C}}(\mathbf{x}) : \tilde{\boldsymbol{\varepsilon}}(\mathbf{x})$. Therefore, $\tilde{\mathbf{C}}$ can be seen as the stiffness of the (filtered) mesostructure. It should be noticed, however, that this tensor does not exhibit the major symmetry. Note that two different admissible kernels could be selected in order to define the mesoscopic stress $\tilde{\boldsymbol{\sigma}}$ and strain $\tilde{\boldsymbol{\varepsilon}}$ fields (see equation (15)). However, noticing that the kernel actually defines the mesoscopic scale for the field under consideration (and then, the probabilistic properties of the random field thus defined), and given the linear

relation between the filtered quantities $\tilde{\sigma}$ and $\tilde{\varepsilon}$, there is no *a priori* physical reason to do so. The following equations then hold for all \mathbf{x} in Ω

$$\nabla \cdot \tilde{\sigma} = \mathbf{0}, \quad (18a)$$

$$\tilde{\sigma}(\mathbf{x}) = \tilde{\mathbf{C}}(\mathbf{x}) : \tilde{\varepsilon}(\mathbf{x}), \quad (18b)$$

$$\tilde{\varepsilon}(\mathbf{x}) = \nabla^s \tilde{\mathbf{u}}, \quad (18c)$$

$$\tilde{\mathbf{u}}(\mathbf{x}) = \langle \tilde{\varepsilon} \rangle \cdot \mathbf{x} + \tilde{\mathbf{u}}^{\text{per}}(\mathbf{x}). \quad (18d)$$

Consequently, the mesoscopic stress and strain fields are the solution to the boundary value problem defined with the mesoscopic stiffness. Observing that convolution with a normalized kernel does not affect volume average, i.e.

$$\langle \sigma \rangle = \langle \tilde{\sigma} \rangle, \quad \langle \varepsilon \rangle = \langle \tilde{\varepsilon} \rangle, \quad (19)$$

[Bignonnet et al. \(2014\)](#) concluded that the microstructure \mathbf{C} and the mesostructure $\tilde{\mathbf{C}}$ have the same homogenized properties. In other words, the mesoscopic tensor random fields thus defined satisfy the macroscopic consistency condition. It follows that the apparent properties of the initial microstructure over Ω can readily be obtained by solving the problem stated by equation (18) and involving the filtered microstructure. In practice, the latter problem turns out to be more tractable from a computational standpoint than the original one defined at microscale, as the mesoscopic elasticity field turns out to be much smoother than its microscopic counterpart. It should be noticed that adjusting the size of the filter allows for a continuous description of the local stiffness of heterogeneous materials ranging from microscale to macroscale. Finally, one may note that the computation of the mesoscopic stiffness $\tilde{\mathbf{C}}$ requires the original problem (given by equation (5)) to be solved. Therefore, the above filtering framework does not help reducing the computational effort in a deterministic setting, and finds its very purpose while applied to random heterogeneous microstructures.

1.3 Outline of the first part

In this first part, we address the numerical simulation and probabilistic modeling of mesoscopic elasticity random fields, with the aim to reduce the computational time associated with the homogenization of heterogeneous microstructures with (potentially multiple) non-separated scales and/or high mechanical contrasts. For this purpose, we follow a four-step methodology described below.

First, we perform numerical simulations of mesoscopic fields. Such computations, which are performed within the filtering framework proposed in ([Bignonnet et al., 2014](#)) (as the latter satisfies the macroscopic consistency condition introduced in section 1.1.1), allow fundamental features of the random fields to be estimated (such as the mean function, the correlation structure and the exhibited material symmetry), and constitute a database that will subsequently be used for calibration and validation purposes. These issues are discussed in chapter 2.

Second, we construct, in chapter 3 (see sections 3.1, 3.2 and 3.3), an information-theoretic probabilistic model of the aforementioned non-gaussian mesoscopic elasticity random fields. Such models are derived in the framework of information theory ([Jaynes, 1957a,b](#)) and are

therefore intended to be the most objective ones (in the sense that the modeling bias is reduced) with respect to available information, such as fundamental mathematical requirements (e.g. positive-definiteness) or phenomenological concerns. In addition, these models involve a low-dimensional parametrization, hence making the identification task more tractable. Simulation aspects are briefly reviewed in section 3.4.

In a third step detailed in section 3.5, we investigate the identification of the hyperparameters involved in the stochastic model. These parameters typically define the family of first-order marginal distributions of the non-gaussian random fields, as well as spatial correlation lengths. This task is discussed using either direct statistical estimators (which may require a large set of samples to achieve convergence) or the maximum likelihood method (which may be more suitable when data are limited).

Finally, we discuss the validation of both the probabilistic framework and the calibration strategy (see [Noshadravan et al. \(2013\)](#) for instance). Since the validation procedure only holds for a particular quantity of interest, we specifically address this task by investigating the capability of the calibrated stochastic model to mimic, on the one hand, given features extracted from the database (such as second-order statistics), and on the other hand to predict the effective properties with a reasonable accuracy. These points are in section 3.6. Conclusions and some perspectives of the first part are then drawn in chapter 4.

Chapter 2

Monte Carlo simulations of the mesoscopic stiffness tensor

This chapter is devoted to the simulation of the microscopic $\{\mathbf{C}(\mathbf{x}), \mathbf{x} \in \Omega\}$ and mesoscopic $\{\tilde{\mathbf{C}}(\mathbf{x}), \mathbf{x} \in \Omega\}$ elasticity random fields. The microstructure under consideration is chosen as a homogeneous matrix reinforced by non-overlapping bi-disperse spherical inclusions. Since the aim is to estimate the effective behavior, which requires the macroscopic consistency condition to be satisfied, realizations of the mesoscopic elasticity tensor random field are computed from the realizations of the microstructure by means of the filtering framework introduced in section 1.2.2.

This chapter is organized as follows. Section 2.1 addresses the generation of the realizations for microscopic and mesoscopic stiffness tensor. This set of realizations will be called as *numerical experiments*. In section 2.2, we perform the statistical characterization of the numerical experiments, in which we focus on the mean, coefficient of variation as well as the material symmetry and the correlation structure of mesoscopic elasticity random field.

2.1 Generation of the elasticity fields

The generation of the realizations of the microscopic and mesoscopic elasticity tensor fields can be summarized as follows.

- First, the realizations $\{\mathbf{C}(\mathbf{x}, \theta_k), \mathbf{x} \in \Omega\}$, $k = 1, \dots, N_{\text{exp}}$ of the microscopic stiffness tensor random field are generated using a standard algorithm for assemblies of hard spheres (see section 2.1.1).
- Second, and following section 1.1.2, the boundary value problem at microscale, defined by equation (5), is numerically solved for all realizations (see section 2.1.2).
- Third, the associated realizations $\{\tilde{\mathbf{C}}(\mathbf{x}, \theta_k), \mathbf{x} \in \Omega\}$, $k = 1, \dots, N_{\text{exp}}$ of the mesoscopic stiffness tensor random field are computed by equation (17) (see section 2.1.3).
- Finally, the mesoscale problem defined by equation (18) is in turn solved for the N_{exp} realizations – these results can be used in order to estimated the effective stiffness tensor, and will essentially be used for validation purposes (see section 3.6).

2.1.1 Generation of microstructures

A simple but non trivial microstructure, namely a bidisperse assembly of spherical inclusions, is selected as a model microstructure. To highlight the effect of not well-separated length scales, the diameter of the smallest inclusions is purposely fixed at $D/3$, where D denotes the diameter of the largest inclusions. The size of the periodic domain Ω is $L = 6D$. The volume fraction of the largest (resp. smallest) inclusions is 20 % (resp. 10 %). The microstructures are generated by means of a standard Monte Carlo simulation for an assembly of hard spheres (Allen and Tildesley, 1987), starting from initial configurations generated by random sequential addition (Torquato, 2002). In order to ensure the convergence of the statistical estimators, a set of $N_{\text{exp}} = 700$ independent realizations is generated. As an illustration, one realization of the microstructure can be visualized in figure 2.1.

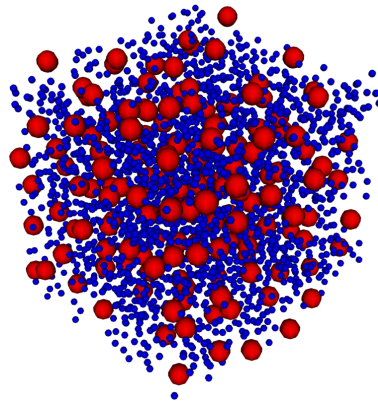


Figure 2.1. One realization of the microstructure (which contains more than 2,000 inclusions). The largest inclusions appear in red ($f = 20\%$), while the smallest inclusions are colored in blue ($f = 10\%$).

Let $\mathcal{S}_2^{(\alpha\beta)}(\mathbf{x}, \mathbf{y}) = \mathbb{E}\{\chi_\alpha(\mathbf{x})\chi_\beta(\mathbf{y})\}$ denote the two-point probability function (Torquato, 2002), in which $\chi_\alpha(\mathbf{x})$ is the characteristic function of phase α . Owing to statistical homogeneity and isotropy, $\mathcal{S}_2^{(\alpha\beta)}(\mathbf{x}, \mathbf{y})$ only depends on the norm $\tau = \|\mathbf{x} - \mathbf{y}\|$. For a two-phase microstructure, it can be shown that (Willis, 1982)

$$\mathcal{S}_2^{(\alpha\beta)}(\tau) - f_\alpha f_\beta = f_\alpha(\delta_{\alpha\beta} - f_\beta)\mathcal{R}(\tau), \quad (\text{no sum}) \quad (20)$$

where $f_\alpha = \mathbb{E}\{\chi_\alpha(\mathbf{x})\}$ is the volume fraction of phase α and $\mathcal{R}(\tau)$ is the (two-point) correlation function. The plot of $\mathcal{R}(\tau)$ as a function of τ/L , estimated using the generated database, is shown in figure 2.2.

As expected, it is seen that $\mathcal{R}(\tau)$ is independent of the direction under consideration. In what follows, the generated microstructures will be used as inputs to compute the local fields in the numerical homogenization method. In the next part, we present the computation of the local stress and local strain by means of the FFT-based homogenization method.

2.1.2 Computation of the apparent stiffness tensor of the microstructure

The determination of the mesoscopic stiffness tensor requires the local stress and strain fields (see equation (15)) to be known. In this work, we resort to FFT-based homogenization methods, initially introduced in Moulinec and Suquet (1994, 1998). More precisely, a variational form of

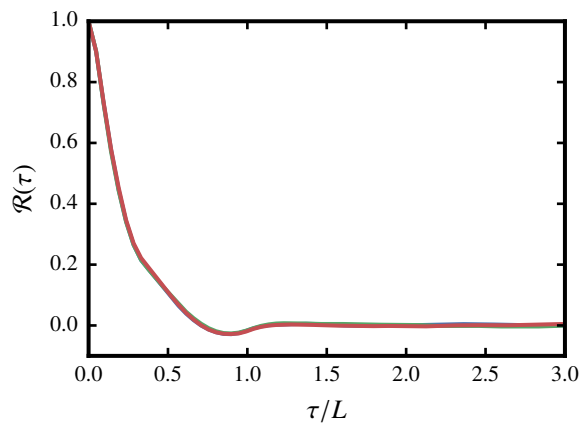


Figure 2.2. Plot of $\tau/L \mapsto \mathcal{R}(\tau)$ along \mathbf{e}_i , $1 \leq i \leq 3$.

this method (Brisard and Dormieux, 2010, 2012) is used to solve the auxiliary problem defined by equations (5) and (18). A more detail discussion on FFT based method can be found in appendix A. It should be noted that the methodology presented hereafter is not restricted to FFT based schemes but remains valid for any other numerical homogenization method.

The microstructures are discretized on a Cartesian grid of $128 \times 128 \times 128$ voxels, and the two constitutive phases are assumed to be elastic, linear and isotropic. The matrix phase and inclusions share the same Poisson's ratio $\nu = 0.2$, and the shear modulus of the inclusions is taken as $\mu_i = 1,000 \times \mu_m$, where μ_m denotes the shear modulus of the matrix. It should be noted that the elastic contrast was purposely fixed at a high value in order to illustrate the robustness of the model. The reference material to be used in the aforementioned numerical scheme is chosen to be softer than all phases, with $\mu_0 = 0.9\mu_m$ and $\nu_0 = 0.2$. In order to compute the local strain $\boldsymbol{\varepsilon}$ and strain localization tensor \mathbf{A} (see equation (14)), six linearly independent macroscopic strains $\langle \boldsymbol{\varepsilon} \rangle$ are specified on the boundary $\partial\Omega$.

In terms of computational resources, the numerical solutions to the local boundary value problems are obtained using parallel computing (with 64 cores) and Janus code ¹. Each core contains a Intel(R) Xeon(R) CPU E5-2640 running at 2.50GHz. It is noticed that the computation time is about 10 minutes (CPU time) per realization and per macroscopic loading.

2.1.3 Computation of the mesoscopic stiffness tensor random field

Once the solution of the boundary value problem at microscale has been obtained (for a given realization of the microstructure), the associated mesoscopic stiffness tensor random field can be computed through equation (17), making use of a centered Gaussian filter with standard deviation σ . For numerical convenience, this filter is truncated over a cubic window of width H , and the kernel ρ takes the form

$$\begin{aligned} \rho(\mathbf{x}) &= \alpha \exp\left(-\frac{1}{2} \frac{\|\mathbf{x}\|^2}{\sigma^2}\right), \text{ if } |x_i| \leq H/2, \forall i \in \llbracket 1, d \rrbracket, \\ &= 0, \text{ otherwise,} \end{aligned} \quad (21)$$

¹Available at <https://github.com/sbrisard/janus>.

where we choose $H = 6\sigma$ (as typically selected in the field of image analysis). The value of α is deduced from the normalization property given by equation (16). It should be noticed that despite the anisotropic truncation, the above kernel is practically isotropic since the ratio σ/H is taken small enough. In addition, this kernel induces a mass concentration at the origin, which is physically consistent with the definition of the mesoscopic fields. One realization of a microscopic elasticity random field, together with the associated mesoscopic field, are shown in figure 2.3.

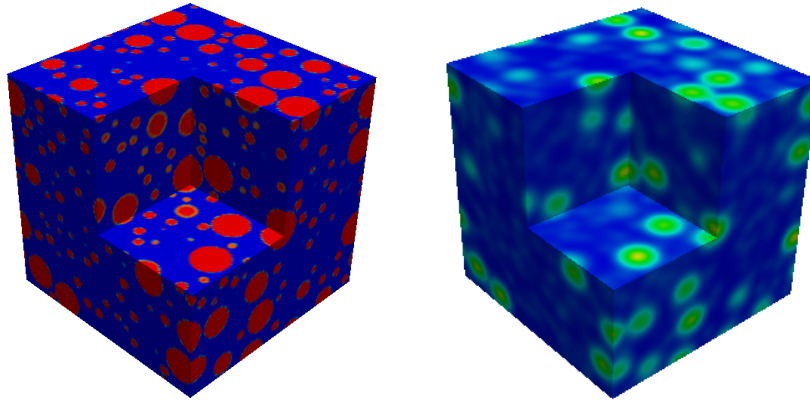


Figure 2.3. One realization of microscopic elasticity random field $\{C_{1111}(\mathbf{x}, \theta), \mathbf{x} \in \Omega\}$ (left) and associated filtered random field $\{\tilde{C}_{1111}(\mathbf{x}, \theta), \mathbf{x} \in \Omega\}$ with $H = 2D$ (right).

The effect of progressive smoothing induced by filter parameter H/D is further shown in figure 2.4.

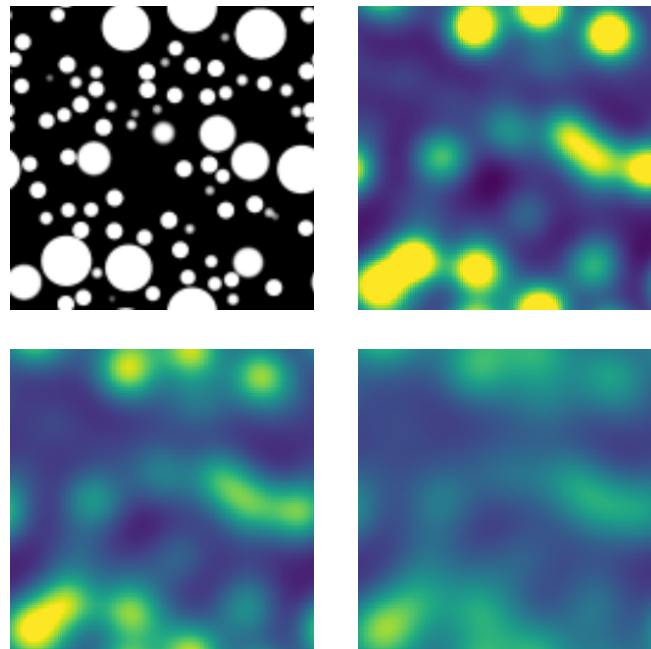


Figure 2.4. One realization (2D slice) of microscopic elasticity random field $\{C_{1111}(\mathbf{x}, \theta), \mathbf{x} \in \Omega\}$ (top-left) and associated mesoscale random fields $\{\tilde{C}_{1111}(\mathbf{x}, \theta), \mathbf{x} \in \Omega\}$ obtained for $H = 2D$ (top-right), $H = 2.5D$ (bottom-left) and $H = 3D$ (bottom-right). The same color scale was used for all mesoscale random fields to highlight the evolution of the contrast.

More specifically, it is observed that increasing the parameter H/D results in decreasing the spatial mechanical contrast of the mesoscopic stiffness tensor. Unless otherwise stated, the value $H/D = 3$ will be used from now on.

2.2 Characterization of the mesoscopic random fields

This section is devoted to the characterization of a few statistical properties for the mesoscopic elasticity tensor random field, with the aim to subsequently construct a suitable random field model. Such a random field model should have the capability to reproduce some fundamental features of the generated random fields, such as symmetry (self-adjointness), material symmetry and correlation structure. These properties are specifically investigated below. In accordance with the periodic setting, the mesoscopic elasticity random field $\{\tilde{\mathbf{C}}(\mathbf{x}, \theta), \mathbf{x} \in \mathbb{R}^d\}$ is identified with the periodized version, in the almost sure sense, of $\{\tilde{\mathbf{C}}(\mathbf{x}, \theta), \mathbf{x} \in \Omega\}$. Note that in the sequel, such an extension will be used with no specific notation for any decomposition of the elasticity random field.

2.2.1 Degree of asymmetry

As reported in [Bignonnet et al. \(2014\)](#), it turns out that the mesoscopic stiffness tensor does not obey minor symmetry. In order to quantify the degree of asymmetry, let $\{\epsilon_{\text{asym}}(\mathbf{x}, \theta), \mathbf{x} \in \Omega\}$ be the \mathbb{R}^+ -valued random field measuring the normalized distance, for all \mathbf{x} fixed in Ω , between $\tilde{\mathbf{C}}(\mathbf{x}, \theta)$ and its symmetric counterpart

$$\forall \mathbf{x} \in \Omega, \quad \epsilon_{\text{asym}}(\mathbf{x}, \theta) = \frac{\|\tilde{\mathbf{C}}(\mathbf{x}, \theta) - \tilde{\mathbf{C}}^T(\mathbf{x}, \theta)\|_F}{2\|\tilde{\mathbf{C}}(\mathbf{x}, \theta)\|_F}, \quad (22)$$

where $C^T_{ijkl} = C_{klij}$ and the euclidean (Frobenius) norm is defined by $\|\mathbf{X}\|_F = (X_{ijkl}X_{ijkl})^{1/2}$. The mean field $\mathbf{x} \mapsto \mathbb{E}\{\epsilon_{\text{asym}}(\mathbf{x})\}$ of the above random field is then determined through the following estimator

$$\forall \mathbf{x} \in \Omega, \quad \mathbb{E}\{\epsilon_{\text{asym}}(\mathbf{x})\} = \frac{1}{N_{\text{exp}}} \sum_{i=1}^{N_{\text{exp}}} \epsilon_{\text{asym}}(\mathbf{x}, \theta_i). \quad (23)$$

The convergence of the statistical estimator at the center of the domain Ω is shown in [figure 2.5](#), where the 99% confidence interval is also reported.

The plot of the mean function $(x_2, x_3) \mapsto 100 \mathbb{E}\{\epsilon_{\text{asym}}(L/2, x_2, x_3)\}$ is depicted in [figure 2.6](#), and it is seen that the relative error between the filtered tensor and its symmetric counterpart is reasonably small.

Similar conclusions can be drawn, both in mean and variance, at all observation points in Ω , hence suggesting the use of a symmetric approximation. Furthermore, the influence of filter parameter H/D on the degree of asymmetry is illustrated in [figure 2.7](#).

As expected, it is observed that increasing the filter parameter reduces the maximum of the mean function $\mathbf{x} \mapsto \mathbb{E}\{\epsilon_{\text{asym}}(\mathbf{x})\}$. In conclusion, it is observed that the realizations of mesoscopic elasticity random field are almost symmetric for $H/D = 3$, so that the mesoscopic stiffness tensor random field can be modeled accurately by a random field with values in the set of symmetric tensors.

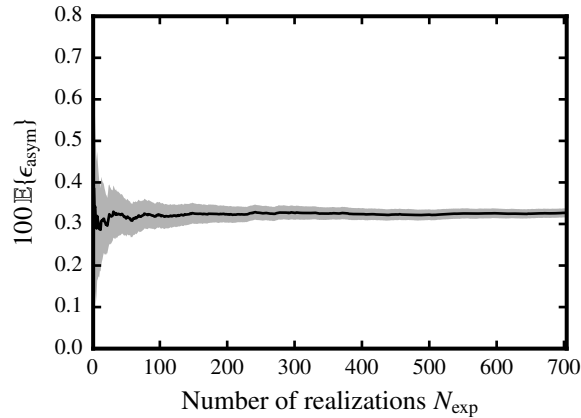


Figure 2.5. Convergence of the statistical estimator for the mean field of $\{\epsilon_{\text{asym}}(\mathbf{x}, \theta), \mathbf{x} \in \Omega\}$ at the center of domain Ω . The error bar (gray zone) represents 99% confidence interval.

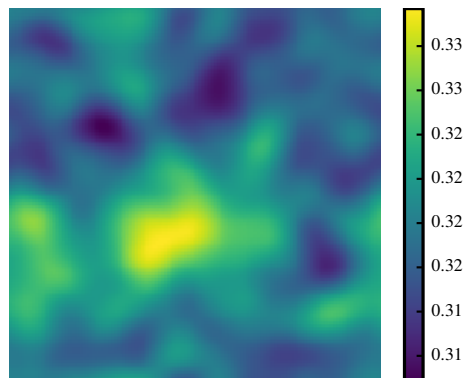


Figure 2.6. Plot of mean function $(x_2, x_3) \mapsto 100 \mathbb{E}\{\epsilon_{\text{asym}}(L/2, x_2, x_3)\}$.

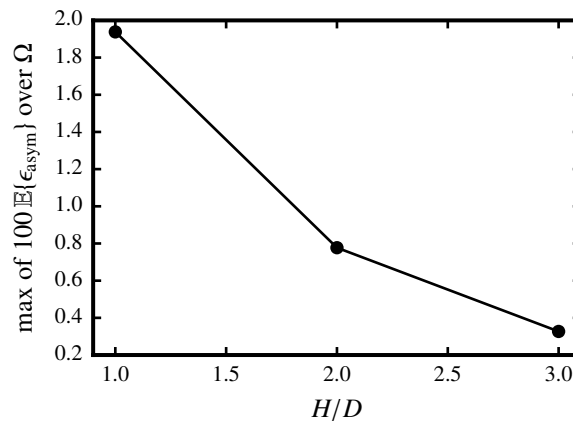


Figure 2.7. Maximum value of mean function $\mathbf{x} \mapsto 100 \mathbb{E}\{\epsilon_{\text{asym}}(\mathbf{x})\}$ over Ω .

2.2.2 Material symmetry

We now turn to the characterization of the material symmetry that is exhibited by the elasticity random field at mesoscale (we recall here that such a random field is, in general, anisotropic almost surely). Given the microstructure under consideration, we specifically investigate the relevance of an isotropic approximation $\{\tilde{\mathbf{C}}^{\text{iso}}(\mathbf{x}, \theta), \mathbf{x} \in \Omega\}$, which can be defined (following e.g.

Moakher and Norris (2006)) through an euclidean projection

$$\forall \mathbf{x} \in \Omega, \quad \tilde{\mathbf{C}}^{\text{iso}}(\mathbf{x}, \theta) = \mathcal{P}^{\text{iso}}(\tilde{\mathbf{C}}(\mathbf{x}, \theta)) = \underset{\mathbf{M} \in \mathbb{M}_n^{\text{iso}}(\mathbb{R})}{\text{argmin}} \|\tilde{\mathbf{C}}(\mathbf{x}, \theta) - \mathbf{M}\|, \quad (24)$$

where $\mathbb{M}_n^{\text{iso}}(\mathbb{R})$ is the set of all isotropic tensors. In order to quantify the error induced by this approximation, let us introduce the normalized distance random field $\{d(\mathbf{x}, \theta), \mathbf{x} \in \Omega\}$ (see Guillemint and Soize (2012) for instance)

$$\forall \mathbf{x} \in \Omega, \quad d(\mathbf{x}, \theta) = \frac{\|\tilde{\mathbf{C}}(\mathbf{x}, \theta) - \tilde{\mathbf{C}}^{\text{iso}}(\mathbf{x}, \theta)\|}{\|\tilde{\mathbf{C}}(\mathbf{x}, \theta)\|}. \quad (25)$$

Let $\mathbf{x} \mapsto \mathbb{E}\{d(\mathbf{x})\}$ be the mean function of the above random field. The convergence of the statistical estimator of $\mathbb{E}\{d(\mathbf{x})\}$ at the center of domain Ω is shown in figure 2.8.

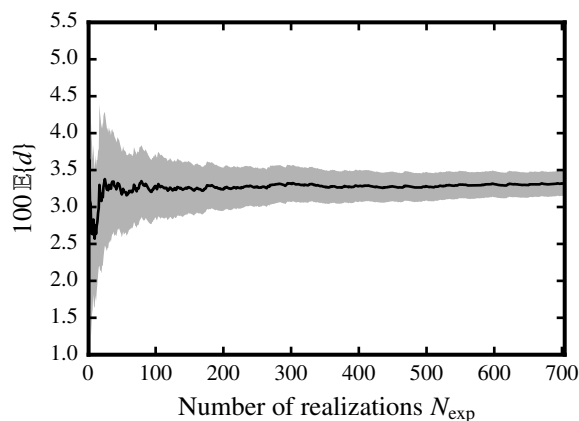


Figure 2.8. Statistical estimator of distance field at the center of domain Ω . The error bar (gray zone) represents 99% confidence interval.

The graph of the mean function $(x_2, x_3) \mapsto \mathbb{E}\{d(L/2, x_2, x_3)\}$ is shown in figure 2.9.

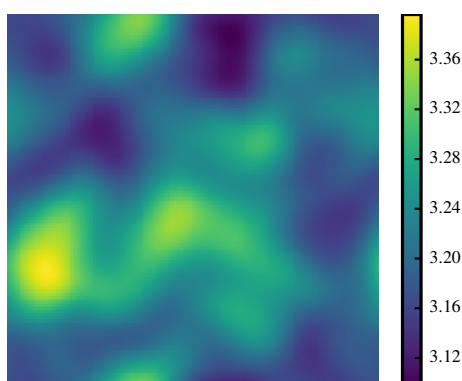


Figure 2.9. Plot of mean function $(x_2, x_3) \mapsto 100 \mathbb{E}\{d(L/2, x_2, x_3)\}$.

It is seen on these graphs that the relative error is fairly small (with a maximum value of 3.3% approximately) in mean, and exhibits contained fluctuations. These quantitative results show that the realizations of the mesoscopic stiffness can be approximated by isotropic ones, which may facilitate the modeling and simulation tasks. Finally, the influence of the ratio H/D on the level of isotropy is illustrated in figure 2.10.

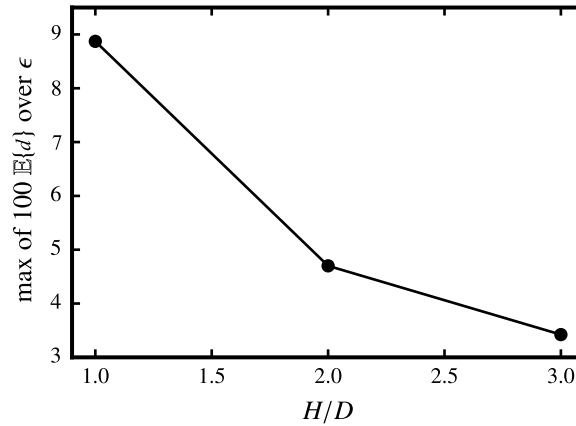


Figure 2.10. Maximum value of mean function $\mathbf{x} \mapsto 100 \mathbb{E}\{d(\mathbf{x})\}$ over Ω .

As expected, it is seen that the stochastic residual decreases, in mean, as the ratio H/D gets larger. It worth mentioning that the euclidean metric is not invariant under inversion (see [Moakher and Norris \(2006\)](#)), so that the distance random field $\{d(\mathbf{x}, \theta), \mathbf{x} \in \Omega\}$ may exhibit slightly different properties depending on whether the stiffness or compliance tensor is considered. It follows that the mesoscopic stiffness random field is modeled, from now on, as almost isotropic field (note that isotropy here refers to the material symmetry, and not to a property related to the correlation structure). It is then characterized by bulk and shear moduli random fields, the properties of which are characterized in the next section.

2.2.3 Second-order characterization

An estimator of the mean function $\mathbf{x} \mapsto \mathbb{E}\{\tilde{\mathbf{C}}(\mathbf{x})\}$ associated with the mesoscopic stiffness random field is determined as

$$\forall \mathbf{x} \in \Omega, \quad \mathbb{E}\{\tilde{\mathbf{C}}(\mathbf{x})\} = \frac{1}{N_{\text{exp}}} \sum_{i=1}^{N_{\text{exp}}} \tilde{\mathbf{C}}(\mathbf{x}, \theta_i). \quad (26)$$

The graph of mean function $(x_2, x_3) \mapsto \mathbb{E}\{\tilde{\mathbf{C}}_{1111}(L/2, x_2, x_3)\}$ is shown in figure 2.11 and may suggest that the statistical mean field $\mathbf{x} \mapsto \mathbb{E}\{\tilde{\mathbf{C}}(\mathbf{x})\}$ fluctuates over Ω .

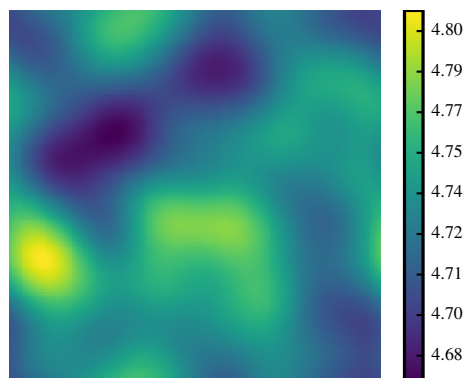


Figure 2.11. Plot of mean function $(x_2, x_3) \mapsto \mu_m^{-1} \mathbb{E}\{\tilde{\mathbf{C}}_{1111}(L/2, x_2, x_3)\}$.

It should, however, be noticed that the range of fluctuations falls within the confidence interval at 99%, so that the observed spatial fluctuations may likely be explained by finite-sampling. The

spatial fluctuations of mean function $\mathbf{x} \mapsto \mathbb{E}\{\tilde{\mathbf{C}}(\mathbf{x})\}$ are further characterized by the parameter $\delta_{\mathbb{E}\{\tilde{\mathbf{C}}(\mathbf{x})\}}$ defined as

$$\delta_{\mathbb{E}\{\tilde{\mathbf{C}}(\mathbf{x})\}} = \left\{ \left(N_p^{-1} \sum_{i=1}^{N_p} \|\mathbb{E}\{\tilde{\mathbf{C}}(\mathbf{x}_i)\} - \langle \mathbb{E}\{\tilde{\mathbf{C}}\} \rangle\|_F^2 \right) \|\langle \mathbb{E}\{\tilde{\mathbf{C}}\} \rangle\|_F^{-2} \right\}^{1/2}, \quad (27)$$

where N_p is the number of voxels in domain Ω ($N_p = 128^3$) and $\langle \mathbb{E}\{\tilde{\mathbf{C}}\} \rangle$ denotes the spatial average of mean field $\mathbf{x} \mapsto \mathbb{E}\{\tilde{\mathbf{C}}(\mathbf{x})\}$

$$\frac{1}{\mu_m} \langle \mathbb{E}\{\tilde{\mathbf{C}}\} \rangle = \begin{bmatrix} 4.740 & 1.154 & 1.154 & 0 & 0 & -0.001 \\ 1.154 & 4.742 & 1.154 & 0.001 & 0 & -0.001 \\ 1.154 & 1.154 & 4.740 & 0 & 0.001 & 0 \\ 0 & 0.001 & 0 & 3.561 & 0 & 0 \\ 0 & 0 & 0.001 & 0 & 3.562 & 0.001 \\ 0.001 & -0.001 & 0 & 0 & 0.001 & 3.562 \end{bmatrix} \quad (28)$$

The value of $\delta_{\mathbb{E}\{\tilde{\mathbf{C}}(\mathbf{x})\}}$ is found to be reasonably small (0.58%). For these reasons, and taking into account the statistical homogeneity of the underlying microstructure, it is assumed that the mean function does not depend on \mathbf{x} . Furthermore, the normalized distance between $\langle \mathbb{E}\{\tilde{\mathbf{C}}\} \rangle$ and its isotropic projection $\mathcal{P}^{\text{iso}}(\langle \mathbb{E}\{\tilde{\mathbf{C}}\} \rangle)$,

$$d(\langle \mathbb{E}\{\tilde{\mathbf{C}}\} \rangle, \mathcal{P}^{\text{iso}}(\langle \mathbb{E}\{\tilde{\mathbf{C}}\} \rangle)) = \frac{\|\langle \mathbb{E}\{\tilde{\mathbf{C}}\} \rangle - \mathcal{P}^{\text{iso}}(\langle \mathbb{E}\{\tilde{\mathbf{C}}\} \rangle)\|}{\|\langle \mathbb{E}\{\tilde{\mathbf{C}}\} \rangle\|}, \quad (29)$$

is equal to 0.255%, showing that the mean value of the mesoscopic stiffness tensor is almost isotropic. The mean value is therefore approximated by using the projected mean values for both the bulk and shear moduli, namely $\mathbb{E}\{\tilde{\kappa}\} = 2.35\mu_m$ and $\mathbb{E}\{\tilde{\mu}\} = 1.78\mu_m$. The coefficients of variation of the random bulk and shear moduli are further found to be $\delta_{\tilde{\kappa}} \approx 13.9\%$ and $\delta_{\tilde{\mu}} \approx 14.4\%$. Let $\boldsymbol{\tau} \mapsto \mathcal{R}_{\tilde{\kappa}}(\boldsymbol{\tau})$ be the normalized covariance function of the bulk random field, defined for all $\boldsymbol{\tau}$ in \mathbb{R}^d by

$$\mathcal{R}_{\tilde{\kappa}}(\boldsymbol{\tau}) = \frac{\mathbb{E}\{[\tilde{\kappa}(\mathbf{x} + \boldsymbol{\tau}, \theta) - \mathbb{E}\{\tilde{\kappa}(\mathbf{x} + \boldsymbol{\tau}, \theta)\}][\tilde{\kappa}(\mathbf{x}, \theta) - \mathbb{E}\{\tilde{\kappa}(\mathbf{x}, \theta)\}]\}}{([\mathbb{E}\{\tilde{\kappa}(\mathbf{x} + \boldsymbol{\tau}, \theta)^2\} - \mathbb{E}\{\tilde{\kappa}(\mathbf{x} + \boldsymbol{\tau}, \theta)\}^2][\mathbb{E}\{\tilde{\kappa}(\mathbf{x}, \theta)^2\} - \mathbb{E}\{\tilde{\kappa}(\mathbf{x}, \theta)\}^2])^{1/2}}. \quad (30)$$

A similar notation is used for the normalized covariance function associated with the shear modulus random field $\{\tilde{\mu}(\mathbf{x}, \theta), \mathbf{x} \in \Omega\}$. The plot of the normalized covariance functions $\mathcal{R}_{\tilde{\kappa}}$ and $\mathcal{R}_{\tilde{\mu}}$ along the three directions defined by the canonical basis of \mathbb{R}^3 is shown in figure 2.12.

It is seen that the above estimated normalized covariance functions are almost identical regardless of the direction, as expected from the statistical isotropy of the underlying microstructure (note that the retained Gaussian filter also introduces an isotropic smoothing). Interestingly, the normalized covariance functions are almost identical for the bulk and shear moduli, as shown in figure 2.13.

Note that this feature may be explained by the fact that the two constitutive materials share the same Poisson ratio (see section 2.1.2). Furthermore, the correlation structure of bulk and shear moduli random fields seem to suggest that it can be approximated by a squared exponential correlation function type.

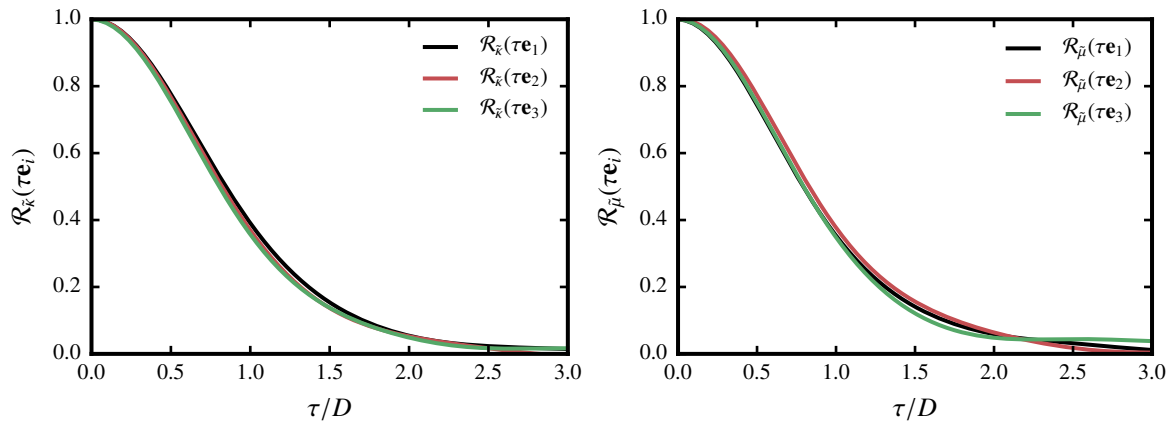


Figure 2.12. Plot of the normalized covariance functions $\tau/D \mapsto \mathcal{R}_{\bar{k}}(\tau\mathbf{e}_i)$ (left) and $\tau/D \mapsto \mathcal{R}_{\bar{\mu}}(\tau\mathbf{e}_i)$ (right), $1 \leq i \leq 3$.

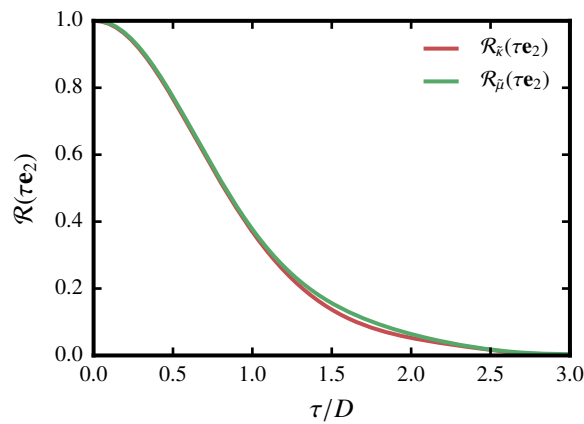


Figure 2.13. Plot of the normalized covariance functions $\tau/D \mapsto \mathcal{R}_{\bar{k}}(\tau\mathbf{e}_2)$ and $\tau/D \mapsto \mathcal{R}_{\bar{\mu}}(\tau\mathbf{e}_2)$.

Finally, let b the parameter defined as

$$b = \int_0^{L/2} |\mathcal{R}(\tau)| d\tau. \quad (31)$$

This parameter is interpreted, in the retained periodic setting, as the correlation length of the mesoscopic elasticity random field (we recall here that by construction, the associated correlation function depends on the norm of the lag vector only). The plot of the correlation length b as a function of the ratio H/D is shown in figure 2.14.

It is observed that the relation between b and H/D is almost linear, hence illustrating the influence of the filter size. The correlation length associated with the random morphology at the microscale is further found to be of the same order as the one associated with the mesostructure, with $H/D = 1$. This can be explained by the fact that the smoothing effect is rather weak at small filter sizes.

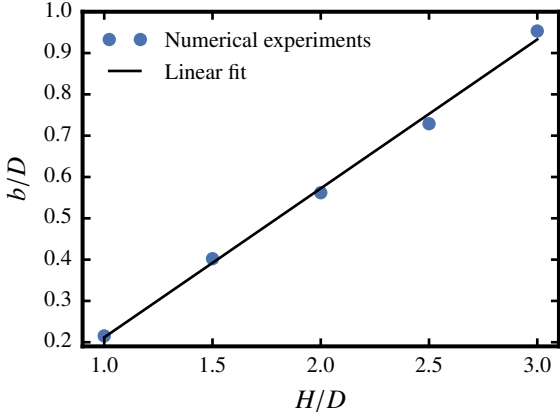


Figure 2.14. Normalized correlation length b/D as a function of H/D .

Chapter 3

Stochastic framework

3.1 Methodology

This section is devoted to the construction of a probabilistic model for the mesoscopic elasticity random field $\{\tilde{\mathbf{C}}(\mathbf{x}, \theta), \mathbf{x} \in \Omega\}$. Following the statistical characterization, it is assumed that:

- for all \mathbf{x} fixed in Ω , the random matrix $\tilde{\mathbf{C}}(\mathbf{x}, \theta)$ is symmetric a.s.;
- the random field $\{\tilde{\mathbf{C}}(\mathbf{x}, \theta), \mathbf{x} \in \Omega\}$ is isotropic a.s. and is therefore completely defined by the associated bulk and shear moduli random fields, denoted by $\{\tilde{\kappa}(\mathbf{x}, \theta), \mathbf{x} \in \Omega\}$ and $\{\tilde{\mu}(\mathbf{x}, \theta), \mathbf{x} \in \Omega\}$ respectively, such that

$$\forall \mathbf{x} \in \Omega, \quad \tilde{\mathbf{C}}(\mathbf{x}, \theta) = d \tilde{\kappa}(\mathbf{x}, \theta) \mathbf{J} + 2 \tilde{\mu}(\mathbf{x}, \theta) \mathbf{K}, \quad (32)$$

with (\mathbf{J}, \mathbf{K}) the classical (deterministic) tensor basis of $\mathbb{M}_n^{\text{iso}}(\mathbb{R})$ ($n = 3, 6$) (Walpole, 1984) and d the physical dimension ($d = 2, 3$);

- the bulk and shear moduli random fields are statistically independent (a discussion for the random matrix case can be found in Guillemint and Soize (2013a)) and exhibit the same L -periodic correlation structure.

In addition, it is assumed that the random fields $\{\tilde{\kappa}(\mathbf{x}, \theta), \mathbf{x} \in \Omega\}$ and $\{\tilde{\mu}(\mathbf{x}, \theta), \mathbf{x} \in \Omega\}$ are bounded from below by the associated matrix properties

$$\tilde{\kappa}(\mathbf{x}, \theta) > \kappa_m, \quad \tilde{\mu}(\mathbf{x}, \theta) > \mu_m \text{ a.s.}, \quad (33)$$

for all \mathbf{x} in Ω , with κ_m and μ_m the bulk and shear moduli of the matrix phase. Equation (33) appears as a reasonable assumption, given that the retained value of parameter H (see equation (21)) is large in the simulations (recall that the heterogeneities are stiffer than the isotropic matrix phase). Note that the strict inequalities mean that the lower bounds must then be reached with a null probability. Consequently, let us introduce two auxiliary \mathbb{R}_*^+ -valued random fields $\{\kappa'(\mathbf{x}, \theta), \mathbf{x} \in \Omega\}$ and $\{\mu'(\mathbf{x}, \theta), \mathbf{x} \in \Omega\}$ such that $\forall \mathbf{x} \in \Omega$

$$\tilde{\kappa}(\mathbf{x}, \theta) = \kappa'(\mathbf{x}, \theta) + \kappa_m, \quad \tilde{\mu}(\mathbf{x}, \theta) = \mu'(\mathbf{x}, \theta) + \mu_m. \quad (34)$$

Below, we address the construction of stochastic representations for random fields $\{\kappa'(\mathbf{x}, \theta), \mathbf{x} \in \Omega\}$ and $\{\mu'(\mathbf{x}, \theta), \mathbf{x} \in \Omega\}$. The methodology, pioneered in the seminal work of Soize (2006) and

extended in [Guilleminot et al. \(2011\)](#); [Guilleminot and Soize \(2013a,b\)](#), proceeds along the following two main steps. First, a stochastic model for random variable $\kappa'(\mathbf{x}, \theta)$ (resp. $\mu'(\mathbf{x}, \theta)$), \mathbf{x} being fixed in Ω , is defined by invoking Jaynes' maximum entropy principle ([Jaynes, 1957a,b](#)) (see section 3.2). Here, it is assumed that the available information on each random variable is independent of \mathbf{x} , so that the probability density functions $p_{\kappa'(\mathbf{x}, \theta)}$ and $p_{\mu'(\mathbf{x}, \theta)}$ defining $\kappa'(\mathbf{x}, \theta)$ and $\mu'(\mathbf{x}, \theta)$ do not depend on \mathbf{x} either. Note that this assumption can be readily relaxed at the expense of notational complexity. Second, the bulk and shear moduli random fields are defined through measurable nonlinear transformations of two underlying \mathbb{R} -valued Gaussian random fields such that $\{\kappa'(\mathbf{x}, \theta), \mathbf{x} \in \Omega\}$ and $\{\mu'(\mathbf{x}, \theta), \mathbf{x} \in \Omega\}$ respectively admit $p_{\kappa'(\mathbf{x}, \theta)}$ and $p_{\mu'(\mathbf{x}, \theta)}$ as their first-order marginal probability density functions. This construction is detailed in section 3.3.

3.2 Construction of an information-theoretic model for the probability density functions

Let \mathbf{x} be fixed in Ω . As mentioned above, probabilistic models for random variables $\kappa'(\mathbf{x}, \theta)$ and $\mu'(\mathbf{x}, \theta)$ can be constructed within the framework of information theory and more precisely, by having recourse to the maximum entropy (MaxEnt) principle (see [Jaynes, 1957a,b](#)). Since the methodology proceeds similarly for the two random moduli, technical aspects are detailed below for the bulk modulus $\kappa'(\mathbf{x}, \theta)$ only – the result for the shear modulus is provided at the end of the section. The MaxEnt principle relies on the maximization of Shannon's differential entropy ([Shannon, 1948](#)) and then states that among all the probability density functions satisfying some constraints (stated in the form of mathematical expectations) related to a given amount of available information, the most objective probability density function (that is, the one that introduces the most reduced modeling bias) is the one that maximizes the above mentioned entropy (as a relative measure of uncertainties).

In this work, we assume that the \mathbb{R}_*^+ -valued random variable $\kappa'(\mathbf{x}, \theta)$ satisfies the following constraints

$$\mathbb{E}\{\kappa'(\mathbf{x}, \theta)\} = \mathbb{E}\{\kappa'\}, \quad (35)$$

$$\mathbb{E}\{\ln(\kappa'(\mathbf{x}, \theta))\} = \vartheta, \quad |\vartheta| < +\infty, \quad (36)$$

where $\mathbb{E}\{\kappa'(\mathbf{x}, \theta)\} = \mathbb{E}\{\tilde{\kappa}(\mathbf{x}, \theta)\} - \kappa_m$. The constraint stated by equation (35) allows for the prescription of the mean value, whereas equation (36) implies (under some given assumptions that will be made more precise later) that $\kappa'(\mathbf{x}, \theta)$ and $\kappa'(\mathbf{x}, \theta)^{-1}$ are second-order random variables. By using the calculus of variations, it can then be shown that the probability density function $p_{\kappa'(\mathbf{x}, \theta)}$ takes the classical form (see e.g. [Guilleminot and Soize \(2012\)](#))

$$p_{\kappa'(\mathbf{x}, \theta)}(k) = 1_{\mathbb{R}_*^+}(k) \times c \times k^{-\lambda_1} \exp(-\lambda_2 k), \quad (37)$$

where $1_{\mathbb{R}_*^+}$ is the indicator function of \mathbb{R}_*^+ , c is a real positive normalization constant and (λ_1, λ_2) is a couple of Lagrange multipliers such that the above constraints are fulfilled. Owing to a change of parameters, it can be easily proven that the above p.d.f. can be written as

$$p_{\kappa'(\mathbf{x}, \theta)}(k) = 1_{\mathbb{R}_*^+}(k) \times c \times \left(\frac{k}{\mathbb{E}\{\kappa'\}} \right)^{1/\delta_{\kappa'}^2 - 1} \exp\left(-\frac{k}{\mathbb{E}\{\kappa'\} \delta_{\kappa'}^2} \right), \quad (38)$$

where $\delta_{\kappa'}$ is the coefficient of variation of bulk modulus $\kappa'(\mathbf{x}, \theta)$ (see [Ta et al. \(2010\)](#) for similar results, as well as [Guilleminot and Soize \(2013a,b\)](#) for random matrix and random field models exhibiting other material symmetry properties). The normalization constant c is then given by

$$c = \frac{1}{\mathbb{E}\{\kappa'\}} \left(\frac{1}{\delta_{\kappa'}^2} \right)^{1/\delta_{\kappa'}^2} \frac{1}{\Gamma(1/\delta_{\kappa'}^2)}, \quad (39)$$

with Γ the Gamma function

$$\Gamma(k) = \int_0^{\infty} t^{k-1} \exp(-t) dt. \quad (40)$$

Note that the condition $\delta_{\kappa'} < 1/\sqrt{2}$ must hold in order to ensure the finiteness of the second-order moments for $\kappa'(\mathbf{x}, \theta)$ and $\kappa'(\mathbf{x}, \theta)^{-1}$ (see [Soize \(2000\)](#)). It can be deduced that $\kappa'(\mathbf{x}, \theta)$ is distributed according to a Gamma distribution with shape parameter $1/\delta_{\kappa'}^2$, and scale parameter $\mathbb{E}\{\kappa'\}\delta_{\kappa'}^2$, (with $\lambda_1 = 1 - 1/\delta_{\kappa'}^2$ and $\lambda_2 = 1/(\mathbb{E}\{\kappa'\}\delta_{\kappa'}^2)$).

Similarly, it can be shown that the random shear modulus $\mu'(\mathbf{x}, \theta)$ follows a Gamma distribution defined by shape parameter $1/\delta_{\mu'}^2$, and scale parameter $\mathbb{E}\{\mu'\}\delta_{\mu'}^2$. Additional comments related to the above construction for the first-order marginal probability distribution are listed below.

- First, it is worthwhile to note that the use of an isotropic approximation is motivated by the statistical characterization detailed in section 2.2.2. The latter shows that the stochastic residual (defined by Eq. (25)) exhibits a negligible mean and a small variance, regardless of the location under consideration.
- Second, and while the recourse to an isotropic model alleviates the computational cost, it is by no means a limitation of the overall methodology that can be readily extended to any symmetry class (see [Guilleminot and Soize \(2013b\)](#) for the construction of the stochastic model for any symmetry class).
- Third, the nature of the statistical dependence essentially depends on the information that is plugged into the principle of maximum entropy. In other words, changing the constraints by adding, for instance, an information on cross-correlation would yield another dependence structure. However, getting converged statistical estimators for high-order moments generally requires a large amount of data, which is not the framework retained in this study. Rather, the model is here tailored in order to allow for a calibration through an underdetermined inverse problem, hence the consideration of minimal mathematical requirements only (these properties allow one to prove the existence and uniqueness of a second-order solution for the associated stochastic boundary value problem) and relies in part on imposing the finiteness of the second order moment for the stiffness tensor (this property is then equivalently imposed on the bulk and shear modulus, with no information on cross-correlation between these parameters, since \mathbf{J} and \mathbf{K} are orthogonal projectors).

3.3 Definition of the mesoscale moduli random fields

As discussed in the above section, the first order marginal of bulk and shear moduli random field model are distributed according to a Gamma distribution. It then can be simulated by means

of the inverse transform method. More specifically, the random bulk and shear moduli can be readily defined through the following local measurable nonlinear transformations

$$\forall \mathbf{x} \in \Omega, \quad \kappa'(\mathbf{x}, \theta) = F_{\mathcal{G}_{\kappa'}}^{-1}(\Phi(\Xi_{\kappa'}(\mathbf{x}, \theta))), \quad \mu'(\mathbf{x}, \theta) = F_{\mathcal{G}_{\mu'}}^{-1}(\Phi(\Xi_{\mu'}(\mathbf{x}, \theta))), \quad (41)$$

where

- $F_{\mathcal{G}_{\kappa'}}^{-1}$ (resp. $F_{\mathcal{G}_{\mu'}}^{-1}$) is the Gamma inverse cumulative distribution function with shape parameter $1/\delta_{\kappa'}^2$ (resp. $1/\delta_{\mu'}^2$) and scale parameter $\mathbb{E}\{\kappa'\}\delta_{\kappa'}^2$ (resp. $\mathbb{E}\{\mu'\}\delta_{\mu'}^2$);
- Φ is the cumulative distribution function of the standard normal distribution;
- $\{\Xi_{\kappa'}(\mathbf{x}, \theta), \mathbf{x} \in \mathbb{R}^d\}$ and $\{\Xi_{\mu'}(\mathbf{x}, \theta), \mathbf{x} \in \mathbb{R}^d\}$ are centered Gaussian random fields such that for all \mathbf{x} in Ω and for all \mathbf{y} in \mathbb{Z}^d

$$\Xi_{\kappa'}(\mathbf{x} + L\mathbf{y}, \theta) = \Xi_{\kappa'}(\mathbf{x}, \theta) \text{ and } \Xi_{\mu'}(\mathbf{x} + L\mathbf{y}, \theta) = \Xi_{\mu'}(\mathbf{x}, \theta) \text{ a.s.} \quad (42)$$

Moreover, and for $(\mathbf{x}, \mathbf{y}) \in \Omega \times \Omega$, the associated normalized correlation functions $\mathcal{R}_{\Xi_{\kappa'}}$ and $\mathcal{R}_{\Xi_{\mu'}}$ are such that

$$\mathcal{R}_{\Xi_{\kappa'}}(\mathbf{x}, \mathbf{y}) = \mathbb{E}\{\Xi_{\kappa'}(\mathbf{x})\Xi_{\kappa'}(\mathbf{y})\}, \quad \mathcal{R}_{\Xi_{\kappa'}}(\mathbf{x}, \mathbf{x}) = 1 \quad (43)$$

and

$$\mathcal{R}_{\Xi_{\mu'}}(\mathbf{x}, \mathbf{y}) = \mathbb{E}\{\Xi_{\mu'}(\mathbf{x})\Xi_{\mu'}(\mathbf{y})\}, \quad \mathcal{R}_{\Xi_{\mu'}}(\mathbf{x}, \mathbf{x}) = 1. \quad (44)$$

The above correlation functions are assumed to be identical (see the discussion in the end of section 2.2.3) and have a separable structure, namely

$$\mathcal{R}_{\Xi_{\kappa'}}(\mathbf{x}, \mathbf{y}) = \mathcal{R}_{\Xi_{\mu'}}(\mathbf{x}, \mathbf{y}) = \prod_{k=1}^d r(|x_k - y_k|) \quad (45)$$

for all (\mathbf{x}, \mathbf{y}) in $\Omega \times \Omega$. It should be note that one primary objective of this work is to calibrate the prior probabilistic model with a small amount of data, hence it is necessary to reduce the number of model parameters. We then assumed that each correlation function depends on a single parameter denoted by α , no matter the Gaussian field or the direction involved. The observation in the end of section 2.2.3 suggests a squared exponential correlation function form. The one-dimensional correlation function r is then chosen to be (Rasmussen and Williams, 2005)

$$\forall \tau \in [0, L], \quad r(\tau) = \exp\left(-\frac{2}{\alpha^2} \sin^2\left(\frac{\pi\tau}{L}\right)\right). \quad (46)$$

An illustration of the correlation function (46) is given in figure 3.1 for $\alpha \in \{0.2, 0.4, 0.6\}$.

The above function can be recovered by introducing polar coordinates in a two-dimensional squared exponential correlation function, so that it can be considered as a correlation function. Finally, it should be noticed that a more accurate representation could be obtained by considering expansions of the correlation functions in Fourier series: such expansions would, however, require an extensive database – hence justifying the alternative path that is followed in this work.

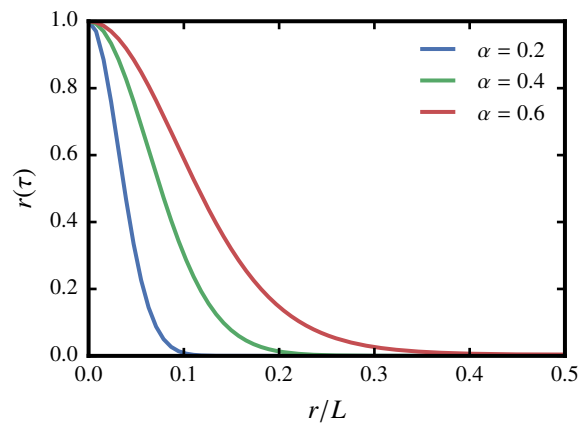


Figure 3.1. Correlation function (46) for various values of α .

It is worth noticing that due to the nonlinear mapping defined by equation (41), the correlation functions of the bulk and shear moduli random fields do not coincide with those of the associated Gaussian random fields. However, numerical evidences show that the nonlinear transformations generally induce similar shapes for the correlation functions of the image random fields, with a slight modification of the correlation length. In practice, parameter α must then be calibrated by solving an inverse problem, so that the resulting random fields $\{\kappa'(\mathbf{x}, \theta), \mathbf{x} \in \Omega\}$ and $\{\mu'(\mathbf{x}, \theta), \mathbf{x} \in \Omega\}$ exhibit the target correlation structure. Note that in a more general context, different correlation functions can readily be introduced for the modeling of bulk and shear moduli random fields. For each random field, different correlation lengths can be considered for each direction. The identification task for the parameters of the probabilistic representation is now addressed in the following section.

It is seen that the generation of the mesoscopic elasticity random field requires the postulated Gaussian random vector (see equation (41)). In the next section, we present relevant materials for the numerical efficient implementation of such problem.

3.4 On the generation of Gaussian random fields

The generation of the mesoscale bulk and shear moduli random fields mentioned in section 3.3 requires the generation of Gaussian random vectors with zero mean and a given correlation matrix (see equation (46)). It should be noted that in the present case, the bulk and shear moduli random fields are sampled over a three-dimensional regular grid of size $128 \times 128 \times 128$ voxels, which rises issues from a sampling standpoint. Indeed, various methods have been proposed in order to sample Gaussian vectors defined on large lattices. Among popular methods, one may resort on factorization-based methods (involving a Cholesky decomposition, a square-root decomposition or the circular embedding technique (Dietrich, 1993), for example), spectral methods (which offer the opportunity to use FFT algorithms (Shinozuka, 1971; Shinozuka and Deodatis, 1991, 1996; Poirion and Soize, 1995)) or iterative algorithms (Chow and Saad, 2014) to list a few. In practice, the choice of an appropriate method depends on various factors, such as the structure of the correlation matrix, the nature of the grid (2D, 3D) and the available computational resources for instance. In the present work, the covariance matrix is found to be

full (because of periodicity and long-range correlations), and the generation of the (discretized) Gaussian random fields is achieved by means of the Krylov subspace method (Chow and Saad, 2014) detailed below.

3.4.1 Krylov subspace method

One of the simplest technique allowing to sample a centered Gaussian random vector \mathbf{U} (with values in \mathbb{R}^n) defined by a correlation matrix \mathcal{R} relies on the decomposition

$$\mathbf{U} = \sqrt{\mathcal{R}}\mathbf{Z}, \quad (47)$$

where $\sqrt{\mathcal{R}}$ is the square-root of the symmetric positive-definite correlation matrix \mathcal{R} and \mathbf{Z} is a standard Gaussian random vector of length n . Indeed, it is readily seen that

$$\mathbb{E}\{\mathbf{U}\} = \mathbb{E}\{\sqrt{\mathcal{R}}\mathbf{Z}\} = \sqrt{\mathcal{R}}\mathbb{E}\{\mathbf{Z}\} = \mathbf{0}, \quad (48)$$

as \mathbf{Z} is centered, and

$$\mathbb{E}\{\mathbf{U}\mathbf{U}^T\} = \mathbb{E}\{\sqrt{\mathcal{R}}\mathbf{Z}\mathbf{Z}^T\sqrt{\mathcal{R}}\} = \sqrt{\mathcal{R}}\mathbb{E}\{\mathbf{Z}\mathbf{Z}^T\}\sqrt{\mathcal{R}} = \mathcal{R}, \quad (49)$$

since $\mathbb{E}\{\mathbf{Z}\mathbf{Z}^T\} = \mathbf{I}$ by definition. In practice, such an algorithm then requires the computation of the square-root $\sqrt{\mathcal{R}}$, which can be computationally expensive when large matrices are involved – and especially, when \mathcal{R} is not sparse.

Krylov subspace method specifically aims at approximating terms of the form $f(\mathcal{R})\mathbf{z}$, where f is a given function and \mathbf{z} a given vector, from a reduced dimensional Krylov subspace. In this work, the Krylov subspace method is used to evaluate samples $\{\mathbf{u}\}$ of \mathbf{U} as $\mathbf{u} = \sqrt{\mathcal{R}}\mathbf{z}$ through a Lanczos process (as \mathcal{R} is symmetric). This numerical procedure is reported below in algorithm 1 for the sake of completeness.

Algorithm 1: Algorithm to approximate $\sqrt{\mathcal{R}}\mathbf{z}$ (see Chow and Saad (2014))

Data: Matrix \mathcal{R} , initial normalized vector \mathbf{v}^1 , integer m

Result: Approximation $\mathbf{y} \approx \sqrt{\mathcal{R}}\mathbf{z}$

Initialization: $\beta_1 = 0$ and $\mathbf{v}^0 = \mathbf{0}$

for $j = 1$ **to** m **do**

$$\mathbf{v} = \mathcal{R}\mathbf{v}^j - \beta_j\mathbf{v}^{j-1}$$

$$\alpha_j = (\mathbf{v}^j)^T\mathbf{v}$$

$$\mathbf{v} = \mathbf{v} - \alpha_j\mathbf{v}^j$$

$$\beta_{j+1} = \|\mathbf{v}\|$$

if $\beta_{j+1} = 0$ **then**

 Set $m = j$ and return

$$\mathbf{v}^{j+1} = (1/\beta_{j+1})\mathbf{v}$$

Form the Lanczos basis $V_m = [\mathbf{v}^0, \mathbf{v}^1, \dots, \mathbf{v}^{j+1}]$

Form the tridiagonal matrix $T_m = \text{Tridiag}[\beta_j, \alpha_j, \beta_{j+1}]$

$$\mathbf{y}^{m+1} = \beta V_m \sqrt{T_m} \mathbf{e}_1$$

NOTA: \mathbf{e}_1 is the first column of the $m \times m$ identity matrix.

If the correlation matrix is well-behaved, the Krylov subspace method is found to run fast at a low computational cost. If the correlation matrix is ill-conditioned, appropriate *symmetric* preconditioner can be adopted to improve the accuracy and convergence rate (Chow and Saad, 2014). The most time-consuming step in algorithm 1 is the computation of the matrix-vector product $\mathcal{R}\mathbf{v}$, which costs $O(n^3)$ in time and $O(n^2)$ in memory requirements (the size of matrix \mathcal{R} is $n \times n$). In the present case, the correlation matrix is defined with respect to points that are located on a regular grid. As a consequence, the correlation matrix possesses a multilevel block Toeplitz structure (see figure 3.2 for an illustration). Interestingly, for this particular case, the storage

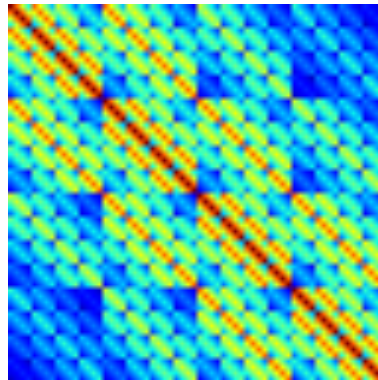


Figure 3.2. Three-level block Toeplitz structure of a correlation matrix evaluated from 4^3 points positioned in a three dimensional grid (see equation (46)).

of correlation matrix reduces to $O(n)$ memory requirements, as only the first row (column) has to be stored (Gray, 2006). Moreover, a fast FFT based algorithm can be adopted to efficiently compute the matrix vector product $\mathcal{R}\mathbf{v}$, which then costs $O(n \log n)$ in time (see algorithm 5). Technical details and materials for the numerical implementation of the algorithm can be found in appendix B.

3.4.2 Algorithmic issues

As suggested by Chow and Saad (2014), the stopping criterion for the Krylov subspace method can be defined by using the following relative error norm ϵ_m

$$\epsilon_m = \frac{\|\mathbf{y}^{m+1} - \mathbf{y}^m\|_2}{\|\mathbf{y}^{m+1}\|_2}, \quad (50)$$

where m is the number of iteration. In the present work, in order to maintain low computation time with satisfactory precision, the Krylov subspace method is stopped in the m^{th} iteration such that $\epsilon_m < 10^{-3}$. Figure 3.3 plots the relative error norm ϵ_m with respect to the number of iteration m .

For $\alpha = 0.5$, it can be deduced that 60 iterations are required in order to reach convergence. In figure 3.4, we present some sample paths for different values of α .

Due to the choice $\epsilon_m < 10^{-3}$ in the stopping criterion, some fluctuations on the sample paths remain noticeable. For future improvement, a symmetric preconditioner (e.g. FSAI (Kolotilina and Yeremin, 1993), AINV (Benzi et al., 2000)) could be adopted in the Krylov subspace method, as it was shown to give more accurate results and improve convergence rates (Chow and Saad, 2014). However, numerical investigation on this aspect are beyond the scope of this work.

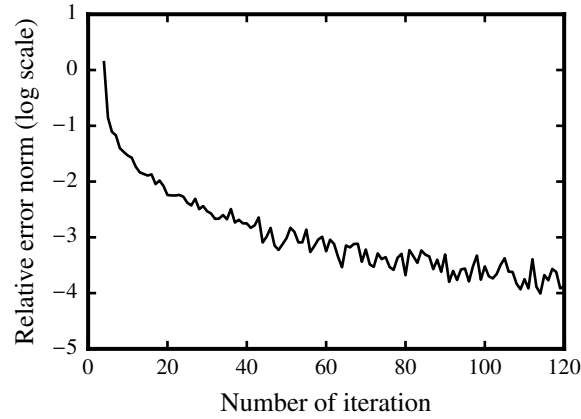


Figure 3.3. Plot of the relative error norm $m \mapsto \epsilon_m$ in log scale, for $\alpha = 0.5$ (see equation (46)).

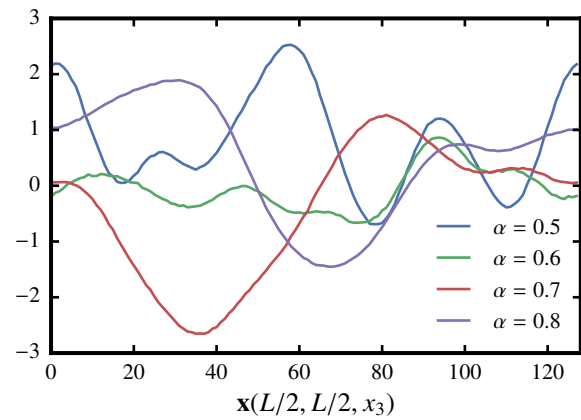


Figure 3.4. Sample paths of the gaussian random field for various values of α (see equation (46)).

3.4.3 Numerical scaling test for the generation of Gaussian random field

Here, we present the computational (CPU) time as a function of grid size. The grid size is varying from 8^3 to 128^3 voxels, which results in a (dense) correlation matrix the size of which ranges from 512×512 to approximately 2 millions \times 2 millions. The computational (CPU) time is computed as the average time over 10 realizations, for each grid size. The stopping criterion is again fixed to 10^{-3} . All the tests were recorded on a Intel i5-3230M CPU running at 2.6GHz (single core). The scaling of the CPU time with respect to the grid size is shown in figure 3.5.

For small grid sizes, the Krylov subspace method gives extremely small computational time (less than 10 seconds). For large grid sizes ($> 64^3$), the computational time is more pronounced and a noticeable lost of performance can be observed for grid sizes larger than 64^3 voxels.

3.5 Calibration of the probabilistic model

This section is concerned with the identification of the hyperparameters of the probabilistic model constructed in section 3.2. To this aim, we investigate below two identification strategies. The first strategy relies on statistical estimators and may require a large set of realizations. The results thus obtained will be notably considered as reference values in the validation task. The second strategy is based on the maximum likelihood method, which may be more suitable when

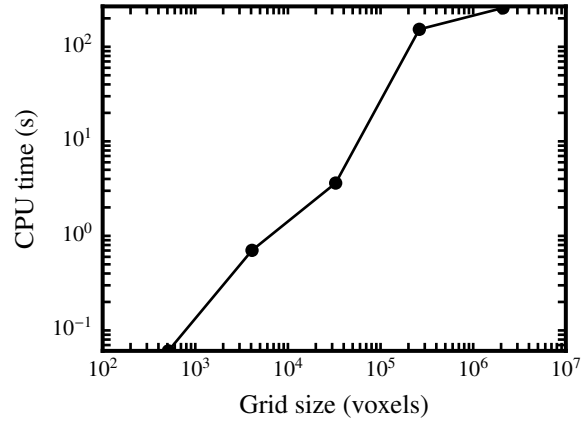


Figure 3.5. Scaling of the CPU time with respect to the grid size.

the affordable number of numerical experiments is small.

3.5.1 Identification through statistical estimators

The stochastic model for the mesoscale random fields depends on hyperparameters that define the first-order marginal distributions (which involves a mean value and a parameter controlling the statistical fluctuations, for each elastic modulus) and the spatial correlation lengths (see section 3.3). The parameters defining the marginal distributions can be obtained from the numerical database by using statistical estimators. The convergence of the estimators for the mean values and the coefficients of variation (at the center of domain Ω) are shown in figures 3.6 and 3.7.

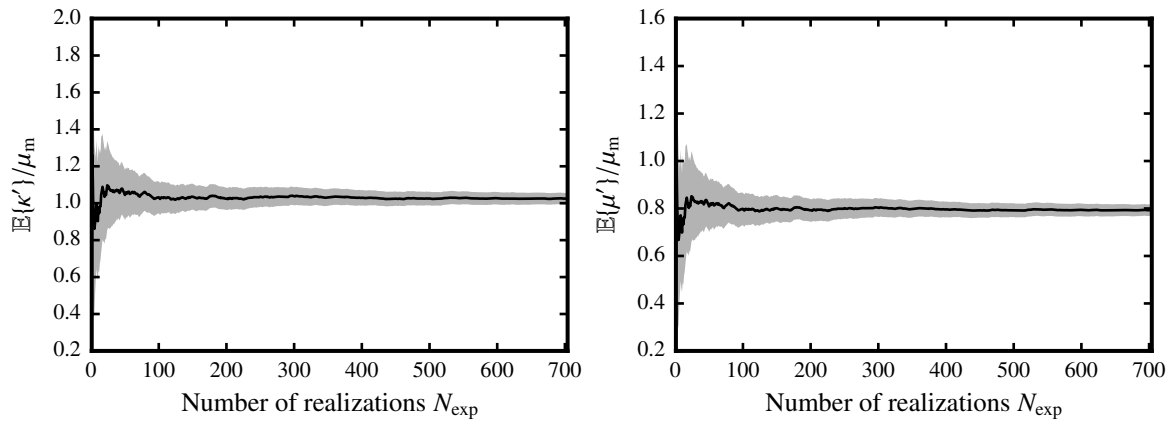


Figure 3.6. Convergence of the statistical estimators for the mean values of the random bulk (left panel) and shear (right panel) moduli. The error bar (gray zone) represents 99% confidence interval.

It is seen that a reasonable level of convergence is reached for $N_{\text{exp}} \geq 400$. The mean values are then found to be

$$\mathbb{E}\{\kappa'\} = 1.02\mu_m, \quad \mathbb{E}\{\mu'\} = 0.78\mu_m, \quad (51)$$

while the coefficients of variation $\delta_{\kappa'}$ and $\delta_{\mu'}$ are given by

$$\delta_{\kappa'} = 0.321, \quad \delta_{\mu'} = 0.329. \quad (52)$$

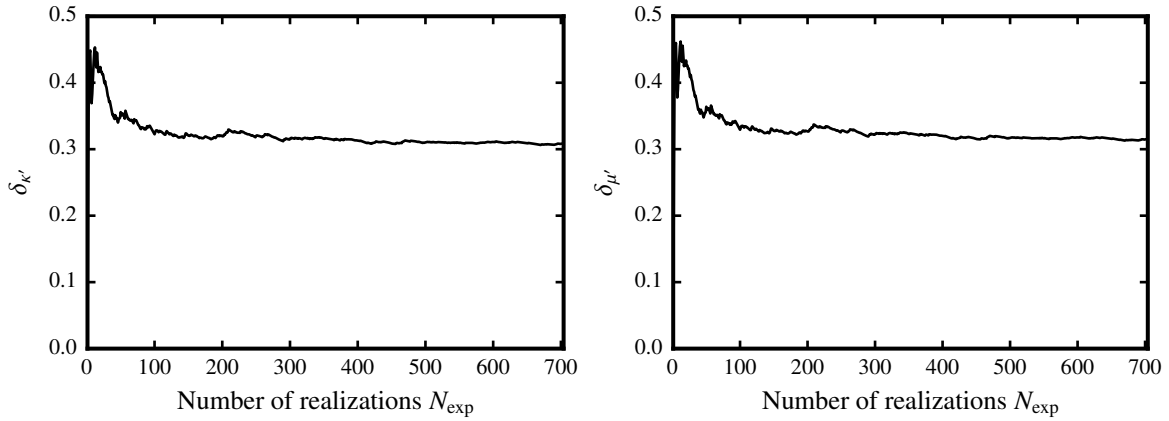


Figure 3.7. Convergence of the statistical estimators for the coefficients of variation of the random bulk (left panel) and shear (right panel) moduli.

We now turn to the calibration of the correlation structure. For this purpose, let $\tau \mapsto \mathcal{R}_{\kappa'}^{\text{mod}}(\tau \mathbf{e}_i; \alpha)$ be the correlation function of the bulk modulus random field defined by the stochastic model (see equation (30)). Note that the dependence of this function on α is made explicit for later use. Let $\tau \mapsto \mathcal{R}_{\kappa'}^{\text{data}}(\tau \mathbf{e}_i)$ be the correlation function of the bulk modulus random field estimated from the generated database. Similar notations are used for the shear modulus random fields. The optimal value α^{opt} of hyperparameter α is then defined as

$$\alpha^{\text{opt}} = \underset{\alpha \in]0, +\infty[}{\text{argmin}} \mathcal{J}(\alpha), \quad (53)$$

where the cost function \mathcal{J} is given by

$$\mathcal{J}(\alpha) = \sum_i^d \int_0^L |\mathcal{R}_{\kappa'}^{\text{mod}}(\tau \mathbf{e}_i; \alpha) - \mathcal{R}_{\kappa'}^{\text{data}}(\tau \mathbf{e}_i)| d\tau. \quad (54)$$

Note that \mathcal{J} only involves the correlation function associated with the bulk modulus random field, since the latter and the shear modulus random field exhibit the same correlation structure, both in the numerical experiments and in the model-based simulations (the situation where the two random fields exhibit different correlation structures could be accommodated as well by adapting the formulation of the cost function). Here, the non-linear optimization problem defined by equation (53) is solved with the Newton method; the plot of cost function $\alpha \mapsto \mathcal{J}(\alpha)$ is shown in figure 3.8. Using this methodology, the optimal value is finally found to be $\alpha^{\text{opt}} = 0.74$.

3.5.2 Identification through the maximum likelihood method

In this section, we address the calibration of the random field model by invoking the maximum likelihood principle, with the aim to substantially reduce the number of corrector problems to be solved. To this aim, we proceed sequentially, and the first-order marginal distributions are calibrated first. Let us consider the random bulk modulus, and define the optimal parameters as

$$(\mathbb{E}\{\kappa'\}, \delta_{\kappa'}) = \underset{(m, \delta) \in \mathbb{V}}{\text{arg max}} \ln(\mathcal{L}(m, \delta)), \quad (55)$$

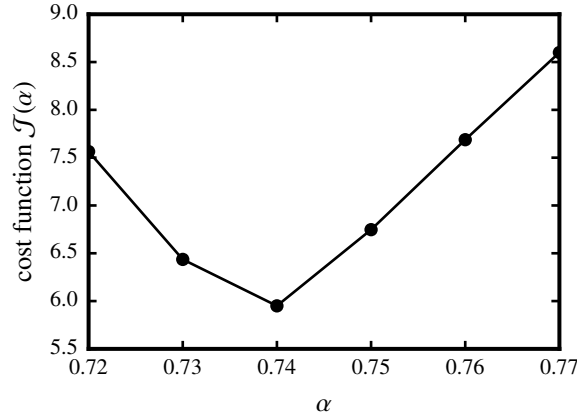


Figure 3.8. Plot of the cost function $\alpha \mapsto \mathcal{J}(\alpha)$ defined by equation (54).

where $\mathbb{V} = \mathbb{R}_+^* \times]0, 1/\sqrt{2}[$ and \mathcal{L} denotes the following likelihood function

$$\mathcal{L}(m, \delta) = \prod_{i=1}^{N_{\text{exp}}} p(\kappa'^{\text{data}}(\theta_i); m, \delta), \quad (56)$$

with $p(\cdot; m, \delta)$ the probability density function of the Gamma distribution with mean m and coefficient of variation δ (see equation (38)), and $\{\kappa'^{\text{data}}(\theta_i)\}_{1 \leq i \leq N_{\text{exp}}}$ a set of digitally generated experimental realizations obtained either from a single realization of the field (by sampling points that are sufficiently far apart from each other) and from several realizations. The parameters for the first-order probability density function associated with the random shear moduli are similarly calibrated by using the digitally generated experimental realizations $\{\mu'^{\text{data}}(\theta_i)\}_{1 \leq i \leq N_{\text{exp}}}$. The graphs of the above cost function for each modulus are shown in figures 3.9 and 3.10 for $N_{\text{exp}} = 50$ and $N_{\text{exp}} = 100$, respectively.

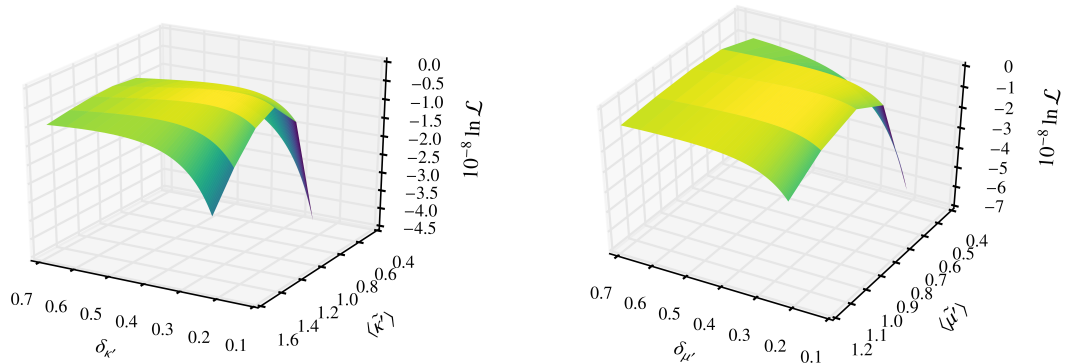


Figure 3.9. Plot of the cost function $(m, \delta) \mapsto \ln(\mathcal{L}(m, \delta))$ associated with the mesoscopic bulk (left panel) and shear (right panel) modulus for $N_{\text{exp}} = 50$.

The optimal parameters calibrated by the maximum likelihood principle are found to be

$$\mathbb{E}\{\kappa'\} = 1.02\mu_m, \quad \delta_{\kappa'} = 0.323, \quad \mathbb{E}\{\mu'\} = 0.78\mu_m, \quad \delta_{\mu'} = 0.332. \quad (57)$$

These values are reasonably close to the ones obtained by using classical statistical estimators (see section 3.5.1). It is worth noticing that although the cost function involved in equation (55)

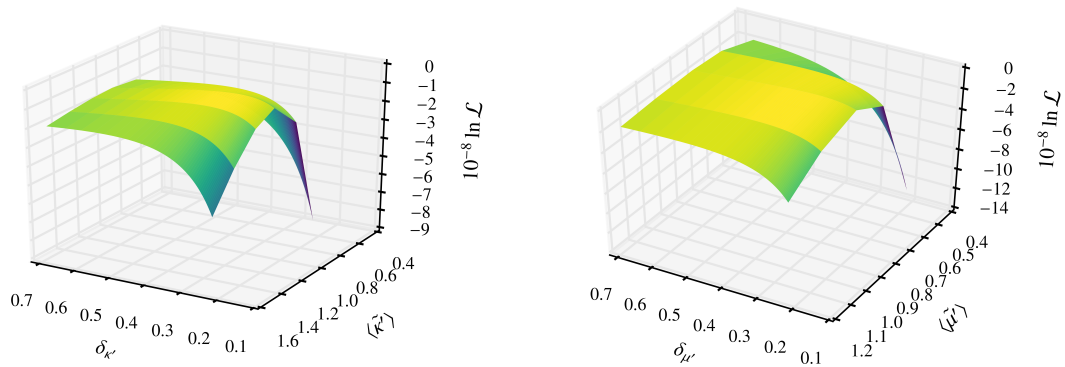


Figure 3.10. Plot of the cost function $(m, \delta) \mapsto \ln(\mathcal{L}(m, \delta))$ associated with the mesoscopic bulk (left) and shear (right) modulus for $N_{\text{exp}} = 100$.

exhibits slightly different shapes as N_{exp} varies in $\{10, 50, 150, 200, 700\}$, the maximum value turns out to be reached at the same point, hence providing a robust estimator for the parameters under consideration.

In order to proceed with the calibration of the parameter α involved in the description of the correlation structure of the underlying Gaussian random field, let us consider a set of points $\{\tilde{\mathbf{x}}^{(i)}\}_{1 \leq i \leq N_p}$ in Ω and introduce the N_p -valued random vector

$$\boldsymbol{\kappa}' = \left(\kappa'(\tilde{\mathbf{x}}^{(1)}), \dots, \kappa'(\tilde{\mathbf{x}}^{(N_p)}) \right). \quad (58)$$

In practice, the above set of points may be selected and optimized, for a given value of N_p , in accordance with the expected structure of correlation. In this work, where the underlying microstructure is statistically isotropic, the points are randomly placed and such that for all $1 \leq i \leq N_p$ and $1 \leq j \leq 3$, $\tilde{x}_j^{(i)}$ corresponds to the absolute value of an independent realization of a Gaussian random variable with a null mean and a standard deviation equal to $L/6$. Note that the probability distribution of $\boldsymbol{\kappa}'$ is unknown. Let $p_{\boldsymbol{\kappa}' \text{ model}}(\cdot; \alpha)$ be the probability density function of $\boldsymbol{\kappa}'$ estimated from realizations of the probabilistic model for the bulk modulus random field, with the first-order marginal defined by the parameters given above (hence, the explicit dependence on α). An optimal value is then sought as

$$\alpha^{\text{opt}} = \arg \max_{\alpha > 0} \ln(\mathcal{L}^*(\alpha)), \quad (59)$$

with

$$\mathcal{L}^*(\alpha) = \prod_{i=1}^{N_{\text{exp}}} p_{\boldsymbol{\kappa}' \text{ model}}(\boldsymbol{\kappa}'^{\text{data}}(\theta_i); \alpha), \quad (60)$$

the multidimensional likelihood function. The plot of the cost function $\alpha \mapsto \mathcal{L}^*(\alpha)$ is shown in figure 3.11 for several values of N_{exp} .

An optimal value is found as $\alpha^{\text{opt}} = 0.85$. It is seen that this estimation on the parameter α is also robust with respect to the number of realizations. It should be noted that the underlying Gaussian random fields are generated through the Krylov iterative method detailed in section 3.4. The choice of the stopping criterion parameter in this method (see equation (50)) may explain the discrepancy between the above estimation and the one obtained from the statistical estimator.

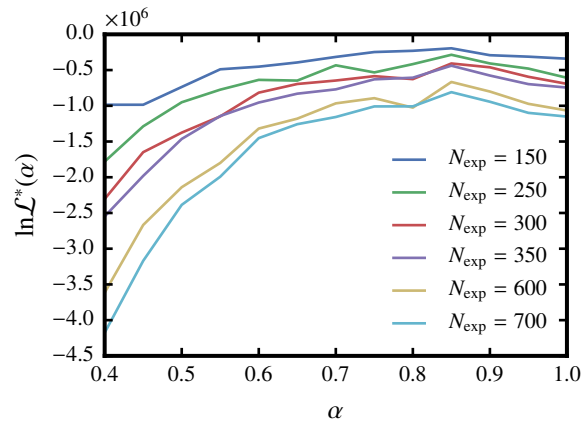


Figure 3.11. Plot of the cost function $\alpha \mapsto \ln(\mathcal{L}^*(\alpha))$.

3.6 Validation of the information-theoretic probabilistic model

This section is concerned with the validation of the probabilistic model calibrated in section 3.5.1. The relevance of model-based predictions is first discussed on the basis of mesoscale quantities of interest in section 3.6.1, whereas a comparison for homogenized apparent properties is provided in section 3.6.2.

3.6.1 Validation on mesoscale quantities of interest

Here, we investigate to what extent the probabilistic model can represent some quantities of interest defined at mesoscale. The probability density functions of shifted bulk and shifted shear moduli at a given point (recall that these quantities are invariant under translation in \mathbb{R}^d) are shown in figures 3.12 and 3.13, both for the numerical experiments and for the model-based simulations.

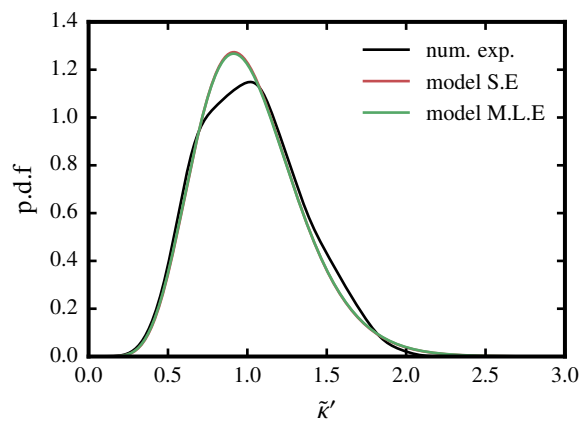


Figure 3.12. Comparison between the probability density functions of shifted mesoscopic bulk moduli obtained from the numerical experiments and from model-based simulations.

A good match is observed, regardless of the modulus under investigation and no matter the calibration strategy (in the present case, the parameters obtained from statistical estimators or from the maximum likelihood principle coincide). Next, the numerical experiments and

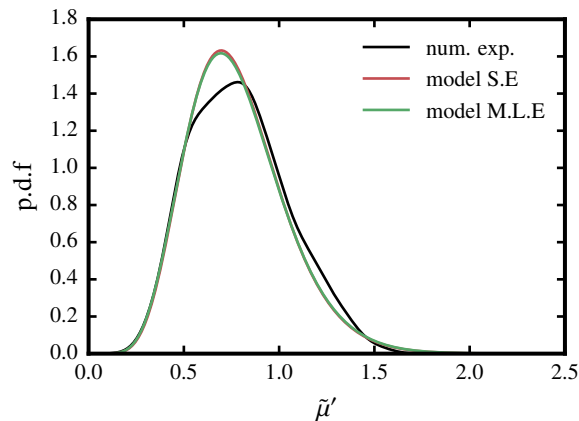


Figure 3.13. Comparison between the probability density functions of shifted mesoscopic shear moduli obtained from the numerical experiments and from model-based simulations.

model-based correlation functions are compared in figure 3.14 for the bulk modulus random field.

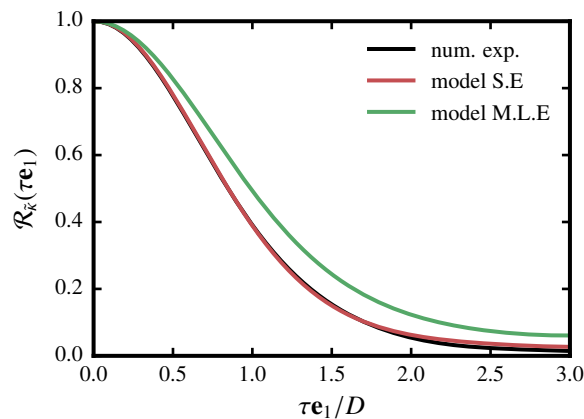


Figure 3.14. Estimated covariance function of the random bulk modulus along the x_1 -axis: comparison between numerical experiments and model-based simulations.

It is seen that the correlation function calibrated by using the statistical estimator reproduces almost perfectly the numerical experiments curve, whereas a small discrepancy with the one based on the likelihood estimator is observed. In the next section, we finally address the validation task in terms of apparent properties.

3.6.2 Validation based on apparent properties

Below, we compare the statistical averages (over 100 realizations) of apparent properties as obtained, either by solving a set of mesoscale corrector problems involving the calibrated stochastic model, or by directly solving the corrector problems defined at the microscale. The results (within the 99% confidence interval) are summarized in table 3.1. It is found that the ensemble average of apparent properties computed from the model are in very good agreement with the ones derived from the numerical experiments. Hence, the model is predictive.

In terms of computational time, and as mentioned previously, the numerical homogenization is realized in parallel over 64 cores, each core containing a Intel(R) Xeon(R) CPU E5-2640

	numerical experiments	Model S.E	Model M.L.E
$\mathbb{E}\{\kappa'\}/\mu_m$		1.02	1.02
$\mathbb{E}\{\mu'\}/\mu_m$		0.78	0.78
$\delta_{\kappa'}$		0.321	0.323
$\delta_{\mu'}$		0.329	0.332
α		0.74	0.85
$\mathbb{E}\{\kappa_{\text{app}}\}/\mu_m$	2.326 ± 0.001	2.331 ± 0.015	2.314 ± 0.087
$\mathbb{E}\{\mu_{\text{app}}\}/\mu_m$	1.767 ± 0.001	1.762 ± 0.012	1.748 ± 0.068

Table 3.1. Comparison between the apparent moduli derived from the numerical experiments and the probabilistic model (the 99% confidence interval is reported).

(running at 2.50GHz). The computation time induced by the homogenization task with the mesoscopic probabilistic models is about 15 seconds, per realization (of the mesostructure) and per macroscopic loading, while the homogenization from microscale to macroscale (see section 2.1.2) takes about 10 minutes per realization. The consideration of the mesoscopic approximation and the use of the probabilistic models within the homogenization procedure thus allow the computational time to be reduced by at least one order of magnitude.

Chapter 4

Conclusions and perspectives

In the first part of this thesis, we have investigated the capability of information-theoretic non-gaussian random field models to accurately represent mesoscopic elasticity fields obtained through the filtering procedure proposed in [Bignonnet et al. \(2014\)](#). For illustration purposes, the analysis has been performed on a simple (but non-trivial) model microstructure, namely an assembly of bidisperse inclusions embedded in a homogeneous matrix.

The statistical characterization of the mesoscopic stiffness tensor random fields was first addressed. It was shown, in particular, that the realizations obtained through the computational experiments can be well approximated by isotropic ones, hence allowing one to restrict the analysis to the bulk and shear moduli random fields. Based on this approximation, the mean fields and the correlation structures of these random fields were also estimated, with the aim to specify target values for the stochastic model in the calibration step.

Stochastic models for the mesoscopic random fields were then derived in the framework of information theory and more specifically, by invoking the principle of maximum entropy ([Jaynes, 1957a,b](#)). The latter forms a rational approach to the construction of stochastic models under some given mathematical and mechanical constraints, and does not generate modeling bias. The probabilistic models were thus constructed by defining the aforementioned random fields as nonlinear point-wise transformations of gaussian fields. These mappings, which are constructed by prescribing the family of information-theoretic first-order marginal distributions, completely (and implicitly) define the system of marginal distributions of the fields. Hence, the probabilistic models involve a small number of hyperparameters (namely the mean values, the coefficients of variation and the parameters defining the spatial correlation lengths), so that the identification task can be completed using a limited number of computational experiments.

This calibration step was subsequently discussed by pursuing two alternative strategies. The first one involves statistical estimators for the set of parameters defining the first-order marginal distributions, and a classical (constrained) least-squares optimization problem for the spatial correlation lengths defining the underlying gaussian fields. This strategy requires an extensive database ensuring the convergence of the statistical estimators and the associated results are considered as reference values. The second methodology relies on the maximum likelihood principle. It is shown that the latter also allows for a robust estimation of the hyperparameters (with respect to the number of realizations), and that the two strategies yield similar quantitative results – although the parameters related to the correlation lengths are found to be slightly different (we note that this difference may be induced by the sampling algorithms).

The validation of the random field models for given quantities of interest (at two different scales) was finally addressed. In particular, it was shown that the probabilistic models allow one to satisfactorily mimic some statistical features that are exhibited, *at mesoscale*, by the set of realizations obtained through the multiscale framework. Furthermore, it was shown that for the case under consideration, solving the mesoscopic boundary value problem (given by equation (18)) with the coefficients sampled from the calibrated models yields accurate predictions of the effective properties. This result shows the relevance of the proposed framework in order to predict, with substantial computational savings, the homogenized properties *at macroscale*.

Whereas the capabilities of the model to mimic the mesoscale features strongly depend on the statistical characteristics of the underlying microstructure, it should be noticed that more elaborated random field models have been proposed elsewhere (see e.g. (Guilleminot and Soize, 2013b)) in order to handle anisotropic material symmetry classes.

Furthermore, the extension of these techniques to nonlinear/inelastic behaviors is worth investigating and rises many difficulties due to the large number of internal variables involved in the constitutive models. In regard of filtering technique, the definition of mesoscopic stress (strain) field remains consistent with macroscopic stress (strain) regardless of the non-linearity. For elastoplastic composites, a promising technique is the Nonuniform Transformation Field Analysis technique (NTFA) (Michel and Suquet, 2003), for instance. The idea behind NTFA is that the anelastic strains can be expressed by a finite number of modes. If the modes are well chosen, the number of internal variables is low and the results still accurate. However, extension of the filtering framework to such behaviors remains unclear. Besides, the construction of suitable probabilistic models is still an open question.

Part III

Stress-gradient elasticity model

Chapter 5

Introduction

It is experimentally observed that size-effects generally occur in nanocomposites (Cho et al., 2006; Chisholm et al., 2005). The elastic properties of polymeric composites reinforced by nano glass beads/alumina particles (Cho et al., 2006) and epoxy matrix reinforced by nano carbon/SiC particles (Chisholm et al., 2005) were shown to depend on the size of inclusions at a fixed volume fraction. At a micrometer length scale, Lam et al. (2003) reported that size-effects also arise in solid epoxy beams undergoing bending, which is manifested by the dependence of normalized bending stiffness on the beam thickness.

In classical continuum (Cauchy) mechanics, interface and interphase models are often invoked to account for size-effects. The interface models are physically motivated by the fact that due to high surface to volume ratio, the surface energy of nanocomposites (which depends on surface area) is no longer negligible to their bulk strain energy. Therefore, interface effects become dominant at small sizes of heterogeneities. On the other hand, interphase models take into consideration a finite-size intermediate phase surrounding the heterogeneities, which strongly affects the macroscopic properties of nanocomposites. Mean field homogenization methods derived by interface and interphase models were shown to exhibit size-effects in the effective properties of nanocomposites (see e.g. Duan et al. (2005), Li et al. (2011b)).

The material model presented in the second part of this thesis falls under the category of so-called generalized continua, which were introduced at the beginning of the 20th century. They extend classical continua in order to describe more general behaviors of heterogeneous materials, including size-effects. In a non-exhaustive manner, generalized continua can be roughly classified into three categories. *Higher order models* aim at equipping material points with additional degrees of freedom, beside classical translation (e.g. Cosserat and Cosserat (1909)). *Higher grade models* include higher order derivatives of the displacement into the strain energy density (e.g. Mindlin and Eshel (1968)). Finally, *non local elasticity models* assume that the stress at a point depends on the strain in a region near that point (e.g. Eringen (1972)). Due to dimensional consistency, generalized continua introduce additional material internal lengths thus allowing to take into consideration e.g. size-effects.

Numerical homogenization of generalized continua is much more costly than classical elasticity (de Borst et al., 1993). This is in particular the case of higher order models where the number of degrees of freedom becomes large. In the matter of higher grade model, the higher order continuity of shape functions may also be tricky to deal with. Note however that standard C^0 -continuous elements can be adapted in a mixed formulation (Shu et al., 1999) but the

computational cost is still high. In addition to numerical homogenization, classical mean field methods, which based on the solution to Eshelby's inclusion problem (Eshelby, 1957), have the main asset that the effective properties of heterogeneous materials can be evaluated analytically (or semi-analytically). Although mean field methods only account for limited morphological information, they stand as an essential step to shed light on the physical insight of generalized continuum models.

In this introductory chapter, we recall some well-known models of generalized continua with a particular focus on their mean field homogenization, in view to predict size-effects. The literature on generalized continua is very rich and we only underlined the most salient features of some models. In the remainder of this chapter, we limit to the case of higher order and higher grade models for linear, isotropic, centrosymmetric materials with quasi-statics loading under infinitesimal strain theory. For the sake of simplicity, body forces (body couples, moments) will be omitted.

This chapter is organized as follows. Section 5.1 recalls some well-known higher order continua which include Cosserat, couple stress and micromorphic model. Section 5.2 is devoted to the class of higher grade models (first and second strain-gradient). Finally, a discussion on the homogenization of generalized continua is addressed in section 5.3.

5.1 Higher order models

Classical elasticity assumes that the motion of a material point is only characterized by a displacement vector, \mathbf{u} . The state of stress at a point is then defined by a symmetric stress tensor. Higher order models generalize classical elasticity by allowing material points to rotate (e.g. Cosserat media (Cosserat and Cosserat, 1909)), stretch or expand (e.g. microstretch media (Eringen, 1990)). More generally, the geometric transform undergone by the material point may be fully described by a micro-deformation tensor (e.g. micromorphic media (Eringen and Suhubi, 1964; Suhubi and Eringen, 1964; Mindlin, 1964; Germain, 1973)). It should be noted that the stress tensor in higher order models is no longer symmetric.

5.1.1 Cosserat (micropolar) model

More than one hundred years ago, Cosserat and Cosserat (1909) developed a generalized model for deformable bodies which assumed that the material point in a solid can rotate independently to its translation. In other words, the motion of a Cosserat body is described by a displacement field, \mathbf{u} , and a micro-rotation field, $\boldsymbol{\theta}$, attributed to each material point. It should be noted that the micro-rotation is different to the macro body rotation $\boldsymbol{\omega} = \frac{1}{2}\text{curl } \mathbf{u}$. It was only several decades later that the Cosserat model was thoroughly investigated with both rigorous mathematical reformulation and attempt to address its physical insight (Truesdell and Toupin, 1960; Toupin, 1962; Mindlin and Tiersten, 1962; Mindlin, 1965; Eringen, 1966, 1967). Eringen (1968) extended the Cosserat model to examine the dynamic effects through the introduction of the so-called *micro inertia* and renamed the Cosserat model as the *micropolar model*.

The strain measures include the strain field and the curvature field which are respectively defined by $\boldsymbol{\epsilon} = \nabla \mathbf{u} + \boldsymbol{\epsilon} \cdot \boldsymbol{\theta}$ and $\boldsymbol{\chi} = \nabla \boldsymbol{\theta}$, where $\boldsymbol{\epsilon}$ denotes the permutation tensor. For a linear,

isotropic, centrosymmetric Cosserat material, the strain energy density function reads

$$w(\mathbf{e}, \boldsymbol{\chi}) = \frac{1}{2} \mathbf{e} : \mathbf{C} : \mathbf{e} + \frac{1}{2} \boldsymbol{\chi} : \mathbf{D} : \boldsymbol{\chi}, \quad (61)$$

in which the elasticity tensors \mathbf{C} , \mathbf{D} obey the major symmetry, i.e. $C_{ijkl} = C_{klij}$, $D_{ijkl} = D_{klij}$ but not minor symmetries due to the asymmetry of the strain measures. The stress, $\boldsymbol{\sigma}$, and couple stress tensor, $\boldsymbol{\mu}$, are respectively energetically conjugate to the strain and curvature tensor

$$\boldsymbol{\sigma} = \frac{\partial w(\mathbf{e}, \boldsymbol{\chi})}{\partial \mathbf{e}} = \lambda \text{tr}(\mathbf{e}) \mathbf{I} + 2\mu \mathbf{e}^s + 2\zeta \mathbf{e}^a, \quad (62a)$$

$$\boldsymbol{\mu} = \frac{\partial w(\mathbf{e}, \boldsymbol{\chi})}{\partial \boldsymbol{\chi}} = \alpha \text{tr}(\boldsymbol{\chi}) \mathbf{I} + 2\beta \boldsymbol{\chi}^s + 2\gamma \boldsymbol{\chi}^a, \quad (62b)$$

where \mathbf{I} denotes the second-rank identity tensor, \mathbf{e}^s and \mathbf{e}^a denote respectively the symmetric and anti-symmetric part of tensor \mathbf{e} .

In addition, the Cosserat model introduces four elastic constants $\alpha, \beta, \gamma, \zeta$ [N] beside two classical Lamé coefficients λ, μ [Pa]. Classical elasticity is obtained as a special case of the Cosserat model for vanishing $\alpha, \beta, \gamma, \zeta$. Furthermore, material stability requires (Eringen, 1968)

$$\mu > 0, \quad \zeta > 0, \quad \beta > 0, \quad \gamma > 0, \quad 2\mu + 3\lambda > 0, \quad 2\beta + 3\alpha > 0. \quad (63)$$

The elastic equilibrium of a Cosserat body loaded at its boundary only reads

$$\nabla \cdot \boldsymbol{\sigma} = \mathbf{0}, \quad \nabla \cdot \boldsymbol{\mu} - \boldsymbol{\epsilon} : \boldsymbol{\sigma} = \mathbf{0}, \quad (64)$$

with prescribed surfaces forces $\mathbf{t} = \boldsymbol{\sigma} \cdot \mathbf{n}$ and surfaces couples $\mathbf{m} = \boldsymbol{\mu} \cdot \mathbf{n}$ on the boundary (\mathbf{n} is the outer normal to the boundary).

The Cosserat model was successfully adopted to explain the formation of finite-width shear bands in granular media (Mühlhaus and Vardoulakis, 1987; Tejchman and Wu, 1993). It also is able to capture size-effects that occur in elastic solid undergoing bending or torsion (Gauthier and Jahsman, 1975; Lakes, 1983, 1986; Anderson and Lakes, 1994), as well as grain-size effects in polycrystals (Forest et al., 2000), etc. Formulations of the Cosserat model for plates and shells were also proposed (see Altenbach et al. (2010) for a detailed review).

5.1.2 Couple stress model

If the micro-rotation is constrained to be equal to the macro rotation vector, $\boldsymbol{\theta} = \boldsymbol{\omega} = \frac{1}{2} \text{curl } \mathbf{u}$, the Cosserat model reduces to the so-called *couple stress model* (Toupin, 1962; Mindlin and Tiersten, 1962; Koiter, 1964). It follows directly that the curvature tensor, $\boldsymbol{\chi} = \nabla \boldsymbol{\theta}$, is deviatoric, $\chi_{ii} = 0$. Assuming that the strain energy density is a function of the strain and curvature tensors, i.e. $w = w(\mathbf{e}, \boldsymbol{\chi})$, the stress and couple stress tensors are defined by (see also equation (62))

$$\boldsymbol{\sigma} = \frac{\partial w(\mathbf{e}, \boldsymbol{\chi})}{\partial \mathbf{e}} = \lambda \text{tr}(\mathbf{e}) \mathbf{I} + 2\mu \mathbf{e}, \quad (65a)$$

$$\boldsymbol{\mu} = \frac{\partial w(\mathbf{e}, \boldsymbol{\chi})}{\partial \boldsymbol{\chi}} = 2\beta \boldsymbol{\chi}^s + 2\gamma \boldsymbol{\chi}^a, \quad (65b)$$

where \mathbf{I} denotes the second-rank identity tensor. The couple stress model contains two additional material parameters β, γ [N] in addition to two Lamé coefficients λ, μ [Pa].

It can be seen from equation (65b) that the couple stress tensor $\boldsymbol{\mu}$ is the derivative of a scalar function w with respect to a deviatoric argument $\boldsymbol{\chi}$, therefore its spherical part cannot be found from the above constitutive equations. Eringen (1968) thus called this model as *indeterminate couple stress* (see also the recent discussion by Neff et al. (2016)). It is worth mentioning that the normal components of the macro rotation cannot be prescribed independently from the displacement at the boundary of a couple stress body.

A sub class of couple stress model was introduced by Yang et al. (2002), in which they postulated additional equilibrium equations for moments of couples. This assumption forces the couple stress tensor to be *symmetric*. The number of material internal length is subsequently reduced to one beside two classical Lamé constants. The strain energy density reads (see equation (43) in Yang et al. (2002))

$$w = \frac{1}{2} \lambda \text{tr}(\boldsymbol{\varepsilon})^2 + \mu (\boldsymbol{\varepsilon} : \boldsymbol{\varepsilon} + \ell^2 \boldsymbol{\chi} : \boldsymbol{\chi}), \quad (66)$$

where $\boldsymbol{\varepsilon} = \nabla^s \mathbf{u}$ and $\boldsymbol{\chi} = \nabla^s \boldsymbol{\theta}$ in which we denote $\nabla^s \mathbf{u}$ as the symmetric part of the gradient of \mathbf{u} , ℓ is the material parameter with dimension of length. The stress and couple stress tensors, work-conjugate to strain and curvature tensors are obtained by

$$\boldsymbol{\sigma} = \frac{\partial w(\boldsymbol{\varepsilon}, \boldsymbol{\chi})}{\partial \boldsymbol{\varepsilon}} = \lambda \text{tr}(\boldsymbol{\varepsilon}) \mathbf{I} + 2\mu \boldsymbol{\varepsilon}, \quad (67a)$$

$$\boldsymbol{\mu} = \frac{\partial w(\boldsymbol{\varepsilon}, \boldsymbol{\chi})}{\partial \boldsymbol{\chi}} = 2\mu \ell^2 \boldsymbol{\chi}. \quad (67b)$$

The Yang et al. (2002) *modified couple stress model* has two assets. It restores the symmetry of the couple stress tensor. Moreover, only one material internal length is involved in the constitutive laws. An energetically-consistent derivation of modified couple stress model by using the principle of minimum total potential energy can be found in Park and Gao (2007). Owing to its simplicity, the modified couple stress model is largely adopted for modeling size-effects, e.g. size-dependent Euler-Bernoulli beam (Park and Gao, 2006), size-dependent Timoshenko beam (Ma et al., 2008).

5.1.3 Micromorphic model

In Eringen's micromorphic model, a classical material *point* is considered as a finite material *volume*. In turn, the motion of a micromorphic body is described by a classical translation and an additional second order micro-deformation tensor $\boldsymbol{\phi}$ (Eringen and Suhubi, 1964; Suhubi and Eringen, 1964; Mindlin, 1964). Germain (1973) generalized Eringen's micromorphic model by introducing additional third and higher order micro-deformation tensor. Field equations were formulated thanks to the principle of virtual work. Up to date, Germain (1973) micromorphic model can be seen as the most general continuum model of materials with microstructure. In the following, we introduce the field equations of Eringen's micromorphic model, which can also be obtained by Germain (1973)'s development with truncation at second order internal variables.

The strain measures in Eringen's micromorphic model include the symmetric strain $\boldsymbol{\varepsilon}$, relative (asymmetric in general) strain \mathbf{e} and the micro-deformation gradient $\boldsymbol{\kappa}$, which are respectively defined by

$$\boldsymbol{\varepsilon} = \nabla^s \mathbf{u}, \quad \mathbf{e} = \nabla \mathbf{u} - \boldsymbol{\phi}, \quad \boldsymbol{\kappa} = \nabla \boldsymbol{\phi}. \quad (68)$$

The strain energy density function depends on the strain, relative strain and micro-deformation gradient, $w = w(\boldsymbol{\varepsilon}, \mathbf{e}, \boldsymbol{\kappa})$. The (symmetric) stress, relative stress and third order stress which are respectively work-conjugate to the strain, relative strain and micro-deformation gradient are defined by

$$\boldsymbol{\sigma} = \frac{\partial w}{\partial \boldsymbol{\varepsilon}} = \mathbf{C} : \boldsymbol{\varepsilon}, \quad (69)$$

$$\mathbf{s} = \frac{\partial w}{\partial \mathbf{e}} = \mathbf{D} : \mathbf{e}, \quad (70)$$

$$\boldsymbol{\mu} = \frac{\partial w}{\partial \boldsymbol{\kappa}} = \mathbf{F} : : \boldsymbol{\kappa}, \quad (71)$$

where elasticity tensors $\mathbf{C}, \mathbf{D}, \mathbf{F}$ obey the major symmetry. In addition the elasticity tensor \mathbf{C} displays the minor symmetry. The equilibrium of a micromorphic body loaded at its boundary only then reads

$$\nabla \cdot (\boldsymbol{\sigma} + \mathbf{s}) = \mathbf{0}, \quad \nabla \cdot \boldsymbol{\mu} + \mathbf{s} = \mathbf{0}, \quad (72)$$

with prescribed tractions $\mathbf{t}_1 = (\boldsymbol{\sigma} + \mathbf{s}) \cdot \mathbf{n}$, $\mathbf{t}_2 = \boldsymbol{\mu} \cdot \mathbf{n}$ on the boundary (\mathbf{n} is the outer normal to the boundary).

It can be seen that the micromorphic model degenerates to the Cosserat model if the micro-deformation reduces to the micro-rotation. The (first) strain-gradient model, which will be introduced in the next section, is retrieved when the micro-deformation is constrained to be the displacement gradient. In a more general point of view, the [Germain \(1973\)](#) micromorphic approach can be regarded as a unifying thermomechanical framework which brings to terms other classes of generalized continua ([Forest and Sievert, 2003](#); [Forest, 2009](#)).

In the previous section, a brief overview of some higher grade models was presented. The enrichment of classical elasticity through the introduction of additional degrees of freedom allows for describing size-effects in materials with microstructure. Due to the difficulty in theoretical analysis and experimental identification of material parameters, several higher grade models with reduced number of material parameters were also introduced. In the following, we consider another class of generalized continua, namely higher grade models.

5.2 Higher grade models

Higher grade models account for higher order derivatives of the displacement in the strain energy density function ([Mindlin, 1964](#)). The most general form accounts for derivatives of any order ([Green and Rivlin, 1964](#)), which theoretically introduces an infinite number of material parameters. The *second* and *third* order derivatives of the displacement are usually considered (or respectively the *first* and *second* order derivatives of strain). These models are called *first strain gradient* ([Mindlin, 1964](#); [Mindlin and Eshel, 1968](#)) and *second strain gradient* models ([Mindlin, 1965](#)).

5.2.1 First strain gradient elasticity

[Mindlin \(1964\)](#) proposed three formulations of the first strain-gradient model. In form I, the strain energy density is assumed to be a quadratic form of the strain and the second order

derivatives of the displacement. In form II, the strain energy density is a function of the strain and its gradient. Form III postulates that the strain energy density is a function of the strain, the rotation gradient $\kappa_{ij} = \frac{1}{2}\epsilon_{imk}u_{m,kj}$ and the symmetric second gradient of the displacement $\kappa_{ijk} = \frac{1}{3}(u_{i,jk} + u_{j,ki} + u_{k,ij})$. Mindlin and Eshel (1968) showed that these three formulations lead to the same displacement-based equations of motion for isotropic materials. However, only form II leads to a symmetric total stress tensor, therefore it is usually used in the literature to analyze size-effects and referred to as the first strain-gradient model (Askes and Aifantis, 2011). In form II, the most general expression of the strain energy density for isotropic, centrosymmetric strain gradient materials reads

$$w = \frac{1}{2}\lambda\epsilon_{ii}\epsilon_{jj} + \mu\epsilon_{ij}\epsilon_{ij} + a_1\kappa_{iik}\kappa_{kjj} + a_2\kappa_{ijj}\kappa_{ikk} + a_3\kappa_{iik}\kappa_{jjk} + a_4\kappa_{ijk}\kappa_{ijk} + a_5\kappa_{ijk}\kappa_{kji}. \quad (73)$$

It is seen that the most general strain-gradient model for isotropic materials contains five additional material constants a_i [N] in addition to two Lamé coefficients λ, μ [Pa]. Due to the difficulty in experimentally identifying the material internal lengths, several models have been proposed, which require a reduced number of material parameters. For instance, Aifantis (1992) formulated a first strain-gradient model with only one material internal length. This model is known as *GRADELA*. The strain energy density is defined by (see equation (2.5) in Mindlin and Eshel (1968))

$$w = \frac{1}{2}\lambda\epsilon_{ii}\epsilon_{jj} + \mu\epsilon_{ij}\epsilon_{ij} + c\left(\frac{1}{2}\lambda\epsilon_{ii,k}\epsilon_{jj,k} + \mu\epsilon_{ij,k}\epsilon_{ij,k}\right), \quad (74)$$

where c is a material parameter having unit of length squared, i.e $c = \ell^2$. Due to its simplicity, the *GRADELA* model was widely adopted, for instance in finite element implementations (Amanatidou and Aravas, 2002). Later, Gao and Park (2007) proposed an energetically consistent derivation of *GRADELA* by using the principle of minimum potential energy. They showed that the boundary conditions in *GRADELA* is incomplete. They proposed the set of complete boundary conditions and named this model as *simplified strain-gradient model*. This model was employed for instance to analyze Eshelby's problem of various inclusion shapes (Gao and Ma, 2009, 2010; Gao and Liu, 2012; Ma and Gao, 2014).

At this stage, it should be noted that the simplified strain-gradient model is often referred to as a *stress-gradient* model owing to the linear relationship between stress and strain. In particular, the stress tensor $\boldsymbol{\sigma}$ and the double stress $\boldsymbol{\mu}$ read

$$\boldsymbol{\sigma} = \frac{\partial w}{\partial \boldsymbol{\epsilon}} = \lambda \text{tr}(\boldsymbol{\epsilon})\mathbf{I} + 2\mu\boldsymbol{\epsilon}, \quad (75a)$$

$$\boldsymbol{\mu} = \frac{\partial w}{\partial \boldsymbol{\kappa}} = c\nabla(\lambda \text{tr}(\boldsymbol{\epsilon})\mathbf{I} + 2\mu\boldsymbol{\epsilon}). \quad (75b)$$

Substituting equation (75a) into equation (75b), we find

$$\boldsymbol{\mu} = c\nabla\boldsymbol{\sigma}, \quad (76)$$

which shows that the double stress is the gradient of the stress. As a consequence, the divergence-free total stress tensor is given by

$$\boldsymbol{\tau} = \boldsymbol{\sigma} - \nabla \cdot \boldsymbol{\mu} = \boldsymbol{\sigma} - c\nabla^2\boldsymbol{\sigma}. \quad (77)$$

However, [Forest and Aifantis \(2010\)](#) pointed out that the presence of the gradient of the stress in this model is rather the result of a specific constitutive assumption in the general model of [Mindlin and Eshel \(1968\)](#) (the simplified strain-gradient model is obtained by setting $a_3 = c\lambda/2$, $a_4 = c\mu$ and other coefficients to zero in equation (73)). Consequently, the model of [Aifantis \(1992\)](#) and [Gao and Park \(2007\)](#) should really be understood as a strain-gradient model.

Simplified models with three material internal lengths were also proposed. For instance, following the idea of [Smyshlyaev and Fleck \(1996\)](#), [Lam et al. \(2003\)](#) first decomposed the strain gradient κ_{ijk} into a symmetric part, κ^s , and an anti-symmetric part, κ^a ,

$$\kappa_{ijk}^s = \frac{1}{3}(\kappa_{ijk} + \kappa_{jki} + \kappa_{kij}), \quad \kappa_{ijk}^a = \frac{2}{3}\epsilon_{ikl}\chi_{lj} + \frac{2}{3}\epsilon_{jkl}\chi_{li}, \quad (78)$$

where χ is the curvature tensor, $\chi_{ij} = \epsilon_{ipq}\kappa_{pqj}$. Note that this tensor can be also be decomposed in symmetric and antisymmetric parts $\chi = \chi^s + \chi^a$. The symmetric strain gradient, κ^s , is further split into a so-called trace part, κ^0 , and a so-called trace-less part, κ^1 ,

$$\kappa_{ijk}^0 = \frac{1}{5}(\delta_{ij}\kappa_{mnk}^s + \delta_{jk}\kappa_{mni}^s + \delta_{ki}\kappa_{mmi}^s), \quad \kappa_{ijk}^1 = \kappa_{ijk}^s - \kappa_{ijk}^0, \quad (79)$$

which were shown to be mutually orthogonal. The higher order stresses $\mu_{ijk}^0, \mu_{ijk}^1, \mu_{ijk}^a$ are work-conjugate to the linearly independent strain gradients $\kappa_{ijk}^0, \kappa_{ijk}^1, \kappa_{ijk}^a$. [Lam et al. \(2003\)](#) further introduced additional equilibrium equation for moment of couples (also done in [Yang et al. \(2002\)](#)). This requires that the couple stress tensor, work-conjugate to the curvature tensor, is symmetric. As a result, the asymmetric part of the curvature tensor is irrelevant to the deformation energy. The number of elastic constants reduces to *three* for linear, isotropic, strain-gradient materials. They further adopted this model to interpret size-effects in solid beams undergoing bending. [Lam et al. \(2003\)](#) successfully identified the material internal lengths from experimental tests on cantilever epoxy beams, and showed that the normalized bending rigidity increases with decreases in beam thickness.

More recently, [Zhou et al. \(2016\)](#) introduced another sub-class of strain-gradient materials. Decomposing the strain gradient κ and the higher-order stress μ according to the above mentioned work of [Lam et al. \(2003\)](#)(see equations (14), (26) in [Zhou et al. \(2016\)](#))

$$\kappa = \kappa^0 + \kappa^1 + \kappa^2 + \kappa^3, \quad (80)$$

$$\mu = \mu^0 + \mu^1 + \mu^2 + \mu^3, \quad (81)$$

[Zhou et al. \(2016\)](#) assumed that the higher-order stresses μ^0, μ^1, μ^2 and μ^3 are work-conjugate to the strain gradients $\kappa^0, \kappa^1, \kappa^2$, and κ^3 , respectively. This assumption results in a sub-class of the general model of [Mindlin and Eshel \(1968\)](#) with *three* material internal lengths only.

5.2.2 Second strain gradient elasticity

[Mindlin \(1965\)](#) showed that the first strain-gradient model is not sufficient to describe internal strains and stresses that develop close to a free surface. He then claimed that a second strain gradient model is required to account for cohesive forces and surface tension in isotropic elastic materials. [Mindlin \(1965\)](#) assumed that the strain energy density is a function of the strain, its first and second gradients

$$w = w(\mathbf{e}, \nabla \mathbf{e}, \nabla \nabla \mathbf{e}). \quad (82)$$

For linear isotropic, centrosymmetric strain gradient materials, this function can be written as (see equation (19) in [Mindlin \(1965\)](#))

$$\begin{aligned}
w = & \frac{1}{2} \lambda \varepsilon_{ii} \varepsilon_{jj} + \mu \varepsilon_{ij} \varepsilon_{ij} + a_1 \varepsilon_{ijj} \varepsilon_{ikk} + a_2 \varepsilon_{iik} \varepsilon_{kjj} + a_3 \varepsilon_{iik} \varepsilon_{jjk} + a_4 \varepsilon_{ijk} \varepsilon_{ijk} + a_5 \varepsilon_{ijk} \varepsilon_{kji} \\
& + b_1 \varepsilon_{iij} \varepsilon_{kkll} + b_2 \varepsilon_{ijkk} \varepsilon_{ijll} + b_3 \varepsilon_{iijk} \varepsilon_{jkl} + b_4 \varepsilon_{iijk} \varepsilon_{llkj} + b_5 \varepsilon_{iijk} \varepsilon_{lljk} + b_6 \varepsilon_{ijkl} \varepsilon_{ijkl} \\
& + b_7 \varepsilon_{ijkl} \varepsilon_{jkli} + c_1 \varepsilon_{ii} \varepsilon_{jjkk} + c_2 \varepsilon_{ij} \varepsilon_{ijkk} + c_3 \varepsilon_{ij} \varepsilon_{kkij} + b_0 \varepsilon_{iijj},
\end{aligned} \tag{83}$$

where ε_{ij} , ε_{ijk} , ε_{ijkl} are respectively the components of $\boldsymbol{\varepsilon}$, $\nabla \boldsymbol{\varepsilon}$ and $\nabla \nabla \boldsymbol{\varepsilon}$. It is seen that there are 18 elastic constants for isotropic second strain-gradient materials. In particular, a_i [N] are similar to their counterparts in the first strain-gradient model. The constants b_i , $i \neq 0$ [N.m²] relate to the second gradient of strain while c_i [N] are coupling constants between the strain and second gradient of strain. The cohesion modulus b_0 [N] was shown to be directly linked to surface energy (work per unit area done by the force that creates the new surface) ([Mindlin, 1965](#)). It was recently shown by [Cordero et al. \(2015\)](#) that the second strain-gradient model can account for both surface energy and surface elasticity effects. More specifically, on the basis of a series of analytical solutions, [Cordero et al. \(2015\)](#) showed that the contribution of surface energy is only related to the cohesion modulus b_0 while surface elasticity effects are directly linked to the coupling moduli c_i .

In the previous section, we recalled some higher order models in which higher order derivatives of the displacement are taken into consideration in the strain energy density. Similarly to higher grade models (see section 5.2), experimental identification of the material internal lengths can be difficult. Therefore, several models with a reduced number of material parameters were proposed. Due to its simplicity, the first strain gradient model with only one internal material length is often invoked to account for size-effects. This model was misleadingly regarded as a stress-gradient model.

In the next section, the homogenization of generalized continua (higher order and higher grade models) is summarized with an emphasis on mean field approaches as they are less expensive than full field computations.

5.3 Homogenization of generalized continua

5.3.1 Some remarks on the homogenization of generalized continua

In a homogenization context, generalized continua may arise at the microscopic scale and/or at the macroscopic scale. In the present section, we list three different combinations which have been previously investigated in the literature.

The first case corresponds to Cauchy heterogeneous materials which are homogenized as generalized continua ([Forest and Sab, 1998](#); [Forest, 1998, 2002](#); [Feyel, 2003](#); [Bigoni and Drugan, 2006](#)). This situation may occur if the scale separation condition is not fulfilled (see section 1.1.1). For instance, the characteristic length of the loading might be large but not much larger than the typical size of the heterogeneities. The heterogeneous material is then expected to behave macroscopically as a generalized continuum. Some microscale features (e.g. boundary layers) are transferred to the macroscopic scale and still appear at this level.

By means of asymptotic expansions [Boutin \(1996\)](#); [Triantafyllidis and Bardenhagen \(1996\)](#); [Smyshlyaev and Cherednichenko \(2000\)](#) constructed higher order constitutive relations for the overall behavior of periodic (Cauchy) heterogeneous media. They showed that the higher order gradients of the macroscopic strain were involved. For composites with spherical inclusions, [Bigoni and Drugan \(2006\)](#) demonstrated that a homogeneous Cosserat medium can approximate a heterogeneous Cauchy medium when the inclusions are softer than the matrix. Otherwise, Cosserat effects were shown to be negligible. This observation is consistent with experimental tests conducted by [Gauthier and Jahsman \(1975\)](#); [Gauthier \(1982\)](#) in which Cosserat effects were shown to be absent for reinforced composites. In general, it turns out that more general non homogeneous boundary conditions (for instance, polynomial displacements) have to be specified in order to enable the contribution of effective generalized continua at the macroscopic scale. A comprehensive discussion of several such boundary conditions can be found in [Forest and Trinh \(2011\)](#); [Trinh et al. \(2012\)](#).

The second case corresponds to generalized heterogeneous materials which are homogenized as generalized continua. This situation again occurs in the absence of scale separation. Attention must then be paid to the boundary conditions for the auxiliary boundary-value problem at the micro-scale. [Ma and Gao \(2014\)](#) employed quadratic displacement boundary conditions, which give rise to a macroscopic strain-gradient continuum. A set of boundary conditions for Cosserat media that satisfies the Hill–Mandel lemma can be also found in [Li and Liu \(2009\)](#); [Li et al. \(2010b,a, 2011a\)](#).

The last case corresponds to generalized heterogeneous materials which are homogenized as Cauchy materials. This situation occurs in particular if the scale separation condition is met and the material internal length ℓ is comparable or much smaller than the typical size of the heterogeneities. In particular, [Forest et al. \(2001\)](#) showed that the homogenization of Cosserat medium leads to a macroscopic homogeneous Cauchy medium. Under this assumption, the homogenization of fiber composite materials was performed in [Xun et al. \(2004a,b\)](#).

The present work is restricted to this last case where the material internal length is comparable or much smaller than the size of the heterogeneities. Following the same argument as [Forest et al. \(2001\)](#), stress-gradient materials will be homogenized as Cauchy materials. To do so, three approaches can be invoked: numerical homogenization by means of full-field calculations, mean field methods and bounds. However, numerical homogenization methods are costly for generalized continua ([Feyel, 2003](#)). We therefore focus on mean field methods and bounds, that will be discussed in the following two sections.

5.3.2 Mean field homogenization methods

Classical mean field methods, e.g. [Mori and Tanaka \(1973\)](#); [Benveniste \(1987\)](#), can provide satisfactory estimation on the effective properties of heterogeneous materials with almost zero computational cost. They are mainly based on the solution to Eshelby’s inclusion problem ([Eshelby, 1957, 1959](#)). In classical elasticity, for a given eigenstrain $\boldsymbol{\varepsilon}^*$, the Eshelby’s tensor \mathbb{S} relates the perturbations strain inside the inclusion $\boldsymbol{\varepsilon}$ to its eigenstrain

$$\boldsymbol{\varepsilon} = \mathbb{S} : \boldsymbol{\varepsilon}^*. \quad (84)$$

For ellipsoidal inclusions, [Eshelby \(1957\)](#) found that the Eshelby’s tensor is a constant tensor,

hence the stress and strain inside the inclusion are uniform.

In order to account for size-effects, it is then natural to examine Eshelby's problem for generalized continua. However, it turns out that Eshelby's theorem (Eshelby, 1957) does not hold within the framework of generalized continua. Indeed, the strain (stress) is no longer uniform within the inclusion and Eshelby's tensor is not constant. As a consequence, an inhomogeneity can not be replaced by an equivalent inclusion with prescribed *uniform* eigenstrain but rather by *non uniform* fields. In other words, the following equation does not hold (Sharma and Dasgupta, 2002; Zhang and Sharma, 2005)

$$\langle \mathbb{S}(\mathbf{x}) : \boldsymbol{\varepsilon}^*(\mathbf{x}) \rangle \neq \langle \mathbb{S}(\mathbf{x}) \rangle : \langle \boldsymbol{\varepsilon}^*(\mathbf{x}) \rangle, \quad (85)$$

where $\mathbb{S}(\mathbf{x})$ is the non uniform Eshelby's tensor(s), $\boldsymbol{\varepsilon}^*(\mathbf{x})$ is the non uniform eigenstrain. The inequality (85) was also encountered in classical elasticity for non-ellipsoidal inclusions (Nozaki and Taya, 2000). Note that, in general the computation of non uniform eigenstrain is analytically intractable. In order to overcome this shortcoming, the approximate equivalent inclusion assumption (Nozaki and Taya, 2000; Sharma and Dasgupta, 2002; Zhang and Sharma, 2005) is usually made, i.e. the eigenstrain is assumed to be uniform. The inequality in equation (85) becomes an (approximate) equality.

Under the above assumption, Eshelby's inclusion problem was solved for various generalized continuum models. For instance, Eshelby tensor of spherical (Cheng and He, 1995), cylindrical (Cheng and He, 1997), ellipsoidal (Ma and Hu, 2007) inclusions embedded in an infinite matrix of a Cosserat material were solved with the help of Green functions derived earlier by Sandru (1966). Zheng and Zhao (2004); Zhang and Sharma (2005) derived an explicit form of Eshelby's tensor for spherical inclusions used couple stress model. The simplified strain-gradient model (Aifantis, 1992; Gao and Park, 2007) was used to derive Eshelby tensor of ellipsoidal (Gao and Ma, 2010), cylindrical (Ma and Gao, 2009), polyhedral (Gao and Liu, 2012), polygonal (Liu and Gao, 2013) inclusions.

Mori-Tanaka estimates of the effective properties of generalized continua materials can then be produced. For isotropic materials, it was observed that the effective modulus increases as the size of the inclusions decreases, which is known as the stiffening size-effect (Sharma and Dasgupta, 2002; Zhang and Sharma, 2005). Prescribing quadratic boundary conditions, Ma and Gao (2014) extended these estimates to the homogenization of strain-gradient materials as strain-gradient materials.

To close this section, it should be noted that Xun et al. (2004a) took a different route to the Mori-Tanaka homogenization of generalized continua. These authors solved directly Eshelby's inhomogeneity (not inclusion) problem for a Cosserat matrix reinforced by circular Cauchy fibers. The strain localization tensor was then obtained in closed form, with no need to resort to the equivalent inclusion approximation. These authors again showed that the effective shear modulus exhibits a stiffening size-effect.

Quite interestingly, these authors compared their predictions to that of (Sharma and Dasgupta, 2002) (which were obtained within the equivalent inclusion approximation). Both were shown to be in good agreement. In other words, Eshelby's inhomogeneity and inclusion problems deliver similar Mori-Tanaka estimates of the effective properties. In the present work, we chose to solve Eshelby's inhomogeneity problem.

5.3.3 Variational principles and bounds

Bounds are valuable tools which consistency checks for numerical and mean field homogenization methods. In classical elasticity, some well-known bounds include Voigt-Reuss (first order bounds) and Hashin and Shtrikman (1963) (second order bounds) which only depend on the mechanical properties and volume fraction of each phase (under the assumption of statistical isotropy for the latter).

Substitution of uniform trial fields in energy principle (complementary, potential) is expected to lead to classical Voigt-Reuss bounds. This is showed by Smyshlyaev and Fleck (1994) for an incompressible couple stress material. The obtained bounds are thus irrelevant for predicting size dependent elastic properties. This result suggests that enriched (non uniform) trial fields are required to derive size dependent bounds (as done in Mühlich et al. (2012) for strain-gradient materials).

Variational principle and bounds of Hashin Shtrikman type were also established for linear, isotropic, incompressible couple stress materials by Smyshlyaev and Fleck (1994). They later extended the bounds to plasticity strain-gradient materials (Smyshlyaev and Fleck, 1995), polycrystals materials (Smyshlyaev and Fleck, 1996) and incompressible strain-gradient plasticity for two-phase materials (Fleck and Willis, 2004). It should be noted that their approach was mainly based on the general variational framework developed by Willis (1977, 1983); Talbot and Willis (1985) for non-linear Cauchy materials. Interestingly, they showed that the bounds depend explicitly on the two point probability function, which is contrary to classical elasticity. However, this dependency was not quantitatively analyzed in the above mentioned works.

5.4 Methodology

Owing to their unusual mechanical properties, nanocomposites have been used in many engineering applications. The question of predicting their mechanical properties is obviously of tremendous interest. In sections 5.1 and 5.2, some generalized continuum models were briefly presented. As argued at the end of section 5.3, when the size of the material internal length is comparable or smaller than the typical size of the heterogeneities, homogenization of generalized continua leads to a macroscopically homogeneous Cauchy medium (under the classical separation of scale condition), albeit with size effects induced by the introduction of material internal length(s). As such, generalized continua stand as attractive material models to account for size-effects in nanocomposites.

The work presented in the second part of this thesis is dedicated to the homogenization of a new class of generalized continua, recently introduced by Forest and Sab (2012) (see also Sab et al., 2016), namely *stress-gradient materials*. At first glance, the stress- and strain-gradient models are conceptually similar. In particular, while the strain-gradient model relies on the elastic strain energy depending on the strain and its first-gradient, the stress-gradient model relies on the complementary elastic strain energy depending on the stress and its first gradient. Owing to the linear stress-strain relationship, this might lead to a misconception that stress- and strain-gradient models are equivalent (see also the discussion in section 5.2.1). In fact, as will be shown in the present work, the two models define widely different materials.

For example, stress- and strain-gradients induce opposite size-effects. While the effective

stiffness of strain-gradient composites increases when the size of the heterogeneities decreases (the so-called *stiffening* size-effect), the opposite trend is observed with stress-gradient materials (the so-called *softening* size-effect). It is observed experimentally that most nanocomposites exhibit the stiffening size-effect; for such materials, the strain-gradient model is therefore relevant. However, numerical evidence from atomistic simulation suggests that some polymer nanocomposites (Odegard et al., 2005; Davydov et al., 2014) or nano silicon beams (Sun et al., 2007) might exhibit the softening size-effect. The strain-gradient model would not be able to account for such effects, while the stress-gradient model has the required qualitative behavior. This pleads for a more thorough investigation of heterogeneous stress-gradient materials. As a first step, mean field homogenization methods and bounds will be implemented. Despite the fact that they only account for limited statistical description of the underlying microstructure (up to second order), they are relatively simple to put in practice while allowing for satisfactory and predictive results. Besides, these approaches lend themselves to parametric studies. As such, they offer an insight into the meaning of all material parameters and are a prerequisite to numerical homogenization techniques which, being much more costly, would not allow for such qualitative analysis of the stress-gradient model.

The second part of this thesis is organized as follows. The stress-gradient model is first revisited in chapter 6. In particular, we present an energetically consistent derivation of the stress-gradient model by minimizing the complementary energy. The role of the *trace* (to be defined in chapter 6) of the stress-gradient is discussed in detail. Then, general energy principles are derived. Drawing inspiration from the works of Aifantis (1992) and Gao and Park (2007) (see section 5.2.1), we propose a stress-gradient model with only one material internal length (this model will be referred to as the simplified stress-gradient model).

We then set up a theoretical framework for the homogenization of stress-gradient materials in chapter 7. We derive boundary conditions that are suitable to the computation of the apparent compliance of linearly elastic stress-gradient materials. We further show that contrary to strain-gradient materials, stress-gradient materials exhibit the softening size-effect. In view to derive estimates of the effective mechanical properties of stress-gradient composites by mean field methods, we solve Eshelby's spherical inhomogeneity. The resulting analytical solution is then implemented in a Mori–Tanaka scheme to produce estimates of the effective properties of stress-gradient composites with monodisperse, spherical inhomogeneities.

In chapter 8, we derive Hashin–Shtrikman bounds for stress-gradient materials. As in the case of strain-gradient composites, the bounds are expected to depend on the microstructure (the two-point probability function). For specific choices of this function, the bounds are given explicitly. It is shown that the sensitivity to the two-point probability function is rather weak.

Chapter 9 summarizes this study and gives some perspectives for future research.

Chapter 6

The stress-gradient model

This chapter is devoted to the formulation of the stress-gradient model of [Forest and Sab \(2012\)](#) (see also [Sab et al. \(2016\)](#) for a mathematical analysis). It opens with some preliminary mathematical definitions (see section 6.1). We then turn to the derivation of the stress-gradient model by minimizing the complementary strain energy in section 6.2. We then show that the trace of the stress gradient (to be defined below) plays the role of a generalized prestress in section 6.3. Energy principles for stress-gradient bodies will be formulated in section 6.4. For further analysis, we restrict to linear stress-gradient elasticity in which we propose a stress-gradient model with only one material internal length in section 6.5, in line with the simplified strain gradient model of [Aifantis \(1992\)](#); [Gao and Park \(2007\)](#) previously introduced in section 5.2.1.

This chapter closes with an instructive example, namely the pure bending of rectangular beams (see section 6.6). We show that the simplified stress-gradient model gives rise to boundary layers near the free surfaces, which result in size-dependent behavior.

6.1 Preliminary linear algebra

Since we will deal with second-, third-, four- and sixth- order tensors in this work, it is convenient to introduce the space of these tensors

$$\begin{aligned} {}^2\mathcal{T} &= \left\{ {}^2\mathbf{T} = T_{ij}\mathbf{e}_i \otimes \mathbf{e}_j, \text{ such that } T_{ij} = T_{ji} \right\} \\ {}^3\mathcal{T} &= \left\{ {}^3\mathbf{T} = T_{ijk}\mathbf{e}_i \otimes \mathbf{e}_j \otimes \mathbf{e}_k, \text{ such that } T_{ijk} = T_{jik} \right\} \\ {}^4\mathcal{T} &= \left\{ {}^4\mathbf{T} = T_{ijkl}\mathbf{e}_i \otimes \mathbf{e}_j \otimes \mathbf{e}_k \otimes \mathbf{e}_l, \text{ such that } T_{ijkl} = T_{jikl} = T_{ijlk} \right\} \\ {}^6\mathcal{T} &= \left\{ {}^6\mathbf{T} = T_{ijkpqr}\mathbf{e}_i \otimes \mathbf{e}_j \otimes \mathbf{e}_k \otimes \mathbf{e}_p \otimes \mathbf{e}_q \otimes \mathbf{e}_r, \text{ such that } T_{ijkpqr} = T_{jikpqr} = T_{ijkqpr} \right\} \end{aligned}$$

In other words, ${}^2\mathcal{T}$ denotes the space of symmetric, second-rank tensors; ${}^3\mathcal{T}$ denotes the space of third-rank tensors which are symmetric with respect to their first two indices; ${}^4\mathcal{T}$ denotes the space of fourth-rank tensors which obey the major and minor symmetries and ${}^6\mathcal{T}$ denotes the space of sixth-rank tensors with the following symmetry $T_{ijkpqr} = T_{jikpqr} = T_{ijkqpr}$. In most case, the rank of tensor under consideration can be determined from the context. Wherever confusion can occur, we will specify its rank, e.g. ${}^2\boldsymbol{\sigma}$. We recall the components of second-, fourth- and sixth-rank identity tensors

$${}^2\mathbf{I} = \delta_{ij}\mathbf{e}_i \otimes \mathbf{e}_j, \quad {}^4\mathbf{I} = \frac{1}{2} (\delta_{ik}\delta_{jl} + \delta_{il}\delta_{jk}) \mathbf{e}_i \otimes \mathbf{e}_j \otimes \mathbf{e}_k \otimes \mathbf{e}_l, \quad {}^6\mathbf{I} = I_{ijpq}\delta_{kr} \mathbf{e}_i \otimes \mathbf{e}_j \otimes \mathbf{e}_k \otimes \mathbf{e}_p \otimes \mathbf{e}_q \otimes \mathbf{e}_r. \quad (86)$$

6.1.1 Linear algebra of the trace and the trace-free part of third rank tensors

The stress-gradient model developed in this chapter assumes that the complementary energy density depends on both the stress $\boldsymbol{\sigma}$ and its first gradient $\nabla\boldsymbol{\sigma}$. In the remainder of this work, we define the trace of a third-rank tensor as its contraction with respect to its last two indices. It is then observed that the trace of the stress-gradient is fixed from the equilibrium equation, $\nabla \cdot \boldsymbol{\sigma} + \mathbf{b} = \mathbf{0}$, since $(\nabla\boldsymbol{\sigma}) : \mathbf{I} = \nabla \cdot \boldsymbol{\sigma}$. This suggests to decompose the stress-gradient $\nabla\boldsymbol{\sigma}$ as a sum of two orthogonal (with respect to the \cdot product) tensors, one of which being trace-free

$$\nabla\boldsymbol{\sigma} = \mathbf{R} + \mathbf{Q}, \quad (87)$$

where $\mathbf{R} : {}^2\mathbf{I} = \mathbf{0}$ and $\mathbf{R} \cdot \mathbf{Q} = 0$. In the present section, we prove that the above decomposition exists and is unique for any third-rank tensor $\mathbf{T} \in {}^3\mathcal{T}$. We further provide closed-form expressions of the sixth-rank projectors \mathbf{J} and \mathbf{K} such that

$$\mathbf{R} = \mathbf{K} \cdot \mathbf{T}, \quad \mathbf{Q} = \mathbf{J} \cdot \mathbf{T}, \quad (88)$$

where \mathbf{K} is the orthogonal projection onto the space ${}^3\mathcal{D}$ of trace-free, third rank tensors defined as follows

$$\mathbf{T} \in {}^3\mathcal{D} \Leftrightarrow \mathbf{T} : {}^2\mathbf{I} = \mathbf{0}. \quad (89)$$

We first consider an arbitrary vector \mathbf{v} ; then ${}^4\mathbf{I} \cdot \mathbf{v} \in {}^3\mathcal{T}$ and, for all trace-free tensors $\mathbf{R} \in {}^3\mathcal{D}$

$$({}^4\mathbf{I} \cdot \mathbf{v}) \cdot \mathbf{R} = \mathbf{R} \cdot ({}^4\mathbf{I} \cdot \mathbf{v}) = \mathbf{v} \cdot \mathbf{R} : {}^2\mathbf{I} = 0, \quad (90)$$

where the identity $\mathbf{R} \cdot ({}^4\mathbf{I} \cdot \mathbf{v}) = \mathbf{R} : {}^2\mathbf{I}$ has been used. In equation (90), the last equality follows from the fact that \mathbf{R} is trace-free. In other words, we showed that the third-rank tensor ${}^4\mathbf{I} \cdot \mathbf{v}$ is orthogonal to ${}^3\mathcal{D}$. Furthermore, the trace of the third-rank tensor ${}^4\mathbf{I} \cdot \mathbf{v}$ is

$$({}^4\mathbf{I} \cdot \mathbf{v}) : {}^2\mathbf{I} = \frac{d+1}{2}\mathbf{v}, \quad (91)$$

where d denotes the dimension of the physical space.

We now consider $\mathbf{T} \in {}^3\mathcal{T}$, and introduce the following third-rank tensor

$$\mathbf{Q} = \frac{2}{d+1} {}^4\mathbf{I} \cdot (\mathbf{T} : {}^2\mathbf{I}). \quad (92)$$

From equation (91), we find that \mathbf{T} and \mathbf{Q} have same trace; thus, $\mathbf{R} = \mathbf{T} - \mathbf{Q}$ is trace-free. Furthermore, $\mathbf{Q} \cdot \mathbf{R} = 0$, since \mathbf{Q} is of the form $\mathbf{I} \cdot \mathbf{v}$. In other words, we have produced the orthogonal decomposition $\mathbf{T} = \mathbf{Q} + \mathbf{R}$, where \mathbf{R} is trace-free. It is handy to introduce the sixth-rank projectors \mathbf{J} and \mathbf{K} such that equation (88) holds. It follows from the above developments that

$$\mathbf{K} + \mathbf{J} = \mathbf{I}, \quad \mathbf{K} \cdot \mathbf{K} = \mathbf{K}, \quad \mathbf{J} \cdot \mathbf{J} = \mathbf{J}, \quad \mathbf{K} \cdot \mathbf{J} = \mathbf{J} \cdot \mathbf{K} = \mathbf{0} \quad (93)$$

and

$$\mathbf{J} \cdot \mathbf{T} = \frac{2}{d+1} {}^4\mathbf{I} \cdot (\mathbf{T} : {}^2\mathbf{I}). \quad (94)$$

Furthermore, for a stress field $\boldsymbol{\sigma}$ statically admissible with the body forces \mathbf{b}

$$\mathbf{J} \cdot (\nabla\boldsymbol{\sigma}) = \frac{2}{d+1} {}^4\mathbf{I} \cdot (\nabla\boldsymbol{\sigma}) : {}^2\mathbf{I} = \frac{2}{d+1} {}^4\mathbf{I} \cdot (\nabla \cdot \boldsymbol{\sigma}) = -\frac{2}{d+1} {}^4\mathbf{I} \cdot \mathbf{b}. \quad (95)$$

6.1.2 The \boxtimes -product of a fourth-rank tensor and a second-rank tensor

In this section, we define the \boxtimes -product which will appear in the formulation of simplified stress-gradient model (see section 6.5). We consider a fourth-rank tensor $\mathbf{A} \in {}^4\mathcal{T}$ and a second-rank tensor $\mathbf{B} \in {}^2\mathcal{T}$. By definition, $\mathbf{A} \boxtimes \mathbf{B}$ is the following sixth-rank tensor

$$\mathbf{A} \boxtimes \mathbf{B} = A_{ijpq} B_{kr} \mathbf{e}_i \otimes \mathbf{e}_j \otimes \mathbf{e}_k \otimes \mathbf{e}_p \otimes \mathbf{e}_q \otimes \mathbf{e}_r, \quad (96)$$

For any third-rank tensor $\mathbf{x} \in {}^3\mathcal{T}$, it can be verified from the definition of the \boxtimes -product that

$$(\mathbf{A} \boxtimes \mathbf{B}) \therefore \mathbf{x} = \mathbf{A} : \mathbf{x} \cdot \mathbf{B}^T, \quad (97)$$

from which it results that the sixth-rank identity is the \boxtimes -product of the fourth-rank identity and the second-rank identity

$${}^6\mathbf{I} = {}^4\mathbf{I} \boxtimes {}^2\mathbf{I}. \quad (98)$$

Furthermore, for all $\mathbf{A}, \mathbf{A}' \in {}^4\mathcal{T}$ and $\mathbf{B}, \mathbf{B}' \in {}^2\mathcal{T}$

$$(\mathbf{A} \boxtimes \mathbf{B}) \therefore (\mathbf{A}' \boxtimes \mathbf{B}') = (\mathbf{A} : \mathbf{A}') \boxtimes (\mathbf{B} \cdot \mathbf{B}'), \quad (99)$$

which shows that the inverse of $\mathbf{A} \boxtimes \mathbf{B}$ with respect to the “ \therefore ” product is

$$(\mathbf{A} \boxtimes \mathbf{B})^{-1} = \mathbf{A}^{-1} \boxtimes \mathbf{B}^{-1}, \quad (100)$$

provided that \mathbf{A} and \mathbf{B} are not singular (with respect to the “ \therefore ” and “ \cdot ” products, respectively). Finally, the transpose of $\mathbf{A} \boxtimes \mathbf{B}$ with respect to the “ \therefore ” scalar product of third-rank tensors reads

$$(\mathbf{A} \boxtimes \mathbf{B})^T = \mathbf{A}^T \boxtimes \mathbf{B}^T. \quad (101)$$

The above mathematical definitions will ease the derivation of the stress-gradient model of [Forest and Sab \(2012\)](#), which we now address.

6.2 Derivation of the stress-gradient model by minimizing the complementary energy

6.2.1 Complementary strain energy of stress-gradient bodies

We consider a heterogeneous body occupying the domain $\Omega \subset \mathbb{R}^d$ subjected to body forces \mathbf{b} , where d is the physical dimension ($d = 2, 3$). w^* denotes the volume density of complementary strain energy. In classical elasticity, w^* depends on the local stress and the observation point, i.e. $w^* = w^*(\mathbf{x}, \boldsymbol{\sigma}(\mathbf{x}))$. Assuming that Ω is fully clamped, the classical elasticity boundary value problem is established by minimizing the complementary energy

$$W^*(\boldsymbol{\sigma}) = \int_{\mathbf{x} \in \Omega} w^*(\mathbf{x}, \boldsymbol{\sigma}(\mathbf{x})) dV_{\mathbf{x}}, \quad (102)$$

under the constraint that $\boldsymbol{\sigma}$ be statically admissible with \mathbf{b} , that is $\nabla \cdot \boldsymbol{\sigma} + \mathbf{b} = \mathbf{0}$.

The (first) strain-gradient model extends classical elasticity by accounting for the gradient of strain in the strain energy density function. By a complementary approach, the stress-gradient model would assume that W^* depends on the local stress $\boldsymbol{\sigma}$ and its gradient $\nabla\boldsymbol{\sigma}$. In other words, the complementary energy functional to be minimized now reads

$$W^*(\boldsymbol{\sigma}) = \int_{\Omega} w^*(\boldsymbol{\sigma}, \nabla\boldsymbol{\sigma}) dV, \quad (103)$$

where the explicit dependency on the observation point \mathbf{x} has been omitted. The above functional must again be minimized under the constraint $\nabla \cdot \boldsymbol{\sigma} + \mathbf{b} = \mathbf{0}$. The resulting constrained minimization problem defines in principle a fully clamped (in a sense that remains to be specified) stress-gradient material. In order to ease the constrained optimization of W^* , the stress gradient tensor is decomposed as follows (see section 6.1.1)

$$\nabla\boldsymbol{\sigma} = \mathbf{R} + \mathbf{Q}, \quad (104)$$

where $\mathbf{R} \in {}^3\mathcal{D}$ and $\mathbf{R} \cdot \mathbf{Q} = 0$. In equation (103), $w^*(\boldsymbol{\sigma}, \nabla\boldsymbol{\sigma})$ is then equivalently replaced with $w^*(\boldsymbol{\sigma}, \mathbf{R}, \mathbf{Q})$. It should however be noted that $\mathbf{Q} = -\frac{2}{d+1}\mathbf{I} \cdot \mathbf{b}$ (see equation (95)). In other words, \mathbf{Q} is fully constrained. As a consequence, there is no strain measure associated with \mathbf{Q} , which indeed plays the role of a prestress, as will be shown in section 6.3.

This prestress will be omitted in the remainder of this work, as its physical meaning remains unclear. More precisely, it will be assumed that the complementary strain energy density w^* depends on $\boldsymbol{\sigma}$ and \mathbf{R} only. Equation (103) then becomes

$$W^*(\boldsymbol{\sigma}) = \int_{\Omega} w^*(\boldsymbol{\sigma}, \mathbf{R}) dV. \quad (105)$$

6.2.2 Equilibrium of a clamped, stress-gradient body

As previously argued in section 6.2.1, the equilibrium of the clamped, stress-gradient body is defined by the minimization of the complementary strain energy W^* defined by equation (105). Taking its first variation yields

$$\delta W^* = \int_{\Omega} \left[\frac{\partial w^*}{\partial \boldsymbol{\sigma}} : \delta\boldsymbol{\sigma} + \frac{\partial w^*}{\partial \mathbf{R}} \cdot \mathbf{K} \cdot (\nabla\delta\boldsymbol{\sigma}) \right] dV, \quad (106)$$

for all divergence-free stress variation $\delta\boldsymbol{\sigma}$. This suggests to introduce the strain measures $\mathbf{e} = \partial_{\boldsymbol{\sigma}} w^*$ and $\boldsymbol{\phi} = \partial_{\mathbf{R}} w^*$, energy conjugates of $\boldsymbol{\sigma}$ and \mathbf{R}

$$\mathbf{e} = \frac{\partial w^*(\boldsymbol{\sigma}, \mathbf{R})}{\partial \boldsymbol{\sigma}}, \quad (107a)$$

$$\boldsymbol{\phi} = \frac{\partial w^*(\boldsymbol{\sigma}, \mathbf{R})}{\partial \mathbf{R}}. \quad (107b)$$

From equation (107b), it follows that $\boldsymbol{\phi}$ is a trace-free third-rank tensor since it is the gradient of a scalar function w^* with respect to a trace-free argument \mathbf{R} . Upon substitution in the last part of equation (106) and integration by parts of the first term, it is found that for all divergence-free stress variation $\delta\boldsymbol{\sigma}$

$$\delta W^* = \int_{\Omega} [\mathbf{e} : \delta\boldsymbol{\sigma} + \boldsymbol{\phi} \cdot (\nabla\delta\boldsymbol{\sigma})] dV = \int_{\Omega} (\mathbf{e} - \nabla \cdot \boldsymbol{\phi}) : \delta\boldsymbol{\sigma} dV + \int_{\partial\Omega} \delta\boldsymbol{\sigma} : \boldsymbol{\phi} \cdot \mathbf{n} dS. \quad (108)$$

Stationarity of W^* with respect to the variation of stress requires that $\delta W^* = 0$ for all divergence-free stress variation $\delta\sigma$. Assuming first that $\delta\sigma = \mathbf{0}$ on $\partial\Omega$, and applying Theorem 1 in [Moreau \(1979\)](#), we find that

$$\mathbf{e} - \nabla \cdot \boldsymbol{\phi} = \nabla^s \mathbf{u}, \quad (109)$$

for some vector field \mathbf{u} . Plugging equation (109) in equation (108) and integrating by parts on the first term, we obtain

$$\delta W^* = \int_{\partial\Omega} \delta\sigma : \left(\mathbf{u} \overset{s}{\otimes} \mathbf{n} + \boldsymbol{\phi} \cdot \mathbf{n} \right) dS, \quad (110)$$

where \mathbf{n} denotes the outer normal to the boundary of Ω and we denoted $\mathbf{u} \overset{s}{\otimes} \mathbf{n} = \frac{1}{2}(\mathbf{u} \otimes \mathbf{n} + \mathbf{n} \otimes \mathbf{u})$. Therefore, $\mathbf{u} \overset{s}{\otimes} \mathbf{n} + \boldsymbol{\phi} \cdot \mathbf{n} = \mathbf{0}$ on $\partial\Omega$.

Gathering the above results, the elastic equilibrium of a clamped stress-gradient body Ω is defined by the following field equations in Ω

- Equilibrium

$$\nabla \cdot \boldsymbol{\sigma} + \mathbf{b} = \mathbf{0}, \quad \mathbf{R} = \mathbf{K} \therefore (\nabla\boldsymbol{\sigma}). \quad (111a)$$

- Generalized constitutive laws

$$\mathbf{e} = \frac{\partial w^*(\boldsymbol{\sigma}, \mathbf{R})}{\partial \boldsymbol{\sigma}}, \quad \boldsymbol{\phi} = \frac{\partial w^*(\boldsymbol{\sigma}, \mathbf{R})}{\partial \mathbf{R}}. \quad (111b)$$

- Compatibility condition

$$\mathbf{e} = \nabla^s \mathbf{u} + \nabla \cdot \boldsymbol{\phi}. \quad (111c)$$

and the boundary conditions on $\partial\Omega$

$$\mathbf{u} \overset{s}{\otimes} \mathbf{n} + \boldsymbol{\phi} \cdot \mathbf{n} = \mathbf{0}, \quad \text{on } \partial\Omega. \quad (112)$$

6.2.3 Extension to stress-free and mixed boundary conditions

The boundary value problem defined by equations (111) and (112) corresponds to the equilibrium of a fully clamped stress-gradient body, since its solution minimizes the complementary strain energy. Stress-free boundary conditions were also explored by [Forest and Sab \(2012\)](#) (see also [Sab et al. \(2016\)](#)). Quite remarkably, for the problem to be well-posed, the *full* stress tensor $\boldsymbol{\sigma}$ must then be prescribed at the boundary $\partial\Omega$. This is at odds with classical Cauchy materials, for which only the traction $\boldsymbol{\sigma} \cdot \mathbf{n}$ is prescribed (\mathbf{n} : outer normal to the boundary $\partial\Omega$). In other words, the equilibrium of a stress-gradient body Ω with stress-free boundary conditions is defined by equations (111), together with the following boundary condition on $\partial\Omega$

$$\boldsymbol{\sigma} = \mathbf{0}. \quad (113)$$

To conclude this section, it should be noted that mixed boundary conditions have also been proposed by [Sab et al. \(2016\)](#). Such conditions allow to prescribe only the traction $\boldsymbol{\sigma} \cdot \mathbf{n}$ (rather than the full stress tensor) at the boundary. In addition, $\boldsymbol{\phi} \cdot \mathbf{n}$ must then also be prescribed.

6.3 Contribution of the trace of the stress gradient

In this section we will show that taking into consideration \mathbf{Q} into the complementary strain energy functional results in a prestress. We consider the following general complementary density energy function

$$w^* = \frac{1}{2} \boldsymbol{\sigma} : \mathbf{S} : \boldsymbol{\sigma} + \frac{1}{2} (\nabla \boldsymbol{\sigma}) \cdot \mathbf{M}_{\nabla \nabla} \cdot (\nabla \boldsymbol{\sigma}), \quad (114)$$

where the fourth-rank tensor \mathbf{S} is the classical compliance tensor and the sixth-rank tensor $\mathbf{M}_{\nabla \nabla}$ is the generalized compliance. The complementary energy density function defined by equation (114) accounts for the full stress-gradient rather than its trace-free part (see equation (105)). Owing to the symmetry of the stress $\boldsymbol{\sigma}$, it can readily be shown that $\mathbf{M}_{\nabla \nabla}$ obeys the following symmetry $M_{\nabla \nabla, i j k p q r} = M_{\nabla \nabla, p q r i j k} = M_{\nabla \nabla, j i k p q r} = M_{\nabla \nabla, i j k q p r}$. Expanding the identity $\mathbf{M}_{\nabla \nabla} = (\mathbf{J} + \mathbf{K}) \cdot \mathbf{M}_{\nabla \nabla} \cdot (\mathbf{J} + \mathbf{K})$, the following expression of the complementary energy density is found

$$w^* = \frac{1}{2} \boldsymbol{\sigma} : \mathbf{S} : \boldsymbol{\sigma} + \frac{1}{2} \mathbf{R} \cdot \mathbf{M} \cdot \mathbf{R} + \mathbf{R} \cdot \mathbf{M}' \cdot \mathbf{Q} + \frac{1}{2} \mathbf{Q} \cdot \mathbf{M}'' \cdot \mathbf{Q}, \quad (115)$$

where we denoted

$$\mathbf{M} = \mathbf{K} \cdot \mathbf{M}_{\nabla \nabla} \cdot \mathbf{K}, \quad \mathbf{M}' = \mathbf{K} \cdot \mathbf{M}_{\nabla \nabla} \cdot \mathbf{J}, \quad \mathbf{M}'' = \mathbf{J} \cdot \mathbf{M}_{\nabla \nabla} \cdot \mathbf{J} \quad (116)$$

The constitutive laws (111) now become

$$\mathbf{e} = \mathbf{S} : \boldsymbol{\sigma}, \quad (117a)$$

$$\boldsymbol{\phi} = \mathbf{M} \cdot \mathbf{R} + \mathbf{M}' \cdot \mathbf{Q} = \mathbf{M} \cdot \mathbf{R} - \frac{2}{d+1} (\mathbf{M}' \cdot \mathbf{I}) \cdot \mathbf{b}, \quad (117b)$$

where we used the equality (95), $\mathbf{J} \cdot (\nabla \boldsymbol{\sigma}) = -\frac{2}{d+1} \mathbf{I} \cdot \mathbf{b}$. The second term in the right side of equation (117b) is imposed and effectively plays the role of a generalized prestress.

We now turn to formulate the energy principle for stress gradient materials.

6.4 Energy principles

In this section, we derive the principles of minimum complementary and potential energy for stress-gradient materials. We first define the set of statically admissible stress field $\mathbb{S}\mathbb{A}$ and kinematically admissible displacement and micro-displacement field $\mathbb{K}\mathbb{A}$. The boundary domain $\partial\Omega$ is decomposed into two mutually disjoint subsets $\partial\Omega_{\sigma}$ and $\partial\Omega_{u\phi}$ such that

$$\partial\Omega = \partial\Omega_{\sigma} \cup \partial\Omega_{u\phi}, \quad \partial\Omega_{\sigma} \cap \partial\Omega_{u\phi} = \emptyset, \quad (118)$$

the stress field $\bar{\boldsymbol{\sigma}}$ (not necessary uniform) is prescribed on the boundary part $\partial\Omega_{\sigma}$ while $\bar{\mathbf{u}} \otimes \mathbf{n} + \bar{\boldsymbol{\phi}} \cdot \mathbf{n}$ (not necessary uniform either) is specified on $\partial\Omega_{u\phi}$. In the remainder of this thesis, overlined quantities are prescribed.

The set of statically admissible stress fields is defined as follows

$$\mathbb{S}\mathbb{A}(\bar{\boldsymbol{\sigma}}) = \{\boldsymbol{\sigma}, \boldsymbol{\sigma} \text{ continuous, } \nabla \cdot \boldsymbol{\sigma} + \mathbf{b} = \mathbf{0} \text{ on } \Omega, \boldsymbol{\sigma} = \bar{\boldsymbol{\sigma}} \text{ on } \partial\Omega_{\sigma}\}, \quad (119)$$

where it is emphasized that the *full* stress $\boldsymbol{\sigma}$ (rather than the traction $\boldsymbol{\sigma} \cdot \mathbf{n}$) is continuous everywhere (this is in line with boundary condition (113), see also Sab et al. (2016)).

The set of kinematically admissible displacement \mathbf{u} and micro-displacement $\boldsymbol{\phi}$ fields is then defined as

$$\mathbb{KA}(\bar{\mathbf{u}}, \bar{\boldsymbol{\phi}}) = \{(\mathbf{u}, \boldsymbol{\phi}), \mathbf{u} \otimes \mathbf{n}_\Sigma + \boldsymbol{\phi} \cdot \mathbf{n}_\Sigma \text{ continuous,} \\ \mathbf{u} \otimes \mathbf{n} + \boldsymbol{\phi} \cdot \mathbf{n} = \bar{\mathbf{u}} \otimes \mathbf{n} + \bar{\boldsymbol{\phi}} \cdot \mathbf{n} \text{ on } \partial\Omega_{u\phi}\}, \quad (120)$$

where \mathbf{n}_Σ denotes the normal to any discontinuity surface Σ . Again, the continuity requirements on \mathbf{u} and $\boldsymbol{\phi}$ are in line with boundary condition (112), see also Sab et al. (2016).

6.4.1 Minimum complementary energy principle

It is recalled that the complementary strain energy W^* of the body Ω is given by (see equation (105))

$$W^*(\boldsymbol{\sigma}) = \int_{\Omega} w^*(\boldsymbol{\sigma}, \mathbf{K} \cdot (\nabla \boldsymbol{\sigma})) \, dV. \quad (121)$$

Following the same argument as in classical elasticity, it can be shown that the solution to the boundary value problem defined by equation (111) and the boundary conditions defined above minimizes the total complementary energy

$$\Pi^*(\boldsymbol{\sigma}) = W^*(\boldsymbol{\sigma}) - \int_{\partial\Omega} \bar{\boldsymbol{\sigma}} : (\mathbf{u} \otimes \mathbf{n} + \boldsymbol{\phi} \cdot \mathbf{n}) \, dS, \quad (122)$$

under the constraint that $\boldsymbol{\sigma} \in \mathbb{SA}(\bar{\boldsymbol{\sigma}})$, where we recall that $\mathbb{SA}(\bar{\boldsymbol{\sigma}})$ is the set of statically admissible stress fields defined by (119).

6.4.2 Minimum potential energy principle

The volume density of strain energy w is classically defined as the following supremum

$$w(\boldsymbol{\varepsilon}, \boldsymbol{\phi}) = \sup_{\boldsymbol{\sigma}, \mathbf{R}} \{\boldsymbol{\sigma} : \boldsymbol{\varepsilon} + \mathbf{R} \cdot \boldsymbol{\phi} - w^*(\boldsymbol{\sigma}, \mathbf{R})\}, \quad (123)$$

where $\boldsymbol{\varepsilon} \in {}^2\mathcal{T}$ and $\boldsymbol{\phi}, \mathbf{R} \in {}^3\mathcal{D}$. The strain energy W of the body Ω then reads

$$W(\mathbf{u}, \boldsymbol{\phi}) = \int_{\Omega} w(\nabla^s \mathbf{u} + \nabla \cdot \boldsymbol{\phi}, \boldsymbol{\phi}) \, dV, \quad (124)$$

and it can then be shown that solving problem (111) of the equilibrium of a clamped, stress-gradient body is equivalent to minimizing the following total potential energy

$$\Pi(\mathbf{u}, \boldsymbol{\phi}) = W(\mathbf{u}, \boldsymbol{\phi}) - \int_{\Omega} \mathbf{b} \cdot \mathbf{u} \, dV, \quad (125)$$

under the constraint that $(\mathbf{u}, \boldsymbol{\phi}) \in \mathbb{KA}(\bar{\mathbf{u}}, \bar{\boldsymbol{\phi}})$, where we recall that $\mathbb{KA}(\bar{\mathbf{u}}, \bar{\boldsymbol{\phi}})$ is the set of kinematically admissible displacement and micro-displacement field defined by (120).

6.5 Linear stress-gradient elasticity

The general formulation of stress-gradient model introduced in section 6.2 is rather complex in general. For further developments, we restrict to the case of linear stress-gradient elasticity assuming material isotropy. We first derive the general form of the generalized compliance tensor for isotropic stress-gradient materials. Drawing inspiration from the work of Aifantis (1992) and Gao and Park (2007), we further introduce a simplified form of the generalized compliance tensor with only one material internal length.

6.5.1 General form of isotropic compliance tensor

It is convenient to introduce the basis ($\mathbf{T}_1, \dots, \mathbf{T}_6$) of the space of sixth-rank isotropic tensors proposed by Monchiet and Bonnet (2010)

$$T_{1,ijkpqr} = \delta_{ij}\delta_{pq}\delta_{kr}, \quad T_{3,ijkpqr} = I_{ijkr}\delta_{pq}, \quad T_{5,ijkpqr} = \frac{1}{2}(I_{ijpr}\delta_{kq} + I_{ijqr}\delta_{kp}), \quad (126a)$$

$$T_{2,ijkpqr} = I_{ijpq}\delta_{kr}, \quad T_{4,ijkpqr} = I_{pqkr}\delta_{ij}, \quad T_{6,ijkpqr} = \frac{1}{2}(I_{pqir}\delta_{jk} + I_{pqjr}\delta_{ik}), \quad (126b)$$

where $I_{ijkl} = \frac{1}{2}(\delta_{ik}\delta_{jl} + \delta_{il}\delta_{jk})$ denotes the components of the fourth-rank identity tensor ${}^4\mathbf{I}$ (see equation (86)). Multiplication of the \mathbf{T}_i for the \cdot product is also provided in Table 1 in Monchiet and Bonnet (2010). The generalized sixth order isotropic compliance tensor, \mathbf{M} , thus can be written as

$$\mathbf{M} = m_1\mathbf{T}_1 + m_2\mathbf{T}_2 + m_3(\mathbf{T}_3 + \mathbf{T}_4) + m_5\mathbf{T}_5 + m_6\mathbf{T}_6, \quad (127)$$

where the coefficients of \mathbf{T}_3 and \mathbf{T}_4 are equal since \mathbf{M} is symmetric. We recall that when applied to a trace-free third-rank tensor, $\mathbf{R} \in {}^3\mathcal{D}$, the resulting product $\mathbf{M} \cdot \mathbf{R}$ also delivers a trace-free third-rank tensor, $\mathbf{M} \cdot \mathbf{R} \in {}^3\mathcal{D}$. As a consequence, the following relation must hold (see equation (116))

$$\mathbf{M} = \mathbf{K} \cdot \mathbf{M} \cdot \mathbf{K}. \quad (128)$$

Furthermore, the sixth-rank projectors (\mathbf{K}, \mathbf{J}) can be expressed in the Monchiet and Bonnet (2010) basis as

$$\mathbf{J} = \frac{1}{2}\mathbf{T}_6 \quad \text{and} \quad \mathbf{K} = \mathbf{T}_2 - \frac{1}{2}\mathbf{T}_6. \quad (129)$$

Using the multiplication Table 1 in Monchiet and Bonnet (2010), equation (128) leads to

$$2m_1 + 4m_3 + m_5 = 0, \quad (130a)$$

$$2m_1 - 4m_2 - m_5 - 8m_6 = 0, \quad (130b)$$

In other words, the generalized compliance tensor of a linear, isotropic, centrosymmetric stress-gradient material is completely characterized by *three* material parameters, namely: m_1, m_2 and m_5 . For further simplification, it is convenient to introduce the tensors \mathbf{H} and \mathbf{H}' defined as follows

$$\mathbf{H} = \mathbf{T}_1 - \frac{\mathbf{T}_3 + \mathbf{T}_4}{2} + \frac{\mathbf{T}_6}{4} \quad \text{and} \quad \mathbf{H}' = \mathbf{T}_5 - \frac{\mathbf{T}_3 + \mathbf{T}_4}{4} - \frac{\mathbf{T}_6}{8}, \quad (131)$$

with

$$\mathbf{H} \cdot \mathbf{H} = \frac{5}{2}\mathbf{H}, \quad \mathbf{H}' \cdot \mathbf{H}' = \frac{1}{2}\mathbf{K} - \frac{1}{8}\mathbf{H} + \frac{1}{2}\mathbf{H}', \quad \mathbf{H} \cdot \mathbf{H}' = \mathbf{H}' \cdot \mathbf{H} = -\frac{1}{4}\mathbf{H}, \quad (132)$$

$$\mathbf{H} \cdot \mathbf{K} = \mathbf{K} \cdot \mathbf{H} = \mathbf{H}, \quad \mathbf{H}' \cdot \mathbf{K} = \mathbf{K} \cdot \mathbf{H}' = \mathbf{H}' \quad (133)$$

The generalized compliance tensor thus can be expressed in a compact form as follows

$$\mathbf{M} = m_2\mathbf{K} + m_1\mathbf{H} + m_5\mathbf{H}'. \quad (134)$$

6.5.2 Simplified stress-gradient model

On the basis of the discussion in section 5.2, it is highly desirable to formulate a stress-gradient model with one material internal length only (rather than three in the general, isotropic case). It facilitates the theoretical development and is more practical for experimental identification. A natural simplified model is the one symmetric to the simplified strain gradient model of Aifantis (1992); Gao and Park (2007). With the help of the \boxtimes tensor product defined in section 6.1.2, the generalized stiffness tensor in the simplified strain-gradient model of Aifantis (1992); Gao and Park (2007) can be written as

$$\mathbf{L} = \ell^2\mathbf{C} \boxtimes \mathbf{I}. \quad (135)$$

Similarly, keeping in mind that relation (128) must hold, we propose the following generalized compliance tensor for stress-gradient elasticity

$$\mathbf{M} = \ell^2\mathbf{K} \cdot (\mathbf{S} \boxtimes \mathbf{I}) \cdot \mathbf{K}. \quad (136)$$

In equation (136), ℓ is a stress-gradient material length. Employing the definition and algebra of the tensor product \boxtimes in section 6.1.2, the generalized compliance tensor (136) can be further simplified to the form

$$\mathbf{M} = \frac{\ell^2}{2\mu} \left(\mathbf{K} - \frac{\nu}{1+\nu}\mathbf{H} \right), \quad (137)$$

(see equation (131) for the definition of tensor \mathbf{H}) where μ, ν are respectively the classical shear modulus and the Poisson coefficient of the stress-gradient material under consideration. The generalized stiffness \mathbf{L} is obtained by inversion in the space of trace-free, third-rank tensors ${}^3\mathcal{D}$. Based on the equality in equation (133), we find

$$\mathbf{L} = \frac{2\mu}{\ell^2} \left(\mathbf{K} + \frac{2\nu}{2-3\nu}\mathbf{H} \right). \quad (138)$$

It should be noted that classical Cauchy elasticity is retrieved for $\ell \rightarrow 0$. Conversely, for the complementary energy density w^* to remain finite (see equation (105)), the trace-free part \mathbf{R} of the stress-gradient must vanish when $\ell \rightarrow +\infty$. Furthermore, in the absence of body-forces, $\nabla \cdot \boldsymbol{\sigma} = \mathbf{0}$, and we find that the full stress-gradient vanishes. In other words, the stress field tends to be phase-wise constant when the internal material length becomes large.

In the next section, the simplified stress-gradient model will be adopted to demonstrate the existence of boundary layers near the interface of a stress-gradient material.

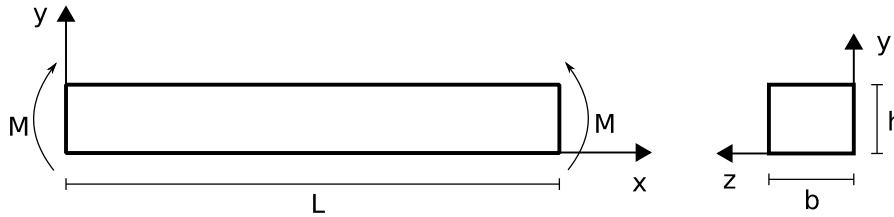


Figure 6.1. Rectangular cross section beam subjected to end moments

6.6 Saint-Venant problem: existence of boundary layers

6.6.1 Saint-Venant pure bending problem

In this section, we show that the simplified stress-gradient model, formulated in section 6.5.2, may give rise to boundary layers near material interfaces. The width of these layers depends on the material internal length, which indicates a size dependent behavior. This phenomenon is explored by means of an instructive example, namely the pure bending of a beam with rectangular cross section. For Cosserat media, an abstract solution to this problem can be found in [Ieşan \(1971\)](#). An approximate polynomial solution was also recently proposed by [Lakes and Drugan \(2015\)](#) (see also [Polizzotto \(2016\)](#) for an approximate solution for stress-gradient materials).

Cartesian coordinates are defined in what follows according to figure 6.1. The length of the beam is denoted by L , the beam width is denoted by b and the height of the cross section is denoted by h . The beam under consideration is subjected to a moment M at both ends (z -axis is the rotation axis). Following Saint-Venant approach, we postulate the stress field

$$\boldsymbol{\sigma} = \sigma(y, z) \mathbf{e}_x \otimes \mathbf{e}_x. \quad (139)$$

In terms of the boundary conditions, the lateral surface is free which requires *all components* of the stress tensor to vanish

$$\sigma(0, z) = 0, \quad \sigma(h, z) = 0, \quad \sigma(y, 0) = 0, \quad \sigma(y, b) = 0, \quad (140)$$

and at both ends of the beam, we impose

$$\int_S \sigma(y, z) dS = 0, \quad - \int_S y \sigma(y, z) dS = M, \quad \int_S z \sigma(y, z) dS = 0, \quad (141)$$

where S denotes the cross-section, $S = [0, h] \times [0, b]$. The resulting equilibrium problem will be solved as follows.

- Compute the trace-free part of stress gradient from the postulated stress field: $\mathbf{R} = \mathbf{K} \cdot (\nabla \boldsymbol{\sigma})$.
- Compute the micro-deformation from constitutive equation: $\boldsymbol{\phi} = \mathbf{M} \cdot \mathbf{R}$.
- Evaluate the total deformation $\mathbf{e} = \mathbf{S} : \boldsymbol{\sigma}$.
- Find the Cauchy deformation from $\boldsymbol{\varepsilon} = \mathbf{e} - \nabla \cdot \boldsymbol{\phi}$.

- Integrate the compatibility conditions for ε .
- Use the boundary conditions to evaluate the integration constants.

Integrating the compatibility conditions of Cauchy strain ε , we obtain the following equation

$$\ell^2 \Delta \sigma - \sigma = C_1 y + C_2 z + C_3, \quad (142)$$

which is to be solved on the rectangular domain S , subjected to boundary conditions defined by equations (140), (141). C_1, C_2, C_3 are integration constants to be determined from boundary conditions. Equation (142) suggests to expand σ as a series of the eigenmodes of the Laplacian (Dirichlet boundary conditions)

$$\sigma = \sum_{m,n=1}^{\infty} \sigma_{mn} \sin\left(\frac{\pi n}{h} y\right) \sin\left(\frac{\pi m}{b} z\right). \quad (143)$$

Plugging equation (143) into equation (142), we find

$$C_1 y + C_2 z + C_3 = - \sum_{m,n=1}^{\infty} f_{mn} \sin\left(\frac{\pi n}{h} y\right) \sin\left(\frac{\pi m}{b} z\right), \quad (144)$$

where the coefficients f_{mn} in the Fourier series are given by

$$f_{mn} = \frac{4}{bh} \int_0^b \int_0^h (-C_1 u - C_2 v - C_3) \sin\left(\frac{\pi n}{h} u\right) \sin\left(\frac{\pi m}{b} v\right) du dv. \quad (145)$$

Further simplification of equation (142) yields

$$- \sum_{m,n=1}^{\infty} \left[\left(\frac{\pi n}{h}\right)^2 + \left(\frac{\pi m}{b}\right)^2 + \frac{1}{\ell^2} \right] \sigma_{mn} \sin\left(\frac{\pi n}{h} y\right) \sin\left(\frac{\pi m}{b} z\right) = - \sum_{m,n=1}^{\infty} \frac{f_{mn}}{\ell^2} \sin\left(\frac{\pi n}{h} y\right) \sin\left(\frac{\pi m}{b} z\right). \quad (146)$$

By equating the coefficients of the above series, we deduce

$$\sigma_{mn} = \frac{f_{mn}}{\ell^2 \left[\left(\frac{\pi n}{h}\right)^2 + \left(\frac{\pi m}{b}\right)^2 + 1 \right]}. \quad (147)$$

Gathering the above results, we finally obtain the axial stress

$$\begin{aligned} \sigma(y, z) &= \frac{4}{bh} \int_0^b \int_0^h \sum_{m,n=1}^{\infty} (-C_1 u - C_2 v - C_3) \frac{\sin\left(\frac{\pi n}{h} y\right) \sin\left(\frac{\pi m}{b} z\right) \sin\left(\frac{\pi n}{h} u\right) \sin\left(\frac{\pi m}{b} v\right)}{\ell^2 \left[\left(\frac{\pi n}{h}\right)^2 + \left(\frac{\pi m}{b}\right)^2 + 1 \right]} du dv \\ &= -\frac{4b^2 h^2}{\pi^2} [C_1 A_{mn}(y, z) + C_2 B_{mn}(y, z) + C_3 C_{mn}(y, z)], \end{aligned} \quad (148)$$

where

$$A_{mn}(y, z) = \sum_{m,n=1}^{\infty} \frac{(-1)^n [(-1)^m - 1]}{b^2 h \ell^2 m n \left[\left(\frac{\pi n}{h}\right)^2 + \left(\frac{\pi m}{b}\right)^2 + \frac{1}{\ell^2} \right]} \sin\left(\frac{\pi n}{h} y\right) \sin\left(\frac{\pi m}{b} z\right), \quad (149a)$$

$$B_{mn}(y, z) = \sum_{m,n=1}^{\infty} \frac{(-1)^n [(-1)^m - 1]}{b h^2 \ell^2 m n \left[\left(\frac{\pi n}{h}\right)^2 + \left(\frac{\pi m}{b}\right)^2 + \frac{1}{\ell^2} \right]} \sin\left(\frac{\pi n}{h} y\right) \sin\left(\frac{\pi m}{b} z\right), \quad (149b)$$

$$C_{mn}(y, z) = \sum_{m,n=1}^{\infty} \frac{[(-1)^n - 1][(-1)^m - 1]}{b^2 h^2 \ell^2 m n \left[\left(\frac{\pi n}{h}\right)^2 + \left(\frac{\pi m}{b}\right)^2 + \frac{1}{\ell^2} \right]} \sin\left(\frac{\pi n}{h} y\right) \sin\left(\frac{\pi m}{b} z\right). \quad (149c)$$

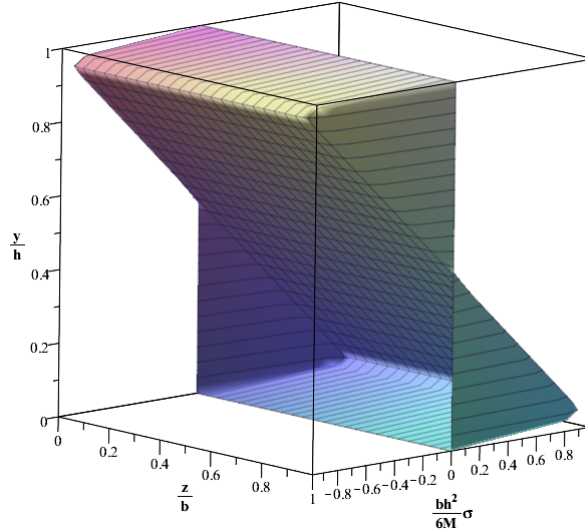


Figure 6.2. Normalized stress field $\frac{bh^2}{6M}\sigma(y, z)$ for $\ell/h = 0.01$. It is clearly seen that the stress on lateral surface is vanished.

The three integration constants C_1, C_2, C_3 are determined from the boundary conditions (141). Their expression is not reported here. It should be noted that care must be taken for the numerical evaluation of the infinite series involved in the stress solution as it is not uniformly convergent (Cole and Yen, 2001). It can be shown that the series in equations (149) can be evaluated analytically for one dimension (along m or n). The remaining infinite series (along n or m) is then summed numerically from its smallest value to its largest value in order to limit round-off errors.

6.6.2 Discussion

Figure 6.2 shows the normalized stress $\frac{bh^2}{6M}\sigma(y, z)$ over the normalized direction y/h and z/b . A two dimensional section at $z/b = 1/2$ is plotted in figure 6.3. Away from the lateral (free) surface of the beam, the stress is closely approximated by the classical elasticity solution for small values of the material internal length. It is further observed that in the vicinity of the lateral surface, the stress vanishes abruptly in a boundary layer (while it remains non-zero in classical elasticity). The size of this boundary layer is proportional to the internal length, ℓ , and inversely proportional to the beam width h . When ℓ/h is small, the normalized stress is almost identical to the classical elasticity values, except at the free surface where stress-gradient solution is enforced to be zero.

For a solid beam undergoing pure bending, the bending stiffness D is defined as the ratio of the applied bending moment M to the curvature κ

$$M = D\kappa, \quad (150)$$

Figure 6.4 plots the normalized bending stiffness, D^{SG}/D^C at fixed material internal length for various values of the ratio h/ℓ (D^C : classical elasticity; D^{SG} : stress-gradient elasticity). It is observed that the normalized bending stiffness decreases for decreasing values of h/ℓ . In other words, stress gradient materials exhibit softening size-effects.

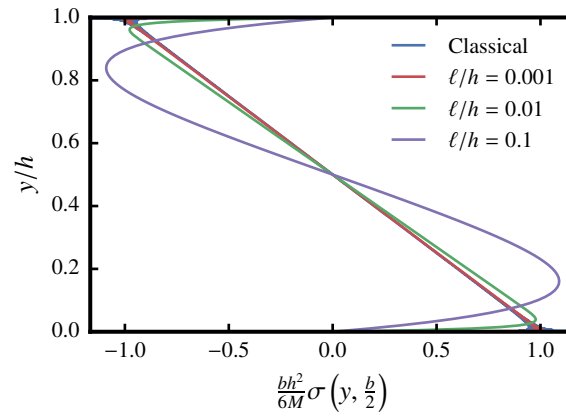


Figure 6.3. Normalized stress field $\frac{bh^2}{6M}\sigma\left(y, \frac{b}{2}\right)$ as a function of $\frac{y}{h}$ for various internal length values: $\ell/h = 0.001$ (red line), $\ell/h = 0.01$ (green line); $\ell/h = 0.1$ (magenta line). The classical elasticity value is plotted by blue line.

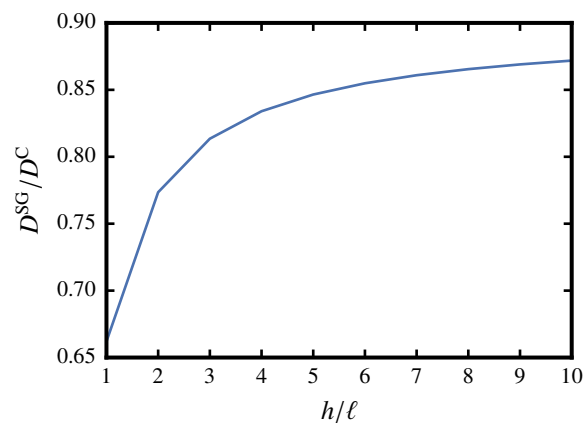


Figure 6.4. The ratio between the bending stiffness estimated by stress-gradient model D^{SG} and classical elasticity D^C as a function of h/ℓ .

This result is contrary to what is generally observed experimentally. For example, Lam et al. (2003) reported that the normalized bending stiffness of a cantilever beam increases for decreasing values of h/ℓ . They then successfully applied the strain gradient model to account for this stiffening size-effect, which would not be possible with a stress gradient model.

Conversely, atomistic simulations suggest that some materials (for example, nano silicon beam, Sun et al. (2007)) might exhibit the opposite, softening size-effect. Strain-gradient models would not be able to account for such effects, while stress-gradient models would be better suited.

In this chapter, we presented an energetically consistent derivation of the stress-gradient model by minimizing the complementary strain energy. In the course of the derivation, it was shown that the trace of stress-gradient plays the role of a generalized prestress. Interestingly, the stress-free boundary conditions of a stress-gradient body requires that the *full* stress tensor $\boldsymbol{\sigma}$ rather than the traction vector $\boldsymbol{\sigma} \cdot \mathbf{n}$ be specified at the boundary. We then formulated generalized energy principles for stress-gradient bodies.

For linear, isotropic, centrosymmetric stress-gradient materials, the stress-gradient model contains *three* material internal length. In line with previous work in strain-gradient model (Aifantis, 1992; Gao and Park, 2007), a stress-gradient model with only one material internal length was proposed (the so-called *simplified stress-gradient model*).

This model revealed the existence of boundary layers near the free surface of a rectangular beam undergoing pure bending. Furthermore, it was shown that the normalized bending stiffness decreases when the beam thickness decreases (the material internal length being fixed). In other words, the stress-gradient model predicts a softening size-effect. While most nano-materials exhibit stiffening size-effects, atomistic simulations suggest that some materials might indeed exhibit a softening size-effect. For these materials, the model presented in this chapter might be relevant.

In the next chapter, we investigate the homogenization of stress-gradient materials, under the assumptions that the material internal length is comparable or much smaller than the size of the heterogeneities. In particular, it will again be shown that stress-gradient materials exhibit a softening size-effect.

Chapter 7

Homogenization of stress-gradient materials

In this chapter, we set up a framework for the homogenization of stress-gradient composites. The simplified stress-gradient model developed in section 6.5.2 is adopted throughout this chapter. We first derive boundary conditions that are suitable to the computation of the apparent compliance of linearly elastic materials in section 7.1. The solution to Eshelby's spherical inhomogeneity problem is then derived in section 7.2. Based on this solution, Mori-Tanaka estimates of the effective properties are finally produced in section 7.3.

7.1 General framework

7.1.1 Effective compliance of a representative volume element

We consider a heterogeneous stress-gradient body \mathcal{B} occupying the domain $\Omega \subset \mathbb{R}^d$, ($d = 2, 3$). Similar to classical elasticity, three length scales are first introduced. The typical size d of the heterogeneities, the size L_{RVE} of the representative volume element (the existence of which is postulated) and the typical size L_{macro} of the structure and the length scale of its loading. Moreover, for a stress-gradient material, the material internal length, ℓ , is also involved.

We assume that the heterogeneous material that the body \mathcal{B} is made of is *homogenizable* and seek its effective properties. This requires the scale separation condition

$$d \ll L_{\text{RVE}} \ll L_{\text{macro}}. \quad (151)$$

As previously discussed in section 5.3, Forest et al. (2001) showed that a Cosserat heterogeneous medium is homogenized as a macroscopic homogeneous Cauchy medium if the material internal length is comparable or much smaller than the size of heterogeneities. The same argument would apply here, leading to the same conclusion. In other words, assuming that

$$\ell \sim d \quad \text{or} \quad \ell \ll d, \quad (152)$$

the heterogeneous body \mathcal{B} behaves macroscopically as a Cauchy material. The macroscopic behavior is characterized by the effective compliance \mathbf{S}_{eff} , which relates the macroscopic strain $\langle \mathbf{e} \rangle$ to the macroscopic stress $\langle \boldsymbol{\sigma} \rangle$ through the standard constitutive equation

$$\langle \mathbf{e} \rangle = \mathbf{S}^{\text{eff}} : \langle \boldsymbol{\sigma} \rangle, \quad (153)$$

where the macroscopic variables are the average stress $\langle \boldsymbol{\sigma} \rangle$ and the average *total* strain $\langle \mathbf{e} \rangle$ (defined by equation (111c))

$$\langle \boldsymbol{\sigma} \rangle = \frac{1}{V} \int_{\Omega} \boldsymbol{\sigma} \, dV, \quad (154)$$

$$\begin{aligned} \langle \mathbf{e} \rangle &= \frac{1}{V} \int_{\Omega} \mathbf{e} \, dV = \frac{1}{V} \int_{\Omega} (\nabla^s \mathbf{u} + \nabla \cdot \boldsymbol{\phi}) \, dV \\ &= \frac{1}{V} \int_{\Omega} \nabla^s \mathbf{u} \, dV + \frac{1}{V} \int_{\partial\Omega} \boldsymbol{\phi} \cdot \mathbf{n} \, dS, \end{aligned} \quad (155)$$

(V : volume of the RVE Ω). It should be noted that in a random setting (assuming that $\boldsymbol{\phi}$ is a statistically homogeneous and ergodic random process), the last term in equation (155) vanishes for Ω sufficiently large. In other words, the macroscopic strain is the average of the symmetrized gradient of the microscopic displacement.

Following the terminology introduced by Huet (1990) (see also (Ostoja-Starzewski, 2006)), the effective compliance is defined in the present work as the limit for large statistical volume elements (SVE) of the *apparent* compliance. We therefore provide in section 7.1.2 four definitions of this quantity, all of which are expected to converge to the same value as the size of the SVE grows to infinity under the assumption of statistical homogeneity and ergodicity (see Sab (1992) in classical elasticity).

7.1.2 Apparent compliance of a statistical volume element

We consider a SVE Ω of finite size L . Its apparent compliance is retrieved from the solution to an auxiliary problem defined by the following field equations in Ω

$$\nabla \cdot \boldsymbol{\sigma} = \mathbf{0}, \quad (156a)$$

$$\mathbf{R} = \mathbf{K} \cdot (\nabla \boldsymbol{\sigma}), \quad (156b)$$

$$\mathbf{e} = \mathbf{S} : \boldsymbol{\sigma}, \quad (156c)$$

$$\boldsymbol{\phi} = \mathbf{M} \cdot \mathbf{R}, \quad (156d)$$

$$\mathbf{e} = \nabla^s \mathbf{u} + \nabla \cdot \boldsymbol{\phi}. \quad (156e)$$

This problem has to be complemented with appropriate boundary conditions (to be specified below) in order to ensure well-posedness. In the above equations, the local compliance tensors \mathbf{S} and \mathbf{M} depend on the observation point \mathbf{x} due to material inhomogeneity. Note that, since $\boldsymbol{\sigma}$ is divergence-free (see equation (156a)), its gradient is trace-free. In other words, equation (156b) should really read $\mathbf{R} = \nabla \boldsymbol{\sigma}$. Therefore, in the remainder of chapter 7, \mathbf{R} will generally be substituted with its expression as the gradient of $\boldsymbol{\sigma}$.

At the interface between two phases, it is required that both higher-order displacement and local stress be continuous

$$[[\mathbf{u} \otimes \mathbf{n} + \boldsymbol{\phi} \cdot \mathbf{n}]] = \mathbf{0}, \quad (157a)$$

$$[[\boldsymbol{\sigma}]] = \mathbf{0}, \quad (157b)$$

where \mathbf{n} denotes the normal to the interface, while $[[\mathbf{T}]]$ denotes the jump of \mathbf{T} across the interface. Similarly to the boundary condition (113), where the full stress $\boldsymbol{\sigma}$ (rather than the traction $\boldsymbol{\sigma} \cdot \mathbf{n}$) is imposed, it is emphasized that the full stress (rather than the traction) must be continuous.

We now turn to the boundary conditions which must complement equations (156) and (157). Suitable boundary conditions are selected in section 7.1.3 so as to ensure that Hill–Mandel lemma holds. The classical kinematic uniform (see section 7.1.3.1), static uniform (see section 7.1.3.2) and periodic (see section 7.1.3.3) boundary conditions (Kanit et al., 2003) are first extended to stress-gradient materials. Mixed boundary conditions are also proposed (see section 7.1.3.4). These boundary conditions are then discussed in section 7.1.4.

7.1.3 Hill–Mandel lemma for stress-gradient materials

We consider a divergence-free stress tensor σ_1 , a displacement vector \mathbf{u}_2 and a microdisplacement tensor ϕ_2 (third-rank, trace-free tensor). Introducing the total strain \mathbf{e}_2

$$\mathbf{e}_2 = \nabla^s \mathbf{u}_2 + \nabla \cdot \phi_2, \quad (158)$$

we explore the conditions on σ_1 and \mathbf{e}_2 under which the micro- and macroscopic internal works coincide (Hill–Mandel lemma), that is

$$\langle \sigma_1 : \mathbf{e}_2 + (\nabla \sigma_1) \cdot \phi_2 \rangle = \langle \sigma_1 \rangle : \langle \mathbf{e}_2 \rangle, \quad (159)$$

where the term $\langle \nabla \sigma_1 \rangle \cdot \langle \phi_2 \rangle$ has been discarded, because the homogenized stress-gradient material is expected to behave as a Cauchy material. Substituting equation (158) into the left-hand side of equation (159) and integrating by parts, we find

$$\begin{aligned} \langle \sigma_1 : \mathbf{e}_2 + (\nabla \sigma_1) \cdot \phi_2 \rangle &= \frac{1}{V} \int_{\Omega} [\sigma_1 : (\nabla^s \mathbf{u}_2 + \nabla \cdot \phi_2) + (\nabla \sigma_1) \cdot \phi_2] dV, \\ &= \frac{1}{V} \int_{\Omega} [\nabla \cdot (\mathbf{u}_2 \cdot \sigma_1) - \mathbf{u}_2 \cdot (\nabla \cdot \sigma_1) + \nabla \cdot (\sigma_1 : \phi_2)] dV, \\ &= \frac{1}{V} \int_{\Omega} [\nabla \cdot (\mathbf{u}_2 \cdot \sigma_1) + \nabla \cdot (\sigma_1 : \phi_2)] dV, \end{aligned} \quad (160)$$

where the fact that $\nabla \cdot \sigma_1 = \mathbf{0}$ has been used. From the divergence formula, it is finally found that

$$\langle \sigma_1 : \mathbf{e}_2 + (\nabla \sigma_1) \cdot \phi_2 \rangle = \frac{1}{V} \int_{\partial\Omega} \sigma_1 : (\mathbf{u}_2 \otimes^s \mathbf{n} + \phi_2 \cdot \mathbf{n}) dS, \quad (161)$$

where \mathbf{n} denotes the outer normal to the boundary $\partial\Omega$ of the SVE Ω . It is emphasized that no assumptions on the values of σ_1 , \mathbf{u}_2 and ϕ_2 at the boundary were made to derive the above identity. As a result, if the following condition also holds

$$\int_{\partial\Omega} \phi_2 \cdot \mathbf{n} dS = \mathbf{0}, \quad (162)$$

then

$$\langle \mathbf{e}_2 \rangle = \langle \nabla^s \mathbf{u}_2 \rangle. \quad (163)$$

Indeed, applying first equation (161) to $\sigma_1 = \text{const.} = \langle \sigma_1 \rangle$, \mathbf{e}_2 and ϕ_2 and plugging equation (162), we find

$$\langle \mathbf{e}_2 \rangle = \frac{1}{V} \int_{\partial\Omega} \mathbf{u}_2 \otimes^s \mathbf{n} dS. \quad (164)$$

We then apply a second time equation (161) to $\sigma_1 = \text{const.} = \langle \sigma_1 \rangle$, \mathbf{e}_2 and $\mathbf{0}$ and find

$$\langle \nabla^s \mathbf{u}_2 \rangle = \frac{1}{V} \int_{\partial\Omega} \mathbf{u}_2 \otimes^s \mathbf{n} dS, \quad (165)$$

which completes the proof of equation (163).

At this stage, various assumptions that lead to Hill–Mandel lemma can be made on the values of σ_1 , \mathbf{u}_2 and ϕ_2 at the boundary.

7.1.3.1 Kinematic uniform boundary conditions (KUBC)

It is first assumed that $\mathbf{u}_2(\mathbf{x}) = \bar{\mathbf{e}}_2 \cdot \mathbf{x}$ and $\phi_2(\mathbf{x}) \cdot \mathbf{n}(\mathbf{x}) = \mathbf{0}$ for $\mathbf{x} \in \partial\Omega$ (where $\bar{\mathbf{e}}_2$ is a constant tensor). Applying equation (161) to σ_1 , \mathbf{u}_2 , ϕ_2 and σ_1 , $\bar{\mathbf{e}}_2 \cdot \mathbf{x}$, $\mathbf{0}$, successively, it is found that

$$\langle \sigma_1 : \mathbf{e}_2 + \mathbf{R}_1 \cdot \phi_2 \rangle = \langle \sigma_1 \rangle : \bar{\mathbf{e}}_2, \quad (166)$$

which further implies (taking $\sigma_1 = \text{const.} = \langle \sigma_1 \rangle$) that $\bar{\mathbf{e}}_2 = \langle \mathbf{e}_2 \rangle$, and Hill–Mandel lemma holds. The classical kinematic uniform boundary conditions can therefore be extended to stress-gradient materials as follows. The loading parameter is the macroscopic strain $\bar{\mathbf{e}}$; the displacement \mathbf{u} and the normal micro-displacement ϕ are prescribed at the boundary of the SVE Ω

$$\mathbf{u}(\mathbf{x}) = \bar{\mathbf{e}} \cdot \mathbf{x}, \quad (167a)$$

$$\phi(\mathbf{x}) \cdot \mathbf{n}(\mathbf{x}) = \mathbf{0}, \quad (167b)$$

for all $\mathbf{x} \in \partial\Omega$. The macroscopic stress is then computed *a posteriori* as the volume average $\langle \sigma \rangle$ of the local stress σ . It depends linearly on the macroscopic strain, and the apparent stiffness \mathbf{C}_{KUBC} is defined as the linear operator which maps $\langle \mathbf{e} \rangle = \bar{\mathbf{e}}$ to $\langle \sigma \rangle$

$$\langle \sigma \rangle = \mathbf{C}_{\text{KUBC}} : \bar{\mathbf{e}} \quad (\mathbf{S}_{\text{KUBC}} = \mathbf{C}_{\text{KUBC}}^{-1}). \quad (168)$$

7.1.3.2 Static uniform boundary conditions (SUBC)

It is then assumed that $\sigma_1(\mathbf{x}) = \bar{\sigma}_1$ for $\mathbf{x} \in \partial\Omega$ (where $\bar{\sigma}_1$ is a constant tensor). Applying equation (161) to σ_1 , \mathbf{u}_2 , ϕ_2 and $\bar{\sigma}_1$, \mathbf{u}_2 , ϕ_2 , successively, it is found that

$$\langle \sigma_1 : \mathbf{e}_2 + \mathbf{R}_1 \cdot \phi_2 \rangle = \bar{\sigma}_1 : \langle \mathbf{e}_2 \rangle, \quad (169)$$

which further implies (taking $\mathbf{u}_2(\mathbf{x}) = \bar{\mathbf{e}}_2 \cdot \mathbf{x}$, $\bar{\mathbf{e}}_2 = \text{const.}$ and $\phi_2 = \mathbf{0}$) that $\bar{\sigma}_1 = \langle \sigma_1 \rangle$, and Hill–Mandel lemma again holds. The classical static uniform boundary conditions can therefore be extended to stress-gradient materials as follows. The loading parameter is the macroscopic stress $\bar{\sigma}$ (volume average of the local stress); the *full* stress tensor σ is prescribed at the boundary of the SVE Ω

$$\sigma(\mathbf{x}) = \bar{\sigma}, \quad (170)$$

for all $\mathbf{x} \in \partial\Omega$. The macroscopic strain is then computed *a posteriori* as the volume average $\langle \mathbf{e} \rangle$ of the local strain \mathbf{e} . It depends linearly on the macroscopic stress, and the apparent compliance \mathbf{S}_{SUBC} is defined as the linear operator which maps $\langle \sigma \rangle = \bar{\sigma}$ to $\langle \mathbf{e} \rangle$

$$\langle \mathbf{e} \rangle = \mathbf{S}_{\text{SUBC}} : \bar{\sigma}. \quad (171)$$

7.1.3.3 Periodic boundary conditions (PBC)

In this section, the case where the SVE Ω is a rectangular prism is considered, $\Omega = (0, L_1) \times \dots \times (0, L_d)$. It is assumed that

$$\sigma_1 \text{ is } \Omega\text{-periodic,} \quad (172a)$$

$$\text{sym}(\mathbf{u}'_2 \otimes \mathbf{n}) + \boldsymbol{\phi}_2 \cdot \mathbf{n} \text{ is } \Omega\text{-skew-periodic,} \quad (172b)$$

where $\mathbf{u}'_2(\mathbf{x}) = \mathbf{u}_2(\mathbf{x}) - \bar{\mathbf{e}}_2 \cdot \mathbf{x}$ and $\bar{\mathbf{e}}_2$ is a constant tensor. Plugging first σ_1 , \mathbf{u}_2 , $\boldsymbol{\phi}_2$, then σ_1 , $\bar{\mathbf{e}}_2 \cdot \mathbf{x}$, $\mathbf{0}$ into equation (161), it is found that

$$\langle \sigma_1 : \mathbf{e}_2 + \mathbf{R}_1 \cdot \boldsymbol{\phi}_2 \rangle = \langle \sigma_1 \rangle : \bar{\mathbf{e}}_2, \quad (173)$$

which further implies (taking $\sigma_1 = \text{const.} = \langle \sigma_1 \rangle$) that $\bar{\mathbf{e}}_2 = \langle \mathbf{e}_2 \rangle$ and Hill–Mandel lemma holds. The classical periodic boundary conditions can therefore be extended to stress-gradient materials as follows. The loading parameter is the macroscopic strain $\bar{\mathbf{e}}$. The boundary conditions are such that

$$\sigma \text{ is } \Omega\text{-periodic,} \quad (174a)$$

$$\text{sym}(\mathbf{u}' \otimes \mathbf{n}) + \boldsymbol{\phi} \cdot \mathbf{n} \text{ is } \Omega\text{-skew-periodic,} \quad (174b)$$

where $\mathbf{u}'(\mathbf{x}) = \mathbf{u}(\mathbf{x}) - \bar{\mathbf{e}} \cdot \mathbf{x}$. The macroscopic stress is then computed *a posteriori* as the volume average $\langle \sigma \rangle$ of the local stress σ . It depends linearly on the macroscopic strain, and the apparent stiffness \mathbf{C}_{PBC} is defined as the linear operator which maps $\langle \mathbf{e} \rangle = \bar{\mathbf{e}}$ to $\langle \sigma \rangle$

$$\langle \sigma \rangle = \mathbf{C}_{\text{PBC}} : \bar{\mathbf{e}} \quad (\mathbf{S}_{\text{PBC}} = \mathbf{C}_{\text{PBC}}^{-1}). \quad (175)$$

7.1.3.4 Mixed boundary conditions (MBC)

It is finally assumed that $\sigma_1(\mathbf{x}) \cdot \mathbf{n}(\mathbf{x}) = \bar{\boldsymbol{\sigma}}_1 \cdot \mathbf{n}(\mathbf{x})$ and $\boldsymbol{\phi}_2(\mathbf{x}) \cdot \mathbf{n}(\mathbf{x}) = \mathbf{0}$ for $\mathbf{x} \in \partial\Omega$ (where $\bar{\boldsymbol{\sigma}}_1$ is a constant tensor). Applying again equation (161) to σ_1 , \mathbf{u}_2 , $\boldsymbol{\phi}_2$ and $\bar{\boldsymbol{\sigma}}_1$, \mathbf{u}_2 , $\mathbf{0}$, successively, it is found that

$$\langle \sigma_1 : \mathbf{e}_2 + \mathbf{R}_1 \cdot \boldsymbol{\phi}_2 \rangle = \bar{\boldsymbol{\sigma}}_1 : \langle \nabla^s \mathbf{u}_2 \rangle = \bar{\boldsymbol{\sigma}}_1 : \langle \mathbf{e}_2 \rangle, \quad (176)$$

where equation (220a) has been used (since equation (162) holds). The above identity further implies (taking $\mathbf{u}_2(\mathbf{x}) = \tilde{\mathbf{e}}_2 \cdot \mathbf{x}$, $\tilde{\mathbf{e}}_2 = \text{const.}$ and $\boldsymbol{\phi}_2 = \mathbf{0}$) that $\bar{\boldsymbol{\sigma}}_1 = \langle \sigma_1 \rangle$, and Hill–Mandel lemma again holds. The above analysis suggests the following mixed boundary conditions. The loading parameter is the macroscopic stress $\bar{\boldsymbol{\sigma}}$. The traction $\sigma \cdot \mathbf{n}$ and the normal microdisplacement $\boldsymbol{\phi} \cdot \mathbf{n}$ are prescribed at the boundary of the SVE Ω

$$\sigma(\mathbf{x}) \cdot \mathbf{n}(\mathbf{x}) = \bar{\boldsymbol{\sigma}} \cdot \mathbf{n}(\mathbf{x}), \quad (177a)$$

$$\boldsymbol{\phi}(\mathbf{x}) \cdot \mathbf{n}(\mathbf{x}) = \mathbf{0}, \quad (177b)$$

for all $\mathbf{x} \in \partial\Omega$. The macroscopic strain is then computed *a posteriori* as the volume average $\langle \mathbf{e} \rangle$ of the local strain \mathbf{e} . It depends linearly on the macroscopic stress, and the apparent compliance \mathbf{S}_{MBC} is defined as the linear operator which maps $\bar{\boldsymbol{\sigma}} = \langle \sigma \rangle$ to $\langle \mathbf{e} \rangle$

$$\langle \mathbf{e} \rangle = \mathbf{S}_{\text{MBC}} : \bar{\boldsymbol{\sigma}}. \quad (178)$$

For stress-gradient materials, it might be argued that the above-defined mixed boundary conditions are more natural than the static uniform boundary conditions, as they are in better agreement with the homogenization of Cauchy materials. Indeed, MBC prescribe only the traction vector (rather than the full stress tensor). Besides, boundary conditions (177b) ensure that the macroscopic strain coincides with the volume average of the symmetric gradient of the local displacement (see equation (163)).

7.1.4 Discussion of the boundary conditions KUBC, SUBC, PBC and MBC

Sab et al. (2016) have recently shown that the boundary-value problem defined by equations (156), (157) complemented with KUBC (167), SUBC (170), MBC (177) is well-posed. It can be also proved for PBC (174). Furthermore, Hill–Mandel lemma holds for all four types of boundary conditions. As a result, the corresponding apparent compliances \mathbf{S}_{KUBC} , \mathbf{S}_{SUBC} , \mathbf{S}_{PBC} and \mathbf{S}_{MBC} are symmetric, fourth-rank tensors. Under the assumption of statistical homogeneity and ergodicity, all four apparent compliances \mathbf{S}_{KUBC} , \mathbf{S}_{SUBC} , \mathbf{S}_{PBC} and \mathbf{S}_{MBC} are expected to converge to the effective compliance \mathbf{S}_{eff} as the size of the SVE Ω grows to infinity (Sab, 1992).

For kinematic uniform, periodic and mixed boundary conditions, the flux of $\boldsymbol{\phi}$ across $\partial\Omega$ vanishes. Therefore equation (163) holds and the macroscopic strain coincides rigorously with the volume average of the symmetrized gradient of the local displacement. For static uniform boundary conditions, this result holds only for large SVEs (see comment at the end of section 7.1.1).

The apparent compliances for kinematic and static boundary conditions can be given a variational definition. Indeed, the solution to the KUBC problem defined by equations (156), (157) and (167) minimizes the strain energy W defined by equation (124). More precisely,

$$\frac{1}{2} \bar{\mathbf{e}} : \mathbf{C}_{\text{KUBC}} : \bar{\mathbf{e}} = \{ \inf W(\mathbf{u}, \boldsymbol{\phi}), (\mathbf{u}, \boldsymbol{\phi}) \in \mathbb{KA}(\bar{\mathbf{e}} \cdot \mathbf{x}, \mathbf{0}) \}, \quad (179)$$

where \mathbb{KA} was defined in section 6.4 (see equation (120)). In particular, using $\bar{\mathbf{e}} = \text{const.}$, $\mathbf{u}(\mathbf{x}) = \bar{\mathbf{e}} \cdot \mathbf{x}$ and $\boldsymbol{\phi}(\mathbf{x}) = \mathbf{0}$ as test functions, the classical Voigt upper bound is readily retrieved

$$\mathbf{C}_{\text{KUBC}} \leq \langle \mathbf{C} \rangle = \mathbf{C}_{\text{Voigt}}. \quad (180)$$

Similarly, the solution to the SUBC problem defined by equations (156), (157) and (170) minimizes the complementary strain energy W^* defined by equation (105). More precisely,

$$\frac{1}{2} \bar{\boldsymbol{\sigma}} : \mathbf{S}_{\text{SUBC}} : \bar{\boldsymbol{\sigma}} = \{ \inf W^*(\boldsymbol{\sigma}), \boldsymbol{\sigma} \in \mathbb{SA}(\bar{\boldsymbol{\sigma}}) \}, \quad (181)$$

where \mathbb{SA} was defined in section 6.4 (see equation (119)). In particular, using $\boldsymbol{\sigma}(\mathbf{x}) = \bar{\boldsymbol{\sigma}} = \text{const.}$ as test function, the classical Reuss bound is readily retrieved

$$\mathbf{S}_{\text{SUBC}} \leq \langle \mathbf{S} \rangle = \mathbf{S}_{\text{Reuss}}. \quad (182)$$

Furthermore, it can be verified that $\mathbf{S}_{\text{KUBC}} \leq \mathbf{S}_{\text{SUBC}}$ (same proof as for the homogenization of elastic Cauchy materials). Since both \mathbf{S}_{KUBC} and \mathbf{S}_{SUBC} converge to \mathbf{S}_{eff} , the following inequalities are finally obtained

$$\mathbf{S}_{\text{Voigt}} \leq \mathbf{S}_{\text{KUBC}} \leq \mathbf{S}_{\text{eff}} \leq \mathbf{S}_{\text{SUBC}} \leq \mathbf{S}_{\text{Reuss}}, \quad (183)$$

where it is emphasized that \mathbf{S}_{KUBC} and \mathbf{S}_{SUBC} depend on the SVE Ω .

7.1.5 Softening size-effect in stress-gradient materials

As previously mentioned in section 6.6.2, the stress-gradient model tends to soften the bending stiffness of rectangular cross section beam as the thickness of the beam decreases. By contrast, the strain-gradient model tends to stiffen the bending stiffness. In this section, we will show that stress-gradient model tends to soften heterogeneous materials (in a sense that will be specified below).

We consider two heterogeneous stress-gradient materials with compliances \mathbf{S}^I and \mathbf{S}^{II} . At any point of domain Ω , we assume that material I is “softer” than material II in the sense

$$\mathbf{S}^I \leq \mathbf{S}^{II}, \quad \mathbf{M}^I \leq \mathbf{M}^{II} \quad (184)$$

For a given macroscopic stress loading $\bar{\sigma}$, the resulting local stress and trace-free parts of its gradient in each domain are respectively (σ^I, \mathbf{R}^I) and $(\sigma^{II}, \mathbf{R}^{II})$. Applying equation (181) for material I with the trial field $\sigma^{II} \in \mathbb{SA}(\langle \sigma \rangle)$, we find

$$\frac{1}{2} \bar{\sigma} : \mathbf{S}_{\text{SUBC}}^I : \bar{\sigma} \leq \int_{\Omega} \left[\frac{1}{2} \sigma^{II} : \mathbf{S}^I : \sigma^{II} + \frac{1}{2} \mathbf{R}^{II} : \mathbf{M}^I : \mathbf{R}^{II} \right] dV. \quad (185)$$

Note that inequality (184) holds, we then find

$$\frac{1}{2} \bar{\sigma} : \mathbf{S}_{\text{SUBC}}^I : \bar{\sigma} \leq \int_{\Omega} \left[\frac{1}{2} \sigma^{II} : \mathbf{S}^{II} : \sigma^{II} + \frac{1}{2} \mathbf{R}^{II} : \mathbf{M}^{II} : \mathbf{R}^{II} \right] dV = \frac{1}{2} \bar{\sigma} : \mathbf{S}_{\text{SUBC}}^{II} : \bar{\sigma}, \quad (186)$$

where the equation (181) was applied for material II with $\sigma^{II} \in \mathbb{SA}(\bar{\sigma})$. We finally deduce

$$\mathbf{S}_{\text{SUBC}}^I \leq \mathbf{S}_{\text{SUBC}}^{II}. \quad (187)$$

As the size of domain Ω tends to infinity, $|\Omega| \rightarrow \infty$, we find

$$\mathbf{S}^{I, \text{eff}} \leq \mathbf{S}^{II, \text{eff}}. \quad (188)$$

For the simplified stress-gradient model with one internal material length (see section 6.5.2), the above result means that increasing the internal material length (the size of the heterogeneities being unchanged) tends to decrease the effective stiffness. Conversely, decreasing the size of the heterogeneities (the internal material length being unchanged) tends to decrease the effective stiffness. In other words, stress-gradient materials exhibit softening size-effect.

This proof confirms once again that stress- and strain-gradient are two distinct models. Strain-gradient models are often invoked to account for size-effects in nanocomposites. This is relevant for most nanocomposites, where so-called stiffening size-effects are usually observed. However, numerical evidence from atomistic simulations suggest that some nanoparticles/polymer composites (Odegard et al., 2005; Davydov et al., 2014) might exhibit softening size-effects. For such materials, strain-gradient models are inadequate, while stress-gradient have the required qualitative behavior. It should be noted that the softening size-effect exhibited by stress-gradient materials has already been observed by Polizzotto (2014) and Challamel et al. (2016), albeit in somewhat different circumstances.

In the above section, boundary conditions that fulfill the Hill–Mandel lemma were proposed. We now turn to the analysis of Eshelby’s spherical inhomogeneity problem, which is the essential ingredient for mean field homogenization methods (such as Mori-Tanaka estimate).

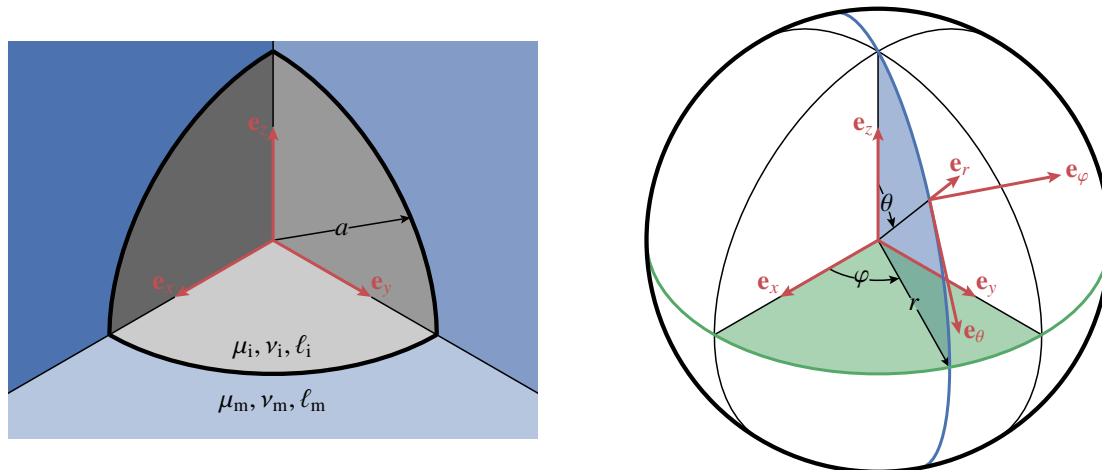


Figure 7.1. Eshelby's spherical inhomogeneity problem. *Left:* a spherical inhomogeneity embedded in an infinite matrix. *Right:* the spherical coordinates used in sections 7.2.2 and 7.2.3.

7.2 Eshelby's spherical inhomogeneity problem

As previously discussed in section 5.3.2, various mean field homogenization methods were proposed for the homogenization of generalized continua. In this chapter, we adopt the Mori-Tanaka approach. The basic building block of the Mori-Tanaka scheme is the dilute stress concentration tensor \mathbf{B}^∞ (to be defined below) which is derived from the solution to Eshelby's spherical *inhomogeneity* problem. This section is organized as follows. A general description of the problem is given in section 7.2.1. The solution to Eshelby's spherical inhomogeneity problem with isotropic loading at infinity is addressed in section 7.2.2, and with uniaxial loading at infinity in section 7.2.3. Finally, the dilute stress concentration tensor is derived in section 7.2.4.

7.2.1 General description

We consider a spherical inhomogeneity occupying the domain Ω_i , embedded in an unbounded matrix occupying the domain $\Omega_m = \mathbb{R}^3 \setminus \Omega_i$. At this stage, it is convenient to introduce the spherical coordinates (r, θ, ϕ) centered at the origin of the inhomogeneity (see figure 7.1, right). Both matrix and inhomogeneity are stress-gradient materials. The matrix (resp. inhomogeneity) is characterized by the compliance \mathbf{S}_m (resp. \mathbf{S}_i), generalized compliance \mathbf{M}_m (resp. \mathbf{M}_i) with material internal length ℓ_m (resp. ℓ_i) (see figure 7.1, left). The local compliance \mathbf{S} and generalized compliance \mathbf{M} are therefore defined as follows

$$\mathbf{S}(\mathbf{x}) = \chi_m(\mathbf{x}) \mathbf{S}_m + \chi_i(\mathbf{x}) \mathbf{S}_i, \quad (189)$$

$$\mathbf{M}(\mathbf{x}) = \chi_m(\mathbf{x}) \mathbf{M}_m + \chi_i(\mathbf{x}) \mathbf{M}_i, \quad (190)$$

where χ_m (resp. χ_i) is the indicator function of the matrix (resp. inhomogeneity). The inhomogeneity is subjected to a uniform stress at infinity

$$\boldsymbol{\sigma} \rightarrow \boldsymbol{\sigma}^\infty. \quad (191)$$

Eshelby's problem for spherical inhomogeneity is defined by the field equations (156), continuity condition (157) at the interface $r = a$ ($\mathbf{n} = \mathbf{e}_r$) and boundary conditions (191). The

procedure introduced in section 6.6, which we reproduce below, will be followed to solve this problem

- Compute the trace-free part of stress gradient from the postulated stress field: $\mathbf{R} = \mathbf{K} : (\nabla\sigma)$.
- Compute the micro-deformation from constitutive equation: $\phi = \mathbf{M} : \mathbf{R}$.
- Evaluate the total deformation from Hooke's law $\mathbf{e} = \mathbf{S} : \sigma$.
- Find the Cauchy deformation from $\boldsymbol{\varepsilon} = \mathbf{e} - \nabla \cdot \phi$.
- Integrate the compatibility conditions for $\boldsymbol{\varepsilon}$.
- Use the boundary conditions to evaluate the integration constants.

Owing to the linearity of Eshelby's problem, the average stress over the inhomogeneity depends linearly on the loading parameter σ^∞ . The dilute stress concentration tensor \mathbf{B}^∞ is then defined as the linear operator which maps the stress at infinity σ^∞ to the average stress over the inhomogeneity

$$\frac{1}{\text{vol } \Omega_i} \int_{\Omega_i} \boldsymbol{\sigma} \, dV = \mathbf{B}^\infty : \sigma^\infty. \quad (192)$$

For spherical inhomogeneities and isotropic materials, it is sufficient to solve Eshelby's inhomogeneity problem for the uniaxial case $\sigma^\infty = \sigma^\infty \mathbf{e}_z \otimes \mathbf{e}_z$ to obtain the strain concentration tensor \mathbf{B}^∞ . However, it is instructive to first solve this problem in the isotropic case $\sigma^\infty = \sigma^\infty \mathbf{I}$ (see section 7.2.2). The uniaxial case, which is significantly more involved, is then addressed (see section 7.2.3).

To close this section, it is noted that the solution procedure requires tedious algebra, but is easily implemented in a computer algebra system. The solution is then systematically expressed in a matrix form that is similar to [Herve and Zaoui \(1993\)](#). Integration constants are then solved for numerically.

7.2.2 Isotropic loading at infinity

This section is devoted to the case where the loading at infinity is isotropic, $\sigma^\infty = \sigma^\infty \mathbf{I}$. Owing to the symmetry of the problem, the stress tensor has only dependence on the radial coordinate. It is convenient to introduce the following second order tensors

$$\mathbf{p} = \mathbf{e}_r \otimes \mathbf{e}_r, \quad (193a)$$

$$\mathbf{q} = \mathbf{e}_\theta \otimes \mathbf{e}_\theta + \mathbf{e}_\phi \otimes \mathbf{e}_\phi. \quad (193b)$$

We then postulate the following divergence-free stress tensor

$$\boldsymbol{\sigma} = \sigma^\infty f(r) \mathbf{I} + \frac{\sigma^\infty}{2} r f'(r) \mathbf{q}, \quad (194)$$

where f denotes a dimensionless, scalar function of r and f' its derivative with respect to r .

Evaluation of the gradient of the stress tensor $\boldsymbol{\sigma}$ given by equation (194) requires $\nabla \mathbf{q}$. From the identity $\mathbf{p} + \mathbf{q} = \mathbf{I}$, we have

$$\nabla \mathbf{q} = -(\mathbf{e}_r \otimes \mathbf{e}_r) \otimes \nabla = -\partial_\theta (\mathbf{e}_r \otimes \mathbf{e}_r) \otimes \frac{\mathbf{e}_\theta}{r} - \partial_\varphi (\mathbf{e}_r \otimes \mathbf{e}_r) \otimes \frac{\mathbf{e}_\varphi}{r \sin \theta}, \quad (195)$$

which, upon substitution of the partial derivatives of \mathbf{e}_r with respect to θ and φ , leads to

$$\nabla \mathbf{q} = -\frac{2}{r} \left[\left(\mathbf{e}_r \overset{s}{\otimes} \mathbf{e}_\theta \right) \otimes \mathbf{e}_\theta + \left(\mathbf{e}_r \overset{s}{\otimes} \mathbf{e}_\varphi \right) \otimes \mathbf{e}_\varphi \right], \quad (196)$$

which finally leads to

$$\mathbf{R} = \nabla \boldsymbol{\sigma} = \frac{\sigma^\infty}{2} (rf'' - f') \mathbf{q} \otimes \mathbf{e}_r + \sigma^\infty f' \mathbf{a}. \quad (197)$$

In the above identity, the third-rank tensor \mathbf{a} is defined as follows

$$\mathbf{a} = 2\mathbf{q} \otimes \mathbf{e}_r + \mathbf{e}_r \otimes \mathbf{e}_r \otimes \mathbf{e}_r - \left(\mathbf{e}_r \overset{s}{\otimes} \mathbf{e}_\theta \right) \otimes \mathbf{e}_\theta - \left(\mathbf{e}_r \overset{s}{\otimes} \mathbf{e}_\varphi \right) \otimes \mathbf{e}_\varphi, \quad (198)$$

and simple algebra leads to the following identities

$$\mathbf{K} \cdot \mathbf{a} = \mathbf{a}, \quad \mathbf{H} \cdot \mathbf{a} = \frac{5}{2} \mathbf{a}, \quad (199)$$

where the sixth-rank tensors \mathbf{K} and \mathbf{H} have been defined in section 6.1.1 and 6.5.1, respectively. Combining equations (194), (197) and (199) with the constitutive relations (156c) and (156d), we can compute the total strain and micro-deformation tensor

$$\boldsymbol{\varepsilon} = \mathbf{S} : \boldsymbol{\sigma} = \frac{\sigma^\infty}{2\mu(1+\nu)} [vr f' + (1-2\nu)f] \mathbf{I} + \frac{\sigma^\infty}{4\mu} r f' \mathbf{q}, \quad (200a)$$

$$\boldsymbol{\phi} = \mathbf{M} \cdot \mathbf{R} = \frac{\ell^2 \sigma^\infty}{4\mu} \left[(rf'' - f') \mathbf{q} \otimes \mathbf{e}_r + \left(2 \frac{1-\nu}{1+\nu} f' - \frac{vr}{1+\nu} f'' \right) \mathbf{a} \right], \quad (200b)$$

where the indices ‘‘i’’ and ‘‘m’’ have been omitted.

Evaluation of the divergence of the micro-displacement $\boldsymbol{\phi}$ requires the divergence of $\mathbf{q} \otimes \mathbf{e}_r$ and \mathbf{a} , the derivation of which is similar to that of $\nabla \mathbf{q}$

$$\nabla \cdot (\mathbf{q} \otimes \mathbf{e}_r) = \frac{2}{r} \mathbf{q}, \quad \nabla \cdot \mathbf{a} = \frac{4}{r} \mathbf{I} - \frac{1}{r} \mathbf{q}. \quad (201)$$

Then, taking the divergence of equation (200b)

$$\nabla \cdot \boldsymbol{\phi} = \frac{\ell^2 \sigma^\infty}{4\mu(1+\nu)r} \left\{ [vr^2 f''' + (2-7\nu)rf'' + 8(1-\nu)f'] \mathbf{I} + (r^2 f''' + 4rf'' - 4f') \mathbf{q} \right\}, \quad (202)$$

we must express that $\boldsymbol{\varepsilon} = \boldsymbol{\varepsilon} - \nabla \cdot \boldsymbol{\phi}$ is geometrically compatible. To do so, it is observed that

$$\boldsymbol{\varepsilon} = \varepsilon_1(r) \mathbf{I} + \varepsilon_2(r) \mathbf{q}, \quad (203)$$

so that the general compatibility conditions in spherical coordinates reduce to a unique scalar equation $\varepsilon_1 = [r(\varepsilon_1 + \varepsilon_2)]'$. Furthermore, the displacement is given by $\mathbf{u} = r(\varepsilon_1 + \varepsilon_2) \mathbf{e}_r$. Simple but tedious algebra finally leads to the following equation for f

$$\ell^2 (r^3 f^{(4)} + 8r^2 f''' + 8rf'' - 8f') - (r^3 f'' + 4r^2 f') = 0, \quad (204)$$

which admits four linearly independent solutions

$$1, \quad \frac{\ell^3}{r^3}, \quad \left(\frac{\ell^3}{r^3} - \frac{\ell^2}{r^2} \right) \exp(r/\ell) \quad \text{and} \quad \left(\frac{\ell^3}{r^3} + \frac{\ell^2}{r^2} \right) \exp(-r/\ell) \quad (205)$$

Recalling that σ remains finite as $r \rightarrow 0$ and that $\sigma \rightarrow \sigma^\infty \mathbf{I}$ as $r \rightarrow +\infty$, it is finally found that

$$f(r) = \begin{cases} f_m(r) = 1 + A_2 \frac{\rho_m^3}{\alpha_m^3} + A_4 \rho_m^2 (1 + \rho_m) \exp\left(\frac{a-r}{\ell_m}\right) & (r > a), \\ f_i(r) = B_1 + \rho_i^2 B_3 (\rho_i \mathfrak{S}_i - \mathfrak{C}_i) & (r < a), \end{cases} \quad (206)$$

where we have introduced $\alpha_m = \ell_m/a$, $\rho_m = \ell_m/r$, $\alpha_i = \ell_i/a$, $\rho_i = \ell_i/r$ and

$$\mathfrak{C}_i = \exp\left(-\frac{a}{\ell_i}\right) \cosh\left(\frac{r}{\ell_i}\right), \quad (207a)$$

$$\mathfrak{S}_i = \exp\left(-\frac{a}{\ell_i}\right) \sinh\left(\frac{r}{\ell_i}\right). \quad (207b)$$

In equation (206), the integration constants A_2 , A_4 , B_1 and B_3 are found from the continuity of the following scalar quantities at the interface $r = a$ (see equations (157a), (157b))

$$\sigma_{rr}, \quad \sigma_{\theta\theta} = \sigma_{\varphi\varphi}, \quad \phi_{rrr} + u_r \quad \text{and} \quad \phi_{\theta\theta r} = \phi_{\varphi\varphi r}, \quad (208)$$

leading to four linearly independent equations, which are solved numerically.

As an illustration, we consider in Fig. 7.2 the case of a stiff inhomogeneity

$$\mu_i = 10\mu_m, \quad \nu_i = \nu_m = 0.25, \quad (209)$$

and we study the influence of the material internal lengths ℓ_i and ℓ_m on the solution.

Figure 7.2 (left) plots the normalized radial stress $\sigma_{rr}/\sigma^\infty$ for various combinations of (ℓ_i, ℓ_m) . The classical case ($\ell_i = \ell_m = 0$) is also represented. From these plots, it is readily deduced that Eshelby's theorem (Eshelby, 1957) does not hold for stress-gradient elasticity. In other words, the stress is not uniform within the inhomogeneity. Indeed, the continuity condition (157b) induces a boundary layer at the matrix–inhomogeneity interface. The thickness of this boundary layer is about a few ℓ_i within the inhomogeneity (see equation (206)). As a consequence, the stress field is nearly uniform at the core of the inhomogeneity for small values of the material internal length ℓ_i . Similarly, for small values of the material internal length ℓ_m of the matrix, the non-uniform stress within the inhomogeneity is close to the classical value.

Closer inspection of figure 7.2 (left) shows that at a given point within the inhomogeneity, the radial stress does not evolve monotonically with the inhomogeneity's material internal length ℓ_i . This is better illustrated on figure 7.2 (right), which shows the normalized radial stress at the center of the inhomogeneity as a function of ℓ_i , for various values of ℓ_m . It is observed that the radial stress at the center reaches a maximum for a finite value of ℓ_i , which increases as ℓ_m increases.

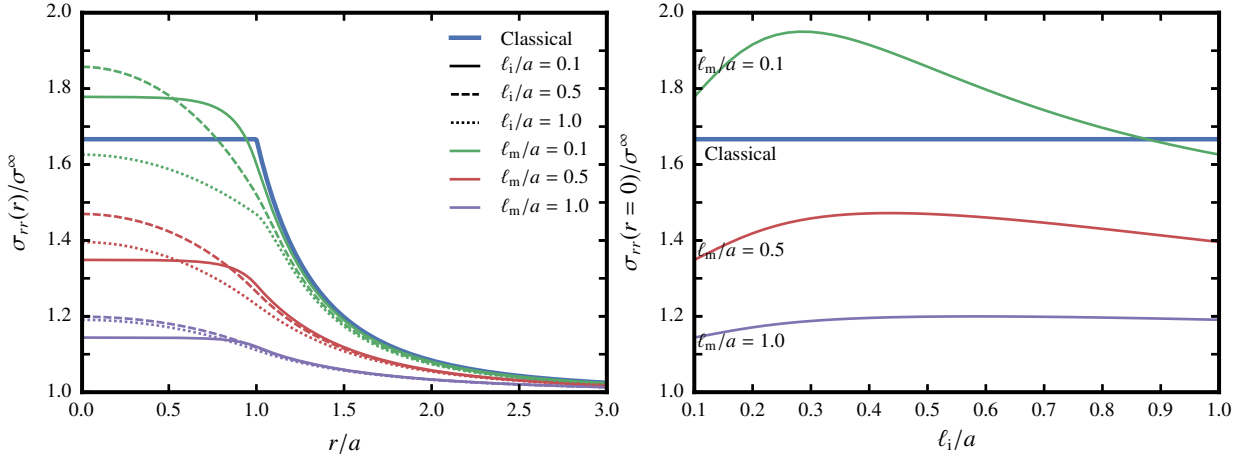


Figure 7.2. Solution to Eshelby's spherical inhomogeneity problem (isotropic loading at infinity). *Left:* plot of the radial stress σ_{rr} as a function of the distance to the center of the inhomogeneity, r . Line types (solid, dashed, dotted) correspond to various values of the material internal length l_i of the inhomogeneity. *Right:* plot of the radial stress $\sigma_{rr}(r=0)$ at the center of the inhomogeneity as a function of the inhomogeneity's material internal length l_i . For both graphs, colors correspond to various values of the material internal length l_m of the matrix. The thick line corresponds to the classical ($l_i = l_m = 0$).

7.2.3 Uniaxial loading at infinity

In this section, we consider the case of a uniaxial loading at infinity, $\sigma^\infty = \sigma^\infty \mathbf{e}_z \otimes \mathbf{e}_z$. The derivation is significantly more involved than in the previous case; it is only briefly outlined here (some details can be found in appendix C). We postulate the following stress tensor

$$\begin{aligned} \boldsymbol{\sigma} = & \sigma^\infty \left[f_1(r) \cos^2 \theta + f_2(r) \sin^2 \theta \right] \mathbf{p} + \sigma^\infty \left[f_3(r) \cos^2 \theta + f_4(r) \sin^2 \theta \right] \mathbf{q} \\ & + \sigma^\infty f_5(r) \cos \theta \mathbf{e}_r \overset{s}{\otimes} \mathbf{e}_z + \sigma^\infty f_6(r) \mathbf{e}_z \otimes \mathbf{e}_z, \end{aligned} \quad (210)$$

where f_1, \dots, f_6 are unknown functions which depend on the radial variable r only. Expressing that the above-defined stress tensor must be divergence-free leads to the following differential equations

$$f_3 = f_2 + \frac{r}{2} f_2' - \frac{1}{2} f_5 - \frac{r}{4} f_5' - \frac{r}{2} f_6', \quad (211a)$$

$$f_4 = f_2 + \frac{r}{2} f_2' + \frac{1}{4} f_5, \quad (211b)$$

$$0 = 2(f_1 - f_2) + r(f_1' - f_2') + 2f_5 + \frac{3r}{2} f_5' + 2r f_6', \quad (211c)$$

where primes again stand for derivation with respect to r . Computing the trace-free part \mathbf{R} of the stress-gradient $\nabla \boldsymbol{\sigma}$, then the micro-displacement $\boldsymbol{\phi}$ and the total strain $\boldsymbol{\varepsilon}$ from the constitutive laws leads after simple but tedious algebra to the following decomposition of $\boldsymbol{\varepsilon} = \boldsymbol{\varepsilon} - \nabla \cdot \boldsymbol{\phi}$

$$\begin{aligned} \boldsymbol{\varepsilon} = & \left[g_1(r) \cos^2 \theta + g_2(r) \sin^2 \theta \right] \mathbf{p} + \left[g_3(r) \cos^2 \theta + g_4(r) \sin^2 \theta \right] \mathbf{q} \\ & + g_5(r) \cos \theta \mathbf{e}_r \overset{s}{\otimes} \mathbf{e}_z + g_6(r) \mathbf{e}_z \otimes \mathbf{e}_z, \end{aligned} \quad (212)$$

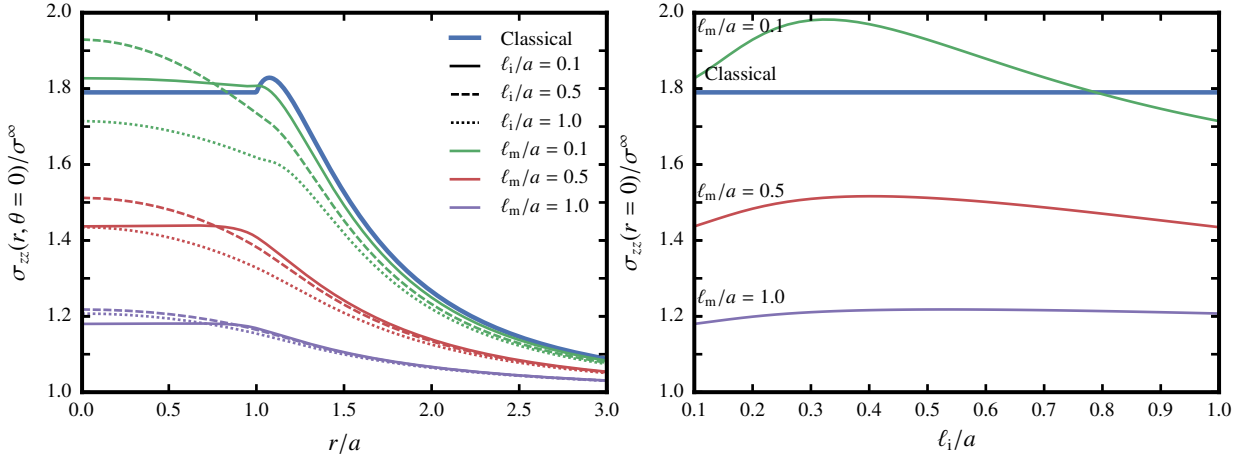


Figure 7.3. Solution to Eshelby's spherical inhomogeneity problem (uniaxial loading at infinity). *Left:* plot of the axial stress σ_{zz} along the polar axis ($\theta = 0$) as a function of the distance to the center of the inhomogeneity, r . Line types (solid, dashed, dotted) correspond to various values of the material internal length ℓ_i of the inhomogeneity. *Right:* plot of the axial stress $\sigma_{zz}(r = 0)$ at the center of the inhomogeneity as a function of the inhomogeneity's material internal length ℓ_i . For both graphs, colors correspond to various values of the material internal length ℓ_m of the matrix. The thick line corresponds to the classical solution ($\ell_i = \ell_m = 0$).

where g_1, \dots, g_6 are linear combinations of the unknown functions f_1, \dots, f_6 and their derivatives with respect to r (the actual relationships between g_1, \dots, g_6 and f_1, \dots, f_6 are too long to be reported here). Expressing that $\boldsymbol{\varepsilon}$ must be compatible (see appendix C.1) results in the following set of differential equations

$$g_1 = -\frac{r^2}{2}g_6'' + \frac{r}{2}g_5' + rg_4' - \frac{g_5}{2}, \quad (213a)$$

$$g_2 = rg_4' + g_4, \quad (213b)$$

$$g_3 = -\frac{r}{2}g_6' + g_4 + \frac{g_5}{2}. \quad (213c)$$

Gathering equations (211) and (213) finally leads to a linear system of six differential equations with f_1, \dots, f_6 as unknowns. The general form of these functions is given in appendix C.2, where twelve integration constants are identified. Enforcing the continuity conditions (157a), (157b) at the interface $r = a$ again results in a linear system, the solution of which gives the values of these constants.

Figure 7.3 (left) plots the normalized axial stress $\sigma_{zz}/\sigma^\infty$ along the polar axis ($\theta = 0$) with respect to the (normalized) radial distance r/a , for various combinations of (ℓ_i, ℓ_m) . Similarly to the isotropic case, it is also observed that Eshelby's theorem does not hold for stress-gradient elasticity. The axial stress inside the inhomogeneity is no longer uniform. A stress boundary layer is again observed at the matrix– inhomogeneity interface; it is induced by the stress continuity condition (157b). The axial stress at the center of the inclusion is not a monotonic function of the inhomogeneity's material length ℓ_i : it reaches a maximum for a finite value of ℓ_i , which increases as ℓ_m increases (the exact location of this maximum differs from the isotropic load case).

7.2.4 The dilute stress concentration tensor of spherical inhomogeneities

The solution to Eshelby's spherical inhomogeneity problem derived in the above section is now employed to evaluate the dilute stress concentration tensor for spherical inhomogeneity \mathbf{B}^∞ . Owing to the symmetries of the problem under consideration, the dilute stress concentration tensor \mathbf{B}^∞ is isotropic. It can be decomposed as follows

$$\mathbf{B}^\infty = (\text{sph}\mathbf{B}^\infty)\mathbf{J} + (\text{dev}\mathbf{B}^\infty)\mathbf{K}, \quad (214)$$

where \mathbf{J}, \mathbf{K} denote the classical fourth-rank spherical and deviatoric projection tensors, respectively, while $\text{sph}\mathbf{B}^\infty$ and $\text{dev}\mathbf{B}^\infty$ denote the (scalar) spherical and deviatoric part of the fourth-rank tensor \mathbf{B}^∞

$$\text{sph}\mathbf{B}^\infty = \mathbf{J} :: \mathbf{B}^\infty, \quad (215)$$

$$\text{dev}\mathbf{B}^\infty = \frac{1}{5}\mathbf{K} :: \mathbf{B}^\infty. \quad (216)$$

Using the general expression (210) of the stress tensor $\boldsymbol{\sigma}$ for the uniaxial load case (see section 7.2.3), it is readily found that the average stress over the inhomogeneity reads

$$\begin{aligned} \frac{1}{\text{vol}\Omega_i} \int_{\Omega_i} \boldsymbol{\sigma} dV &= \frac{\sigma^\infty}{15} (F_1 + 4F_2 + 4F_3 + 6F_4) \mathbf{I} \\ &\quad + \frac{\sigma^\infty}{15} (2F_1 - 2F_2 - 2F_3 + 2F_4 + 5F_5 + 15F_6) \mathbf{e}_z \otimes \mathbf{e}_z, \end{aligned} \quad (217)$$

where we have introduced

$$F_k = \frac{3}{a^3} \int_0^a r^2 f_k(r) dr, \quad (218)$$

for $k = 1, \dots, 6$. From the decomposition (214) of the stress concentration tensor

$$\mathbf{B}^\infty : (\sigma^\infty \mathbf{e}_z \otimes \mathbf{e}_z) = \frac{\sigma^\infty}{3} (\text{sph}\mathbf{B}^\infty - \text{dev}\mathbf{B}^\infty) \mathbf{I} + \sigma^\infty (\text{dev}\mathbf{B}^\infty) \mathbf{e}_z \otimes \mathbf{e}_z. \quad (219)$$

which, upon combination with (217), finally gives

$$\text{sph}\mathbf{B}^\infty = \frac{1}{3} (F_1 + 2F_2 + 2F_3 + 4F_4 + F_5 + 3F_6), \quad (220a)$$

$$\text{dev}\mathbf{B}^\infty = \frac{1}{15} (2F_1 - 2F_2 - 2F_3 + 2F_4 + 5F_5 + 15F_6). \quad (220b)$$

For illustration purpose, we consider in figure 7.4 the case of a stiff inhomogeneity

$$\mu_i = 10\mu_m, \quad \nu_i = \nu_m = 0.25, \quad (221)$$

and we study the influence of the material internal lengths ℓ_i and ℓ_m on the components of the dilute stress concentration tensor. It is observed that $\text{sph}\mathbf{B}^\infty$ and $\text{dev}\mathbf{B}^\infty$ are more sensitive to the matrix internal length ℓ_m than the inhomogeneity internal length ℓ_i . Furthermore, for various values of ℓ_m, ℓ_i , both $\text{sph}\mathbf{B}^\infty$ and $\text{dev}\mathbf{B}^\infty$ are lower than the classical elasticity values.

In the previous section, the dilute stress concentration tensor for spherical inhomogeneity was derived using the solution to Eshelby's inhomogeneity problem. Using this building block, in the next section, we will produce Mori-Tanaka estimates for the effective bulk and shear moduli of stress-gradient composites with monodisperse, spherical inclusions.

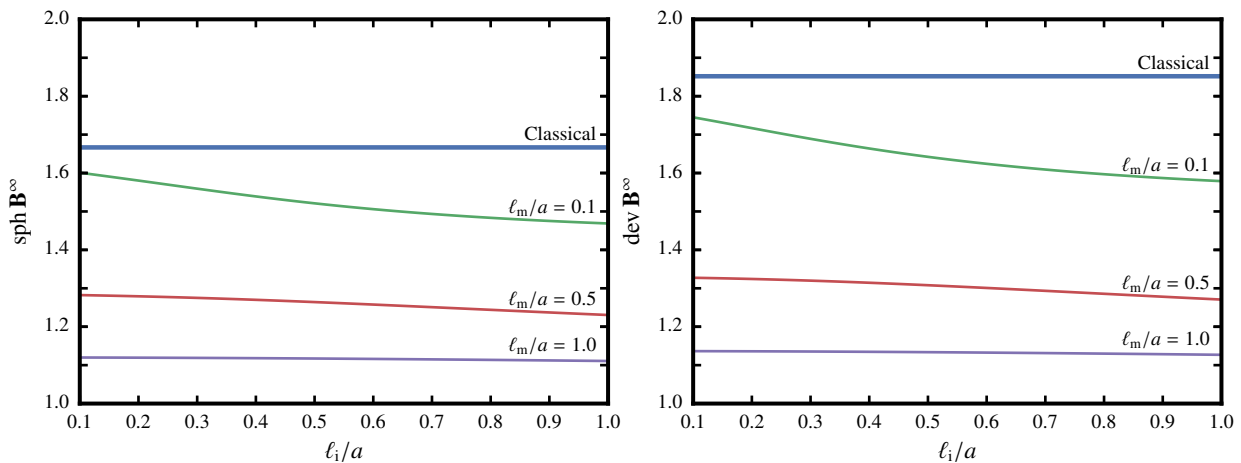


Figure 7.4. The spherical (*left*) and deviatoric (*right*) parts of the dilute stress concentration tensor \mathbf{B}^∞ as a function of the inhomogeneity's material internal length ℓ_i . Like the previous graphs, colors correspond to various values of the material internal length ℓ_m of the matrix. The thick line corresponds to the classical solution ($\ell_i = \ell_m = 0$).

7.3 Mori-Tanaka estimates of the effective properties

In this section, the above obtained dilute stress concentration tensor is used to derive the Mori-Tanaka estimate on the effective modulus of stress-gradient composites with monodisperse, spherical inclusions. For this purpose, the stress-based presentation of [Benveniste \(1987\)](#) will be adopted (in which the outcome is the effective compliance tensor). It can readily be shown that the following expression for the effective compliance tensor remains valid for stress-gradient materials

$$\mathbf{S}_{\text{eff}} = \mathbf{S}_m + f(\mathbf{S}_i - \mathbf{S}_m) : \mathbf{B}^\infty : [(\mathbf{1} - f)\mathbf{I} + f\mathbf{B}^\infty]^{-1}, \quad (222)$$

where f denotes the volume fraction of inclusions, \mathbf{S}_m (resp. \mathbf{S}_i) denotes the compliance of the matrix (resp. the inclusion). In equation (222), the (classical elasticity) dilute stress concentration tensor is substituted with the (stress-gradient) dilute stress concentration tensor \mathbf{B}^∞ derived in section 7.2.4. Inversion of \mathbf{S}_{eff} then gives the effective stiffness tensor \mathbf{C}_{eff} .

As an illustration, we consider the case of a stiff inhomogeneity

$$\mu_i = 10\mu_m, \quad \nu_i = \nu_m = 0.25. \quad (223)$$

Figure 7.5 plots the resulting effective moduli as a function of the volume fraction f of inclusions. We assumed that $\ell_i = \ell_m$ since it was shown in section 7.2.4 that the dilute stress tensor is not very sensitive to ℓ_i . As expected, it is observed that for small values of the material internal length, the proposed estimates are close to the classical [Mori and Tanaka \(1973\)](#) estimates. Conversely, for larger values of the material internal length, these estimates tend to the classical bound of Reuss. This was also expected, for $\ell_m, \ell_i \rightarrow \infty$, the trace-free part of stress gradient tensor, \mathbf{R} , must vanish to ensure that the complementary strain energy density remains finite. In the absence of the body forces, the full stress gradient tensor vanishes and the stress field is phase-wise constant. It should be noted that the Mori-Tanaka estimate is produced under the scale separation condition (152),

$$\ell \sim d, \text{ or } \ell \ll d, \quad (224)$$

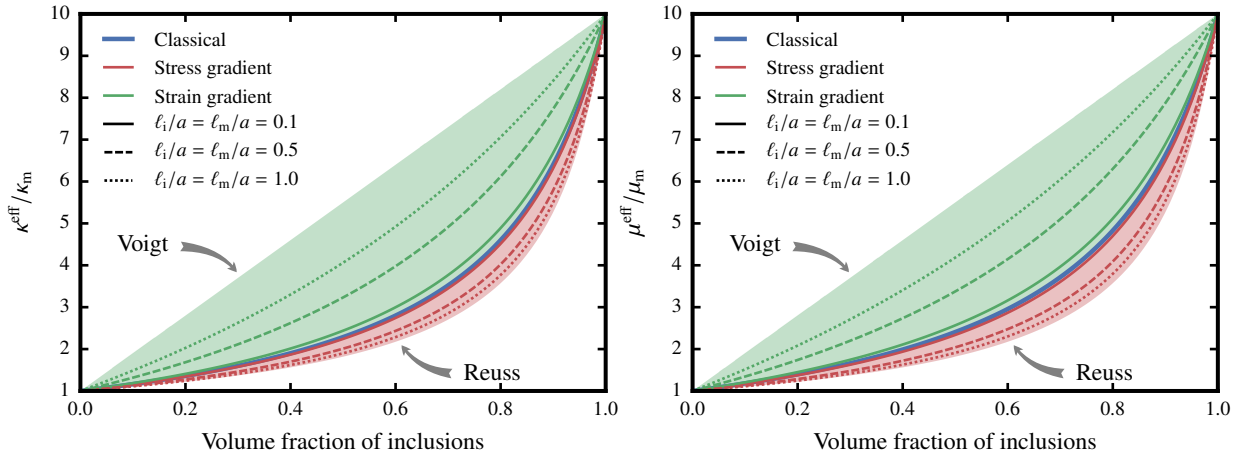


Figure 7.5. Mori–Tanaka estimates of the effective bulk (*left*) and shear (*right*) moduli of the composite κ^{eff} and μ^{eff} , as a function of the volume fraction of inclusions, f . The estimates are represented for both stress- and strain-gradient materials.

and the limit $\ell_m, \ell_i \rightarrow \infty$ is thus purely formal. The largest material internal length considered in figure 7.5 is $\ell_i = \ell_m = a$.

Figure 7.5 also shows the recently published Mori–Tanaka estimates of the effective elastic properties of strain-gradient materials (Ma and Gao, 2014). These estimates are based on the simplified strain gradient model (Aifantis, 1992; Gao and Park, 2007). It is recalled that our own simplified material model (described in section 6.5.2), is very close in spirit to that of Gao and Park (2007), which makes the comparison in Figure 7.5 relevant.

Figure 7.5 is a visual illustration of the essential differences between strain- and stress-gradient materials that were already pointed out in section 7.1.5. Indeed, the region comprised between the Reuss and Voigt bounds is clearly divided in two non-overlapping subregions. Strain-gradient materials systematically fall in the region comprised between the classical effective properties and the corresponding upper-bounds of Voigt (stiffening size-effect), while stress-gradient materials systematically fall in the region comprised between the classical effective properties and the corresponding lower-bounds of Reuss (softening size-effect). This again shows that, although conceptually similar (one might be tempted to say that they are “dual”), the strain- and stress-gradient models define widely different materials.

In this chapter, a framework for the homogenization of stress-gradient materials is established. Heterogeneous stress-gradient materials are homogenized as a macroscopic homogeneous Cauchy material under the classical scale separation condition and additional assumption that the material internal length is at most of the same order as the typical size of the heterogeneities. Kinematic uniform, static uniform, periodic and mixed boundary conditions is derived that fulfill the (generalized) Hill-Mandel lemma. Variational definitions of the effective elastic properties are then proposed, from which it results that stress-gradient materials exhibit a softening size effect.

Furthermore, the Eshelby spherical inhomogeneity problem is solved analytically and used to produce Mori–Tanaka estimates of the effective mechanical properties of stress-gradient composites. The resulting estimate is compared to previously derived strain-gradient estimates Ma and Gao (2014) (with a very close material model). It is shown that stress- and strain-

gradient models define clearly divided, non overlapping region bounded by the Voigt and Reuss bounds. This result again shows that stress- and strain gradient models define different materials.

It should be noted that the above derived Mori–Tanaka estimate does not account for interactions between inclusions, and fails for high concentrations of inhomogeneities. In the next chapter, following the approach of [Hashin and Shtrikman \(1962b\)](#), we derive rigorous bounds for stress-gradient composites.

Chapter 8

Hashin-Shtrikman variational principle and bounds

In this chapter, we aim at bounding the effective properties of stress-gradient composites by extending the classical [Hashin and Shtrikman \(1962b\)](#) bounds. The resulting stress-gradient bounds are expected to be a function of the material internal length. We begin with the derivation of the variational principle of Hashin and Shtrikman for stress-gradient materials in section 8.1. This requires the explicit expressions of the Green operators, which will be derived in section 8.2. Bounds are then established for stress-gradient composites by employing phase-wise constant trial fields in section 8.3.

8.1 Hashin-Shtrikman variational principle

In this section, we derive the Hashin-Shtrikman variational principle for stress-gradient materials. We adopt the general variational framework developed by [Willis \(1983\)](#); [Talbot and Willis \(1985\)](#); [Willis \(1991\)](#) for non-linear Cauchy materials.

We consider a heterogeneous body Ω occupying the domain $\Omega \subset \mathbb{R}^3$ which is made of a stress-gradient material. The stiffness (resp. generalized stiffness) of Ω is denoted by $\mathbf{C}(\mathbf{x})$ (resp. $\mathbf{L}(\mathbf{x})$), which depends on the observation point \mathbf{x} to account for material heterogeneity. Following [Hashin and Shtrikman \(1962a,b\)](#), it is convenient to introduce a homogeneous, stress-gradient, reference medium with positive-definite stiffness \mathbf{C}_0 and generalized stiffness \mathbf{L}_0 . We assume that $\mathbf{C} > \mathbf{C}_0, \mathbf{L} > \mathbf{L}_0$. The strain energy density function $w_0(\mathbf{x}, \mathbf{e}(\mathbf{x}), \boldsymbol{\phi}(\mathbf{x}))$ of the reference medium reads

$$w_0(\mathbf{x}, \mathbf{e}(\mathbf{x}), \boldsymbol{\phi}(\mathbf{x})) = \frac{1}{2} \mathbf{e}(\mathbf{x}) : \mathbf{C}_0 : \mathbf{e}(\mathbf{x}) + \frac{1}{2} \boldsymbol{\phi}(\mathbf{x}) \cdot \mathbf{L}_0 \cdot \boldsymbol{\phi}(\mathbf{x}), \quad \forall \mathbf{x} \in \Omega. \quad (225)$$

For the sake of compactness, the dependence on the observation point \mathbf{x} will be omitted hereafter except otherwise stated. The above strain energy density of the reference medium is chosen such that at each point $\mathbf{x} \in \Omega$, the function $w(\mathbf{e}, \boldsymbol{\phi}) - w_0(\mathbf{e}, \boldsymbol{\phi})$ grows faster than linearly at large \mathbf{e} and $\boldsymbol{\phi}$. The following function $V(\boldsymbol{\tau}, \boldsymbol{\kappa})$ can be defined

$$V(\boldsymbol{\tau}, \boldsymbol{\kappa}) = \sup_{\mathbf{e}, \boldsymbol{\phi}} \{ \boldsymbol{\tau} : \mathbf{e} + \boldsymbol{\phi} \cdot \boldsymbol{\kappa} - w(\mathbf{e}, \boldsymbol{\phi}) + w_0(\mathbf{e}, \boldsymbol{\phi}) \}, \quad (226)$$

for arbitrary symmetric second-rank tensor $\boldsymbol{\tau} \in {}^2\mathcal{T}$ and third-order trace-free tensor $\boldsymbol{\kappa} \in {}^3\mathcal{D}$. Equation (226) readily yields

$$V(\boldsymbol{\tau}, \boldsymbol{\kappa}) = \frac{1}{2} \boldsymbol{\tau} : (\mathbf{C} - \mathbf{C}_0)^{-1} : \boldsymbol{\tau} + \frac{1}{2} \boldsymbol{\kappa} \cdot\cdot (\mathbf{L} - \mathbf{L}_0)^{-1} \cdot\cdot \boldsymbol{\kappa}, \quad (227)$$

and equality is reached if

$$\boldsymbol{\tau} = (\mathbf{C} - \mathbf{C}_0) : \mathbf{e}, \quad \boldsymbol{\kappa} = (\mathbf{L} - \mathbf{L}_0) \cdot\cdot \boldsymbol{\phi}, \quad (228)$$

which are of similar form to the stress polarization tensor in classical elasticity (see also [Smyshlyaev and Fleck \(1994\)](#) for analogue in strain-gradient model). We shall call $\boldsymbol{\tau}, \boldsymbol{\kappa}$ stress and stress gradient polarization tensors. It can be deduced from equation (226) that

$$w(\mathbf{e}, \boldsymbol{\phi}) \geq w_0(\mathbf{e}, \boldsymbol{\phi}) + \mathbf{e} : \boldsymbol{\tau} + \boldsymbol{\phi} \cdot\cdot \boldsymbol{\kappa} - V(\boldsymbol{\tau}, \boldsymbol{\kappa}), \quad (229)$$

for any values of $\mathbf{e}, \boldsymbol{\phi}, \boldsymbol{\tau}, \boldsymbol{\kappa}$. Taking the volume average of the above expression over the whole domain Ω , we find

$$\frac{1}{V} \int_{\Omega} w(\mathbf{e}, \boldsymbol{\phi}) \, dV \geq \frac{1}{V} \int_{\Omega} [w_0(\mathbf{e}, \boldsymbol{\phi}) + \mathbf{e} : \boldsymbol{\tau} + \boldsymbol{\phi} \cdot\cdot \boldsymbol{\kappa} - V(\boldsymbol{\tau}, \boldsymbol{\kappa})] \, dV \quad (230)$$

We minimize equation (230) under the constraint $(\mathbf{u}, \boldsymbol{\phi}) \in \mathbb{KA}(\bar{\mathbf{e}} \cdot \mathbf{x}, \mathbf{0})$, with $\mathbf{e} = \nabla^s \mathbf{u} + \nabla \cdot \boldsymbol{\phi}$ (see equation (120) for the definition of \mathbb{KA}). The infimum of both sides results in

$$\frac{1}{2} \bar{\mathbf{e}} : \mathbf{C}_{\text{eff}} : \bar{\mathbf{e}} = \inf_{\mathbf{u}, \boldsymbol{\phi}} \frac{1}{V} \int_{\Omega} w(\mathbf{e}, \boldsymbol{\phi}) \, dV \geq \inf_{\mathbf{u}, \boldsymbol{\phi}} \frac{1}{V} \int_{\Omega} [w_0(\mathbf{e}, \boldsymbol{\phi}) + \mathbf{e} : \boldsymbol{\tau} + \boldsymbol{\phi} \cdot\cdot \boldsymbol{\kappa} - V(\boldsymbol{\tau}, \boldsymbol{\kappa})] \, dV, \quad (231)$$

where the equality in equation (231) follows from equation (179). Introducing

$$I(\mathbf{e}, \boldsymbol{\phi}) = \frac{1}{V} \int_{\Omega} [w_0(\mathbf{e}, \boldsymbol{\phi}) + \mathbf{e} : \boldsymbol{\tau} + \boldsymbol{\phi} \cdot\cdot \boldsymbol{\kappa}] \, dV, \quad (232)$$

similar to classical elasticity, it can be shown that stationary value of $I(\mathbf{e}, \boldsymbol{\phi})$ is reached for the solution to the following auxiliary problem

$$\nabla \cdot \boldsymbol{\sigma} = \mathbf{0}, \quad (233a)$$

$$\mathbf{R} = \mathbf{K} \cdot\cdot (\nabla \boldsymbol{\sigma}), \quad (233b)$$

$$\boldsymbol{\sigma} = \mathbf{C}_0 : \mathbf{e} + \boldsymbol{\tau}, \quad (233c)$$

$$\mathbf{R} = \mathbf{L}_0 \cdot\cdot \boldsymbol{\phi} + \boldsymbol{\kappa}, \quad (233d)$$

$$\mathbf{e} = \nabla^s \mathbf{u} + \nabla \cdot \boldsymbol{\phi}, \quad (233e)$$

complemented with the boundary conditions $\mathbf{u}(\mathbf{x}) = \bar{\mathbf{e}} \cdot \mathbf{x}$ and $\boldsymbol{\phi}(\mathbf{x}) = \mathbf{0}$ for all $\mathbf{x} \in \partial\Omega$. Owing to the linearity of the above problem, the total strain \mathbf{e} and micro-displacement $\boldsymbol{\phi}$ are related to the stress and stress-gradient polarizations $\boldsymbol{\tau}$ and $\boldsymbol{\kappa}$ as follows

$$\mathbf{e}(\mathbf{x}) = \bar{\mathbf{e}} - {}^4\Gamma_{0,e\tau}[\boldsymbol{\tau}](\mathbf{x}) - {}^5\Gamma_{0,e\kappa}[\boldsymbol{\kappa}](\mathbf{x}), \quad (234a)$$

$$\boldsymbol{\phi}(\mathbf{x}) = -{}^5\Gamma_{0,\phi\tau}[\boldsymbol{\tau}](\mathbf{x}) - {}^6\Gamma_{0,\phi\kappa}[\boldsymbol{\kappa}](\mathbf{x}), \quad (234b)$$

where ${}^4\Gamma_{0,e\tau}, {}^5\Gamma_{0,e\kappa}, {}^5\Gamma_{0,\phi\tau}, {}^6\Gamma_{0,\phi\kappa}$ are four Green operators yet to be determined.

Upon substituting equation (234) in equation (231), we find after some straightforward calculation

$$\frac{1}{2} \bar{\mathbf{e}} : \mathbf{C}_{\text{eff}} : \bar{\mathbf{e}} \geq \mathcal{H}(\boldsymbol{\tau}, \boldsymbol{\kappa}), \quad (235)$$

where the functional of Hashin and Shtrikman \mathcal{H} is defined as follows

$$\begin{aligned} \mathcal{H}(\boldsymbol{\tau}, \boldsymbol{\kappa}) = & \frac{1}{2} \bar{\mathbf{e}} : \mathbf{C}_0 : \bar{\mathbf{e}} + \bar{\mathbf{e}} : \langle \boldsymbol{\tau} \rangle - \frac{1}{2} \langle \boldsymbol{\tau} : (\mathbf{C} - \mathbf{C}_0)^{-1} : \boldsymbol{\tau} \rangle - \frac{1}{2} \langle \boldsymbol{\kappa} : (\mathbf{L} - \mathbf{L}_0)^{-1} : \boldsymbol{\kappa} \rangle \\ & - \frac{1}{2} \langle \boldsymbol{\tau} : \boldsymbol{\Gamma}_{0,e\tau}[\boldsymbol{\tau}] \rangle - \frac{1}{2} \langle \boldsymbol{\tau} : \boldsymbol{\Gamma}_{0,e\kappa}[\boldsymbol{\kappa}] \rangle - \frac{1}{2} \langle \boldsymbol{\kappa} : \boldsymbol{\Gamma}_{0,\phi\tau}[\boldsymbol{\tau}] \rangle - \frac{1}{2} \langle \boldsymbol{\kappa} : \boldsymbol{\Gamma}_{0,\phi\kappa}[\boldsymbol{\kappa}] \rangle. \end{aligned} \quad (236)$$

Equation (235) is the maximum principle of Hashin and Shtrikman for stress-gradient materials. In comparison with classical elasticity, it involves four generalized Green operators.

By standard lines of argument, it can be shown that for $\mathbf{C} < \mathbf{C}_0, \mathbf{L} < \mathbf{L}_0$, we find the Hashin-Shtrikman minimum principle

$$\frac{1}{2} \bar{\mathbf{e}} : \mathbf{C}_{\text{eff}} : \bar{\mathbf{e}} \leq \mathcal{H}(\boldsymbol{\tau}, \boldsymbol{\kappa}). \quad (237)$$

In the above derivation of the variational principle of Hashin and Shtrikman, we have introduced formally four Green operators. In the next section, we derive a closed-form expression of these operators for periodic and infinite domains.

8.2 Green operators of an infinite body

Equation (233) together with the kinematic uniform boundary conditions define the fundamental solution and Green operators for stress-gradient materials. Closed-form expressions of these operators cannot be established for bounded domains. Therefore, we present below a derivation of the Green operators of an *infinite stress-gradient body*. These operators are derived in Fourier space. In what follows, we adopt the following normalization of the Fourier transform and its inverse

$$\hat{f}(\mathbf{k}) = \int_{\mathbb{R}^d} f(\mathbf{x}) \exp(-i\mathbf{k} \cdot \mathbf{x}) \, d\mathbf{x}, \quad f(\mathbf{x}) = \frac{1}{(2\pi)^d} \int_{\mathbb{R}^d} \hat{f}(\mathbf{k}) \exp(i\mathbf{k} \cdot \mathbf{x}) \, d\mathbf{k}. \quad (238)$$

The derivation presented below is intrinsic (coordinate-free). In appendix D, an alternative, matrix-based derivation is proposed. This last approach, which is systematic, can be useful for numerical implementation.

In the remainder of section 8.2, the "0" subscript referring to the reference medium will be omitted (e.g. \mathbf{C}_0 will be denoted by \mathbf{C}) unless otherwise stated.

8.2.1 On the relationship between the four Green operators

Interestingly, it can be shown that all four Green operators introduced above (see equation (234)) can be derived from ${}^4\boldsymbol{\Gamma}_{e\tau}$. Indeed, the boundary value problem in equation (233) reads in real

space (left) and Fourier space (right)

$$\nabla \cdot \boldsymbol{\sigma} = \mathbf{0}, \quad \hat{\boldsymbol{\sigma}} \cdot i\mathbf{k} = \mathbf{0}, \quad (239a)$$

$$\mathbf{R} = \nabla \boldsymbol{\sigma}, \quad \hat{\mathbf{R}} = \hat{\boldsymbol{\sigma}} \otimes i\mathbf{k}, \quad (239b)$$

$$\boldsymbol{\sigma} = \mathbf{C} : \mathbf{e} + \boldsymbol{\tau}, \quad \hat{\boldsymbol{\sigma}} = \mathbf{C} : \hat{\mathbf{e}} + \hat{\boldsymbol{\tau}}, \quad (239c)$$

$$\mathbf{R} = \mathbf{L} \cdot \boldsymbol{\phi} + \boldsymbol{\kappa}, \quad \hat{\mathbf{R}} = \mathbf{L} \cdot \hat{\boldsymbol{\phi}} + \hat{\boldsymbol{\kappa}}, \quad (239d)$$

$$\mathbf{e} = \nabla^s \mathbf{u} + \nabla \cdot \boldsymbol{\phi}, \quad \hat{\mathbf{e}} = i\hat{\mathbf{u}} \otimes \mathbf{k} + \hat{\boldsymbol{\phi}} \cdot i\mathbf{k}, \quad (239e)$$

Equation (234) then read, in Fourier space

$$\hat{\mathbf{e}} = -\hat{\Gamma}_{e\tau}^{\infty} : \hat{\boldsymbol{\tau}} - \hat{\Gamma}_{e\kappa}^{\infty} \cdot \hat{\boldsymbol{\kappa}}, \quad \hat{\boldsymbol{\phi}} = -\hat{\Gamma}_{\phi\tau}^{\infty} : \hat{\boldsymbol{\tau}} - \hat{\Gamma}_{\phi\kappa}^{\infty} \cdot \hat{\boldsymbol{\kappa}}. \quad (240)$$

Introducing $\tilde{\boldsymbol{\phi}} = \boldsymbol{\phi} + \mathbf{M} \cdot \boldsymbol{\kappa}$, equation (239c) and (239d) can be rewritten as

$$\boldsymbol{\sigma} = \mathbf{C} : \tilde{\mathbf{e}} + \tilde{\boldsymbol{\tau}}, \quad \mathbf{R} = \mathbf{L} \cdot \tilde{\boldsymbol{\phi}}, \quad (241)$$

where $\tilde{\mathbf{e}}$ and $\tilde{\boldsymbol{\tau}}$ are defined by

$$\tilde{\mathbf{e}} = \mathbf{e} + \nabla \cdot \boldsymbol{\eta}, \quad \tilde{\boldsymbol{\tau}} = \boldsymbol{\tau} - \mathbf{C} : (\nabla \cdot \boldsymbol{\eta}), \quad \boldsymbol{\eta} = \mathbf{M} \cdot \boldsymbol{\kappa}. \quad (242)$$

The set of local fields $\tilde{\mathbf{e}}, \tilde{\boldsymbol{\tau}}, \tilde{\boldsymbol{\phi}}$ define a new auxiliary problem where $\tilde{\boldsymbol{\tau}}$ plays the role of the stress polarization tensor.

$$\nabla \cdot \boldsymbol{\sigma} = \mathbf{0}, \quad (243a)$$

$$\mathbf{R} = \nabla \boldsymbol{\sigma}, \quad (243b)$$

$$\boldsymbol{\sigma} = \mathbf{C} : \tilde{\mathbf{e}} + \tilde{\boldsymbol{\tau}}, \quad (243c)$$

$$\mathbf{R} = \mathbf{L} \cdot \tilde{\boldsymbol{\phi}}, \quad (243d)$$

$$\tilde{\mathbf{e}} = \mathbf{e} + \nabla \cdot \tilde{\boldsymbol{\phi}}. \quad (243e)$$

By definition of the Green operators (see equations (233) and (234)), the solution to equation (243) can be expressed as

$$\hat{\mathbf{e}} = -\hat{\Gamma}_{e\tau}^{\infty} : \hat{\boldsymbol{\tau}}, \quad \hat{\boldsymbol{\phi}} = -\hat{\Gamma}_{\phi\tau}^{\infty} : \hat{\boldsymbol{\tau}}, \quad (244)$$

which can be further rearranged to obtain

$$\hat{\mathbf{e}} = -\hat{\Gamma}_{e\tau}^{\infty} : \hat{\boldsymbol{\tau}} + i\hat{\Gamma}_{e\tau}^{\infty} : [\mathbf{C} : (\hat{\boldsymbol{\eta}} \cdot \mathbf{k})] - i\hat{\boldsymbol{\eta}} \cdot \mathbf{k}, \quad (245a)$$

$$\hat{\boldsymbol{\phi}} = -\hat{\Gamma}_{\phi\tau}^{\infty} : \hat{\boldsymbol{\tau}} + i\hat{\Gamma}_{\phi\tau}^{\infty} : [\mathbf{C} : (\hat{\boldsymbol{\eta}} \cdot \mathbf{k})] - \hat{\boldsymbol{\eta}}. \quad (245b)$$

Combining equation (240) and (244), we find

$$\hat{\Gamma}_{e\kappa}^{\infty} = -\left[(\hat{\Gamma}_{e\tau}^{\infty} : \mathbf{C} - \mathbf{I}) \otimes i\mathbf{k} \right] \cdot \mathbf{M}, \quad (246a)$$

$$\hat{\Gamma}_{\phi\kappa}^{\infty} = -\left[\hat{\Gamma}_{\phi\tau}^{\infty} : (\mathbf{C} \otimes i\mathbf{k}) - \mathbf{I} \right] \cdot \mathbf{M}, \quad (246b)$$

Finally, it can be shown that (see appendix E)

$$\langle \boldsymbol{\tau} : \mathbf{\Gamma}_{e\kappa}^{\infty}[\boldsymbol{\kappa}] \rangle = \langle \boldsymbol{\kappa} \cdot \mathbf{\Gamma}_{\phi\tau}^{\infty}[\boldsymbol{\tau}] \rangle, \quad (247)$$

from which we can derive $\mathbf{\Gamma}_{\phi\tau}^{\infty}$ in terms of $\mathbf{\Gamma}_{e\kappa}^{\infty}$, which in turn can be deduced from $\mathbf{\Gamma}_{e\tau}^{\infty}$ thanks to equation (246a). Equations (246a), (246b) and (247) show that all Green operators can be deduced from the sole operator $\mathbf{\Gamma}_{e\tau}^{\infty}$, which we now set out to evaluate.

8.2.2 Evaluation of $\hat{\Gamma}_{e\tau}^{\infty}$

To compute $\Gamma_{e\tau}^{\infty}$, we plug $\kappa = \mathbf{0}$ in equation (239)

$$\nabla \cdot \boldsymbol{\sigma} = \mathbf{0}, \quad \hat{\boldsymbol{\sigma}} \cdot i\mathbf{k} = \mathbf{0}, \quad (248a)$$

$$\mathbf{R} = \nabla \boldsymbol{\sigma}, \quad \hat{\mathbf{R}} = \hat{\boldsymbol{\sigma}} \otimes i\mathbf{k}, \quad (248b)$$

$$\boldsymbol{\sigma} = \mathbf{C} : \mathbf{e} + \boldsymbol{\tau}, \quad \hat{\boldsymbol{\sigma}} = \mathbf{C} : \hat{\mathbf{e}} + \hat{\boldsymbol{\tau}}, \quad (248c)$$

$$\mathbf{R} = \mathbf{L} \cdot \boldsymbol{\phi}, \quad \hat{\mathbf{R}} = \mathbf{L} \cdot \hat{\boldsymbol{\phi}}, \quad (248d)$$

$$\mathbf{e} = \nabla^s \mathbf{u} + \nabla \cdot \boldsymbol{\phi}, \quad \hat{\mathbf{e}} = i\hat{\mathbf{u}} \otimes \mathbf{k} + \hat{\boldsymbol{\phi}} \cdot i\mathbf{k}. \quad (248e)$$

Substituting equation (248e), (248b) into equation (248c), we find

$$\hat{\boldsymbol{\sigma}} = i(\mathbf{C} \cdot \hat{\mathbf{u}}) \cdot \mathbf{k} - \mathbf{C} : ([\mathbf{M} \cdot (\hat{\boldsymbol{\sigma}} \otimes \mathbf{k})] \cdot \mathbf{k}) + \hat{\boldsymbol{\tau}}, \quad (249)$$

where the generalized compliance tensor is defined in section 6.5.2 (see equation (136))

$$\mathbf{M} = \ell^2 \mathbf{K} \cdot (\mathbf{S} \boxtimes \mathbf{I}) \cdot \mathbf{K}. \quad (250)$$

It follows from equation (249) that

$$\mathbf{M} \cdot (\hat{\boldsymbol{\sigma}} \otimes \mathbf{k}) = \ell^2 \mathbf{K} \cdot [(\mathbf{S} : \hat{\boldsymbol{\sigma}}) \otimes \mathbf{k}] = \ell^2 (\mathbf{S} : \hat{\boldsymbol{\sigma}}) \otimes \mathbf{k} - \frac{\ell^2}{2} \mathbf{I} \cdot [(\mathbf{S} : \hat{\boldsymbol{\sigma}}) \cdot \mathbf{k}], \quad (251)$$

where we used the property $\mathbf{K} = \mathbf{I} - \mathbf{J}$. Plugging equation (251) in equation (249), we have

$$\hat{\boldsymbol{\sigma}} = i(\mathbf{C} \cdot \hat{\mathbf{u}}) \cdot \mathbf{k} - \ell^2 k^2 \hat{\boldsymbol{\sigma}} + \frac{\ell^2}{2} (\mathbf{C} \cdot [(\mathbf{S} : \hat{\boldsymbol{\sigma}}) \cdot \mathbf{k}]) \cdot \mathbf{k} + \hat{\boldsymbol{\tau}}, \quad (252)$$

which can be further rearranged to obtain

$$\hat{\boldsymbol{\sigma}} = \mathbf{X}^{-1} : [i(\mathbf{C} \cdot \hat{\mathbf{u}}) \cdot \mathbf{k} + \hat{\boldsymbol{\tau}}], \quad (253)$$

where we denote $\mathbf{X} = (1 + \ell^2 k^2) \mathbf{I} - \frac{\ell^2}{2} (\mathbf{C} \cdot \mathbf{k}) \cdot (\mathbf{k} \cdot \mathbf{S})$ and $k = \|\mathbf{k}\|$. Combining equation (248a) and equation (253), we find

$$\hat{\mathbf{u}} = i\mathbf{A}^{-1} \cdot (\mathbf{k} \cdot \mathbf{X}^{-1}) : \hat{\boldsymbol{\tau}}, \quad (254)$$

where

$$\mathbf{A} = \mathbf{k} \cdot (\mathbf{X}^{-1} : \mathbf{C}) \cdot \mathbf{k} = \frac{4k^2 \mu (1 - \nu)}{(1 - 2\nu)(2 + k^2 \ell^2)} \mathbf{p} + \frac{4k^2 \mu}{3\ell^2 k^2 + 4} \mathbf{q}, \quad (255)$$

which can be seen as an analogue of the acoustic tensor $\mathbf{k} \cdot \mathbf{C} \cdot \mathbf{k}$ in classical elasticity. It can be verified that this tensor coincides with the classical acoustic tensor for vanishing material internal length $\ell = 0$. Note that the above second-rank projectors \mathbf{p} , \mathbf{q} are respectively defined by

$$\mathbf{p} = \mathbf{n} \otimes \mathbf{n}, \quad \mathbf{q} = \mathbf{I} - \mathbf{n} \otimes \mathbf{n}, \quad (256)$$

where $\mathbf{n} = \mathbf{k}/\|\mathbf{k}\|$.

Once the displacement is determined, the Cauchy deformation $\boldsymbol{\varepsilon}$ is obtained as the symmetric gradient of the displacement. We introduce the auxiliary Green operator $\hat{\mathbf{\Gamma}}_{\varepsilon\tau}^{\infty}$ that maps the stress polarization tensor $\boldsymbol{\tau}$ to the (opposite of the) strain $\boldsymbol{\varepsilon}$

$$\hat{\boldsymbol{\varepsilon}} = \frac{i}{2}(\mathbf{k} \otimes \mathbf{u} + \mathbf{u} \otimes \mathbf{k}) = -\hat{\mathbf{\Gamma}}_{\varepsilon\tau}^{\infty} : \hat{\boldsymbol{\tau}}. \quad (257)$$

Using the compact notation of [Walpole \(1984\)](#) for fourth-rank, transversely isotropic tensors (see appendix F), $\hat{\mathbf{\Gamma}}_{\varepsilon\tau}^{\infty}$ reads

$$\hat{\mathbf{\Gamma}}_{\varepsilon\tau} = \left(\frac{1}{4\mu(1-\nu^2)(1+k^2\ell^2)} \begin{bmatrix} 2(-\nu^2(k^2\ell^2+2) + (1-\nu)(k^2\ell^2+1)) & -\sqrt{2}\nu k^2\ell^2(1-\nu) \\ 0 & 0 \end{bmatrix}, 0, \frac{1}{2\mu} \right). \quad (258)$$

Interestingly, it is seen that the Green operator $\hat{\mathbf{\Gamma}}_{\varepsilon\tau}^{\infty}$ is not symmetric when $\ell \neq 0$. For vanishing material internal length, $\hat{\mathbf{\Gamma}}_{\varepsilon\tau}$ reduces to its counterpart in classical elasticity (which is symmetric) as expected. Substituting expression (254) of the displacement in equation (253), we find

$$\hat{\boldsymbol{\sigma}} = \left(\frac{1}{(1+k^2\ell^2)(1-\nu)} \begin{bmatrix} 0 & 0 \\ -\sqrt{2}\nu & 1-\nu \end{bmatrix}, \frac{1}{\ell^2 k^2 + 1}, 0 \right) : \hat{\boldsymbol{\tau}}, \quad (259)$$

then

$$\hat{\boldsymbol{\phi}} \cdot i\mathbf{k} = -\hat{\mathbf{\Gamma}}_{\nabla\cdot\boldsymbol{\phi},\boldsymbol{\tau}}^{\infty} : \hat{\boldsymbol{\tau}}, \quad (260)$$

where

$$\hat{\mathbf{\Gamma}}_{\nabla\cdot\boldsymbol{\phi},\boldsymbol{\tau}}^{\infty} = \left(\frac{k^2\ell^2}{4\mu(1-\nu^2)(1+k^2\ell^2)} \begin{bmatrix} -2\nu^2 & \sqrt{2}\nu(1-\nu) \\ 2\sqrt{2}\nu(1-\nu) & 2(1-\nu)^2 \end{bmatrix}, \frac{k^2\ell^2}{2\mu(k^2\ell^2+1)}, 0 \right). \quad (261)$$

The above operator $\hat{\mathbf{\Gamma}}_{\nabla\cdot\boldsymbol{\phi},\boldsymbol{\tau}}^{\infty}$ is not symmetric either when $\ell \neq 0$. It vanishes for $\ell = 0$. Gathering the above results, we finally find

$$\hat{\boldsymbol{\varepsilon}} = \hat{\boldsymbol{\varepsilon}} + \hat{\boldsymbol{\phi}} \cdot i\mathbf{k} = (-\hat{\mathbf{\Gamma}}_{\varepsilon\tau}^{\infty} - \hat{\mathbf{\Gamma}}_{\nabla\cdot\boldsymbol{\phi},\boldsymbol{\tau}}^{\infty}) : \hat{\boldsymbol{\tau}} = \hat{\mathbf{\Gamma}}_{\varepsilon\tau}^{\infty} : \hat{\boldsymbol{\tau}},$$

which yields

$$\begin{aligned} \hat{\mathbf{\Gamma}}_{\varepsilon\tau}^{\infty} &= \hat{\mathbf{\Gamma}}_{\varepsilon\tau}^{\infty} + \hat{\mathbf{\Gamma}}_{\nabla\cdot\boldsymbol{\phi},\boldsymbol{\tau}}^{\infty}, \\ &= \left(\frac{1}{2\mu(1-\nu^2)(1+k^2\ell^2)} \begin{bmatrix} (1-\nu)(1+k^2\ell^2) - 2\nu^2 & -\sqrt{2}\nu k^2\ell^2 \\ -\sqrt{2}\nu k^2\ell^2 & k^2\ell^2(1-\nu)^2 \end{bmatrix}, \frac{k^2\ell^2}{2\mu(k^2\ell^2+1)}, \frac{1}{2\mu} \right). \end{aligned} \quad (262)$$

The Green operator $\hat{\mathbf{\Gamma}}_{\varepsilon\tau}^{\infty}$ is symmetric. Furthermore, for vanishing internal length, $\ell \rightarrow 0$, we recover the Green operator for strains in classical elasticity

$$\hat{\mathbf{\Gamma}}^{\infty} = \left(\frac{1}{2\mu(1-\nu)} \begin{bmatrix} 1-2\nu & 0 \\ 0 & 0 \end{bmatrix}, 0, \frac{1}{2\mu} \right). \quad (263)$$

From $\hat{\mathbf{I}}_{e\tau}^\infty$, the remaining Green operators $\hat{\mathbf{I}}_{e\kappa}^\infty$, $\hat{\mathbf{I}}_{\phi\tau}^\infty$, $\hat{\mathbf{I}}_{\phi\kappa}^\infty$ can readily be derived as shown in section 8.2.1.

The Green operators derived above depend on the material internal length ℓ of the reference medium through the dimensionless product $k\ell$ ($k = \|\mathbf{k}\|$), which suggests that the variational principle of Hashin and Shtrikman developed in section 8.1 should lead to size dependent bounds. This will be explored in the next section, where we restore the subscript “0” referring to the reference medium.

8.3 Hashin-Shtrikman bounds

On the basis of the Hashin-Shtrikman variational principle developed in section 8.1, we derive bounds on the effective properties of N -phase isotropic stress-gradient materials. Assuming statistical isotropy, the effective stiffness is an isotropic tensor (i.e. characterized by effective bulk and shear moduli). Following Hashin and Shtrikman (1963), we use phase-wise constant polarization fields

$$\boldsymbol{\tau}(\mathbf{x}) = \sum_{\alpha=1}^N \chi_{\alpha}(\mathbf{x}) \boldsymbol{\tau}_{\alpha}, \quad \boldsymbol{\kappa}(\mathbf{x}) = \sum_{\alpha=1}^N \chi_{\alpha}(\mathbf{x}) \boldsymbol{\kappa}_{\alpha}, \quad (264)$$

where $\chi_{\alpha}(\mathbf{x})$ is the indicator function of phase α and $\boldsymbol{\tau}_{\alpha}, \boldsymbol{\kappa}_{\alpha}$ are constant tensors.

Evaluating the functional \mathcal{H} of Hashin and Shtrikman (see equation (236)) with the above choice of polarization fields then delivers bounds on the effective properties.

8.3.1 Evaluation of the functional of Hashin and Shtrikman for phase-wise constant polarization fields

It can readily be shown that

$$1 = \sum_{\alpha=1}^N f_{\alpha}, \quad \langle \boldsymbol{\tau} \rangle = \sum_{\alpha=1}^N f_{\alpha} \boldsymbol{\tau}_{\alpha}, \quad \langle \boldsymbol{\kappa} \rangle = \sum_{\alpha=1}^N f_{\alpha} \boldsymbol{\kappa}_{\alpha}, \quad (265)$$

where f_{α} denotes the volume fraction of phase α . Evaluation of the first three terms of \mathcal{H} (see equation (236)) is straightforward

$$\bar{\mathbf{e}} : \langle \boldsymbol{\tau} \rangle = \bar{\mathbf{e}} : \sum_{\alpha=1}^N f_{\alpha} \boldsymbol{\tau}_{\alpha}, \quad (266)$$

$$\langle \boldsymbol{\tau} : (\mathbf{C} - \mathbf{C}_0)^{-1} : \boldsymbol{\tau} \rangle = \sum_{\alpha=1}^N f_{\alpha} \boldsymbol{\tau}_{\alpha} : (\mathbf{C}_{\alpha} - \mathbf{C}_0)^{-1} : \boldsymbol{\tau}_{\alpha}, \quad (267)$$

$$\langle \boldsymbol{\kappa} \cdot: (\mathbf{L} - \mathbf{L}_0)^{-1} \cdot: \boldsymbol{\kappa} \rangle = \sum_{\alpha=1}^N f_{\alpha} \boldsymbol{\kappa}_{\alpha} \cdot: (\mathbf{L}_{\alpha} - \mathbf{L}_0)^{-1} \cdot: \boldsymbol{\kappa}_{\alpha}. \quad (268)$$

The terms involving the Green operators for strains are more difficult to evaluate. It should be noted that, the Green operators for a bounded domain Ω are generally unknown. Within the framework of classical elasticity, Willis (1977) heuristically argued that the integral involving the

Green operator Γ_0 over the domain Ω can be approximated by an integral over \mathbb{R}^3 . The Green operator Γ_0 for finite domain is thus replaced by Γ_0^∞ for infinite domain, which has a simple expression in Fourier space due to its translational invariance. More specifically, Willis (1977) applied Γ_0^∞ on the fluctuation part of polarization tensor τ :

$$\langle \tau : \Gamma_0[\tau] \rangle \approx \frac{1}{V} \int_{\mathbf{x}, \mathbf{y} \in \Omega} \tau(\mathbf{x}) : \Gamma_0^\infty(\mathbf{y} - \mathbf{x}) : (\tau(\mathbf{y}) - \langle \tau \rangle) d\mathbf{x} d\mathbf{y}. \quad (269)$$

The Green operator for infinite body Γ_0^∞ is singular at the origin and the integral in equation (269) has to be interpreted in the sense of distributions. The approximation in equation (269) was rigorously justified by Brisard et al. (2013) for Cauchy elasticity. The work of these authors has not yet been extended to stress-gradient elasticity, and we will therefore assume that the approximation (269) of Willis (1977) holds for stress-gradient materials. In other words, the Green operators of finite body Ω will be replaced by their counterparts of the unbounded domain, the explicit expressions of which were found in section 8.2.

Owing to the statistical homogeneity and ergodicity, we have

$$\begin{aligned} \langle \tau : \Gamma_{0,e\tau}^\infty[\tau - \chi\langle \tau \rangle] \rangle &= \mathbb{E}\{\langle \tau : \Gamma_{0,e\tau}^\infty[\tau - \chi\langle \tau \rangle] \rangle\} \\ &= \mathbb{E}\left\{ \frac{1}{V} \int_{\mathbf{x}, \mathbf{y} \in \Omega} \tau(\mathbf{x}) : \Gamma_{0,e\tau}^\infty(\mathbf{y} - \mathbf{x}) : (\tau(\mathbf{y}) - \chi\langle \tau \rangle) d\mathbf{x} d\mathbf{y} \right\} \\ &= \frac{1}{V} \sum_{\alpha, \beta=1}^N \tau_\alpha : \int_{\mathbf{x}, \mathbf{y} \in \Omega} (\mathbb{E}\{\chi_\alpha(\mathbf{x})\chi_\beta(\mathbf{y})\} - f_\alpha f_\beta) \Gamma_{0,e\tau}^\infty(\mathbf{y} - \mathbf{x}) d\mathbf{x} d\mathbf{y} : \tau_\beta \\ &= \frac{1}{V} \sum_{\alpha, \beta=1}^N \tau_\alpha : \int_{\mathbf{x}, \mathbf{y} \in \Omega} (\mathcal{S}_2^{(\alpha\beta)}(\mathbf{y} - \mathbf{x}) - f_\alpha f_\beta) \Gamma_{0,e\tau}^\infty(\mathbf{y} - \mathbf{x}) d\mathbf{x} d\mathbf{y} : \tau_\beta, \end{aligned} \quad (270)$$

where χ is the characteristic function of the domain Ω , $\mathcal{S}_2^{(\alpha\beta)}(\mathbf{y} - \mathbf{x}) = \mathbb{E}\{\chi_\alpha(\mathbf{x})\chi_\beta(\mathbf{y})\}$ denotes the two-point probability function. We deduce that

$$\langle \tau : \Gamma_{0,e\tau}^\infty[\tau - \chi\langle \tau \rangle] \rangle = \frac{1}{V} \sum_{\alpha, \beta=1}^N \tau_\alpha : \int_{\mathbf{r} \in \mathbb{R}^3} (\mathcal{S}_2^{(\alpha\beta)}(r) - f_\alpha f_\beta) \Gamma_{0,e\tau}^\infty(\mathbf{r}) d\mathbf{r} : \tau_\beta = \sum_{\alpha, \beta=1}^N \tau_\alpha : \mathbf{A}_{\alpha\beta}^{e\tau} : \tau_\beta, \quad (271)$$

where we denote

$$\mathbf{A}_{\alpha\beta}^{e\tau} = \frac{1}{V} \int_{\mathbf{r} \in \mathbb{R}^3} (\mathcal{S}_2^{(\alpha\beta)}(r) - f_\alpha f_\beta) \Gamma_{0,e\tau}^\infty(\mathbf{r}) d\mathbf{r}, \quad (272)$$

which is equivalent to the influence tensor $\mathbf{A}_{\alpha\beta}$ introduced by Willis (1977) in classical elasticity. Similarly

$$\langle \tau : \Gamma_{0,e\kappa}^\infty[\kappa] \rangle = \sum_{\alpha, \beta=1}^N \tau_\alpha : \mathbf{A}_{\alpha\beta}^{e\kappa} \cdot \cdot \kappa_\beta, \quad (273)$$

$$\langle \kappa : \Gamma_{0,\phi\tau}^\infty[\tau] \rangle = \sum_{\alpha, \beta=1}^N \kappa_\alpha \cdot \cdot \mathbf{A}_{\alpha\beta}^{\phi\tau} : \tau_\beta, \quad (274)$$

$$\langle \kappa \cdot \cdot \Gamma_{0,\phi\kappa}^\infty[\kappa] \rangle = \sum_{\alpha, \beta=1}^N \kappa_\alpha \cdot \cdot \mathbf{A}_{\alpha\beta}^{\phi\kappa} \cdot \cdot \kappa_\beta. \quad (275)$$

We recall that the Green operators $\Gamma_{0,ek}^\infty(\mathbf{r})$, $\Gamma_{0,\phi\tau}^\infty(\mathbf{r})$ are odd functions of \mathbf{r} (see section (8.2)) while $\mathcal{S}_2^{(\alpha\beta)}(r)$ is an even function of \mathbf{r} . As a consequence, $\mathbf{A}_{\alpha\beta}^{ek} = \mathbf{A}_{\alpha\beta}^{\phi\tau} = \mathbf{0}$.

In classical elasticity, Willis (1977) showed that $\mathbf{A}_{\alpha\beta}$ does not depend on the two-point probability function (in the case of statistical isotropy and isotropic elasticity). This is no longer true of stress-gradient materials, where both $\mathbf{A}_{\alpha\beta}^{e\tau}$ and $\mathbf{A}_{\alpha\beta}^{\phi\kappa}$ depend the two-point probability function.

8.3.2 Optimization of the functional of Hashin and Shtrikman

Gathering the above results, the functional of Hashin and Shtrikman (236) reduces to

$$\begin{aligned} \mathcal{H} = & \frac{1}{2} \bar{\mathbf{e}} : \mathbf{C}_0 : \bar{\mathbf{e}} + \bar{\mathbf{e}} : \sum_{\alpha=1}^N f_\alpha \boldsymbol{\tau}_\alpha \\ & - \frac{1}{2} \sum_{\alpha=1}^N f_\alpha \boldsymbol{\tau}_\alpha : (\mathbf{C}_\alpha - \mathbf{C}_0)^{-1} : \boldsymbol{\tau}_\alpha - \frac{1}{2} \sum_{\alpha=1}^N f_\alpha \boldsymbol{\kappa}_\alpha : (\mathbf{L}_\alpha - \mathbf{L}_0)^{-1} : \boldsymbol{\kappa}_\alpha \\ & - \frac{1}{2} \sum_{\alpha,\beta=1}^N \boldsymbol{\tau}_\alpha : \mathbf{A}_{\alpha\beta}^{e\tau} : \boldsymbol{\tau}_\beta - \frac{1}{2} \sum_{\alpha,\beta=1}^N \boldsymbol{\kappa}_\alpha : \mathbf{A}_{\alpha\beta}^{\phi\kappa} : \boldsymbol{\kappa}_\beta. \end{aligned} \quad (276)$$

To obtain the lower (resp. upper) bound, we have to maximize (resp. minimize) the function \mathcal{H} with respect to $(\boldsymbol{\tau}_1, \dots, \boldsymbol{\tau}_N, \boldsymbol{\kappa}_1, \dots, \boldsymbol{\kappa}_N)$. It is observed that in the above expression of \mathcal{H} , $\boldsymbol{\tau}_\alpha$ and $\boldsymbol{\kappa}_\alpha$ are uncoupled. Optimization is thus carried out independently with respect to these two families of tensors, leading to the following system of equations

$$f_\alpha (\mathbf{C}_\alpha - \mathbf{C}_0)^{-1} : \boldsymbol{\tau}_\alpha + \sum_{\beta=1}^N \mathbf{A}_{\alpha\beta}^{e\tau} : \boldsymbol{\tau}_\beta = f_\alpha \bar{\mathbf{e}}, \quad (277a)$$

$$f_\alpha (\mathbf{L}_\alpha - \mathbf{L}_0)^{-1} : \boldsymbol{\kappa}_\alpha + \sum_{\beta=1}^N \mathbf{A}_{\alpha\beta}^{\phi\kappa} : \boldsymbol{\kappa}_\beta = \mathbf{0}. \quad (277b)$$

Equation (277b) yields $\boldsymbol{\kappa}_\alpha = \mathbf{0}$ for $\alpha = 1, \dots, N$. We finally obtain

- lower bound:

$$\bar{\mathbf{e}} : \mathbf{C}_{\text{eff}} : \bar{\mathbf{e}} \geq \bar{\mathbf{e}} : \mathbf{C}_0 : \bar{\mathbf{e}} + \bar{\mathbf{e}} : \langle \boldsymbol{\tau}^{\text{opt}} \rangle, \quad \text{for } \mathbf{C} \geq \mathbf{C}_0, \mathbf{L} \geq \mathbf{L}_0, \quad (278)$$

- upper bound:

$$\bar{\mathbf{e}} : \mathbf{C}_{\text{eff}} : \bar{\mathbf{e}} \leq \bar{\mathbf{e}} : \mathbf{C}_0 : \bar{\mathbf{e}} + \bar{\mathbf{e}} : \langle \boldsymbol{\tau}^{\text{opt}} \rangle, \quad \text{for } \mathbf{C} \leq \mathbf{C}_0, \mathbf{L} \leq \mathbf{L}_0, \quad (279)$$

where $\boldsymbol{\tau}^{\text{opt}}$ solves (277a).

Under the assumption of statistical isotropy, classical Hashin-Shtrikman bounds depend on the mechanical properties and volume fractions of each constituent only. However, For stress-gradient composites, these bounds depend also on the two-point probability function. In order to go further, we must specify the underlying microstructure (the two-point probability function).

8.3.3 On the choice of the two-point probability function

As previously argued, the two-point probability function must be specified to obtain explicit expressions of the bounds. The present analysis is restricted to two-phase materials, for which (Willis, 1982)

$$\mathcal{S}_2^{(\alpha\beta)}(r) - f_\alpha f_\beta = f_\alpha (\delta_{\alpha\beta} - f_\beta) \mathcal{R}(r), \quad (\text{no sum}) \quad (280)$$

where $\mathcal{R}(r)$ is the two point correlation function. In order to obtain reliable predictions on the effective properties of stress-gradient composites, realistic correlation functions are necessary in our formulation. In practical applications, nanocomposites are often made up of spherical particles embedded in a homogeneous matrix. Therefore, the Verlet and Weis (1972) model is particularly suited to this kind of materials (see section 8.3.3.1). We first consider the correlation function of Debye et al. (1957), which is instructive as it leads to closed-form expressions (see section 8.3.3.2).

8.3.3.1 Debye's correlation function

The correlation function of Debye et al. (1957) describes so-called ‘‘perfect’’ disorder. It is given by the following expression

$$\mathcal{R}_D(r) = \exp\left(-\frac{r}{b}\right), \quad \hat{\mathcal{R}}_D(k) = \frac{8\pi b^3}{(1 + k^2 b^2)^2}, \quad (281)$$

where b is a constant interpreted as a correlation length. To the best of our knowledge, \mathcal{R}_D is not realizable (in the sense that the authors do not produce microstructure that realize this correlation function). Evaluation of the general bounds of section 8.3.2 delivers the explicit expressions

- lower bound: for $\mathbf{C} > \mathbf{C}_0, \mathbf{L} > \mathbf{L}_0$

$$\mathbf{C}_{\text{eff}} \geq \mathbf{C}_{\text{lower}}^{\text{HS}} = \left\{ \sum_{\alpha=1}^2 f_\alpha \mathbf{C}_\alpha : [\mathbf{I} + \mathbf{P} : (\mathbf{C}_\alpha - \mathbf{C}_0)]^{-1} \right\} : \left\{ \sum_{\beta=1}^2 f_\beta [\mathbf{I} + \mathbf{P} : (\mathbf{C}_\beta - \mathbf{C}_0)] \right\}^{-1}, \quad (282)$$

- upper bound: for $\mathbf{C} < \mathbf{C}_0, \mathbf{L} < \mathbf{L}_0$

$$\mathbf{C}_{\text{eff}} \leq \mathbf{C}_{\text{upper}}^{\text{HS}} = \left\{ \sum_{\alpha=1}^2 f_\alpha \mathbf{C}_\alpha : [\mathbf{I} + \mathbf{P} : (\mathbf{C}_\alpha - \mathbf{C}_0)]^{-1} \right\} : \left\{ \sum_{\beta=1}^2 f_\beta [\mathbf{I} + \mathbf{P} : (\mathbf{C}_\beta - \mathbf{C}_0)] \right\}^{-1}, \quad (283)$$

where \mathbf{P} is the following isotropic, fourth-rank tensor (which is derived in appendix G)

$$\mathbf{P} = 3p\mathbf{J} + 2q\mathbf{K}, \quad (284)$$

with

$$p = \frac{(1 - 2\nu_0)(1 + \nu_0 + 3h(2 + h)(1 - \nu_0))}{18\mu_0(1 - \nu_0^2)(1 + h)^2}, \quad q = \frac{8 - 10\nu_0 + 15h(2 + h)(1 - \nu_0)}{60\mu_0(1 - \nu_0)(1 + h)^2}, \quad (285)$$

in which we denoted $h = \ell_0/b$. For vanishing material internal length $\ell_0 \rightarrow 0$, this tensor reduces to the classical Hill tensor of a spherical inclusion embedded in a Cauchy reference medium with stiffness \mathbf{C}_0 . It is observed that, although the classical Hill tensor depends on the properties of the reference material and the *shape* of the inclusion only, \mathbf{P} also depends on the correlation length b and the material internal length ℓ_0 .

If the reference medium is chosen such that

$$\kappa_0 \leq \min(\kappa_1, \kappa_2), \quad \mu_0 \leq \min(\mu_1, \mu_2), \quad \frac{\mu_0}{\ell_0^2} \leq \min\left(\frac{\mu_1}{\ell_1^2}, \frac{\mu_2}{\ell_2^2}\right), \quad (286)$$

$$\frac{4(3\kappa_0 - 2\mu_0)\mu_0}{(3\kappa_0 + 10\mu_0)\ell_0^2} \leq \min\left(\frac{4(3\kappa_1 - 2\mu_1)\mu_1}{(3\kappa_1 + 10\mu_1)\ell_1^2}, \frac{4(3\kappa_2 - 2\mu_2)\mu_2}{(3\kappa_2 + 10\mu_2)\ell_2^2}\right), \quad (287)$$

we then obtain the Hashin-Shtrikman lower bound. The inequality in equation (282) reduces to

$$\kappa_{\text{eff}} \geq \frac{(1-f)\kappa_1[p(\kappa_0 - \kappa_2) - 1] + f\kappa_2[p(\kappa_0 - \kappa_1) - 1]}{(1-f)[p(\kappa_0 - \kappa_2) - 1] + f[p(\kappa_0 - \kappa_1) - 1]}, \quad (288a)$$

$$\mu_{\text{eff}} \geq \frac{(1-f)\mu_1[q(\mu_0 - \mu_2) - 1] + f\mu_2[q(\mu_0 - \mu_1) - 1]}{(1-f)[q(\mu_0 - \mu_2) - 1] + f[q(\mu_0 - \mu_1) - 1]}, \quad (288b)$$

where p and q are the components of tensor \mathbf{P} . If the reference medium is chosen to be stiffer than all phases, the Hashin-Shtrikman upper bound is obtained (inequalities (288) are reversed).

When $\ell_0 \rightarrow 0$ (b being fixed), the classical Hashin-Shtrikman bounds are retrieved regardless of the correlation length (and the material internal lengths of the composite). Conversely, for $b \rightarrow 0$ (ℓ_0 being fixed) (the medium Ω is nearly uncorrelated), the above bounds reduce to the classical Reuss bounds. This was not unexpected, since this case is formally equivalent to $\ell_0 \rightarrow \infty$ (b being fixed), which was discussed at the end of section 6.5.

8.3.3.2 The model of Verlet and Weis

An important statistical characterization of nanocomposites made up by non overlapping spherical inclusion is the radial distribution function $g(r)$ (Torquato, 2002). It shows how the number density varies as a function of distance from a fixed particle. Markov and Willis (1998) showed that the two-point correlation function $\mathcal{R}(r)$ of a random dispersion of non overlapping spheres can be expressed as a sum of a *well-stirred* part $\mathcal{R}^{\text{ws}}(r)$ (see also Torquato and Stell (1985)) and a correction term $\mathcal{R}^*(r)$ which involves the radial distribution function $g(r)$

$$\mathcal{R}(r) = \mathcal{R}^{\text{ws}}(r) + \mathcal{R}^*(r), \quad (289)$$

where $\mathcal{R}^*(r)$ can be neglected for $f \leq 12.5\%$. The expressions of $\mathcal{R}^{\text{ws}}(r)$ and $\mathcal{R}^*(r)$, expressed in terms of $\rho = r/a$, are reported here for convenience

$$\mathcal{R}^{\text{ws}}(\rho) = \begin{cases} \frac{1}{1-f} \left[(1-f) - \frac{3\rho}{4} + \frac{(1+3f)\rho^3}{16} - \frac{9f\rho^4}{160} + \frac{f\rho^6}{2240} \right], & 0 \leq \rho \leq 2 \\ \frac{f}{1-f} \frac{(\rho-4)^4(36-34\rho-16\rho^2-\rho^3)}{2240\rho}, & 2 \leq \rho \leq 4 \\ 0, & 4 \leq \rho \end{cases} \quad (290)$$

and

$$\mathcal{R}^*(\rho) = \begin{cases} \frac{f}{1-f} \int_{\rho}^{\rho+2} F(\rho, \eta)[g(\eta) - 1] d\eta, & 0 \leq \rho \leq 2 \\ \frac{f}{1-f} \left[\int_2^{\rho} F(-\rho, -\eta)[g(\eta) - 1] d\eta + \int_{\rho}^{\rho+2} F(\rho, \eta)[g(\eta) - 1] d\eta \right], & 2 \leq \rho \leq 4 \\ \frac{f}{1-f} \left[\int_{\rho-2}^{\rho} F(-\rho, -\eta)[g(\eta) - 1] d\eta + \int_{\rho}^{\rho+2} F(\rho, \eta)[g(\eta) - 1] d\eta \right], & 4 \leq \rho \end{cases} \quad (291)$$

in which the function $F(\rho, \eta)$ is defined by

$$F(\rho, \eta) = \frac{3\eta(2 + \rho - \eta)^3[4 - 6(\rho - \eta) + (\rho - \eta)^2]}{160\rho}. \quad (292)$$

We recall that, in order to derive Hashin-Shtrikman bounds, we need to evaluate the Fourier transform of the correlation function

$$\hat{\mathcal{R}}(k) = \int_{\mathbb{R}^3} \mathcal{R}(\mathbf{r}) \exp(-i\mathbf{k} \cdot \mathbf{x}) d\mathbf{x} = \frac{4\pi a^2}{k} \int_0^{\infty} \mathcal{R}(\rho) \rho \sin(ak\rho) d\rho. \quad (293)$$

From equation (293) and equation (289), we have

$$\hat{\mathcal{R}}(k) = \frac{4\pi a^2}{k} \int_0^{\infty} [\mathcal{R}^{\text{ws}}(\rho) + \mathcal{R}^*(\rho)] \rho \sin(ak\rho) d\rho. \quad (294)$$

By using equation (291), the calculation of $\int_0^{\infty} \mathcal{R}^{\text{ws}}(\rho) \rho \sin(ak\rho) d\rho$ is straightforward and can be given in closed-form. Upon interchanging the order of integration, the calculation of $\int_0^{\infty} \mathcal{R}^*(\rho) \rho \sin(ak\rho) d\rho$ leads to

$$\begin{aligned} & \int_0^{\infty} \mathcal{R}^*(\rho) \rho \sin(ak\rho) d\rho \\ &= \frac{f}{1-f} \int_2^{\infty} \left[\int_{\eta-2}^{\eta} F(\rho, \eta) \rho \sin(ak\rho) d\rho + \int_{\eta}^{\eta+2} F(-\rho, -\eta) \rho \sin(ak\rho) d\rho \right] [g(\eta) - 1] d\eta \\ &= \frac{9f}{1-f} \frac{(\cos(ak)ak - \sin(ak))^2}{a^6 k^6} \int_2^{\infty} \eta \sin(ak\eta) [g(\eta) - 1] d\eta. \end{aligned} \quad (295)$$

If the radial distribution function is given, we can compute $\hat{\mathcal{R}}(k)$ which is needed to the evaluation of Hashin-Shtrikman bounds. For low densities of non overlapping, mono-sized sphere, the most well-known statistical model is the [Percus and Yevick \(1958\)](#) model (later solved exactly by [Wertheim \(1963\)](#), see also [Lebowitz \(1964\)](#) for a mixture of spheres). The Percus-Yevick model is shown to be in very good agreement with numerical computations ([Alder and Wainwright, 1960](#)) for low densities of spheres. The closed form solution of [Wertheim \(1963\)](#) can be written as (see also [Drugan and Willis \(1996\)](#); [Monetto and Drugan \(2004\)](#))

$$\begin{cases} g_{\text{PY}}(\rho, f) = 0 \text{ for } 0 \leq \rho \leq 2, \\ \int_0^{\infty} \rho [g_{\text{PY}}(\rho, f) - 1] \exp(-s\rho) d\rho = \frac{2sL(2s)}{3f[L(2s) + M(2s) \exp(2s)]} - \frac{1}{s^2}, \end{cases} \quad (296)$$

where the function $L(s)$ and $M(s)$ are defined by

$$L(s) = 12f \left[\left(1 + \frac{f}{2} \right) s + 1 + 2f \right], \quad (297)$$

$$M(s) = (1 - f)^2 s^3 + 6f(1 - f)s^2 + 18f^2 s - 12f(1 + 2f) \quad (298)$$

It should be noted however that this model does not give good predictions at high densities of spheres. To overcome this shortcoming, [Verlet and Weis \(1972\)](#) introduced an empirical correction to the model of [Percus and Yevick \(1958\)](#), which greatly improves the accuracy of the radial distribution function at very high densities of spheres. The radial distribution function of [Verlet and Weis \(1972\)](#) can be written as ([Monetto and Drugan, 2004](#))

$$g_{\text{vw}}(\rho, f) = g_{\text{PY}}(\rho/\phi, f') + \delta(\rho) \text{ for } \rho \geq 2, \quad (299)$$

where $f' = f - \frac{1}{16}f^2$, $\phi = (f'/f)^{1/3}$ and

$$\delta(\rho) = \frac{\alpha}{\rho} \exp[\beta(2 - \rho)] \cos[\beta(2 - \rho)]. \quad (300)$$

In the above expressions, g_{PY} denotes the radial distribution function of [Percus and Yevick \(1958\)](#) (see equation (296)) and

$$\alpha = \frac{3}{2} \frac{f'^2(1 - 0.7117f' - 0.114f'^2)}{(1 - f')^4}, \quad \beta = 12\alpha \frac{(1 - f')^2}{f'(2 + f')}. \quad (301)$$

In the following, we will evaluate the Hashin-Shtrikmand bounds for the radial distribution function of [Verlet and Weis \(1972\)](#). Since $g(r) = 0$ for $r < 2a$, the last term of equation (295) can be rewritten as

$$\int_2^\infty \eta \sin(ak\eta)[g(\eta) - 1] d\eta = \int_0^\infty \eta \sin(ak\eta)[g(\eta) - 1] d\eta + \int_0^2 \eta \sin(ak\eta) d\eta. \quad (302)$$

Upon substituting equation (299), we find

$$\begin{aligned} & \int_2^\infty \eta \sin(ak\eta)[g(\eta) - 1] d\eta \\ &= \phi^2 \int_0^\infty \eta \sin(ak\phi\eta)[g_{\text{PY}}(\eta, f') - 1] d\eta + \int_2^\infty \eta \sin(ak\eta)\delta(\eta) d\eta + \int_0^2 \eta \sin(ak\eta) d\eta. \end{aligned} \quad (303)$$

By employing the identity

$$\sin(s\eta) = \frac{1}{2i} [\exp(is\eta) - \exp(-is\eta)], \quad (304)$$

and using equation (296), we find

$$2i \int_0^\infty \eta \sin(ak\phi\eta)[g_{\text{PY}}(\eta, f') - 1] d\eta \quad (305)$$

$$= \lim_{s \rightarrow -iak\phi} \int_0^\infty \eta [g_{\text{PY}}(\eta, f') - 1] \exp(-s\eta) d\eta - \lim_{s \rightarrow iak\phi} \int_0^\infty \eta [g_{\text{PY}}(\eta, f') - 1] \exp(-s\eta) d\eta, \quad (306)$$

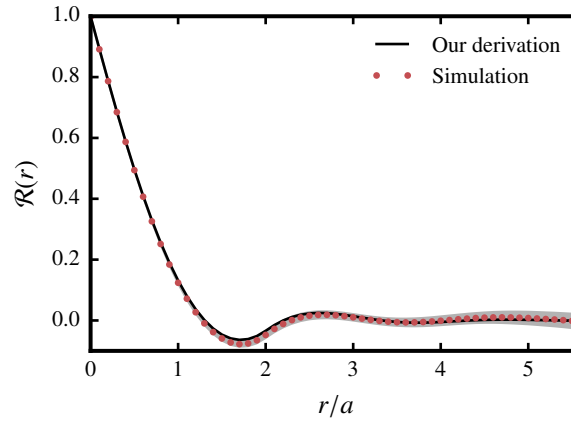


Figure 8.1. The two point correlation function $\mathcal{R}(r)$ plotted as a function of (normalized) radial distance, r/a . This function is evaluated from Monte-Carlo simulations of assemblies of hard spheres (red dots), and compared to a direct computation by means of the model of [Verlet and Weis \(1972\)](#). The gray zone represents the 99% confidence interval.

so that equation (294) can be explicitly evaluated. However, the expression is too long to be reported here (see section 8.3.3.3 for a numerical evaluation of the bounds).

To close this section, we demonstrate that the model of [Verlet and Weis \(1972\)](#) indeed delivers an excellent approximation of the correlation function, even at high volume fractions of spherical inclusions. To do so, we used a standard Monte-Carlo simulation ([Allen and Tildesley, 1987](#)) to generate assemblies of monodisperse hard-spheres. The two point correlation function, $\mathcal{R}(r)$ was then sampled.

Figure 8.1 compares the two point correlation function $\mathcal{R}(r)$ thus obtained (with 300 realizations of assemblies of 4000 spheres) to that of [Verlet and Weis \(1972\)](#). The volume fraction of particles was 30%. Both approaches are found to be in excellent agreement, which demonstrates the robustness of the model of [Verlet and Weis \(1972\)](#).

8.3.3.3 Discussions

In this section, we present numerical illustrations of the Hashin-Shtrikman bounds obtained within the frame of the model of Verlet and Weis. We consider successively the case of stiff inhomogeneities and soft inhomogeneities in which the material internal lengths of matrix and inclusions are equal

$$\mu_i = 10\mu_m, \quad \nu_i = \nu_m = 0.125, \quad \ell_i = \ell_m = 0.2a, \quad (307)$$

and

$$\mu_i = 0.1\mu_m, \quad \nu_i = \nu_m = 0.125, \quad \ell_i = \ell_m = 0.2a. \quad (308)$$

Figure 8.2 plots the bounds on the effective bulk (left) and shear (right) moduli as a function of the volume fraction of inclusions in the case of stiff inhomogeneities. The reference medium is chosen to be the matrix (lower bound) or the inclusion (upper bound). Interestingly, it is observed that the Mori-Tanaka estimate does not coincide with the Hashin-Shtrikman lower bound. It is at odds with classical Cauchy materials, for which the Mori-Tanaka estimate yields the Hashin-Shtrikman lower (resp. upper) bound for stiff (resp. soft) spherical inclusions.

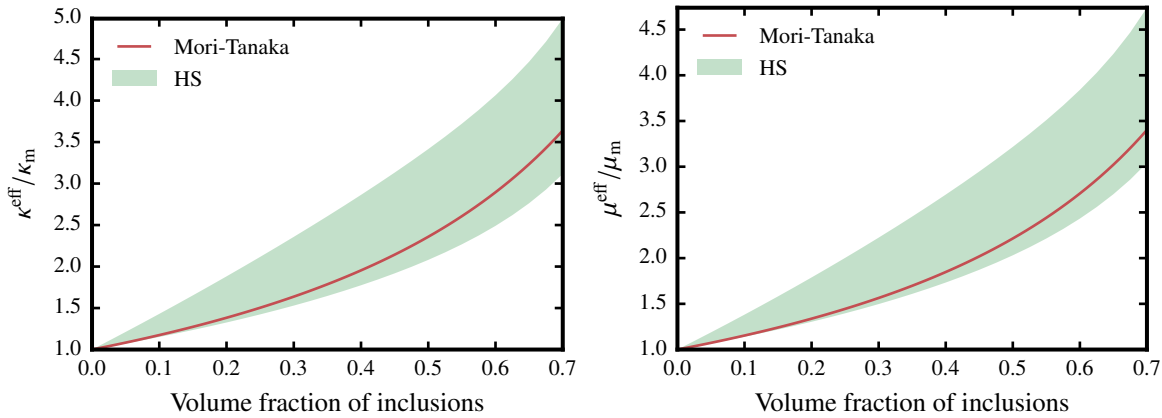


Figure 8.2. Stiff inhomogeneity case: Hashin-Shtrikman bounds derived by using the Verlet-Weis model on the effective bulk (left) and shear (right) moduli. $\mu_i = 10\mu_m$, $\nu_i = \nu_m = 0.125$, $\ell_i = \ell_m = 0.2a$.

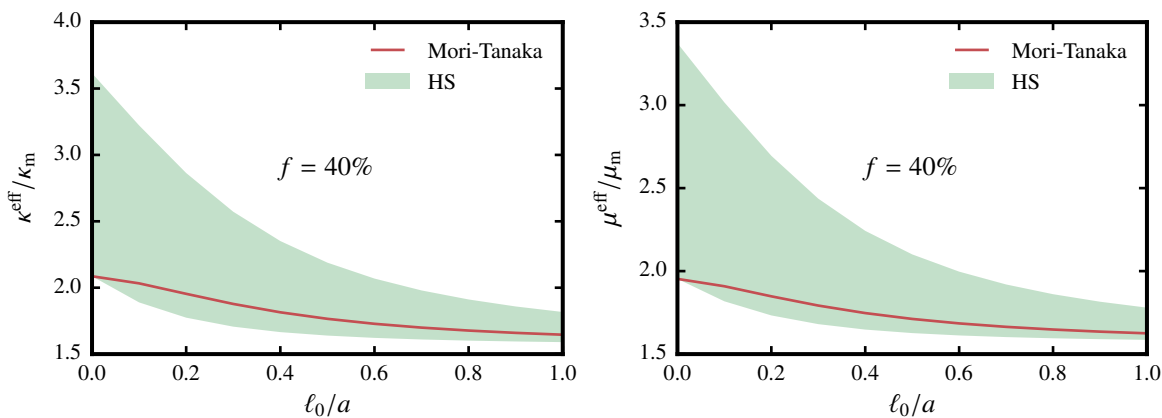


Figure 8.3. Stiff inhomogeneity case: Hashin-Shtrikman bounds derived by using the Verlet-Weis model on the effective bulk (left) and shear (right) moduli. $\mu_i = 10\mu_m$, $\nu_i = \nu_m = 0.125$. The volume fraction is fixed at 40%.

Figure 8.3 plots the bounds at a fixed volume fraction $f = 40\%$ for various values of the material internal length. It is observed that the Mori-Tanaka estimate only coincides with the Hashin-Shtrikman lower bound for $\ell/a \rightarrow 0$ (classical elasticity case).

It should be noted that the Mori-Tanaka estimation is based on the solution to Eshelby's spherical inhomogeneity problem (see section 7.3). In fact, it does not account for the interaction between inclusions. As a consequence, for high densities of spheres, Mori-Tanaka estimate fails to deliver reliable results. This is better illustrated in figure 8.4 (the case of soft inhomogeneity) where the Mori-Tanaka estimate falls outside Hashin-Shtrikman bounds for volume fractions larger than 30%. Note that the reference medium is chosen to be the inclusion (lower bound) or the matrix (upper bound). Figure 8.5 plots the bounds at a fixed volume fraction $f = 40\%$ for various values of material internal length. Similarly to the stiff case, it is observed that the Mori-Tanaka estimate only coincides with the Hashin-Shtrikman upper bound for $\ell/a \rightarrow 0$ (classical elasticity case).

To close this section, we discuss the sensitivity of the Hashin-Shtrikman bounds to the microstructure. It is recalled that for stress-gradient materials, the bounds are found to depend on the microstructure through the correlation function. This is at odds with the same bounds for

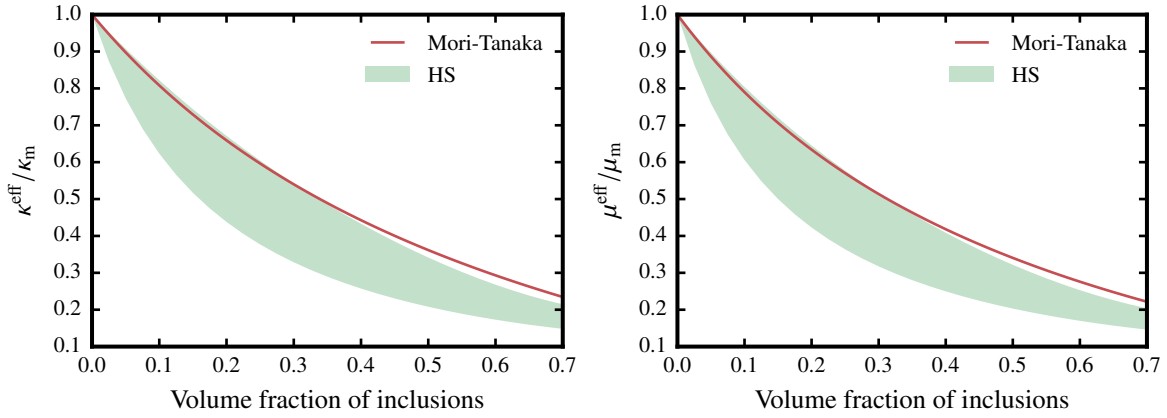


Figure 8.4. Soft inhomogeneity case: Hashin-Shtrikman bounds derived by using the Verlet-Weiss model on the effective bulk (left) and shear (right) moduli. $\mu_i = 0.1\mu_m, \nu_i = \nu_m = 0.125, \ell_i = \ell_m = 0.2a$.

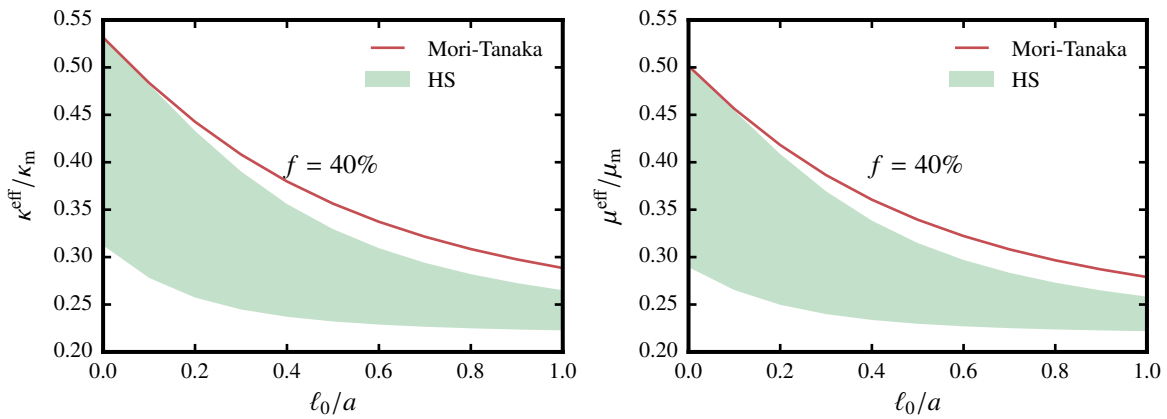


Figure 8.5. Soft inhomogeneity case: Hashin-Shtrikman bounds derived by using the Verlet-Weiss model on the effective bulk (left) and shear (right) moduli. $\mu_i = 0.1\mu_m, \nu_i = \nu_m = 0.125$. The volume fraction is fixed at 40%.

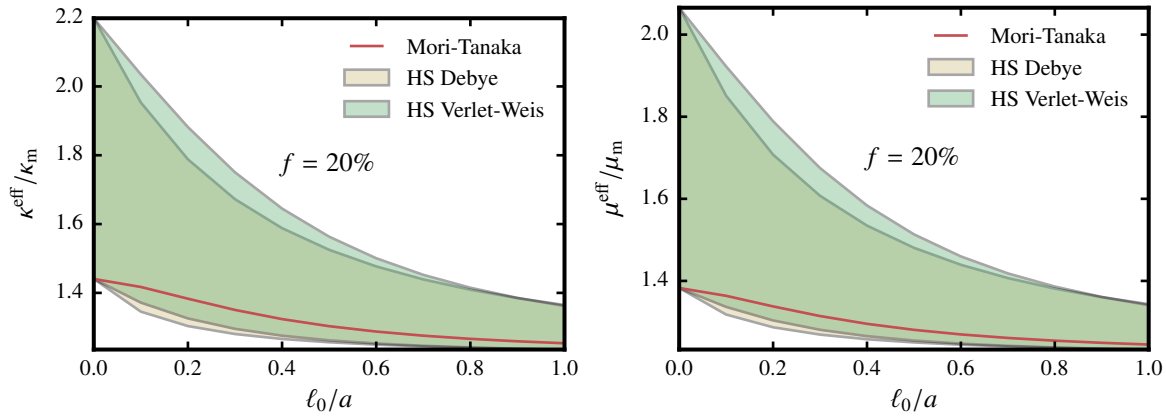


Figure 8.6. Hashin-Shtrikman bounds derived by Verlet-Weis model (green) and Debye model (yellow) on the effective bulk (left) and shear modulus (right) as a function of ℓ/a . The volume fraction is fixed at $f = 20\%$. The mechanical properties of materials $\mu_i = 10\mu_m$, $\nu_i = \nu_m = 0.125$.

classical (Cauchy) materials, for which the correlation function vanishes (in the isotropic case).

In order to quantify this dependency, it is interesting to compare the bounds obtained with the correlation function of [Verlet and Weis \(1972\)](#) with those obtained with the correlation function of [Debye et al. \(1957\)](#) (material parameters and volume fractions being identical in both cases). In order to allow for a relevant comparison, we need to relate the correlation length b in the model of [Debye et al. \(1957\)](#) to the radius a of the particles in the model of [Verlet and Weis \(1972\)](#). We chose the following identification

$$b = \int_0^\infty \mathcal{R}_D(r) dr = \int_0^\infty \mathcal{R}_{VW}(r) dr. \quad (309)$$

We found $b = 0.578a$ for $f = 20\%$ and $b = 0.478a$ for $f = 40\%$. These values of the correlation length b are then plugged in equation (288) to derive the Hashin-Shtrikman bounds.

The Hashin-Shtrikman bounds derived by Verlet-Weis model (green zone) and Debye model (yellow) are plotted as a function of material internal length of the reference medium for two volume fractions, $f = 20\%$ (figure 8.6) and $f = 40\%$ (figure 8.7). In both cases, the material properties were $\mu_i = 10\mu_m$, $\nu_i = \nu_m = 0.125$ and $\ell_i = \ell_m$. In the same plot, we present the Mori-Tanaka estimate produced in section 7.3. As expected, both families of bounds coincide for $\ell_0 \rightarrow 0$.

More interestingly, we observe no significant difference between the bounds produced by the models of [Verlet and Weis \(1972\)](#) and [Debye et al. \(1957\)](#) for a wide range of material internal lengths. This result suggests that although the Hashin-Shtrikman bounds for stress-gradient composites depend on the underlying microstructure (unlike classical Cauchy materials), this dependency is rather weak.

In this chapter, we established the variational principle of Hashin-Shtrikman for stress-gradient composites. The derivation followed the general variational framework developed by [Willis \(1983\)](#); [Talbot and Willis \(1985\)](#); [Willis \(1991\)](#) for non-linear Cauchy materials. In turn, Hashin-Shtrikman bounds were derived by using phase-wise constant trial fields. An interesting (but expected) result is that the bounds depend on the two-point probability function, which is not the case in classical elasticity.

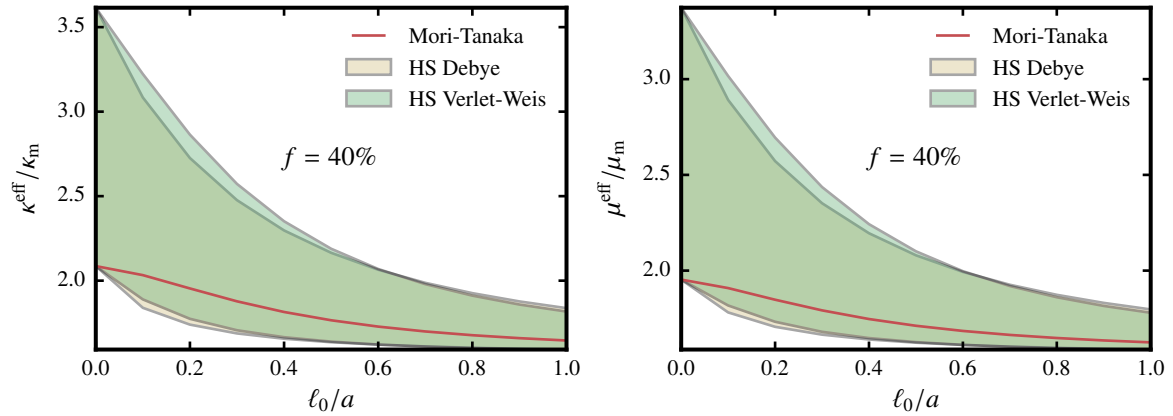


Figure 8.7. Hashin-Shtrikman bounds derived by Verlet-Weis model (green) and Debye model (yellow) on the effective bulk (left) and shear modulus (right) as a function of ℓ/a . The volume fraction is fixed at $f = 40\%$. The mechanical properties of materials $\mu_i = 10\mu_m$, $\nu_i = \nu_m = 0.125$.

The general bounds were then evaluated for two-phase stress-gradient composites. This required to specify the two-point probability function. We used successively the [Debye et al. \(1957\)](#) and [Verlet and Weis \(1972\)](#) models. The latter corresponds to an assembly of mono-sized hard sphere particles and remains accurate at relatively high densities. Quite remarkably, the Mori–Tanaka estimate derived in chapter 7 falls outside the Hashin–Shtrikman bounds for soft inhomogeneities, even at moderate volume fractions. This result is in disagreement with isotropic Cauchy materials where the Mori–Tanaka estimate coincides with the lower (stiff inhomogeneity) or upper bounds (soft inhomogeneity) (under the assumption of statistical isotropy).

As already mentioned, the Hashin–Shtrikman bounds depend explicitly on the two-point probability function. This chapter closes with a study on the sensitivity of these bounds to the two-point probability function. For fixed correlation length and identical mechanical material properties, we observed no significant difference between the bounds produced by the models of [Debye et al. \(1957\)](#) and [Verlet and Weis \(1972\)](#). This result is consistent with classical Cauchy elasticity (where no dependence at all is observed).

Chapter 9

Conclusions & Perspectives

Nanocomposites are widely used engineering materials. As such, the estimation of their macroscopic mechanical properties is of great concern. To this end, generalized continua are attractive material models which are able to reproduce (at least qualitatively) some tendencies (e.g. size-effects). With this goal in mind, the stress-gradient model introduced by [Forest and Sab \(2012\)](#) (see also [Sab et al., 2016](#)) was investigated in the second part of this thesis. Due to the existence of at least one material internal length, the homogenization of stress-gradient model results in macroscopically homogeneous materials exhibiting size-effects.

In chapter 6, the derivation of the stress-gradient model was first revisited by minimizing the complementary strain energy. We showed that the equilibrium equations require the stress-gradient to be work-conjugate to a trace-free generalized strain variable (the trace of the stress-gradient being constrained). We also stated and discussed the essential boundary conditions; unlike Cauchy mechanics, the *full* stress tensor (rather than the traction vector) is prescribed at the boundary. We then extended the classical (potential, complementary) energy principles to stress-gradient bodies. Drawing inspiration from the work of [Aifantis \(1992\)](#) and [Gao and Park \(2007\)](#), we proposed a simplified model of stress-gradient, linear elasticity. It requires only one (rather than three in the general, isotropic case) material internal length. We further showed that this model induces boundary layers near the free-surface of a rectangular beam undergoing pure bending. Interestingly, the normalized bending stiffness of the beam decreases as the beam thickness decreases (the material internal length being fixed): this is an example of *softening* size-effect. While this result is not relevant for most nano-beams where the *stiffening* size-effect is generally observed experimentally, atomistic simulation suggests that some nano silicon beam might exhibit softening size-effect. For such materials, the strain-gradient model is inadequate, while the stress-gradient model has the required qualitative behavior.

In chapter 7, a framework based on a (generalized) Hill–Mandel lemma for the homogenization of stress gradient composites was then established. In which we assumed that the material internal length is comparable or much smaller than the typical size of the heterogeneities. In this case, the stress-gradient material is homogenized as a macroscopically homogeneous Cauchy material. We derived boundary conditions (kinematic uniform, static uniform, periodic and mixed boundary conditions) that are suitable to the computation of the apparent compliance of linearly elastic materials. Remarkably, we concluded that stress-gradient materials exhibit a softening size-effect in the effective properties. More precisely, a decrease of the size of the heterogeneities (the material internal length being kept constant) induces a decrease of the

macroscopic stiffness. This result shows that, although conceptually similar, stress-gradient materials are not equivalent to strain-gradient materials (which predict the opposite, stiffening size-effect). Based on the solution to Eshelby's spherical inhomogeneity problem, which was derived for isotropic and uniaxial loading, we produced Mori–Tanaka estimates of the effective properties of stress-gradient composites with spherical inclusions.

In chapter 8, Hashin–Shtrikman variational principle for stress-gradient materials were then derived. Upon substituting phase-wise constant trial fields, we found the Hashin–Shtrikman bounds for stress-gradient composites. This requires the Green operators of an infinite stress-gradient body that we then obtained explicitly. As expected, the bounds depend on the two-point probability function. This is at odds with isotropic Cauchy materials where this function vanishes (under the assumption of statistical isotropy). We then obtained explicitly expressions of bounds for Debye et al. (1957) and Verlet and Weis (1972) model. Remarkably, the Mori–Tanaka estimate previously obtained falls outside the bounds for moderate volume fractions ($> 30\%$). This result is at odds with classical elasticity where the Mori–Tanaka estimate coincides with the lower (stiff inhomogeneity) or the upper (soft inhomogeneity) bounds. This results underlines the fact that the Mori–Tanaka estimate does not account for the interaction between inclusions. Furthermore, we also addressed the sensitivity of the obtained bounds to the two-point probability function (the correlation length being fixed). It was shown that this sensitivity is weak for the case under consideration.

The work presented in the second part of this thesis can be extended or improved in several directions. Firstly, more advanced homogenization techniques such as full field simulations can be invoked to account for fine-scale microstructure features. In this case, the Lippmann–Schwinger formalism based on the closed-form expression of the Green operators derived in section 8.2 (see also appendix D) can be adopted in a FFT based framework (Moulinec and Suquet, 1994, 1998) for stress-gradient materials (it should be observed that in Fourier space, the Green operators of periodic and unbounded bodies coincide). It should be noted however that Lippmann–Schwinger solvers for stress-gradient elasticity are much more costly than their classical elasticity counterparts (the number of unknowns per cell is much higher and evaluation of the Green operator is more costly).

Secondly, the closed-form solution to Eshelby's problem for other kind of inclusion shapes (ellipsoidal, polygonal, etc) is of great interest. This solution would help to explore the effect of various geometrical parameters (e.g. aspect ratio of ellipsoidal inclusion) on the effective properties of stress-gradient composites. However, the solution to the inhomogeneity problem might not be analytically tractable.

Thirdly, the Hashin–Shtrikman bounds derived in chapter 8 can be further improved by using enriched (non uniform) trial fields. This is expected to produce sharper bounds. Furthermore, the Hashin–Shtrikman bounds were derived under the assumption that the Green operators of a finite body can be replaced by their counterparts of an infinite body. Its rigorous justification remains an open question for both stress- and strain- gradient materials. Other kinds of bounds could also be considered. For instance, the security-sphere bounds (Keller et al., 1967) which remain finite at infinite mechanical contrast. In this case, the solution to Eshelby's spherical inhomogeneity embedded in a *finite* matrix can be employed as trial fields in the minimum (complementary, potential) energy principle.

Finally, although the work presented above is restricted to linear elasticity, it probably

proposes basic building blocks for the extension to nonlinear mechanical behaviors.

Part IV

Closing remark

In this work, we have investigated the computation of the macroscopic mechanical properties of heterogeneous materials. Depending on the characteristic length(s) considered, the material model was described, at the microscale, by Cauchy or generalized continua. Under the scale separation condition, homogenization of such materials leads to a macroscopic homogeneous Cauchy medium.

In the first part, a Cauchy medium was considered at the microscale, and homogenization of random microstructures was numerically performed over a large number of realizations. In order to alleviate the associated computational cost, we proposed a homogenization approach relying on a mesoscopic description of the random materials (within a filtering framework). In particular, we presented the construction, identification and validation of a random field model representing the elasticity tensor at the mesoscopic scale. It was shown that the random field model parameters can be successfully identified from a limited number of realizations (using the maximum likelihood method). The model is further shown to deliver accurate results on the ensemble average apparent properties. The proposed methodology is general and was illustrated on a prototypical microstructure.

In the second part, the homogenization of stress-gradient composites was discussed, and a general framework for the homogenization of such materials was notably established. As a very first step towards the full field homogenization of such materials, a mean field approach was adopted. It was shown that the stress- and strain-gradient models define complementary behaviors. In particular, the stress-gradient model describes a class of materials that exhibit a softening size-effect. In addition, Mori-Tanaka estimate and Hashin-Shtrikman bounds for stress-gradient composites were then derived. Interestingly, the Hashin-Shtrikman bounds depend on the microstructure as expected, this dependency is weak (in terms of effective properties).

The work presented in this thesis was concerned with linear elastic materials. It may pave the way to extensions to nonlinear mechanical behaviors.

Part V
Appendix

Appendix A

Numerical resolution of the auxiliary problem

This part gives a brief introduction about FFT based methods to numerically resolve the auxiliary problem defined by equations (5) and (18). It relies on the discretization of the so-called Lippmann–Schwinger equation. For a homogeneous reference material with stiffness \mathbf{C}_0 , we introduce the stress polarization tensor $\boldsymbol{\tau}(\mathbf{x})$ as

$$\boldsymbol{\tau}(\mathbf{x}) := (\mathbf{C}(\mathbf{x}) - \mathbf{C}_0) : \boldsymbol{\varepsilon}(\mathbf{x}). \quad (310)$$

The corrector problem defined by equation (5) can be rewritten as

$$\nabla \cdot \boldsymbol{\sigma} = \mathbf{0}, \quad (311a)$$

$$\boldsymbol{\sigma}(\mathbf{x}) = \mathbf{C}_0 : \boldsymbol{\varepsilon}(\mathbf{x}) + \boldsymbol{\tau}(\mathbf{x}), \quad (311b)$$

$$\boldsymbol{\varepsilon}(\mathbf{x}) = \nabla^s \mathbf{u}, \quad (311c)$$

$$\mathbf{u}(\mathbf{x}) = \bar{\boldsymbol{\varepsilon}} \cdot \mathbf{x} + \mathbf{u}^{\text{per}}(\mathbf{x}), \quad (311d)$$

where the loading parameter $\bar{\boldsymbol{\varepsilon}}$ coincides with the average strain, $\bar{\boldsymbol{\varepsilon}} = \langle \boldsymbol{\varepsilon} \rangle$. The solution to equation (311) can be expressed in terms of the Green operator for strains (Kröner, 1977)

$$\boldsymbol{\varepsilon}(\mathbf{x}) = \bar{\boldsymbol{\varepsilon}} - \int_{\Omega} \boldsymbol{\Gamma}_0(\mathbf{x} - \mathbf{y}) \boldsymbol{\tau}(\mathbf{y}) d\Omega = \bar{\boldsymbol{\varepsilon}} - \boldsymbol{\Gamma}_0[\boldsymbol{\tau}](\mathbf{x}). \quad (312)$$

Upon substituting (310) in equation (312), we finally find that

$$\boldsymbol{\varepsilon}(\mathbf{x}) = \bar{\boldsymbol{\varepsilon}} - \boldsymbol{\Gamma}_0[(\mathbf{C} - \mathbf{C}_0) : \boldsymbol{\varepsilon}](\mathbf{x}), \quad (313)$$

which is known as the Lippmann-Schwinger equation (Zeller and Dederichs, 1973).

In their seminal work, Moulinec and Suquet (1994, 1998) proposed to discretize equation (313) on a cartesian grid. They seek for the strain tensor in the space of band-limited, symmetric, second-order tensors $\boldsymbol{\varepsilon}^\beta$ and solve the equation (β : voxel index)

$$\boldsymbol{\varepsilon}^\beta + \boldsymbol{\Gamma}_0^{\text{trunc}} [(\mathbf{C}^\beta - \mathbf{C}_0) : \boldsymbol{\varepsilon}^\beta] = \bar{\boldsymbol{\varepsilon}}, \quad (314)$$

by a fixed point method, where $\boldsymbol{\Gamma}_0^{\text{trunc}}$ is the truncated Green operator for strains and the stiffness tensor \mathbf{C}^β is constant in voxel β . The main asset is that the convolution product appearing in

equation (314) can be efficiently computed by Fast Fourier Transform algorithm (see Frigo and Johnson (2005)).

The resulting numerical scheme is simple and efficient. However, it does not converge for rigid inclusions or pores (Moulinec and Suquet, 1994, 1998). Moreover, how to handle heterogeneous voxels remains unclear. In order to overcome this shortcoming, numerous contributions have been proposed

- Accelerated schemes to reduce the number of iterations: the accelerated-scheme combined with a multigrid approach of Eyre and Milton (1999), the augmented Lagrangian approach of Michel et al. (2001), the accelerated scheme by conjugate gradients of Zeman et al. (2010), the polarization-based approach of Monchiet and Bonnet (2012), the filtering scheme Gélébart and Ouaki (2015), etc.
- Approximate discrete Green operators for improving both the accuracy of local fields and the convergence rate: truncated (Moulinec and Suquet, 1994, 1998), filtered (Brisard and Dormieux, 2010, 2012), finite difference (Willot et al., 2014; Willot, 2015), etc
- Extensions to more complex mechanical behavior: viscoelasticity (Šmilauer and Bažant, 2010), nonlinear (Gélébart and Mondon-Cancel, 2013), elasto viscoplastic (Lebensohn et al., 2012), permeability (Bignonnet and Dormieux, 2014), etc

Recent contributions of Brisard and Dormieux (2010, 2012) introduce a unified framework for FFT based method. The discretization of the Lippmann–Schwinger equation and the resolution of the associated linear system are clearly separated. A consistent rule to deal with heterogeneous voxels was also proposed. With the help of equation (310), (Brisard and Dormieux, 2010, 2012) rewrite equation (312) in term of polarization as unknown:

$$(\mathbf{C}(\mathbf{x}) - \mathbf{C}_0)^{-1} : \boldsymbol{\tau}(\mathbf{x}) + \boldsymbol{\Gamma}_0[\boldsymbol{\tau}](\mathbf{x}) = \bar{\boldsymbol{\varepsilon}}. \quad (315)$$

The weak form of (315) reads:

$$\underbrace{\langle \boldsymbol{\varpi} : (\mathbf{C} - \mathbf{C}_0)^{-1} : \boldsymbol{\tau} \rangle}_{a(\boldsymbol{\tau}, \boldsymbol{\varpi})} + \underbrace{\langle \boldsymbol{\varpi} : (\boldsymbol{\Gamma}_0 * \boldsymbol{\tau}) \rangle}_{f(\boldsymbol{\varpi})} = \langle \bar{\boldsymbol{\varepsilon}} : \boldsymbol{\varpi} \rangle, \quad (316)$$

and the resulting variational problem

$$\text{find } \boldsymbol{\tau} \in \mathbb{V} \text{ such that, for all } \boldsymbol{\varpi} \in \mathbb{V} : a(\boldsymbol{\tau}, \boldsymbol{\varpi}) = f(\boldsymbol{\varpi}), \quad (317)$$

where \mathbb{V} is the space of square integrable, symmetric second-order tensors. The Galerkin discretization of equation (316) is then defined by Brisard and Dormieux (2012):

$$\text{find } \boldsymbol{\tau}^h \in \mathbb{V}^h \text{ such that, for all } \boldsymbol{\varpi}^h \in \mathbb{V}^h : a(\boldsymbol{\tau}^h, \boldsymbol{\varpi}^h) = f(\boldsymbol{\varpi}^h), \quad (318)$$

where \mathbb{V}^h is the space of voxel-wise constant polarizations. Interestingly, this provides a consistent rule for the discretization of the stiffness tensor for a heterogeneous voxel β

$$(\mathbf{C}_\beta^h - \mathbf{C}_0)^{-1} = \frac{1}{\Omega_\beta^h} \int_{\Omega_\beta^h} [\mathbf{C}(\mathbf{x}) - \mathbf{C}_0] dV_{\mathbf{x}}. \quad (319)$$

It is worth noticing that the evaluation of $\langle \varpi : (\Gamma_0 * \tau) \rangle$ remains a difficult task. An asymptotically consistent approximation is thus introduced in [Brisard and Dormieux \(2012\)](#) which involves the so-called *filtered Green operator for strains*. The discrete variational form results in a linear system

$$\mathbf{A} \cdot \mathbf{x} = \mathbf{b}, \tag{320}$$

in which the matrix \mathbf{A} is not explicitly written (only the matrix-vector product $\mathbf{x} \mapsto \mathbf{A} \cdot \mathbf{x}$ is implemented). As a consequence, the choice of the linear solver is not limited to fixed point iterations.

Appendix B

Toeplitz and Circulant matrix

The correlation matrix is evaluated for points in a regular grid. As a consequence, it possesses a particular matrix structure that opens opportunity for efficient numerical implementation (storage, matrix-vector product). In this appendix, we present some materials for the numerical implementation of the Toeplitz and circulant matrix.

B.1 Circulant matrix

A $n \times n$ circulant matrix C_n is a matrix of the form

$$C_n = \begin{pmatrix} c_0 & c_1 & \cdots & c_{n-1} \\ c_{n-1} & c_0 & \cdots & c_{n-2} \\ \vdots & \ddots & \ddots & \vdots \\ c_{n-1} & \cdots & \cdots & c_0 \end{pmatrix}. \quad (321)$$

It is completely specified by its first row $c = [c_0 \ c_1 \ \cdots \ c_{n-1}]$. The circulant matrix C_n is diagonalized by the following form:

$$C_n = F_n^{-1} \Lambda F_n, \quad (322)$$

where $\Lambda = \text{diag}(\lambda_0, \dots, \lambda_{n-1})$ is a diagonal matrix containing eigenvalues of C_n : $\Lambda = \text{DFT}[c]$ and F_n is the Fourier matrix: $F_n(j, k) = \frac{1}{\sqrt{n}} \exp(-(j-1)(k-1)2\pi i/n)$. Therefore, the multiplication between a circulant matrix C_n with a vector z can be computed efficiently in $O(N \log N)$ time

Algorithm 2: Fast circulant matrix-vector product

Data: First row c of circulant matrix C_n , vector z

Result: Matrix vector product $y = Cz$

$\hat{z} = \text{DFT}[z]$

$\hat{c} = \text{DFT}[c]$

$y = \text{DFT}^{-1}[\hat{c} \circ \hat{z}]$

NOTA: \circ element-wise vector product.

B.2 Multilevel circulant matrix

A m^{th} -level circulant matrix C has the following form

$$C = \begin{pmatrix} C_0 & C_1 & \cdots & C_{n-1} \\ C_{n-1} & C_0 & \cdots & C_{n-2} \\ \vdots & \ddots & \ddots & \vdots \\ C_{n-1} & \cdots & \cdots & C_0 \end{pmatrix}, \quad (323)$$

where each block C_i ($i = 0 \cdots n-1$) is a $(m-1)^{\text{th}}$ -level circulant matrix. The size of matrix C is $n^m \times n^m$. The m^{th} -level circulant matrix C is completely specified by its first row c .

The product between matrix C with a vector z can be computed efficiently by the following algorithm

Algorithm 3: Fast multilevel circulant matrix-vector product

Data: First row c of m^{th} -level circulant matrix C , vector z

Result: Matrix vector product $y = Cz$

$$c' = c.\text{reshape}(\underbrace{(n, \cdots, n)}_{m \text{ times}})$$

$$z' = z.\text{reshape}(\underbrace{(n, \cdots, n)}_{m \text{ times}})$$

$$\hat{c} = \text{DFT}_m[c']$$

$$\hat{z} = \text{DFT}_m[z']$$

$$y' = \text{DFT}_m^{-1}[\hat{c} \circ \hat{z}]$$

$$y = y'.\text{reshape}(n^m)$$

NOTA: DFT_m multidimensional DFT, \circ element-wise product.

B.3 Toeplitz matrix

A symmetric $n \times n$ Toeplitz matrix T_n have the following form

$$T_n = \begin{pmatrix} t_0 & t_1 & \cdots & t_{n-1} \\ t_1 & t_0 & \cdots & t_{n-2} \\ \vdots & \ddots & \ddots & \vdots \\ t_{n-1} & \cdots & \cdots & t_0 \end{pmatrix}. \quad (324)$$

The Toeplitz matrix T_n is completely specified by its first row $t = [t_0 \ t_1 \ \cdots \ t_{n-1}]$.

For a given vector z , the matrix-vector product Tz can be computed efficiently in $O(N \log N)$ time by first embedded T_n in a $(2n-1) \times (2n-1)$ circulant matrix C_{2n-1} whose first row: $c = [t_0 \ t_1 \ \cdots \ t_{n-1} \ t_{n-1} \ t_{n-2} \ \cdots \ t_1]$. As a consequence, $n-1$ zeros are padded into

the vector z .

Algorithm 4: Fast Toeplitz matrix-vector product

Data: First row $t = [t_0 \ t_1 \ \cdots \ t_{n-1}]$ of Toeplitz matrix T_n , vector z

Result: Matrix vector product $y = Tz$

Construct $c = [t_0 \ t_1 \ \cdots \ t_{n-1} \ t_{n-1} \ t_{n-2} \ \cdots \ t_1]$

Pad $n - 1$ zeros into z : $x = [z \ 0]$

$\hat{x} = \text{DFT}[x]$

$\hat{c} = \text{DFT}[c]$

$y' = \text{DFT}^{-1}[\hat{c} \circ \hat{x}]$

$y(i) = y'(i)$ for $i = 0 \cdots n - 1$

NOTA: \circ element-wise product.

B.4 Multilevel Toeplitz matrix

A m^{th} -level symmetric Toeplitz matrix T has the following form

$$T = \begin{pmatrix} T_0 & T_1 & \cdots & T_{n-1} \\ T_1 & T_0 & \cdots & T_{n-2} \\ \vdots & \ddots & \ddots & \vdots \\ T_{n-1} & \cdots & \cdots & T_0 \end{pmatrix}, \quad (325)$$

where each block T_i ($i = 0 \cdots n - 1$) is a $(m - 1)^{\text{th}}$ -level Toeplitz matrix. The m^{th} -level symmetric Toeplitz matrix C is completely specified by its first row.

The product between matrix T with a vector z can be computed efficiently by first embedded each $n \times n$ Toeplitz block into a $(2n - 1) \times (2n - 1)$ circulant block. This embedding results in a $(2n - 1)^m \times (2n - 1)^m$ m^{th} -level circulant matrix. In the same way, $(2n - 1)^m - n^m$ zeros are padded into vector z .

Algorithm 5: Fast multilevel Toeplitz matrix-vector product

Data: First row t of m^{th} -level Toeplitz matrix T , vector z

Result: Matrix vector product $y = Tz$

For each block T_i ($i = 0 \cdots n - 1$), embedded T_i into the circulant matrix C_i (see 4)

Pad $(2n - 1)^m - n^m$ zeros into vector z resulting in vector z' .

Compute the matrix-vector product $y' = Cz'$ by Algorithm 3

Extract y from y'

Appendix C

On Eshelby's spherical inhomogeneity problem (uniaxial loading at infinity)

C.1 Strain compatibility conditions

The strain compatibility conditions for uniaxial strain is reported here for convenience. The expressions are given in spherical coordinates defined in section (7.2.1). The strain compatibility condition reads

$$\Upsilon = \text{curl curl } \boldsymbol{\varepsilon} = \mathbf{0}, \quad (326)$$

in which the curl operator of $\boldsymbol{\varepsilon}$ is defined as

$$\text{curl } \boldsymbol{\varepsilon} = \nabla \times \boldsymbol{\varepsilon} = \epsilon_{ijk} \varepsilon_{m,j,i} \mathbf{e}_k \otimes \mathbf{e}_m, \quad (327)$$

where ϵ is the permutation tensor, \times denotes the cross product. It worth mentioning that Υ is symmetric.

$$\begin{aligned} \Upsilon_{rr} = & \left(\frac{1}{r^2 \sin \theta} \left(-2 \varepsilon_{r\theta} + 2 \frac{\partial}{\partial \theta} \varepsilon_{\phi\phi} - \frac{\partial}{\partial \theta} \varepsilon_{\theta\theta} \right) - \frac{2 \frac{\partial}{\partial \phi} \varepsilon_{\theta\phi}}{r^2 \sin^2 \theta} \right) \cos \theta \\ & - \frac{1}{r^2 \sin \theta} \left(2 \frac{\partial}{\partial \phi} \varepsilon_{r\phi} + 2 \frac{\partial^2}{\partial \phi \partial \theta} \varepsilon_{\theta\phi} \right) + \frac{\frac{\partial^2}{\partial \phi^2} \varepsilon_{\theta\theta}}{r^2 \sin^2 \theta} \\ & + \frac{1}{r^2} \left(r \frac{\partial}{\partial r} \varepsilon_{\phi\phi} + r \frac{\partial}{\partial r} \varepsilon_{\theta\theta} + 2 \varepsilon_{\theta\theta} - 2 \varepsilon_{rr} - 2 \frac{\partial}{\partial \theta} \varepsilon_{r\theta} + \frac{\partial^2}{\partial \theta^2} \varepsilon_{\phi\phi} \right), \end{aligned} \quad (328)$$

$$\begin{aligned} \Upsilon_{r\theta} = & \left(\frac{1}{r \sin \theta} \left(-\frac{\partial}{\partial r} \varepsilon_{\phi\phi} + \frac{\partial}{\partial r} \varepsilon_{\theta\theta} \right) + \frac{\frac{\partial}{\partial \phi} \varepsilon_{r\phi}}{r^2 \sin^2 \theta} \right) \cos \theta \\ & + \frac{1}{r^2 \sin \theta} \left(r \frac{\partial^2}{\partial \phi \partial r} \varepsilon_{\theta\phi} + \frac{\partial^2}{\partial \phi \partial \theta} \varepsilon_{r\phi} \right) \\ & - \frac{1}{r^2} \left(r \frac{\partial^2}{\partial r \partial \theta} \varepsilon_{\phi\phi} + 2 \varepsilon_{r\theta} - \frac{\partial}{\partial \theta} \varepsilon_{rr} \right) - \frac{\frac{\partial^2}{\partial \phi^2} \varepsilon_{r\theta}}{r^2 \sin^2 \theta}, \end{aligned} \quad (329)$$

$$\begin{aligned} \Upsilon_{r\phi} = & \left(\frac{1}{r^2 \sin \theta} \left(2r \frac{\partial}{\partial r} \varepsilon_{\theta\phi} - \frac{\partial}{\partial \theta} \varepsilon_{r\phi} \right) - \frac{\frac{\partial}{\partial \phi} \varepsilon_{r\theta}}{r^2 \sin^2 \theta} \right) \cos \theta \\ & + \frac{1}{r^2} \left(r \frac{\partial^2}{\partial r \partial \theta} \varepsilon_{\theta\phi} - 2 \varepsilon_{r\phi} - \frac{\partial^2}{\partial \theta^2} \varepsilon_{r\phi} \right) \\ & - \frac{1}{r^2 \sin \theta} \left(r \frac{\partial^2}{\partial \phi \partial r} \varepsilon_{\theta\theta} - \frac{\partial}{\partial \phi} \varepsilon_{rr} - \frac{\partial^2}{\partial \phi \partial \theta} \varepsilon_{r\theta} \right) + \frac{\varepsilon_{r\phi}}{r^2 \sin^2 \theta}, \end{aligned} \quad (330)$$

$$\begin{aligned} \Upsilon_{\theta\theta} = & \frac{1}{r} \left(r \frac{\partial^2}{\partial r^2} \varepsilon_{\phi\phi} + 2 \frac{\partial}{\partial r} \varepsilon_{\phi\phi} - \frac{\partial}{\partial r} \varepsilon_{rr} \right) - \frac{1}{r^2 \sin \theta} \left(2r \frac{\partial^2}{\partial \phi \partial r} \varepsilon_{r\phi} + 2 \frac{\partial}{\partial \phi} \varepsilon_{r\phi} \right) \\ & + \frac{\cos \theta}{r^2 \sin \theta} \left(-2r \frac{\partial}{\partial r} \varepsilon_{r\theta} - 2 \varepsilon_{r\theta} + \frac{\partial}{\partial \theta} \varepsilon_{rr} \right) + \frac{\frac{\partial^2}{\partial \phi^2} \varepsilon_{rr}}{r^2 \sin^2 \theta}, \end{aligned} \quad (331)$$

$$\begin{aligned} \Upsilon_{\theta\phi} = & \left(\frac{1}{r^2 \sin \theta} \left(-r \frac{\partial}{\partial r} \varepsilon_{r\phi} - \varepsilon_{r\phi} \right) + \frac{\frac{\partial}{\partial \phi} \varepsilon_{rr}}{r^2 \sin^2 \theta} \right) \cos \theta \\ & + \frac{1}{r^2 \sin \theta} \left(r \frac{\partial^2}{\partial \phi \partial r} \varepsilon_{r\theta} + \frac{\partial}{\partial \phi} \varepsilon_{r\theta} - \frac{\partial^2}{\partial \phi \partial \theta} \varepsilon_{rr} \right) \\ & - \frac{1}{r^2} \left(r^2 \frac{\partial^2}{\partial r^2} \varepsilon_{\theta\phi} + 2r \frac{\partial}{\partial r} \varepsilon_{\theta\phi} - r \frac{\partial^2}{\partial r \partial \theta} \varepsilon_{r\phi} - \frac{\partial}{\partial \theta} \varepsilon_{r\phi} \right), \end{aligned} \quad (332)$$

$$\Upsilon_{\phi\phi} = \frac{1}{r^2} \left(r^2 \frac{\partial^2}{\partial r^2} \varepsilon_{\theta\theta} + 2r \frac{\partial}{\partial r} \varepsilon_{\theta\theta} - r \frac{\partial}{\partial r} \varepsilon_{rr} - 2r \frac{\partial^2}{\partial r \partial \theta} \varepsilon_{r\theta} - 2 \frac{\partial}{\partial \theta} \varepsilon_{r\theta} + \frac{\partial^2}{\partial \theta^2} \varepsilon_{rr} \right), \quad (333)$$

which give 6 equations for the compatibility of strain.

C.2 General solution

In this case, the general expression (210) of the stress tensor depends on twelve integration constants. Recalling first that $\sigma \rightarrow \sigma^\infty \mathbf{e}_z \otimes \mathbf{e}_z$ as $r \rightarrow +\infty$, it can be shown that the general

solution reads, outside the spherical inhomogeneity ($r > a$)

$$\begin{aligned} f_1 = & - \left[(3\rho_m^2 + 3\rho_m + 1) C_4 + \rho_m (39\rho_m^3 + 39\rho_m^2 + 16\rho_m + 3) C_{10} \right. \\ & + (39\rho_m^4 + 39\rho_m^3 + 9\rho_m^2 - 4\rho_m - 3) C_{11} \left. \right] \frac{\rho_m}{2} \exp\left(\frac{a-r}{\ell_m}\right) \\ & - \frac{2 + \nu_m}{2\nu_m} \frac{\rho_m^3}{\alpha_m^3} C_2 + \frac{\rho_m^3}{\alpha_m^3} C_6 - \frac{13}{2} \frac{\rho_m^5}{\alpha_m^5} C_7, \end{aligned} \quad (334)$$

$$\begin{aligned} f_2 = & \left[\rho_m (3\rho_m^2 + 3\rho_m + 1) C_{10} + (3\rho_m^3 + 3\rho_m^2 - 1) C_{11} \right] \rho_m^2 \exp\left(\frac{a-r}{\ell_m}\right) \\ & + \frac{\rho_m^3}{\alpha_m^3} C_6 + \frac{\rho_m^5}{\alpha_m^5} C_7, \end{aligned} \quad (335)$$

$$\begin{aligned} f_3 = & \left[- (3\rho_m^2 + 3\rho_m + 1) C_4 + (4\rho_m^2 + 1) (3\rho_m^2 + 3\rho_m + 1) C_{10} \right. \\ & + 2 (6\rho_m^4 + 6\rho_m^3 + 9\rho_m^2 + 7\rho_m + 3) C_{11} \left. \right] \frac{\rho_m}{4} \exp\left(\frac{a-r}{\ell_m}\right) \\ & + \frac{1 - \nu_m}{4\nu_m} \frac{\rho_m^3}{\alpha_m^3} C_2 - \frac{1}{2} \frac{\rho_m^3}{\alpha_m^3} C_6 + \frac{\rho_m^5}{\alpha_m^5} C_7, \end{aligned} \quad (336)$$

$$\begin{aligned} f_4 = & \left[(3\rho_m^2 + 3\rho_m + 1) C_4 - \rho_m (3\rho_m^3 + 3\rho_m^2 + 2\rho_m + 1) C_{10} \right. \\ & - (3\rho_m^4 + 3\rho_m^3 + 9\rho_m^2 + 8\rho_m + 1) C_{11} \left. \right] \frac{\rho_m}{4} \exp\left(\frac{a-r}{\ell_m}\right) \\ & + \frac{1}{4} \frac{\rho_m^3}{\alpha_m^3} C_2 - \frac{1}{2} \frac{\rho_m^3}{\alpha_m^3} C_6 - \frac{1}{4} \frac{\rho_m^5}{\alpha_m^5} C_7, \end{aligned} \quad (337)$$

$$\begin{aligned} f_5 = & \left[(3\rho_m^2 + 3\rho_m + 1) C_4 + \rho_m (15\rho_m^3 + 15\rho_m^2 + 6\rho_m + 1) C_{10} \right. \\ & + (15\rho_m^4 + 15\rho_m^3 - 3\rho_m^2 - 8\rho_m - 3) C_{11} \left. \right] \rho_m \exp\left(\frac{a-r}{\ell_m}\right) + \frac{\rho_m^3}{\alpha_m^3} C_2 + 5 \frac{\rho_m^5}{\alpha_m^5} C_7, \end{aligned} \quad (338)$$

$$\begin{aligned} f_6 = & - \left[(2\rho_m^2 + 2\rho_m + 1) C_4 + \rho_m^2 (3\rho_m^2 + 3\rho_m + 1) C_{10} \right. \\ & + (3\rho_m^4 + 3\rho_m^3 - 5\rho_m^2 - 6\rho_m - 3) C_{11} \left. \right] \frac{\rho_m}{2} \exp\left(\frac{a-r}{\ell_m}\right) \\ & + 1 + \frac{1 - 2\nu_m}{6\nu_m} \frac{\rho_m^3}{\alpha_m^3} C_2 - \frac{1}{2} \frac{\rho_m^5}{\alpha_m^5} C_7, \end{aligned} \quad (339)$$

where α_m and ρ_m have been introduced in section 7.2.2, while $C_2, C_4, C_6, C_7, C_{10}$ and C_{11} are integration constants.

Stresses must also remain finite at the center of the inhomogeneity ($r = 0$). This leads to the following form of the general solution, inside the inhomogeneity ($r < a$)

$$\begin{aligned} f_1 = & \left[-\rho_i (3\rho_i^2 + 1) \mathfrak{S}_i + 3\rho_i^2 \mathfrak{C}_i \right] D_3 + \left[-\rho_i^3 (39\rho_i^2 + 16) \mathfrak{S}_i + 3\rho_i^2 (13\rho_i^2 + 1) \mathfrak{C}_i \right] D_8 \\ & + \left[3\rho_i (-13\rho_i^4 - 3\rho_i^2 + 1) \mathfrak{S}_i + \rho_i^2 (39\rho_i^2 - 4) \mathfrak{C}_i \right] D_9 \\ & + D_5 + \left(28 - \frac{7 + 10\nu_i}{\nu_i} \rho_i^{-2} \right) \alpha_i^2 D_{12}, \end{aligned} \quad (340)$$

$$\begin{aligned} f_2 = & \left[2\rho_i^3 (3\rho_i^2 + 1) \mathfrak{S}_i - 6\rho_i^4 \mathfrak{C}_i \right] D_8 + \left[6\rho_i^5 \mathfrak{S}_i - 2\rho_i^2 (3\rho_i^2 - 1) \mathfrak{C}_i \right] D_9 \\ & + D_5 + (28 + \rho_i^{-2}) \alpha_i^2 D_{12}, \end{aligned} \quad (341)$$

$$\begin{aligned}
f_3 = & \frac{1}{2} \left[-\rho_i(3\rho_i^2 + 1)\mathfrak{S}_i + 3\rho_i^2\mathfrak{C}_i \right] D_3 + \frac{1}{2} \left[\rho_i(12\rho_i^4 + 7\rho_i^2 + 1)\mathfrak{S}_i - 3\rho_i^2(4\rho_i^2 + 1)\mathfrak{C}_i \right] D_8 \\
& + \left[3\rho_i(2\rho_i^4 + 3\rho_i^2 + 1)\mathfrak{S}_i - \rho_i^2(6\rho_i^2 + 7)\mathfrak{C}_i \right] D_9 \\
& + D_5 + \left(28 - \frac{7 + 6\nu_i}{\nu_i} \rho_i^{-2} \right) \alpha_i^2 D_{12}, \tag{342}
\end{aligned}$$

$$\begin{aligned}
f_4 = & \frac{1}{2} \left[\rho_i(3\rho_i^2 + 1)\mathfrak{S}_i - 3\rho_i^2\mathfrak{C}_i \right] D_3 + \frac{1}{2} \left[-\rho_i^3(3\rho_i^2 + 2)\mathfrak{S}_i + \rho_i^2(3\rho_i^2 + 1)\mathfrak{C}_i \right] D_8 \\
& + \frac{1}{2} \left[-\rho_i(3\rho_i^4 + 9\rho_i^2 + 1)\mathfrak{S}_i + \rho_i^2(3\rho_i^2 + 8)\mathfrak{C}_i \right] D_9 + D_5 + \left(28 + 5\rho_i^{-2} \right) \alpha_i^2 D_{12}, \tag{343}
\end{aligned}$$

$$\begin{aligned}
f_5 = & \left[2\rho_i(3\rho_i^2 + 1)\mathfrak{S}_i - 6\rho_i^2\mathfrak{C}_i \right] D_3 + \left[6\rho_i^3(5\rho_i^2 + 2)\mathfrak{S}_i - 2\rho_i^2(15\rho_i^2 + 1)\mathfrak{C}_i \right] D_8 \\
& + \left[6\rho_i(5\rho_i^4 - \rho_i^2 - 1)\mathfrak{S}_i - 2\rho_i^2(15\rho_i^2 - 8)\mathfrak{C}_i \right] D_9 + 12 \frac{\alpha_i^2}{\rho_i^2} D_{12}, \tag{344}
\end{aligned}$$

$$\begin{aligned}
f_6 = & \left[-\rho_i(2\rho_i^2 + 1)\mathfrak{S}_i + 2\rho_i^2\mathfrak{C}_i \right] D_3 + \left[-\rho_i^3(3\rho_i^2 + 1)\mathfrak{S}_i + 3\rho_i^4\mathfrak{C}_i \right] D_8 \\
& + \left[-\rho_i(3\rho_i^4 - 5\rho_i^2 - 3)\mathfrak{S}_i + 3\rho_i^2(\rho_i^2 - 2)\mathfrak{C}_i \right] D_9 + D_1 + \frac{7 - 4\nu_i}{\nu_i} \frac{\alpha_i^2}{\rho_i^2} D_{12}, \tag{345}
\end{aligned}$$

where α_i , ρ_i , \mathfrak{C}_i and \mathfrak{S}_i have been introduced in section 7.2.2, while D_1 , D_3 , D_5 , D_8 , D_9 and D_{12} are integration constants. The twelve unknown integration constants are found by enforcing the continuity of $\boldsymbol{\sigma}$ and $\mathbf{u} \otimes \mathbf{e}_r + \boldsymbol{\phi} \cdot \mathbf{e}_r$ at the interface $r = a$.

Appendix D

Green operators: Matrix formulation

Here, we present a matrix formulation to calculate Green operators for strains. This approach is general and some below elements can be useful for the numerical implementation of stress-gradient model.

The Mandel-Voigt representation of the stress tensor and the displacement vector are

$$\sigma = \begin{bmatrix} \sigma_{11} & \sigma_{22} & \sigma_{33} & \sqrt{2}\sigma_{23} & \sqrt{2}\sigma_{13} & \sqrt{2}\sigma_{12} \end{bmatrix}^T, \quad (346)$$

$$\mathbf{u} = \begin{bmatrix} u_1 & u_2 & u_3 \end{bmatrix}^T. \quad (347)$$

The trace-free stress gradient can be represented by a column vector as follow

$$\mathbf{R} = \begin{bmatrix} R_{111} & R_{221} & R_{331} & \sqrt{2}R_{231} & \sqrt{2}R_{131} & \sqrt{2}R_{121}, \\ R_{112} & R_{222} & R_{332} & \sqrt{2}R_{232} & \sqrt{2}R_{132} & \sqrt{2}R_{122}, \\ R_{113} & R_{223} & R_{333} & \sqrt{2}R_{233} & \sqrt{2}R_{133} & \sqrt{2}R_{123} \end{bmatrix}, \quad (348)$$

The Cauchy deformation is derived from the displacement field

$$\mathbf{e} = \begin{bmatrix} e_{11} \\ e_{22} \\ e_{33} \\ \sqrt{2}e_{23} \\ \sqrt{2}e_{13} \\ \sqrt{2}e_{12} \end{bmatrix} = \begin{bmatrix} \partial_1 & 0 & 0 \\ 0 & \partial_2 & 0 \\ 0 & 0 & \partial_3 \\ 0 & \frac{\sqrt{2}}{2}\partial_3 & \frac{\sqrt{2}}{2}\partial_2 \\ \frac{\sqrt{2}}{2}\partial_3 & 0 & \frac{\sqrt{2}}{2}\partial_1 \\ \frac{\sqrt{2}}{2}\partial_2 & \frac{\sqrt{2}}{2}\partial_1 & 0 \end{bmatrix} \begin{bmatrix} u_1 \\ u_2 \\ u_3 \end{bmatrix} = \mathbf{D}_u \cdot \mathbf{u} \quad (349)$$

The stress gradient reads

$$\nabla \sigma = \mathbf{D}_s \cdot \sigma, \quad (350)$$

where

$$\mathbf{D}_s = \begin{bmatrix} \mathbf{D}_s^1 & \mathbf{D}_s^2 & \mathbf{D}_s^3 \end{bmatrix}^T, \quad (351)$$

in which

$$\mathbf{D}_s^i = \begin{bmatrix} \partial_i & 0 & 0 & 0 & 0 & 0 \\ 0 & \partial_i & 0 & 0 & 0 & 0 \\ 0 & 0 & \partial_i & 0 & 0 & 0 \\ 0 & 0 & 0 & \frac{\sqrt{2}}{2}\partial_i & 0 & 0 \\ 0 & 0 & 0 & 0 & \frac{\sqrt{2}}{2}\partial_i & 0 \\ 0 & 0 & 0 & 0 & 0 & \frac{\sqrt{2}}{2}\partial_i \end{bmatrix}. \quad (352)$$

The trace-free stress gradient is obtained by

$$\mathbf{R} = \mathbf{K} \cdot (\nabla \sigma), \quad (353)$$

where \mathbf{K} is the matrix representation of the projector \mathbf{K} .

$$\mathbf{K} = \begin{pmatrix} \frac{1}{2} & 0 & 0 & 0 & 0 & 0 & 0 & 0 & 0 & 0 & 0 & \frac{-\sqrt{2}}{4} & 0 & 0 & 0 & 0 & \frac{-\sqrt{2}}{4} & 0 \\ 0 & 1 & 0 & 0 & 0 & 0 & 0 & 0 & 0 & 0 & 0 & 0 & 0 & 0 & 0 & 0 & 0 & 0 \\ 0 & 0 & 1 & 0 & 0 & 0 & 0 & 0 & 0 & 0 & 0 & 0 & 0 & 0 & 0 & 0 & 0 & 0 \\ 0 & 0 & 0 & 1 & 0 & 0 & 0 & 0 & 0 & 0 & 0 & 0 & 0 & 0 & 0 & 0 & 0 & 0 \\ 0 & 0 & 0 & 0 & \frac{3}{4} & 0 & 0 & 0 & 0 & \frac{-1}{4} & 0 & 0 & 0 & 0 & \frac{-\sqrt{2}}{4} & 0 & 0 & 0 \\ 0 & 0 & 0 & 0 & 0 & \frac{3}{4} & 0 & \frac{-\sqrt{2}}{4} & 0 & 0 & 0 & 0 & 0 & 0 & 0 & \frac{-1}{4} & 0 & 0 \\ 0 & 0 & 0 & 0 & 0 & 0 & 1 & 0 & 0 & 0 & 0 & 0 & 0 & 0 & 0 & 0 & 0 & 0 \\ 0 & 0 & 0 & 0 & 0 & \frac{-\sqrt{2}}{4} & 0 & \frac{1}{2} & 0 & 0 & 0 & 0 & 0 & 0 & 0 & \frac{-\sqrt{2}}{4} & 0 & 0 \\ 0 & 0 & 0 & 0 & 0 & 0 & 0 & 0 & 1 & 0 & 0 & 0 & 0 & 0 & 0 & 0 & 0 & 0 \\ 0 & 0 & 0 & 0 & \frac{-1}{4} & 0 & 0 & 0 & 0 & \frac{3}{4} & 0 & 0 & 0 & 0 & \frac{-\sqrt{2}}{4} & 0 & 0 & 0 \\ 0 & 0 & 0 & 0 & 0 & 0 & 0 & 0 & 0 & 0 & 1 & 0 & 0 & 0 & 0 & 0 & 0 & 0 \\ \frac{-\sqrt{2}}{4} & 0 & 0 & 0 & 0 & 0 & 0 & 0 & 0 & 0 & 0 & \frac{3}{4} & 0 & 0 & 0 & 0 & \frac{-1}{4} & 0 \\ 0 & 0 & 0 & 0 & 0 & 0 & 0 & 0 & 0 & 0 & 0 & 0 & 1 & 0 & 0 & 0 & 0 & 0 \\ 0 & 0 & 0 & 0 & 0 & 0 & 0 & 0 & 0 & 0 & 0 & 0 & 0 & 1 & 0 & 0 & 0 & 0 \\ 0 & 0 & 0 & 0 & \frac{-\sqrt{2}}{4} & 0 & 0 & 0 & 0 & \frac{-\sqrt{2}}{4} & 0 & 0 & 0 & 0 & \frac{1}{2} & 0 & 0 & 0 \\ 0 & 0 & 0 & 0 & 0 & \frac{-1}{4} & 0 & \frac{-\sqrt{2}}{4} & 0 & 0 & 0 & 0 & 0 & 0 & 0 & \frac{3}{4} & 0 & 0 \\ \frac{-\sqrt{2}}{4} & 0 & 0 & 0 & 0 & 0 & 0 & 0 & 0 & 0 & 0 & \frac{-1}{4} & 0 & 0 & 0 & 0 & \frac{3}{4} & 0 \\ 0 & 0 & 0 & 0 & 0 & 0 & 0 & 0 & 0 & 0 & 0 & 0 & 0 & 0 & 0 & 0 & 0 & 1 \end{pmatrix} \quad (354)$$

We pose

$$\mathbf{S} = \begin{bmatrix} \sigma & \mathbf{R} \end{bmatrix}^T, \quad (355)$$

$$\mathbf{U} = \begin{bmatrix} \mathbf{u} & \phi \end{bmatrix}^T, \quad (356)$$

$$\mathbf{E} = \begin{bmatrix} \mathbf{e} & \phi \end{bmatrix}^T. \quad (357)$$

- Equilibrium equations

$$\begin{cases} \nabla \cdot \boldsymbol{\sigma} = \mathbf{0} \\ \mathbf{R} = \mathbf{K} \cdot (\nabla \sigma) \end{cases} \Leftrightarrow \begin{bmatrix} \mathbf{D}_u^T & \mathbf{0}_{3 \times 18} \\ \mathbf{K} \cdot \mathbf{D}_s & -\mathbf{I}_{18 \times 18} \end{bmatrix} \cdot \boldsymbol{\sigma} = \mathbf{0} \Leftrightarrow \mathbf{D} \cdot \mathbf{S} = \mathbf{0}, \quad (358)$$

where $\mathbf{0}_{3 \times 18}$ denotes the 3×18 zero matrix, $\mathbf{I}_{18 \times 18}$ denotes the 18×18 identity matrix. The dimension of matrix \mathbf{D} is 21×24 .

- Constitutive relations

$$\begin{cases} \boldsymbol{\sigma} = \mathbf{C} : \mathbf{e} + \boldsymbol{\tau} \\ \mathbf{R} = \mathbf{L} \cdot \phi + \boldsymbol{\kappa} \end{cases} \Leftrightarrow \mathbf{S} = \begin{bmatrix} \mathbf{C} & \mathbf{0}_{6 \times 18} \\ \mathbf{0}_{18 \times 6} & \mathbf{L} \end{bmatrix} \cdot \begin{bmatrix} \mathbf{e} \\ \phi \end{bmatrix} + \begin{bmatrix} \boldsymbol{\tau} \\ \boldsymbol{\kappa} \end{bmatrix} \Leftrightarrow \mathbf{S} = \mathbf{B} \cdot \mathbf{E} + \mathbf{T}. \quad (359)$$

It can readily be seen that the dimension of matrix \mathbf{B} is 24×24 .

- Compatibility condition

$$\mathbf{e} = \nabla^s \mathbf{u} + \nabla \cdot \boldsymbol{\phi} \Leftrightarrow \begin{bmatrix} \mathbf{D}_u & \mathbf{D}_s^T \\ \mathbf{0}_{18 \times 3} & \mathbf{I}_{18 \times 18} \end{bmatrix} \cdot \begin{bmatrix} \mathbf{u} \\ \boldsymbol{\phi} \end{bmatrix} \Leftrightarrow \mathbf{E} = \mathbf{A} \cdot \mathbf{U}, \quad (360)$$

the dimension of matrix \mathbf{A} is 24×21 .

Gathering together above results, the field equations of stress-gradient model can be represented by matrix formulations as follow

$$\mathbf{D} \cdot \mathbf{S} = 0, \quad (361)$$

$$\mathbf{S} = \mathbf{B} \cdot \mathbf{E} + \mathbf{T}, \quad (362)$$

$$\mathbf{E} = \mathbf{A} \cdot \mathbf{U}, \quad (363)$$

or in Fourier space:

$$\hat{\mathbf{D}} \cdot \hat{\mathbf{S}} = 0, \quad (364)$$

$$\hat{\mathbf{S}} = \hat{\mathbf{B}} \cdot \hat{\mathbf{E}} + \hat{\mathbf{T}}, \quad (365)$$

$$\hat{\mathbf{E}} = \hat{\mathbf{A}} \cdot \hat{\mathbf{U}}. \quad (366)$$

It should be noted that the differential operators are replaced by $i\mathbf{k}$ where \mathbf{k} is the wave vector in Fourier space. From Equation (366), we deduce

$$\hat{\mathbf{E}} = -\hat{\mathbf{A}} \cdot (\hat{\mathbf{D}} \cdot \hat{\mathbf{B}} \cdot \hat{\mathbf{A}})^{-1} \cdot \hat{\mathbf{D}} \cdot \hat{\mathbf{T}}. \quad (367)$$

The Green operators for strains which relate the strains with the polarization fields are thus obtained as

$$\hat{\mathbf{\Gamma}} = \hat{\mathbf{A}} \cdot (\hat{\mathbf{D}} \cdot \hat{\mathbf{B}} \cdot \hat{\mathbf{A}})^{-1} \cdot \hat{\mathbf{D}}. \quad (368)$$

Care has been taken to solve equation (367). It can be seen that there are 24 equations to solve for 21 unknowns. This is due to the fact that there are 3 redundant equations in this system which is transferred from the trace-free stress gradient \mathbf{R} part.

The matrix representation of Green operators $\hat{\mathbf{\Gamma}}$ can be decomposed by block as follow

$$\hat{\mathbf{E}} = -\hat{\mathbf{\Gamma}} \cdot \hat{\mathbf{T}}, \quad (369)$$

$$\begin{bmatrix} \mathbf{e} \\ \boldsymbol{\phi} \end{bmatrix} = \begin{bmatrix} \hat{\mathbf{\Gamma}}_{e\tau} & \hat{\mathbf{\Gamma}}_{e\kappa} \\ \hat{\mathbf{\Gamma}}_{\phi\tau} & \hat{\mathbf{\Gamma}}_{\phi\kappa} \end{bmatrix} \cdot \begin{bmatrix} \boldsymbol{\tau} \\ \boldsymbol{\kappa} \end{bmatrix} \quad (370)$$

Due to lengthy expressions, we only report below the matrix representation of Green operator $\hat{\mathbf{\Gamma}}_{e\tau}(\mathbf{k} = k\mathbf{e}_3)$ (which is sufficient to evaluate the bounds in section 8.3)

$$\hat{\mathbf{\Gamma}}_{e\tau}(k\mathbf{e}_3) = \begin{bmatrix} \frac{k^2 \ell^2}{2\mu(1+\nu)(1+k^2 \ell^2)} & -\frac{\nu k^2 \ell^2}{2\mu(1+\nu)(1+k^2 \ell^2)} & -\frac{\nu k^2 \ell^2}{2\mu(1+\nu)(1+k^2 \ell^2)} & 0 & 0 & 0 \\ -\frac{\nu k^2 \ell^2}{2\mu(1+\nu)(1+k^2 \ell^2)} & \frac{k^2 \ell^2}{2\mu(1+\nu)(1+k^2 \ell^2)} & -\frac{\nu k^2 \ell^2}{2\mu(1+\nu)(1+k^2 \ell^2)} & 0 & 0 & 0 \\ -\frac{\nu k^2 \ell^2}{2\mu(1+\nu)(1+k^2 \ell^2)} & -\frac{\nu k^2 \ell^2}{2\mu(1+\nu)(1+k^2 \ell^2)} & \frac{k^2 \ell^2(1-\nu)-(2\nu^2+\nu-1)}{2\mu(1-\nu^2)(1+k^2 \ell^2)} & 0 & 0 & 0 \\ 0 & 0 & 0 & \frac{1}{2\mu} & 0 & 0 \\ 0 & 0 & 0 & 0 & \frac{1}{2\mu} & 0 \\ 0 & 0 & 0 & 0 & 0 & \frac{k^2 \ell^2}{2\mu(1+k^2 \ell^2)} \end{bmatrix} \quad (371)$$

Appendix E

Green operators: Simplification

In this appendix, we prove equation (247). Note that problem (239) is linear, its solution is obtained as the sum of the solution to two problems (see equation (234)):

- Problem (239), complemented with clamped boundary conditions $(\mathbf{u}, \boldsymbol{\phi}) \in \mathbb{KA}(\mathbf{0}, \mathbf{0})$. The solution to this problem is expressed in term of Green operators

$$\mathbf{e}(\mathbf{x}) = -\Gamma_{e\tau}[\boldsymbol{\tau}](\mathbf{x}) - \Gamma_{e\kappa}[\boldsymbol{\kappa}](\mathbf{x}), \quad (372)$$

$$\boldsymbol{\phi}(\mathbf{x}) = -\Gamma_{\phi\tau}[\boldsymbol{\tau}](\mathbf{x}) - \Gamma_{\phi\kappa}[\boldsymbol{\kappa}](\mathbf{x}), \quad (373)$$

- Problem (239) with no prestresses ($\boldsymbol{\tau} = \mathbf{0}, \boldsymbol{\kappa} = \mathbf{0}$) complemented with kinematic uniform boundary conditions $(\mathbf{u}, \boldsymbol{\phi}) \in \mathbb{KA}(\bar{\mathbf{e}} \cdot \mathbf{x}, \mathbf{0})$. The solution to this problem is trivial (the medium is homogeneous), $\mathbf{e}(\mathbf{x}) = \bar{\mathbf{e}}, \forall \mathbf{x} \in \Omega$.

To study Green operators, only the first problem with clamped boundary conditions is involved. Apply equation (161) for $(\boldsymbol{\sigma}_1, \mathbf{u}_2, \boldsymbol{\phi}_2)$ then $(\boldsymbol{\sigma}_2, \mathbf{u}_1, \boldsymbol{\phi}_1)$ and note that both $(\mathbf{u}_1, \boldsymbol{\phi}_1)$ and $(\mathbf{u}_2, \boldsymbol{\phi}_2) \in \mathbb{KA}(\mathbf{0}, \mathbf{0})$, we find

$$\langle \boldsymbol{\sigma}_1 : \mathbf{e}_2 + \mathbf{R}_1 \cdot \boldsymbol{\phi}_2 \rangle = \frac{1}{V} \int_{\partial\Omega} \boldsymbol{\sigma}_1 : \left(\mathbf{u}_2 \overset{s}{\otimes} \mathbf{n} + \boldsymbol{\phi}_2 \cdot \mathbf{n} \right) dS = 0, \quad (374)$$

$$\langle \boldsymbol{\sigma}_2 : \mathbf{e}_1 + \mathbf{R}_2 \cdot \boldsymbol{\phi}_1 \rangle = \frac{1}{V} \int_{\partial\Omega} \boldsymbol{\sigma}_2 : \left(\mathbf{u}_1 \overset{s}{\otimes} \mathbf{n} + \boldsymbol{\phi}_1 \cdot \mathbf{n} \right) dS = 0, \quad (375)$$

therefore

$$\langle \boldsymbol{\sigma}_1 : \mathbf{e}_2 + \mathbf{R}_1 \cdot \boldsymbol{\phi}_2 \rangle = \langle \boldsymbol{\sigma}_2 : \mathbf{e}_1 + \mathbf{R}_2 \cdot \boldsymbol{\phi}_1 \rangle, \quad (376)$$

which can be written as

$$\langle (\mathbf{C} : \mathbf{e}_1 + \boldsymbol{\tau}_1) : \mathbf{e}_2 + (\mathbf{L}_1 \cdot \boldsymbol{\phi}_1 + \boldsymbol{\kappa}_1) \cdot \boldsymbol{\phi}_2 \rangle = \langle (\mathbf{C} : \mathbf{e}_2 + \boldsymbol{\tau}_2) : \mathbf{e}_1 + (\mathbf{L}_2 \cdot \boldsymbol{\phi}_2 + \boldsymbol{\kappa}_2) \cdot \boldsymbol{\phi}_1 \rangle. \quad (377)$$

By exploiting the symmetry of the stiffness tensor and generalized stiffness tensor, we find

$$\langle (\mathbf{C} : \mathbf{e}_1) : \mathbf{e}_2 + (\mathbf{L}_1 \cdot \boldsymbol{\phi}_1) \cdot \boldsymbol{\phi}_2 \rangle = \langle (\mathbf{C} : \mathbf{e}_2) : \mathbf{e}_1 + (\mathbf{L}_2 \cdot \boldsymbol{\phi}_2) \cdot \boldsymbol{\phi}_1 \rangle, \quad (378)$$

equation (377) then reduces to

$$\langle \boldsymbol{\tau}_1 : \mathbf{e}_2 \rangle + \langle \boldsymbol{\kappa}_1 \cdot \boldsymbol{\phi}_2 \rangle = \langle \boldsymbol{\tau}_2 : \mathbf{e}_1 \rangle + \langle \boldsymbol{\kappa}_2 \cdot \boldsymbol{\phi}_1 \rangle. \quad (379)$$

Writing the total strain and micro-deformation in terms of Green operators and by choosing $\boldsymbol{\tau}_1 = \boldsymbol{\tau}_2 = \mathbf{0}$ then $\boldsymbol{\kappa}_1 = \boldsymbol{\kappa}_2 = \mathbf{0}$, we obtain

$$\langle \boldsymbol{\kappa}_1 \cdot: \boldsymbol{\Gamma}_{\phi\boldsymbol{\kappa}}^{\infty}[\boldsymbol{\kappa}_2] \rangle = \langle \boldsymbol{\kappa}_2 \cdot: \boldsymbol{\Gamma}_{\phi\boldsymbol{\kappa}}^{\infty}[\boldsymbol{\kappa}_1] \rangle, \quad \langle \boldsymbol{\tau}_1 : \boldsymbol{\Gamma}_{e\boldsymbol{\tau}}^{\infty}[\boldsymbol{\tau}_2] \rangle = \langle \boldsymbol{\tau}_2 : \boldsymbol{\Gamma}_{e\boldsymbol{\tau}}^{\infty}[\boldsymbol{\tau}_1] \rangle, \quad (380)$$

the Green operator $\boldsymbol{\Gamma}_{e\boldsymbol{\tau}}^{\infty}$ and $\boldsymbol{\Gamma}_{\phi\boldsymbol{\kappa}}^{\infty}$ are symmetric. Upon substituting equation (379), (380) simplifies to

$$\langle \boldsymbol{\tau}_1 : \boldsymbol{\Gamma}_{e\boldsymbol{\kappa}}^{\infty}[\boldsymbol{\kappa}_2] \rangle + \langle \boldsymbol{\kappa}_1 \cdot: \boldsymbol{\Gamma}_{\phi\boldsymbol{\tau}}^{\infty}[\boldsymbol{\tau}_2] \rangle = \langle \boldsymbol{\tau}_2 : \boldsymbol{\Gamma}_{e\boldsymbol{\kappa}}^{\infty}[\boldsymbol{\kappa}_1] \rangle + \langle \boldsymbol{\kappa}_2 \cdot: \boldsymbol{\Gamma}_{\phi\boldsymbol{\tau}}^{\infty}[\boldsymbol{\tau}_1] \rangle. \quad (381)$$

By choosing $\boldsymbol{\tau}_2 = \mathbf{0}$, we finally find

$$\langle \boldsymbol{\tau}_1 : \boldsymbol{\Gamma}_{e\boldsymbol{\kappa}}^{\infty}[\boldsymbol{\kappa}_2] \rangle = \langle \boldsymbol{\kappa}_2 \cdot: \boldsymbol{\Gamma}_{\phi\boldsymbol{\tau}}^{\infty}[\boldsymbol{\tau}_1] \rangle. \quad (382)$$

The proof is complete.

Appendix F

Walpole's tensor basis

Any fourth-rank transverse isotropic tensor \mathbf{T} is defined by a single direction whose unit vector is denoted by \mathbf{n} . It is convenient to define the following projectors

$$\mathbf{p} = \mathbf{n} \otimes \mathbf{n}, \quad \mathbf{q} = \mathbf{I} - \mathbf{n} \otimes \mathbf{n}, \quad (383)$$

Walpole (1984) showed that \mathbf{T} is a linear combination of the six fourth-order tensor $\mathbf{E}_1, \mathbf{E}_2, \mathbf{E}_3, \mathbf{E}_4, \mathbf{F}, \mathbf{G}$, which are defined as follows

$$\mathbf{E}_1 = \mathbf{p} \otimes \mathbf{p}, \quad \mathbf{E}_2 = \frac{1}{2} \mathbf{q} \otimes \mathbf{q}, \quad \mathbf{E}_3 = \frac{1}{\sqrt{2}} \mathbf{p} \otimes \mathbf{q}, \quad (384)$$

$$\mathbf{E}_4 = \frac{1}{\sqrt{2}} \mathbf{q} \otimes \mathbf{p}, \quad \mathbf{F} = \mathbf{q} \boxtimes^s \mathbf{q} - \frac{1}{2} \mathbf{q} \otimes \mathbf{q}, \quad \mathbf{G} = \mathbf{p} \boxtimes^s \mathbf{q} + \mathbf{q} \boxtimes^s \mathbf{p}, \quad (385)$$

otherwise stated

$$\mathbf{T} = a_{11} \mathbf{E}_1 + a_{22} \mathbf{E}_2 + a_{12} \mathbf{E}_3 + a_{21} \mathbf{E}_4 + f \mathbf{F} + g \mathbf{G}. \quad (386)$$

We recall here the multiplication table for the double contraction ":" of these tensors

:	\mathbf{E}_1	\mathbf{E}_2	\mathbf{E}_3	\mathbf{E}_4	\mathbf{F}	\mathbf{G}	
\mathbf{E}_1	\mathbf{E}_1	$\mathbf{0}$	\mathbf{E}_3	$\mathbf{0}$	$\mathbf{0}$	$\mathbf{0}$	
\mathbf{E}_2	$\mathbf{0}$	\mathbf{E}_2	$\mathbf{0}$	\mathbf{E}_4	$\mathbf{0}$	$\mathbf{0}$	
\mathbf{E}_3	$\mathbf{0}$	\mathbf{E}_3	$\mathbf{0}$	\mathbf{E}_1	$\mathbf{0}$	$\mathbf{0}$	
\mathbf{F}	$\mathbf{0}$	$\mathbf{0}$	$\mathbf{0}$	$\mathbf{0}$	\mathbf{F}	$\mathbf{0}$	
\mathbf{G}	$\mathbf{0}$	$\mathbf{0}$	$\mathbf{0}$	$\mathbf{0}$	$\mathbf{0}$	\mathbf{G}	

(387)

In some case of interest, a more condensed representation of \mathbf{T} can be adopted

$$\mathbf{T} = (A, f, g), \quad (388)$$

where A denotes the matrix

$$A = \begin{bmatrix} a_{11} & a_{12} \\ a_{21} & a_{22} \end{bmatrix}. \quad (389)$$

Using this representation, the double dot product between two transverse isotropic tensor $\mathbf{T} = (A, f, g)$ and $\mathbf{T}' = (A', f', g')$ is particularly simple

$$\mathbf{T} : \mathbf{T}' = (AA', ff', gg'). \quad (390)$$

It can readily be verified that the inversion and the transposition of \mathbf{T} respectively read

$$\mathbf{T}^{-1} = (A^{-1}, 1/f, 1/g), \quad (391)$$

$$\mathbf{T}^T = (A^T, f, g). \quad (392)$$

Appendix G

Stress-gradient Hill's tensor

The fourth order Green's operator $\hat{\Gamma}_{0,e\tau}^{\infty}(\mathbf{k})$ expressed in Walpole basis as (see appendix D)

$$\hat{\Gamma}_{0,e\tau}^{\infty}(\mathbf{k}) = \left(\frac{1}{2\mu(1-\nu^2)(1+k^2\ell^2)} \begin{bmatrix} (1-\nu)(1+k^2\ell^2) - 2\nu^2 & -\sqrt{2}\nu k^2\ell^2 \\ -\sqrt{2}\nu k^2\ell^2 & k^2\ell^2(1-\nu) \end{bmatrix}, \frac{k^2\ell^2}{2\mu(k^2\ell^2+1)}, \frac{1}{2\mu} \right), \quad (393)$$

where $k = \|\mathbf{k}\|$, $\mathbf{k} = k\mathbf{n}$, $\|\mathbf{n}\| = 1$. The contraction of $\hat{\Gamma}_{0,e\tau}^{\infty}(\mathbf{k})$ with the isotropic projection tensor (${}^4\mathbf{J}$, ${}^4\mathbf{K}$) reads

$${}^4\mathbf{J} :: \hat{\Gamma}_{0,e\tau}^{\infty}(\mathbf{k}) = \frac{(1-2\nu)(1+\nu+3k^2\ell^2(1-\nu))}{6\mu(1-\nu^2)(1+k^2\ell^2)}, \quad (394)$$

$${}^4\mathbf{K} :: \hat{\Gamma}_{0,e\tau}^{\infty}(\mathbf{k}) = \frac{8-10\nu+15k^2\ell^2(1-\nu)}{6\mu(1-\nu)(1+k^2\ell^2)}. \quad (395)$$

From equation (371) and equation (280), we have

$$\mathbf{A}_{\alpha\beta}^{e\tau} = f_{\alpha}(\delta_{\alpha\beta} - f_{\beta}) \int_{\mathbf{r} \in \mathbb{R}^3} \mathcal{R}(\mathbf{r}) \Gamma_{0,e\tau}^{\infty}(\mathbf{r}) \, d\mathbf{r} \quad (396)$$

$$= \frac{f_{\alpha}(\delta_{\alpha\beta} - f_{\beta})}{8\pi^3} \int_{\mathbf{k} \in \mathbb{R}^3} \hat{\mathcal{R}}(\mathbf{k}) \hat{\Gamma}_{0,e\tau}^{\infty}(\mathbf{k}) \, d\mathbf{k}, \quad (397)$$

which is followed by Parseval's formula. $\mathbf{A}_{\alpha\beta}^{e\tau}$ is isotropic, it can be decomposed in the Walpole basis as

$$\mathbf{A}_{\alpha\beta}^{e\tau} = f_{\alpha}(\delta_{\alpha\beta} - f_{\beta}) \mathbf{P}, \quad (398)$$

$$\mathbf{P} = 3p\mathbf{J} + 2q\mathbf{K}. \quad (399)$$

Contract resp. both side of equation (397) with \mathbf{J} and \mathbf{K} , we obtain

$$3p = \frac{1}{2\pi^2} \int_0^{\infty} \hat{\mathcal{R}}(k) \frac{(1-2\nu)(1+\nu+3k^2\ell^2(1-\nu))}{6\mu(1-\nu^2)(1+k^2\ell^2)} k^2 \, dk, \quad (400a)$$

$$10q = \frac{1}{2\pi^2} \int_0^{\infty} \hat{\mathcal{R}}(k) \frac{8-10\nu+15k^2\ell^2(1-\nu)}{6\mu(1-\nu)(1+k^2\ell^2)} k^2 \, dk, \quad (400b)$$

We finally deduce

$$p = \frac{(1-2\nu)(1+\nu+3h(2+h)(1-\nu))}{18\mu(1-\nu^2)(1+h)^2}, \quad (401)$$

$$q = \frac{8-10\nu+15h(2+h)(1-\nu)}{60\mu(1-\nu)(1+h)^2}, \quad (402)$$

in which we denoted $h = \ell/b$. For $\ell = 0$, the stress gradient effects vanish. We recover the classical Hill's tensor of domain Ω as expected

$$\mathbf{P} = \frac{1 - 2\nu}{6\mu(1 - \nu)} \mathbf{J} + \frac{4 - 5\nu}{15\mu(1 - \nu)} \mathbf{K}. \quad (403)$$

Bibliography

- Aifantis, E.C., 1992. On the role of gradients in the localization of deformation and fracture. *Int. J. Eng. Sci.* 30, 1279 – 1299.
- Alder, B.J., Wainwright, T.E., 1960. Studies in molecular dynamics. ii. behavior of a small number of elastic spheres. *J. Chem. Phys.* 33, 1439–1451.
- Allen, M.P., Tildesley, D.J., 1987. *Computer simulation of liquids*. Oxford University Press, Oxford.
- Altenbach, J., Altenbach, H., Eremeyev, V.A., 2010. On generalized cosserat-type theories of plates and shells: a short review and bibliography. *Archive of Applied Mechanics* 80, 73–92.
- Amanatidou, E., Aravas, N., 2002. Mixed finite element formulations of strain-gradient elasticity problems. *Computer Methods in Applied Mechanics and Engineering* 191, 1723 – 1751.
- Anderson, W.B., Lakes, R.S., 1994. Size effects due to cosserat elasticity and surface damage in closed-cell polymethacrylimide foam. *J. Mater. Sci.* 29, 6413–6419.
- Askes, H., Aifantis, E.C., 2011. Gradient elasticity in statics and dynamics: An overview of formulations, length scale identification procedures, finite element implementations and new results. *Int. J. Solids Struct.* 48, 1962 – 1990.
- Baxter, S., Graham, L., 2000. Characterization of random composites using moving-window technique. *J. Eng. Mech-ASCE* 126, 389–397.
- Baxter, S., Hossain, M., Graham, L., 2001. Micromechanics based random material property fields for particulate reinforced composites. *Int. J. Solids Struct.* 38, 9209–9220.
- Benveniste, Y., 1987. A new approach to the application of mori-tanaka's theory in composite materials. *Mech. Mater.* 6, 147 – 157.
- Benzi, M., Cullum, J.K., Tuma, M., 2000. Robust approximate inverse preconditioning for the conjugate gradient method. *SIAM J. Sci. Comput.* 22, 1318–1332.
- Bignonnet, F., Dormieux, L., 2014. Fft-based bounds on the permeability of complex microstructures. *Int. J. Numer. Anal. Methods Geomech.* 38, 1707–1723.
- Bignonnet, F., Sab, K., Dormieux, L., Brisard, S., Bisson, A., 2014. Macroscopically consistent non-local modeling of heterogeneous media. *Comput. Method. Appl. M.* 278, 218–238.

- Bigoni, D., Drugan, W.J., 2006. Analytical derivation of cosserat moduli via homogenization. *J. Appl. Mech.* 74, 741–753.
- Bornert, M., Bretheau, T., Gilormini, P., 2001. *Homogénéisation en mécanique des matériaux, Tome 1 : Matériaux aléatoires élastiques et milieux périodiques*. Hermes science.
- de Borst, R., Sluys, L., Muhlhaus, H., Pamin, J., 1993. Fundamental issues in finite element analyses of localization of deformation. *Engineering Computations* 10, 99–121.
- Boutin, C., 1996. Microstructural effects in elastic composites. *Int. J. Solids Struct.* 33, 1023 – 1051.
- Brisard, S., Dormieux, L., 2010. FFT-based methods for the mechanics of composites: A general variational framework. *Comp. Mater. Sci.* 49, 663–671.
- Brisard, S., Dormieux, L., 2012. Combining Galerkin approximation techniques with the principle of Hashin and Shtrikman to derive a new FFT-based numerical method for the homogenization of composites. *Comput. Method. Appl. M.* 217-220, 197–212.
- Brisard, S., Sab, K., Dormieux, L., 2013. New boundary conditions for the computation of the apparent stiffness of statistical volume elements. *J. Mech. Phys. Solids.* 61, 2638 – 2658.
- Challamel, N., Wang, C.M., Elishakoff, I., 2016. Nonlocal or gradient elasticity macroscopic models: A question of concentrated or distributed microstructure. *Mech. Res. Commun.* 71, 25–31.
- Cheng, Z.Q., He, L.H., 1995. Micropolar elastic fields due to a spherical inclusion. *Int. J. Eng. Sci.* 33, 389 – 397.
- Cheng, Z.Q., He, L.H., 1997. Micropolar elastic fields due to a circular cylindrical inclusion. *Int. J. Eng. Sci.* 35, 659 – 668.
- Chisholm, N., Mahfuz, H., Rangari, V.K., Ashfaq, A., Jeelani, S., 2005. Fabrication and mechanical characterization of carbon/sic-epoxy nanocomposites. *Compos. Struct.* 67, 115 – 124.
- Cho, J., Joshi, M., Sun, C., 2006. Effect of inclusion size on mechanical properties of polymeric composites with micro and nano particles. *Compos. Sci. Technol.* 66, 1941 – 1952.
- Chow, E., Saad, Y., 2014. Preconditioned krylov subspace methods for sampling multivariate Gaussian distributions. *SIAM J. Sci. Comput.* 36, 588–608.
- Cole, K.D., Yen, D.H., 2001. Green's functions, temperature and heat flux in the rectangle. *Int. J. Heat. Mass. Trans.* 44, 3883 – 3894.
- Cordero, N.M., Forest, S., Busso, E.P., 2015. Second strain gradient elasticity of nano-objects. *J. Mech. Phys. Solids.* , –.
- Cosserat, E., Cosserat, F., 1909. *Théorie des corps déformables*. A. Hermann et Fils, Paris.

- Davydov, D., Voyiatzis, E., Chatzigeorgiou, G., Liu, S., Steinmann, P., Böhm, M.C., Müller-Plathe, F., 2014. Size effects in a silica-polystyrene nanocomposite: Molecular dynamics and surface-enhanced continuum approaches. *Soft Mater.* 12, S142–S151.
- Debye, P., Anderson, H.R., Brumberger, H., 1957. Scattering by an inhomogeneous solid. ii. the correlation function and its application. *J. Appl. Phys.* 28, 679–683.
- Dietrich, C., 1993. Computationally efficient cholesky factorization of a covariance matrix with block toeplitz structure. *J. Stat. Comput. Simul.* 45, 203–218.
- Drugan, W., Willis, J., 1996. A micromechanics-based nonlocal constitutive equation and estimates of representative volume element size for elastic composites. *J. Mech. Phys. Solids.* 44, 497 – 524.
- Duan, H., Wang, J., Huang, Z., Karihaloo, B., 2005. Size-dependent effective elastic constants of solids containing nano-inhomogeneities with interface stress. *Journal of the Mechanics and Physics of Solids* 53, 1574 – 1596.
- Eringen, A., 1972. Theory of thermomicrofluids. *J. Math. Anal. Appl.* 38, 480 – 496.
- Eringen, A., 1990. Theory of thermo-microstretch elastic solids. *Int. J. Eng. Sci.* 28, 1291 – 1301.
- Eringen, A., Suhubi, E., 1964. Nonlinear theory of simple micro-elastic solids—i. *Int. J. Eng. Sci.* 2, 189 – 203.
- Eringen, A.C., 1966. Linear theory of micropolar elasticity. *J. Math. Mech.* 15, 909–923.
- Eringen, A.C., 1967. *Theory of Micropolar Elasticity*. Technical Report. Princeton University, Department of Aerospace and Mechanical Sciences.
- Eringen, A.C., 1968. *Theory of micropolar elasticity*. In: Liebowitz, H. (Ed.), *Fracture*, vol. 2. Academic Press, New York.
- Eshelby, J.D., 1957. The determination of the elastic field of an ellipsoidal inclusion, and related problems. *Proc. Math. Phys. Eng. Sci.* 241, 376–396.
- Eshelby, J.D., 1959. The elastic field outside an ellipsoidal inclusion. *Proc. Math. Phys. Eng. Sci.* 252, 561–569.
- Eyre, D.J., Milton, G.W., 1999. A fast numerical scheme for computing the response of composites using grid refinement. *The European Physical Journal Applied Physics* 6, 41–47.
- Farmer, C.L., 2002. Upscaling: a review. *Int. J. Numer. Meth. Fl.* 40, 63–78.
- Feyel, F., 2003. A multilevel finite element method (fe²) to describe the response of highly non-linear structures using generalized continua. *Comput. Method. Appl. M.* 192, 3233 – 3244. Multiscale Computational Mechanics for Materials and Structures.

- Fleck, N.A., Willis, J.R., 2004. Bounds and estimates for the effect of strain gradients upon the effective plastic properties of an isotropic two-phase composite. *J. Mech. Phys. Solids*. 52, 1855 – 1888.
- Forest, S., 1998. Mechanics of generalized continua: construction by homogenization. *J. Phys. IV France* 08, Pr4–39–Pr4–48.
- Forest, S., 2002. Homogenization methods and mechanics of generalized continua - part 2. *Theoretical and Applied Mechanics* , 113–144.
- Forest, S., 2009. Micromorphic approach for gradient elasticity, viscoplasticity, and damage. *J. Eng. Mech.* 135, 117–131.
- Forest, S., Aifantis, E.C., 2010. Some links between recent gradient thermo-elasto-plasticity theories and the thermomechanics of generalized continua. *Int. J. Solids Struct.* 47, 3367 – 3376.
- Forest, S., Barbe, F., Cailletaud, G., 2000. Cosserat modelling of size effects in the mechanical behaviour of polycrystals and multi-phase materials. *Int. J. Solids Struct.* 37, 7105 – 7126.
- Forest, S., Pradel, F., Sab, K., 2001. Asymptotic analysis of heterogeneous cosserat media. *Int. J. Solids Struct.* 38, 4585 – 4608.
- Forest, S., Sab, K., 1998. Cosserat overall modeling of heterogeneous materials. *Mech. Res. Commun.* 25, 449 – 454.
- Forest, S., Sab, K., 2012. Stress gradient continuum theory. *Mech. Res. Commun.* 40, 16 – 25.
- Forest, S., Sievert, R., 2003. Elastoviscoplastic constitutive frameworks for generalized continua. *Acta Mech.* 160, 71–111.
- Forest, S., Trinh, D., 2011. Generalized continua and non-homogeneous boundary conditions in homogenisation methods. *Z. Angew. Math. Mech.* 91, 90–109.
- Frigo, M., Johnson, S.G., 2005. The design and implementation of FFTW3. *Proc. IEEE* 93, 216–231. Special issue on “Program Generation, Optimization, and Platform Adaptation”.
- Gao, X.L., Liu, M., 2012. Strain gradient solution for the eshelby-type polyhedral inclusion problem. *J. Mech. Phys. Solids*. 60, 261 – 276.
- Gao, X.L., Ma, H.M., 2009. Green’s function and eshelby’s tensor based on a simplified strain gradient elasticity theory. *Acta Mech.* 207, 163–181.
- Gao, X.L., Ma, H.M., 2010. Strain gradient solution for eshelby’s ellipsoidal inclusion problem. *Proc. Math. Phys. Eng. Sci.* .
- Gao, X.L., Park, S., 2007. Variational formulation of a simplified strain gradient elasticity theory and its application to a pressurized thick-walled cylinder problem. *Int. J. Solids Struct.* 44, 7486 – 7499.

- Gauthier, R.D., 1982. Experimental investigation on micropolar media. *Mechanics of Micropolar Media*, O. Brulin, and R.K.T. Hsieh, eds. (CISM Lecture Notes) , 395–463.
- Gauthier, R.D., Jahsman, W.E., 1975. A Quest for Micropolar Elastic Constants. *J. Appl. Mech.* 42, 369–374.
- Germain, P., 1973. The method of virtual power in continuum mechanics. part 2: Microstructure. *SIAM J. Appl. Math.* 25, 556–575.
- Gélébart, L., Mondon-Cancel, R., 2013. Non-linear extension of fft-based methods accelerated by conjugate gradients to evaluate the mechanical behavior of composite materials. *Computational Materials Science* 77, 430 – 439.
- Gélébart, L., Ouaki, F., 2015. Filtering material properties to improve fft-based methods for numerical homogenization. *J. Comput. Phys.* 294, 90–95.
- Graham, L., Baxter, S., 2001. Simulation of local material properties based on moving-window gmc. *Probab. Eng. Mech.* 16, 295–305.
- Gray, R.M., 2006. Toeplitz and circulant matrices: A review. *Foundations and Trends® in Communications and Information Theory* 2, 155–239.
- Green, A.E., Rivlin, R.S., 1964. Multipolar continuum mechanics. *Arch. Ration. Mech. Anal.* 17, 113–147.
- Guilleminot, J., Noshadravan, A., Soize, C., Ghanem, R., 2011. A probabilistic model for bounded elasticity tensor random fields with application to polycrystalline microstructures. *Computer Methods in Applied Mechanics and Engineering* 200, 1637 – 1648.
- Guilleminot, J., Soize, C., 2012. Stochastic modeling of anisotropy in multiscale analysis of heterogeneous materials: A comprehensive overview on random matrix approaches. *Mech. Mater.* 44, 35 – 46.
- Guilleminot, J., Soize, C., 2013a. On the statistical dependence for the components of random elasticity tensors exhibiting material symmetry properties. *J. Elasticity.* 111, 109–130.
- Guilleminot, J., Soize, C., 2013b. Stochastic model and generator for random fields with symmetry properties: Application to the mesoscopic modeling of elastic random media. *SIAM Multiscale Modeling & Simulation* 11, 840–870.
- Gusev, A.A., 1997. Representative volume element size for elastic composites: A numerical study. *J. Mech. Phys. Solids* 45, 1449 – 1459.
- Hashin, Z., Shtrikman, S., 1962a. On some variational principles in anisotropic and nonhomogeneous elasticity. *J. Mech. Phys. Solids.* 10, 335 – 342.
- Hashin, Z., Shtrikman, S., 1962b. A variational approach to the theory of the elastic behaviour of polycrystals. *J. Mech. Phys. Solids.* 10, 343 – 352.

- Hashin, Z., Shtrikman, S., 1963. A variational approach to the theory of the elastic behaviour of multiphase materials. *J. Mech. Phys. Solids*. 11, 127 – 140.
- Herve, E., Zaoui, A., 1993. n-layered inclusion-based micromechanical modelling. *Int. J. Eng. Sci.* 31, 1 – 10.
- Hill, R., 1963. Elastic properties of reinforced solids: Some theoretical principles. *J. Mech. Phys. Solids* 11, 357 – 372.
- Hou, T.Y., Wu, X.H., 1997. A multiscale finite element method for elliptic problems in composite materials and porous media. *J. Comput. Phys.* 134, 169 – 189.
- Huet, C., 1990. Application of variational concepts to size effects in elastic heterogeneous bodies. *J. Mech. Phys. Solids* 38, 813–841.
- İeşan, D., 1971. On saint-venant's problem in micropolar elasticity. *Int. J. Eng. Sci.* 9, 879 – 888.
- Jaynes, E.T., 1957a. Information theory and statistical mechanics. *Phys. Rev.* 106, 620 – 630.
- Jaynes, E.T., 1957b. Information theory and statistical mechanics. ii. *Phys. Rev.* 108, 171 – 190.
- Kanit, T., Forest, S., Galliet, I., Mounoury, V., Jeulin, D., 2003. Determination of the size of the representative volume element for random composites: statistical and numerical approach. *Int. J. Solids Struct.* 40, 3647 – 3679.
- Keller, J.B., Rubinfeld, L.A., Molyneux, J.E., 1967. Extremum principles for slow viscous flows with applications to suspensions. *Journal of Fluid Mechanics* 30, 97–125.
- Koiter, W., 1964. Couple stresses in the theory of elasticity, i and ii. *Proc. K. Ned. Akad. Wet. (B)* 67, 17–44.
- Kolotilina, L.Y., Yeremin, A.Y., 1993. Factorized sparse approximate inverse preconditionings i. theory. *SIAM J. Matrix Anal. Appl.* 14, 45–58.
- Kröner, E., 1977. Bounds for effective elastic moduli of disordered materials. *J. Mech. Phys. Solids* 25, 137 – 155.
- Lakes, R., 1986. Experimental microelasticity of two porous solids. *Int. J. Solids Struct.* 22, 55 – 63.
- Lakes, R., Drugan, W.J., 2015. Bending of a cosserat elastic bar of square cross section: Theory and experiment. *J. Appl. Mech.* .
- Lakes, R.S., 1983. Size effects and micromechanics of a porous solid. *J. Mater. Sci.* 18, 2572–2580.
- Lam, D., Yang, F., Chong, A., Wang, J., Tong, P., 2003. Experiments and theory in strain gradient elasticity. *J. Mech. Phys. Solids*. 51, 1477 – 1508.

- Lebensohn, R.A., Kanjarla, A.K., Eisenlohr, P., 2012. An elasto-viscoplastic formulation based on fast fourier transforms for the prediction of micromechanical fields in polycrystalline materials. *Int. J. Plast.* 32–33, 59 – 69.
- Lebowitz, J.L., 1964. Exact solution of generalized percus-yevick equation for a mixture of hard spheres. *Phys. Rev.* 133, A895–A899.
- Li, X., Liu, Q., 2009. A version of hill’s lemma for cosserat continuum. *Acta Mech. Sin.* 25, 499–506.
- Li, X., Liu, Q., Zhang, J., 2010a. A micro–macro homogenization approach for discrete particle assembly – cosserat continuum modeling of granular materials. *Int. J. Solids Struct.* 47, 291 – 303.
- Li, X., Zhang, J., Zhang, X., 2011a. Micro-macro homogenization of gradient-enhanced cosserat media. *Eur. J. Mech. A. Solids.* 30, 362 – 372.
- Li, X., Zhang, X., Zhang, J., 2010b. A generalized hill’s lemma and micromechanically based macroscopic constitutive model for heterogeneous granular materials. *Comput. Method. Appl. M.* 199, 3137 – 3152.
- Li, Y., Waas, A.M., Arruda, E.M., 2011b. A closed-form, hierarchical, multi-interphase model for composites—derivation, verification and application to nanocomposites. *Journal of the Mechanics and Physics of Solids* 59, 43 – 63.
- Liu, M., Gao, X.L., 2013. Strain gradient solution for the eshelby-type polygonal inclusion problem. *Int. J. Solids Struct.* 50, 328 – 338.
- Ma, H., Gao, X.L., Reddy, J., 2008. A microstructure-dependent timoshenko beam model based on a modified couple stress theory. *J. Mech. Phys. Solids.* 56, 3379 – 3391.
- Ma, H., Hu, G., 2007. Eshelby tensors for an ellipsoidal inclusion in a microstretch material. *Int. J. Solids Struct.* 44, 3049 – 3061.
- Ma, H.M., Gao, X.L., 2009. Eshelby’s tensors for plane strain and cylindrical inclusions based on a simplified strain gradient elasticity theory. *Acta Mech.* 211, 115–129.
- Ma, H.M., Gao, X.L., 2014. A new homogenization method based on a simplified strain gradient elasticity theory. *Acta Mech.* 225, 1075–1091.
- Markov, K.Z., Willis, J.R., 1998. On the two-point correlation function for dispersions of nonoverlapping spheres. *Math. Models Methods Appl. Sci.* 08, 359–377.
- Mühlhaus, H.B., Vardoulakis, I., 1987. The thickness of shear bands in granular materials. *Géotechnique* 37, 271–283.
- Mühlich, U., Zybelle, L., Kuna, M., 2012. Estimation of material properties for linear elastic strain gradient effective media. *Eur. J. Mech. A. Solids.* 31, 117 – 130.

- Michel, J., Suquet, P., 2003. Nonuniform transformation field analysis. *Int. J. Solids Struct.* 40, 6937 – 6955. Special issue in Honor of George J. Dvorak.
- Michel, J.C., Moulinec, H., Suquet, P., 2001. A computational scheme for linear and non-linear composites with arbitrary phase contrast. *Int. J. Numer. Methods Eng.* 52, 139–160.
- Mindlin, R., 1965. Second gradient of strain and surface-tension in linear elasticity. *Int. J. Solids Struct.* 1, 417 – 438.
- Mindlin, R., Eshel, N., 1968. On first strain-gradient theories in linear elasticity. *Int. J. Solids Struct.* 4, 109 – 124.
- Mindlin, R.D., 1964. Micro-structure in linear elasticity. *Arch. Ration. Mech. Anal.* 16, 51–78.
- Mindlin, R.D., Tiersten, H.F., 1962. Effects of couple-stresses in linear elasticity. *Arch. Ration. Mech. Anal.* 11, 415–448.
- Moakher, M., Norris, A.N., 2006. The closest elastic tensor of arbitrary symmetry to an elasticity tensor of lower symmetry. *J. Elasticity.* , 215–263.
- Monchiet, V., Bonnet, G., 2010. Inversion of higher order isotropic tensors with minor symmetries and solution of higher order heterogeneity problems. *Proc. Math. Phys. Eng. Sci.*
- Monchiet, V., Bonnet, G., 2012. A polarization-based fft iterative scheme for computing the effective properties of elastic composites with arbitrary contrast. *Int. J. Numer. Methods Eng.* 89, 1419–1436.
- Monetto, I., Drugan, W., 2004. A micromechanics-based nonlocal constitutive equation for elastic composites containing randomly oriented spheroidal heterogeneities. *J. Mech. Phys. Solids.* 52, 359 – 393.
- Moreau, J.J., 1979. Duality characterization of strain tensor distributions in an arbitrary open set. *Journal of Mathematical Analysis and Applications* 72, 760–770.
- Mori, T., Tanaka, K., 1973. Average stress in matrix and average elastic energy of materials with misfitting inclusions. *Acta Metall.* 21, 571 – 574.
- Moulinec, H., Suquet, P., 1994. A fast numerical method for computing the linear and nonlinear properties of composites. *C. R. Acad. Sci. Iib. Mec.* 318, 1417–1423.
- Moulinec, H., Suquet, P., 1998. A numerical method for computing the overall response of nonlinear composites with complex microstructure. *Comput. Method. Appl. M.* 157, 69–94.
- Neff, P., Münch, I., Ghiba, I.D., Madeo, A., 2016. On some fundamental misunderstandings in the indeterminate couple stress model. a comment on recent papers of a.r. hadjesfandiari and g.f. dargush. *International Journal of Solids and Structures* 81, 233–243.
- Noshadravan, A., Ghanem, R., Guillemot, J., Atodaria, I., Peralta, P., 2013. Validation of a probabilistic model for mesoscale elasticity tensor of random polycrystals. *International Journal for Uncertainty Quantification* 3, 73–100.

- Nozaki, H., Taya, M., 2000. Elastic fields in a polyhedral inclusion with uniform eigenstrains and related problems. *J. Appl. Mech.* 68, 441–452.
- Odegard, G., Clancy, T., Gates, T., 2005. Modeling of the mechanical properties of nanoparticle/polymer composites. *Polymer* 46, 553–562.
- Ostoja-Starzewski, M., 1994. Micromechanics as a basis of continuum random fields. *Appl. Mech. Rev.* 47, S221–S230.
- Ostoja-Starzewski, M., 1998. Random field models of heterogeneous materials. *Int. J. Solids Struct.* 35, 2429–2455.
- Ostoja-Starzewski, M., 2006. Material spatial randomness: From statistical to representative volume element. *Probab. Eng. Mech.* 21, 112–132.
- Ostoja-Starzewski, M., 2007. *Microstructural Randomness and Scaling in Mechanics of Materials*. Chapman and Hall/CRC.
- Park, S.K., Gao, X.L., 2006. Bernoulli–euler beam model based on a modified couple stress theory. *J. Micromech. Microeng.* 16, 2355.
- Park, S.K., Gao, X.L., 2007. Variational formulation of a modified couple stress theory and its application to a simple shear problem. *Z. Angew. Math. Phys.* 59, 904–917.
- Percus, J.K., Yevick, G.J., 1958. Analysis of classical statistical mechanics by means of collective coordinates. *Phys. Rev.* 110, 1–13.
- Poirion, F., Soize, C., 1995. Numerical methods and mathematical aspects for simulation of homogeneous and non homogeneous gaussian vector fields, in: Krée, P., Wedig, W. (Eds.), *Probabilistic Methods in Applied Physics*. Springer Berlin Heidelberg, Berlin, Heidelberg, pp. 17–53.
- Polizzotto, C., 2014. Stress gradient versus strain gradient constitutive models within elasticity. *Int. J. Solids Struct.* 51, 1809–1818.
- Polizzotto, C., 2016. Variational formulations and extra boundary conditions within stress gradient elasticity theory with extensions to beam and plate models. *International Journal of Solids and Structures* 80, 405 – 419.
- Rasmussen, C.E., Williams, C.K.I., 2005. *Gaussian Processes for Machine Learning (Adaptive Computation and Machine Learning)*. The MIT Press.
- Sab, K., 1992. On the homogenization and the simulation of random materials. *Eur. J. Mech. A. Solids* 11, 585–607.
- Sab, K., Legoll, F., Forest, S., 2016. Stress gradient elasticity theory: Existence and uniqueness of solution. *Journal of Elasticity* 123, 179–201.
- Sandru, N., 1966. On some problems of the linear theory of the asymmetric elasticity. *Int. J. Eng. Sci.* 4, 81 – 94.

- Sena, M., Ostoja-Starzewski, M., Costa, L., 2013. Stiffness tensor random fields through upscaling of planar random materials. *Probab. Eng. Mech.* 34, 131–156.
- Shannon, C.E., 1948. A mathematical theory of communication. *Bell Sys. Tech. J.* 27, 379–423, 623–656.
- Sharma, P., Dasgupta, A., 2002. Average elastic fields and scale-dependent overall properties of heterogeneous micropolar materials containing spherical and cylindrical inhomogeneities. *Phys. Rev. B* 66, 224110.
- Shinozuka, M., 1971. Simulation of multivariate and multidimensional random processes. *The Journal of the Acoustical Society of America* 49, 357–368.
- Shinozuka, M., Deodatis, G., 1991. Simulation of stochastic processes by spectral representation. *Appl. Mech. Rev.* 44.
- Shinozuka, M., Deodatis, G., 1996. Simulation of multi-dimensional Gaussian stochastic fields by spectral representation. *Appl. Mech. Rev.* 49.
- Shu, J.Y., King, W.E., Fleck, N.A., 1999. Finite elements for materials with strain gradient effects. *Int. J. Numer. Methods Eng.* 44, 373–391.
- Šmilauer, V., Bažant, Z.P., 2010. Identification of viscoelastic c-s-h behavior in mature cement paste by fft-based homogenization method. *Cem. Concr. Res.* 40, 197 – 207.
- Smyshlyaev, V., Cherednichenko, K., 2000. On rigorous derivation of strain gradient effects in the overall behaviour of periodic heterogeneous media. *J. Mech. Phys. Solids.* 48, 1325 – 1357.
- Smyshlyaev, V., Fleck, N., 1994. Bounds and estimates for linear composites with strain gradient effects. *J. Mech. Phys. Solids.* 42, 1851 – 1882.
- Smyshlyaev, V., Fleck, N., 1996. The role of strain gradients in the grain size effect for polycrystals. *J. Mech. Phys. Solids.* 44, 465 – 495.
- Smyshlyaev, V.P., Fleck, N.A., 1995. Bounds and estimates for the overall plastic behaviour of composites with strain gradient effects. *Proc. R. Soc. Lond., A* 451, 795–810.
- Soize, C., 2000. A nonparametric model of random uncertainties for reduced matrix models in structural dynamics. *Probabilist. Eng. Mech.* 15, 277 – 294.
- Soize, C., 2006. Non-gaussian positive-definite matrix-valued random fields for elliptic stochastic partial differential operators. *Comput. Method. Appl. M.* 195, 26 – 64.
- Suhubi, E., Eringen, A., 1964. Nonlinear theory of micro-elastic solids—ii. *Int. J. Eng. Sci.* 2, 389 – 404.
- Sun, Z., Wang, X., Soh, A., Wu, H., Wang, Y., 2007. Bending of nanoscale structures: Inconsistency between atomistic simulation and strain gradient elasticity solution. *Computational Materials Science* 40, 108 – 113.

- Ta, Q.A., Clouteau, D., Cottureau, R., 2010. Modeling of random anisotropic elastic media and impact on wave propagation. *European Journal of Computational Mechanics* 19, 241–253.
- Talbot, D.R.S., Willis, J.R., 1985. Variational principles for inhomogeneous non-linear media. *IMA J. Appl. Math.* 35, 39–54.
- Tejchman, J., Wu, W., 1993. Numerical study on patterning of shear bands in a cosserat continuum. *Acta Mech.* 99, 61–74.
- Torquato, S., 2002. *Random Heterogeneous Materials*. Springer, New York.
- Torquato, S., Stell, G., 1985. Microstructure of two-phase random media. v. the n-point matrix probability functions for impenetrable spheres. *J. Chem. Phys.* 82, 980–987.
- Toupin, R.A., 1962. Elastic materials with couple-stresses. *Arch. Ration. Mech. Anal.* 11, 385–414.
- Triantafyllidis, N., Bardenhagen, S., 1996. The influence of scale size on the stability of periodic solids and the role of associated higher order gradient continuum models. *J. Mech. Phys. Solids.* 44, 1891 – 1928.
- Trinh, D.K., Janicke, R., Auffray, N., Diebels, S., Forest, S., 2012. Evaluation of generalized continuum substitution models for heterogeneous materials. *Int. J. Multiscale Comput. Eng.* 10, 527–549.
- Truesdell, C., Toupin, R., 1960. The classical field theories, in: Flügge, S. (Ed.), *Principles of Classical Mechanics and Field Theory / Prinzipien der Klassischen Mechanik und Feldtheorie*. Springer Berlin Heidelberg, Berlin, Heidelberg, pp. 226–858.
- Verlet, L., Weis, J.J., 1972. Equilibrium theory of simple liquids. *Phys. Rev. A* 5, 939–952.
- Walpole, L.J., 1984. Fourth-rank tensors of the thirty-two crystal classes: Multiplication tables. *Proc. R. Soc. Lond., A* 391, 149–179.
- Wertheim, M.S., 1963. Exact solution of the percus-yevick integral equation for hard spheres. *Phys. Rev. Lett.* 10, 321–323.
- Willis, J., 1977. Bounds and self-consistent estimates for the overall properties of anisotropic composites. *J. Mech. Phys. Solids.* 25, 185 – 202.
- Willis, J., 1982. Elasticity theory of composites, in: Hopkins H.G., S.M. (Ed.), *Mechanics of Solids: The R. Hill 60th Anniversary Volume.* Pergamon Press, Oxford, pp. 653–686.
- Willis, J., 1991. On methods for bounding the overall properties of nonlinear composites. *J. Mech. Phys. Solids.* 39, 73 – 86.
- Willis, J.R., 1983. The Overall Elastic Response of Composite Materials. *J. Appl. Mech.* 50, 1202.
- Willet, F., 2015. Fourier-based schemes for computing the mechanical response of composites with accurate local fields. *Comptes Rendus Mécanique* 343, 232–245.

- Willot, F., Abdallah, B., Pellegrini, Y.P., 2014. Fourier-based schemes with modified green operator for computing the electrical response of heterogeneous media with accurate local fields. *Int. J. Numer. Methods Eng.* 98, 518–533.
- Xun, F., Hu, G., Huang, Z., 2004a. Effective in plane moduli of composites with a micropolar matrix and coated fibers. *Int. J. Solids Struct.* 41, 247 – 265.
- Xun, F., Hu, G., Huang, Z., 2004b. Size-dependence of overall in-plane plasticity for fiber composites. *Int. J. Solids Struct.* 41, 4713 – 4730.
- Yang, F., Chong, A., Lam, D., Tong, P., 2002. Couple stress based strain gradient theory for elasticity. *Int. J. Solids Struct.* 39, 2731 – 2743.
- Yue, X., E, W., 2007. The local microscale problem in the multiscale modeling of strongly heterogeneous media: Effects of boundary conditions and cell size. *J. Comput. Phys.* 222, 556 – 572.
- Zeller, R., Dederichs, P.H., 1973. Elastic constants of polycrystals. *physica status solidi (b)* 55, 831–842.
- Zeman, J., Vondřejc, J., Novák, J., Marek, I., 2010. Accelerating a fft-based solver for numerical homogenization of periodic media by conjugate gradients. *J. Comput. Phys.* 229, 8065 – 8071.
- Zhang, X., Sharma, P., 2005. Inclusions and inhomogeneities in strain gradient elasticity with couple stresses and related problems. *Int. J. Solids Struct.* 42, 3833 – 3851.
- Zheng, Q., Zhao, Z.H., 2004. Green's function and eshelby's fields in couple-stress elasticity. *Int. J. Multiscale Comput. Eng.* 2.
- Zhou, S., Li, A., Wang, B., 2016. A reformulation of constitutive relations in the strain gradient elasticity theory for isotropic materials. *Int. J. Solids Struct.* 80, 28–37.